U B
**Universitat Autònoma
de Barcelona**

Electrodeposition of nanostructured nickel-platinum-based electrocatalysts for hydrogen energy systems

Tesi doctoral

Konrad Eiler

Programa de doctorat en Ciència de Materials

Directors:

Eva Pellicer Vilà

Jordi Sort Viñas

Departament de Física

Facultat de Ciències

2021

U B

**Universitat Autònoma
de Barcelona**

Memòria presentada per aspirar al Grau de Doctor per

Konrad Eiler

Vist i plau

Eva Pellicer Vilà   Jordi Sort Viñas

Bellaterra, 30 de juny de 2021

U B
Universitat Autònoma de Barcelona

La **Dra. Eva Pellicer Vilà**, professora agregada del Departament de Física de la Universitat Autònoma de Barcelona,

i el **Dr. Jordi Sort Viñas**, professor ICREA del Departament de Física de la Universitat Autònoma de Barcelona,

CERTIFIQUEN:

Que **Konrad Eiler** ha realitzat sota la seva direcció el treball d'investigació que s'exposa a la memòria titulada «Electrodeposition of nanostructured nickel-platinum-based electrocatalysts for hydrogen energy systems» per optar al grau de **Doctor per la Universitat Autònoma de Barcelona.**

Que el disseny dels experiments, síntesi de mostres, llur caracterització, l'anàlisi dels resultats, la redacció dels articles i d'aquesta memòria són fruit del treball d'investigació realitzat per Konrad Eiler.

I perquè així consti, signen el present certificat,

Eva Pellicer Vilà   Jordi Sort Viñas

Bellaterra, 30 de juny de 2021

Acknowledgements

Primero de todo, gracias a Eva Pellicer y Jordi Sort. Sin vosotros no hubiera sido posible nada de esto. Ha sido genial tener supervisores que dan mucho apoyo y motivación.

Gracias a todo el equipo de Física de Materials II, a Santiago Surinyach y Dolors Baró, siempre dispuestos a ayudar en lo que sea. A Pau, Jordina, Veronica y Cristina, manteniendo un ambiente genial en el despatxo des del primer día. Matteo, siempre dispuesto a todo. Aliona, mi consejera en electroquímica, y mucho más. Gracias a los antiguos Alberto, Doga y Evangelia, de cuyos defensas he podido aprender, y Shauna. A los nuevos, Carla Sofia, Aleksa, Michael, Zhengwei, Erdem. Y a todo el resto, de quienes he podido disfrutar de una u otra manera: Chen, Julius, Patxi, Alex, Pablo, Vassil. Gracias a Jordi M., Dori y Lara por la ayuda con la burocracia.

Special thanks to Maria Lekka and Caterina Zanella for running the show. Thanks go to everyone involved in obtaining the funding for the ITN, welcoming us to their institutions, etc. All of you made it possible for me to be able to do a PhD with so much support, and to continue profiting from this network in the future. Thanks to Halina Krawiec, Lars Fast and Peter Leisner for their hospitality during my secondments.

And of course, thanks to all my fellow companions of the mCBEEs project: Sabrina, Salil, Don, Sajjad, Live, Iryna, Koushik, Ivan, Maurizio, Bruno, Jiaen, Nourhan, Ehsan, Chinmay. Thank you all for the great times we spent together in the pre-pandemic world. Good luck with your own PhDs, I would love to attend every single defence of yours.

Gracias a los servicios internos de microscopia, análisis químico, y difracción de rayos X, y a los servicios externos del ICN2, del ICMAB, y de los CCiTUB.

Les agradezco a mis amigos y familia que compartieron este tiempo de doctorado conmigo, que me apoyaron, y que casi se alegran de mis logros más que yo mismo. Ya sabéis quiénes sois.

Abstract

Electrodeposition is a powerful and facile, yet sophisticated method for the synthesis of nanostructured electrocatalysts. The electrodeposition of nickel-platinum (Ni–Pt) thin films from aqueous media leads to the formation of nanocrystalline, single-phase alloy films with homogeneous composition. Remarkably, the composition is tuneable by simple variation of the potential used in potentiostatic deposition, in a range between 99 at% and 58 at% Ni, i.e. 1–42 at% Pt. With the addition of the amphiphilic block copolymer Pluronic P-123 in the electrolyte, micelle-assisted electrodeposition yields homogeneously mesoporous thin films with a uniform pore size of approx. 10 nm. With respect to dense films synthesised using the same parameters, the mesoporous thin films show identical composition and crystallite size. All electrodeposited Ni–Pt thin films exhibit stable performance during 200 cycles of hydrogen evolution reaction (HER) in 0.5 M H_2SO_4, where $Ni_{84}Pt_{16}$ showed the highest activity with an overpotential of –90 mV at –10 mA/cm^2.

24 h galvanostatic long-term measurements show that this overpotential initially decreases over time before it stabilises. Furthermore, the application of anodic potentials in 0.5 M H_2SO_4 provokes failure of the Ni-rich thin films due to metal dissolution. Thus, reliable long-term application in acidic media is only possible at cathodic potentials. In turn, the Ni–Pt alloy thin films are stable over a wide potential range in 1 M NaOH, and keep their catalytic activity below an irreversible passivation around 1.0 V vs Ag|AgCl. In addition, the reversible redox reaction $Ni(OH)_2 \leftrightarrow NiOOH$ is observed at lower anodic potentials. Notably, this reaction, which is of use in electrochemical supercapacitors, is enhanced by increasing the platinum content, showing that the Pt in the alloy catalyses this redox reaction.

Another potential application of single-phase Ni–Pt alloy thin films are magnetic nano- or microelectromechanical systems, where magnetic and mechanical properties are important. Due to the single-phase nature of the alloy films, saturation magnetisation and Curie temperature scale directly with the Ni content. Interestingly, the same is true for the coercivity of the mesoporous thin films, allowing thus to tune all of these parameters by the

electrodeposition potential. A Curie temperature near room temperature is found for $Ni_{58}Pt_{42}$.

For application at oxygen reduction reaction (ORR), Pt–Ni and Pt–Ni–Mo nanoparticles are electrodeposited onto a gas diffusion layer for proton exchange membrane fuel cells (PEMFC), unifying synthesis and application of the electrocatalyst onto the electrode in a single step. Particle sizes ranging from 40 to 80 nm are obtained for particles with different compositions. The pulse electrodeposition process accomplishes the deposition of nanoparticles onto the most active sites of the substrate leading to very high mass activities at ORR, the highest of which were observed for $Pt_{67}Ni_{33}$ and $Pt_{66}Ni_{32}Mo_2$. These compositions also showed the best durability in PEMFC.

X

Resum

L'electrodeposició és un mètode potent i fàcil, encara que sofisticat, per a la síntesi d'electrocatalitzadors nanoestructurats. L'electrodeposició de capes fines de níquel-platí (Ni–Pt) a partir d'un medi aquós dóna lloc a la formació de capes d'aliatge amb estructura nanocristal·lina, monofàsica, i de composició homogènia. La composició és ajustable tot variant el potencial aplicat durant la deposició potenciostàtica, dins d'un rang d'entre el 99 at% i el 58 at% en Ni, és a dir 1–42 at% en Pt. Amb l'addició del copolímer bloc amfifílic Pluronic P-123 a l'electròlit, l'electrodeposició assistida per micel·les dóna lloc a capes fines amb mesoporositat homogènia, amb una mida uniforma de porus de 10 nm aprox. En relació a les capes denses sintetitzades mitjançant paràmetres idèntics, aquestes mostren la mateixa composició i mida de cristall. Totes les capes fines de Ni–Pt obtingudes per electrodeposició presenten un rendiment estable durant 200 cicles envers a la reacció d'evolució d'hidrogen (HER) en 0.5 M H_2SO_4, essent la mostra $Ni_{84}Pt_{16}$ la que va mostrar l'activitat més elevada amb un sobrepotencial de –90 mV a –10 mA/cm^2.

En mesures galvanostàtiques a llarg termini, de 24 h, es veu que el sobrepotencial decreix inicialment amb el temps abans d'estabilitzar-se. A més a més, l'aplicació de potencials anòdics en el medi 0.5 M H_2SO_4 provoca una pèrdua d'activitat notòria de les capes riques en Ni a causa de la dissolució d'aquest. Així doncs, l'aplicació fiable d'aquestes capes en medi àcid a llarg termini queda restringida a potencials catòdics. Per altra banda, les capes fines d'aliatge Ni–Pt romanen estables en un rang ampli de potencials en 1 M NaOH, en el qual mantenen llur activitat catalítica abans que tingui lloc una passivació irreversible al voltant d'1.0 V vs Ag|AgCl. A més, la reacció redox reversible $Ni(OH)_2 \leftrightarrow NiOOH$ s'observa a potencials anòdics més baixos. Convé remarcar que aquesta reacció, que és útil en supercondensadors electroquímics, millora en incrementar el contingut de platí, bo i demostrant-se que el Pt de l'aliatge catalitza aquesta reacció redox.

Una altra possible aplicació de les capes fines de l'aliatge monofàsic Ni–Pt és en sistemes nano- o microelectromecànics magnètics, on les propietats magnètiques i mecàniques són rellevants. Gràcies a la naturalesa monofàsica de les capes d'aliatge, la magnetització de saturació i la temperatura

de Curie són directament proporcionals al contingut de Ni. Així mateix, la mateixa dependència s'observa amb la coercitivitat de les capes fines mesoporoses, la qual cosa permet ajustar a voluntat tots aquests paràmetres amb el potencial d'electrodeposició. S'ha determinat que la temperatura de Curie és propera a la temperatura ambient en capes de composició $Ni_{58}Pt_{42}$.

Pel que fa la reacció de reducció d'oxigen (ORR), s'han electrodipositat nanopartícules de Pt–Ni i Pt–Ni–Mo en una capa de difusió de gasos per a la pila de combustible de membrana d'intercanvi de protons (PEMFC), tot unificant la síntesi i l'aplicació de l'electrocatalitzador sobre l'elèctrode en un únic pas. Les mides de partícula obtingudes per a partícules amb composicions diferents es troben entre els 40 i els 80 nm. El procés d'electrodeposició per polsos emprat permet la deposició de nanopartícules en els punts més actius del substrat, la qual cosa dóna lloc a activitats de massa d'ORR molt elevades, essent les majors en nanopartícules de $Pt_{67}Ni_{33}$ i $Pt_{66}Ni_{32}Mo_2$. Els elèctrodes amb nanopartícules d'aquestes composicions també van presentar una millor durabilitat en els estudis amb PEMFC.

Preface

This thesis is structured into the following chapters:

1 Motivation A short introduction into the topic, showing the broader perspective and motivation of the work.

2 Fundamentals A description of the fundamental principles and state-of-the-art technology which make up the basis this work adds on to. This includes the basic electrocatalytic reactions, the electrodeposition as a synthesis method, nanoporosity, and the Ni–Pt system.

3 Objectives The main objectives this work is aimed to accomplish.

4 Experimental A detailed record of the electrochemical synthesis and the electrochemical characterisation performed within this work.

5 Results A compilation of the articles prepared as part of this work.

6 General discussion A general, broader discussion of the results aimed at aspects which were not discussed in the articles.

7 Conclusions The most important conclusions of this work, listed in a point-by-point style.

8 Outlook A list of a number of aspects which can be tackled in the future in continuation of this work.

Contents

1 Motivation

With increasing national and international limitations on greenhouse gas emissions and the global striving against the climate change, hydrogen energy is one of the few forms of energy that have the potential to becoming established at large scale and supplying the majority of the global energy demand [1, 2]. While greenhouse gas emissions of hydrogen energy systems are zero, further development is needed to reach sufficient sustainability in terms of service life and performance. In addition, a more rational and efficient use of the precious metal platinum (Pt) is envisaged [3]. The most important property, though, is that hydrogen is never consumed, nor is it produced, even if we often commonly refer to "hydrogen production". In reality, in a "green" cycle, hydrogen is only converted between hydrogen gas and water, and therefore classified as an energy vector. This energy cycle is free of emissions and does not consume any resources [4, 5]. However, there is no natural source of molecular hydrogen, which thus needs to be extracted from water, hydrocarbons, or other molecules.

Consequently, the hydrogen energy cycle has two essential processes: the conversion of water to gaseous hydrogen, which is done in an electrolyser, and the conversion of hydrogen gas to water in a fuel cell, where an electric current is generated. Many fuel cell systems are able to run in a reverse mode, allowing to combine both functions in the same apparatus. Apart from this ideal energy cycle, the majority of hydrogen gas is—to this date—still won by reforming of fossil fuels [6].

Pt is one of the most crucial constituents in hydrogen energy systems: it is almost indispensible as an electrocatalyst for the electrochemical reactions in those systems. Alternatives to Pt exist, however, those alternatives lack in either efficiency, durability, or limit their application to alkaline media with less favourable performance [7]. Pollet et al. argued that it is not necessary to establish a completely Pt-free infrastructure in order to satisfy the global demand for fuel cell vehicles; an efficient use of Pt in fuel cells can actually match the Pt usage of catalysts in combustion engine vehicles. The use of Pt itself is therefore not a showstopper for green hydrogen technology, although its usage should be effectively reduced [8]. Effort is therefore made

to decrease the use of Pt, and to (partially) replace it with more abundant elements in hydrogen technology [9, 10].

This work aims to improve the efficiency of the catalytic processes needed in the hydrogen energy cycle, using nanostructured electrocatalysts produced in a simple and cost-efficient synthesis route. To this end, nickel-platinum (Ni-Pt) catalysts are synthesised by electrodeposition. The principal approaches followed in this work to maximise the efficiency of the catalysts is by alloying Pt in order to optimise its electronic properties, and by nanostructuring the catalyst to provide it with high surface-to-volume (S/V) ratios (since catalysis is a surface process), such as mesoporous thin films, or nanoparticles (NPs). Other than the efficiency of the catalysts, one of the main foci is their corrosion resistance in the relevant environments, in order to evaluate their sustainability.

Apart from the main focus on catalytic reactions, and due to the choice of the ferromagnetic element Ni as alloying element for Pt, magnetic characterisation of the synthesis products was exploited in order to determine other possible areas of applications such as magnetically actuated microelectromechanical systems (MEMS). Ferromagnetic mesoporous or, more generally, nanoporous alloys are also of interest for water remediation [11] as well as magneto-electric effects and magneto-ionics in particular, mostly due to their high surface area [12, 13].

2 Fundamentals

2.1 Electrocatalysis for hydrogen energy

Hydrogen can be seen as a chemical form of energy storage. The chemical energy, stored in the bonds of hydrogen molecules, is much higher than the one stored in water molecules. Thus, the difference in enthalpy between hydrogen and oxygen molecules on the one hand, and water molecules on the other hand, can be transformed into an electric current. The standard enthalpy of formation of water, i.e. the chemical energy that becomes available in the reaction, amounts to –290 J/mol [14].

The two basic instruments of the hydrogen energy cycle, the electrolyser and the fuel cell, rely on four essential catalytic reactions. In the electrolyser, where hydrogen gas is generated from an aqueous electrolyte, the hydrogen evolution reaction (HER) and the oxygen evolution reaction (OER) are taking place.

In a fuel cell, the corresponding catalytic reactions are the oxygen reduction reaction (ORR) and the hydrogen oxidation reaction (HOR). Both electrolysis and fuel cell operation can be theoretically performed at any pH, while most studies focus on either acidic or alkaline media. However, kinetics are more favourable in acidic media, so that studies in alkaline media are mostly done for electrocatalysts which are not stable under acidic conditions [15].

In electrocatalysis in aqueous media, potentials are always referred to the reversible hydrogen electrode (RHE). This electrode is pH-dependent, in contrast to the standard hydrogen electrode (SHE), in which standard potentials are given. Their relation is given by Equation 2.1.

$$E_{\mathrm{RHE}} = E_{\mathrm{SHE}} - 0.059\ \mathrm{pH} \tag{2.1}$$

An overview of all important parameters used in this work is given in Table 2.1.

Table 2.1: Parameters and corresponding units used in this work.

| Parameter	Symbol	Unit
Catalyst loading		mg/cm^2
Double-layer capacitance	C_{dl}	µF
Electric charge	Q	µC
Hydrogen adsorption charge for a monlayer	q_{ML}	µC/cm^2
Charge-transfer coefficient	a	
Current	i	mA
Geometric current density	j	mA/cm^2
Exchange current density	j_0	mA/cm^2
Diffusion-limited current density	j_D	mA/cm^2
Kinetic current density	j_k	mA/cm^2
Limiting current density	j_{lim}	mA/cm^2
Electrochemically active surface area	ECSA	cm^2/mg
Mass activity	MA	mA/mg
Specific activity	SA	mA/cm^2
Current efficiency	η	
Magnetic field strength	H	Oe
Magnetic coercivity	H$_c$	Oe
Magnetisation	M	emu/g
Remanent magnetisation	M$_r$	emu/g
Saturation magnetisation	M$_s$	emu/g
Molar mass	M	g/mol
Potential	E	V
Half-wave potential	$E_{1/2}$	V
Standard electrode potential	E_0	V
Equilibrium potential	E_{eq}	V
Overpotential	η	mV
Overpotential at 10 mA/cm^2 catalytic activity	η_{10}	mV
Roughness factor	R_f	
Tafel slope	b	mV
Temperature	T	K
Curie temperature	T$_C$	K
Time	t	s

2.1.1 Water electrolysis

While steam reforming from fossil fuels is the main route for hydrogen production, there exist several other processes to isolate hydrogen from specific compounds [6]. Among the more environmentally friendly alternatives, there is biomass gasification, methane pyrolysis, and water electrolysis, which is investigated here. Among the advantages of water electrolysis over the other processes is the abundance of water and the fact that hydrogen is converted back to water when used in fuel cells, and the utilisation of electric current which itself can be won by renewable energies. However, in the case that the electric current employed in hydrogen production is not won from renewable energies, the process cannot be considered as entirely emission-free.

The generation of hydrogen gas in an electrolyser is done by water electrolysis. In acidic media, HER is described by the reduction of protons (Equation 2.2). By definition, the standard potential for this reaction is 0 V vs RHE. The energy needed in order to generate hydrogen can be delivered by electrical energy, but also by sunlight irradiation, referred to as photoelectrocatalysis [9, 16–18].

$$2H^+ + 2e^- \rightarrow H_2 \tag{2.2}$$

The reaction is therefore dependent on the concentration of protons in the electrolyte (pH). In alkaline electrolytes, HER takes place under formation of hydroxide anions from water (Equation 2.3).

$$2H_2O + 2e^- \rightarrow H_2 + 2OH^- \tag{2.3}$$
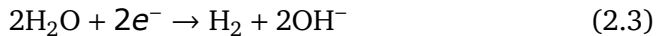
While HER is the key reaction in studies on newly developed catalyst materials, OER is the complementary process, described by the formation of oxygen gas and protons from water for the acidic case (Equation 2.4).

$$2H_2O \rightarrow O_2 + 4H^+ + 4e^- \tag{2.4}$$
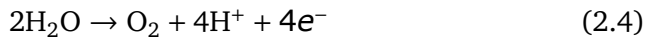
In alkaline media, gaseous oxygen is formed from hydroxide anions (Equation 2.5).

$$4OH^- \rightarrow O_2 + 2H_2O + 4e^- \tag{2.5}$$
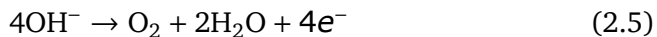
The mechanism of HER on a metal (Me) usually follows three principal steps named after Volmer, Heyrovsky, and Tafel (Equation 2.6–2.8). These reactions are responsible for the kinetics of the HER, and the rate-determining step can be determined from experimentally obtained data (see section 2.1.3).

$$\begin{array}{lrcll} \text{Volmer} & \mathrm{Me} + \mathrm{H^+} + e^- & \rightarrow & \mathrm{MeH_{ads}} & (2.6) \\ \text{Heyrovsky} & \mathrm{MeH_{ads}} + \mathrm{H^+} + e^- & \rightarrow & \mathrm{Me} + \mathrm{H_2} & (2.7) \\ \text{Tafel} & 2\mathrm{MeH_{ads}} & \rightarrow & 2\mathrm{Me} + \mathrm{H_2} & (2.8) \end{array}$$
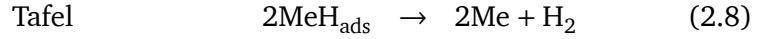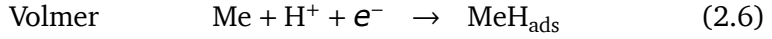
2.1.2 The proton exchange membrane fuel cell

The proton exchange membrane fuel cell (PEMFC) is based on the conduction of protons through a membrane between the anode and the cathode. The cathode reaction is the ORR, which exhibits less favourable kinetics than the HOR (Equation 2.9) at the anode and is therefore at the core of investigations [7]. The environment in PEMFC is acidic, and the reduction of oxygen takes place by recombination with protons through a four-electron pathway (Equation 2.10). In acidic media, the potential of this reaction is 1.23 V vs RHE [14]. An alternative, undesired reaction is the partial reduction of oxygen to hydrogen peroxide instead of water.
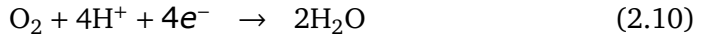
$$\begin{array}{rcll} \mathrm{H_2} & \rightarrow & 2\mathrm{H^+} + 2e^- & (2.9) \\ \mathrm{O_2} + 4\mathrm{H^+} + 4e^- & \rightarrow & 2\mathrm{H_2O} & (2.10) \end{array}$$

The PEMFC has two sides, the cathode where the ORR takes place, and the anode where the HOR takes place, separated by the name-giving proton exchange membrane (PEM) which is a proton conductive polymer film. Cathode and anode side are assembled in identical ways, having the catalyst layer, usually containing carbon-supported platinum (Pt/C) in contact with the membrane, followed by the gas diffusion layer (GDL) made of carbon cloth. The cell is closed by thin metallic flow plates which dispose of channels for the gas supply, and metallic bipolar plates, which are used for electrical connection, and to establish a homogeneous distribution of pressure and temperature over the fuel cell's active area (Figure 2.1). Gaskets are used to ensure leak tightness of the cell. The inner part of the cell located in between the flow plates is also referred to as membrane electrode assembly (MEA). The fuel cell is connected to a control module which regulates the operating conditions (see section 4.4). While pure hydrogen gas is required at the anode, the cathode side can work with the oxygen contained in ambient air. However, higher power outputs are generated if pure oxygen gas is used.

For optimal functioning, the PEMFC relies not only on a highly active electrocatalyst, but also on a correct assembly and morphology of the catalyst in

order to maximise the number of triple phase boundaries (TPB). The TPBs are those points where catalyst, PEM, and gas phase are in contact.

The principal unique characteristic of the PEMFC is its operating temperature below 100 °C. In most applications, several fuel cells are assembled into stacks in order to accumulate the required power for the respective application. This approach, together with the possibility to freely scale the fuel cell unit itself, allows the adaption to practically any kind of electronic application. A number of commercial applications exist, most notably in the automotive sector, such as in the Toyota Mirai motor vehicle [19], and full fuel cell stacks in different dimensions are commercially available by a number of companies. Technological development goals were set by the U.S. Department of Energy (DoE) in 2015. As of then, the state of the art in terms of power density was 640 W/l, with an ultimate target of 850 W/l. Additionally, the peak energy efficiency (in the PEMFC, a certain amount of energy is transformed into heat) was envisaged to be increased from 60 to 70 % [20].

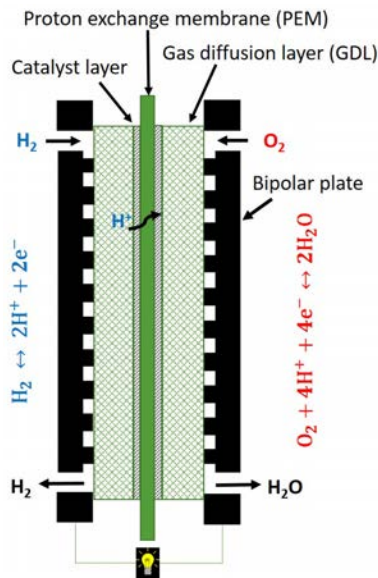Figure 2.1: Schematic representation of a PEMFC including anodic (left) and cathodic reactions (right). Courtesy of L. Mølmen [21].

Apart from decreasing the absolute amount of Pt used, the long-term performance of commercial Pt-based electrocatalysts for ORR is one of the main issues [7]. In their 2020 target, the DoE allows a performance loss of up to 40% after an accelerated degradation test (ADT) protocol. Hence, there still

remains a tremendous potential for improvement in this respect, and recent works show that a quasi-elimination of this performance loss is experimentally achievable using different approaches [22–24]. One of the main causes for the performance loss, the growth of Pt NPs during operation, can be mitigated by the use of Pt alloy NPs, mostly using transition metals as alloying elements [25, 26].

In addition, computational studies based on density functional theory (DFT) allow to determine which elements, alloys, or other compounds are potential candidates as electrocatalysts for ORR (and other electrocatalytic reactions including HER) [27–29].

2.1.3 Electrocatalytic properties

One of the most significant problems for reporting the electrocatalytic activites is the translation of the measured currents into meaningful quantities, i.e. their normalisation. The simplest method is the calculation of the geometric current density j with respect to the two-dimensional surface of the electrode. Naturally, this method only returns correct current densities for perfectly plane electrodes. However, even continuous thin films produced by electrodeposition or sputtering possess a certain roughness resulting in an actual surface area which is significantly higher than their geometric surface area. For electrode structures aiming for high S/V, different ways of obtaining meaningful values of current density need to be employed. The geometric current density does, however, allow the comparison in activity among electrodes with similar or identical structures. It can also reveal the superiority of a certain structure over another, e.g. a significantly higher geometric current density measured on a porous electrode with respect to a dense electrode of the same material does not indicate a higher actual current density, but rather a higher absolute current due to a higher actual surface area.

Another method is the normalisation of the current by absolute mass of the electrode material. While this method does not take the actual surface area of the electrode into account either, it can be used to determine how efficiently the catalyst material is being used, such as to reduce the use of expensive materials. In this way, an electrode with closed (inaccessible) porosity would outperform a dense electrode with the same actual surface area, simply due to its lower mass. The mass-specific activity, or mass activity (MA) obtained in this way is mostly used for fuel cell catalysts, where it is one of the commonly reported properties.

A common method for the determination of the absolute physical surface area is the Brunauer-Emmett-Teller (BET) method, where the adsorption of gas on the surface of the electrode is measured [30]. BET usually requires a relatively large amount of material (in the milligram range) and a free-standing (i.e. substrate-free) electrode or a powder. These requirements make it inapplicable to nanostructured lab-scale electrodes as those investigated in this work.

Finally, one of the most important electrochemical properties of an electrocatalyst is therefore its electrochemically active surface area (ECSA), representing how active the catalyst's surface is with respect to a monolayer [31]. This method is able to determine the absolute area of the electrocatalyst which is actively contributing to electrochemical processes and discards inactive sites of the surface. The most popular method for measuring ECSA is by measuring the hydrogen underpotential deposition (H_{upd}) on the catalyst surface by cyclic voltammetry (CV) [30]. The adsorption and desorption charges of H (H_{ads} and H_{des}) on a Pt monolayer are taken as 210 µC/cm^2. Consequently, the relation of the integrated current measured on the H_{ads} and H_{des} peaks, and the standard monolayer charge returns the catalyst's roughness factor R_f, which represents the factor in surface area between the electrocatalyst and the monolayer (Equation 2.11). Since the H_{ads} peak is often overlaid by HER current, the integration of H_{des} is usually used to determine ECSA. In addition, the effect of the double-layer capacitance C_{dl} is taken into account by assuming a straight line in the constant-current region of the CV, i.e. by subtracting the constant current density j_{dl} originating from the double-layer capacitance (Figure 2.2).

Finally, the normalisation of the current with respect to ECSA is done by applying the roughness factor to the geometric current density, returning the specific activity (SA, Equation 2.12). If the catalyst loading, i.e. the mass of electrocatalyst, is known, the ECSA can be given in surface area per gramme of catalyst material (Equation 2.13). This is usually done for Pt-containing electrocatalysts, often disregarding the contribution of other alloying elements by solely calculating ECSA using the monolayer charge of Pt and the Pt loading. However, hydrogen adsorption charges may also be determined for other electrodes such as Ni or Ni oxides [32].

It further follows that MA can be expressed as the product of SA and ECSA (Equation 2.14). As mentioned above, this value is especially important for fuel cells, where the MA of Pt is a direct indicator for cost efficiency. MA should therefore scale directly with ECSA; a higher S/V should result in a more efficient utilisation of the catalyst material, resulting in cost reduction. Several approaches exist in order to maximise S/V, such as the synthesis of

porous materials, NPs, or thin films. Although NPs are able to reach significantly higher ECSA, their MA is comparable to thin films or other structures since NPs show considerably lower SA [33]. The choice of an electrocatalyst's nanostructure is therefore rather dependent on its application, e.g. NPs are usually used in PEMFC in order to comply with the triple phase boundary requirement.

$$R_f \quad = \quad \frac{1}{q_{\mathrm{ML}}} \int_{t(E_1)}^{t(E_2)} (j(t) - j_{\mathrm{dl}}) \, dt \qquad (2.11)$$

$$\mathrm{SA} \quad = \quad \frac{j}{R_f} \qquad (2.12)$$

$$\mathrm{ECSA} \quad = \quad \frac{R_f}{\mathrm{Catalyst \ loading}} \qquad (2.13)$$

$$\mathrm{MA} \quad = \quad \frac{j}{\mathrm{Catalyst \ loading}} = \mathrm{ECSA} \cdot \mathrm{SA} \qquad (2.14)$$

where t is time, q_{ML} is the theoretical hydrogen adsorption charge of a monolayer of same material; E_1 and E_2 are the onset and end potentials of the measured hydrogen desorption peak, respectively. It is important to note that j refers to the geometric current density.

The electrocatalytic activities of HER and ORR can be recorded via CV or linear sweep voltammetry (LSV). The kinetics of an electrocatalytic reaction, which permits to draw conclusions on the reaction mechanism, can be assessed by determination of the Tafel slope b in the low-current region of the reaction. The Tafel slope corresponds to the slope of the linear part of the curve in semi-logarithmic representation of the E–j curve (Figure 2.3), its unit is millivolt. The lower the Tafel slope, the faster the kinetics of the reaction. For HER, the value of b can reveal the rate-limiting reaction step; at the most favourable value of 30 mV, the reaction is limited by the Tafel step (Equation 2.8), 40 mV correspond to a limitation by the Heyrovsky step (Equation 2.7) and 120 mV to the Volmer step as the rate-limiting step (Equation 2.6) [34, 35]. While a Tafel slope of 30 mV is the theoretical limit for HER, any higher value of b may be the result of other influencing parameters.

Other electrocatalytic properties are dependent on the electrocatalytic reaction of interest. For HER, one of the most commonly used parameters is the overpotential η_{10} at which the geometric current density reaches 10 mA/cm^2 (cf. Figure 2.3). Note that for the case of HER, the overpotential—which is defined as the difference between the applied potential and
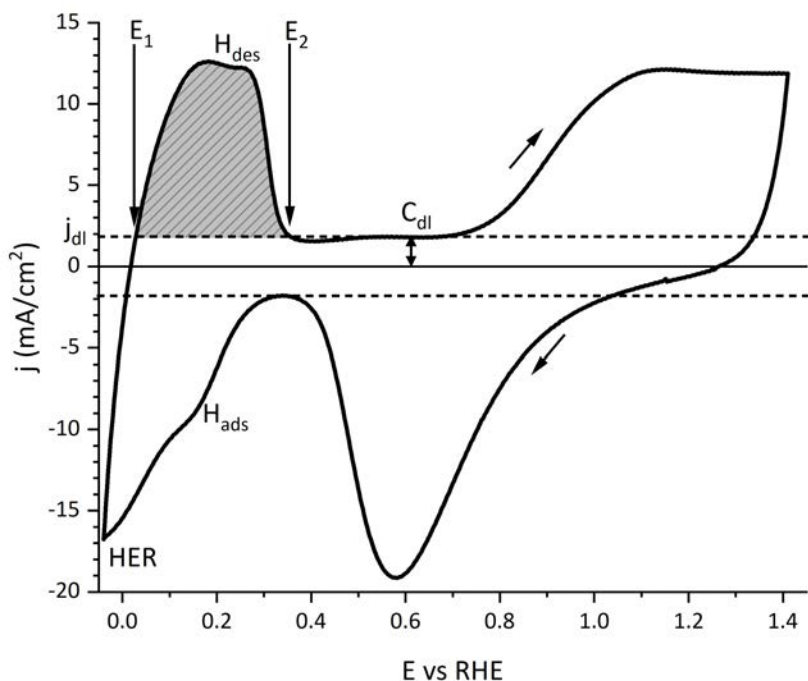
Figure 2.2: CV of electrodeposited Pt–Ni catalyst on GDL showing the hydrogen adsorption and desorption peaks for the determination of ECSA. The arrows indicate the scan direction.
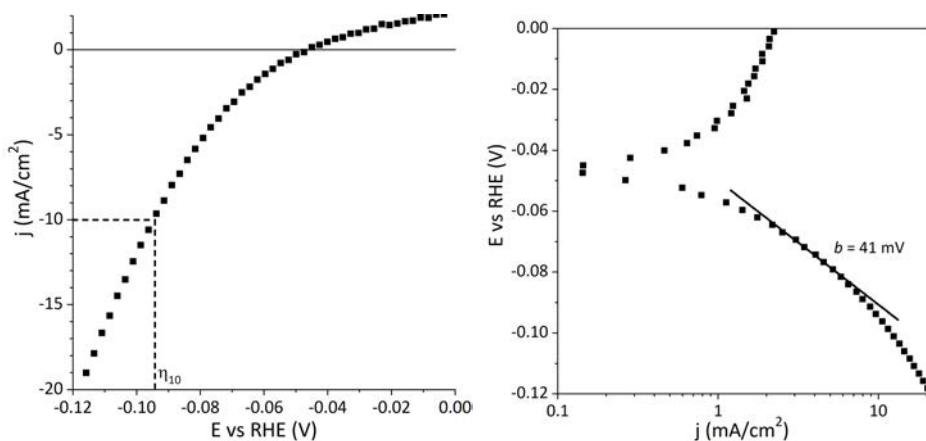

Figure 2.3: LSV (left) and Tafel plot (right) of HER on Ni–Pt thin film in 0.5 M H_2SO_4.

the reaction's equilibrium potential—corresponds directly to the applied potential since the equilibrium potential of HER is 0 V vs RHE. In ORR, the most important parameter is the half-wave potential $E_{1/2}$, the potential at which half of the limiting current density j_{lim} is reached (Figure 2.4). Since the ORR is eventually limited by mass transport, the Koutecký-Levich equation can be used to determine whether the ORR follows the four-electron pathway (Equation 2.10), or the two-electron pathway by reduction to hydrogen peroxide [36, 37]. In ORR, the measured current can be decomposed into mass-transport limited (i.e. diffusion-limited) current density j_D and kinetic current density j_k following the Koutecký-Levich equation (Equation 2.15).
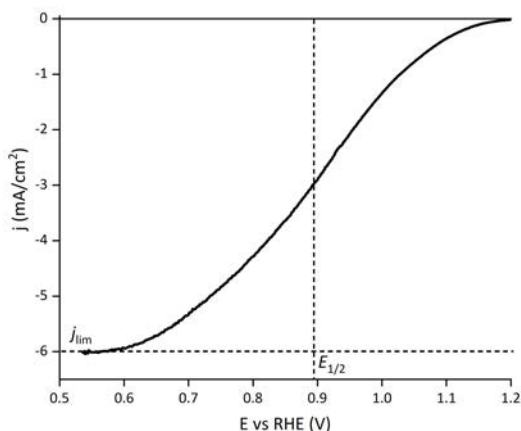
Figure 2.4: Typical forward scan of a CV on Pt/C electrocatalyst in oxygen-saturated acidic electrolyte.

$$\frac{1}{j} = \frac{1}{j_k} + \frac{1}{j_D} \tag{2.15}$$

2.2 Electrodeposition of metals from aqueous solutions

Metal electrodeposition, also called electroplating or electrochemical deposition, is a well-studied and widely employed synthesis technique, which also finds application in a number of industries such as the automotive sector or jewellery. Some purposes of electrodeposited coatings are therefore—depending on the coating material—corrosion protection, diffusion barriers or electrical contacts in electronics, as intermediate layers to provide good adhesion for paint, or simply decorative [38]. It is also a facile method to create patterned structures for microelectromechanical or magnetic devices [39].

The main advantages of electrodeposition are the rather simple synthesis from aqueous media, the ability to work in ambient conditions (in contrast to vacuum deposition techniques), the homogeneity of the coatings, and the ability to coat three-dimensional structures. On the other hand, the process is limited to conductive substrates, and to a number of elements that can be electrodeposited, the most common ones with application at industrial scale being copper, chromium, and nickel [38]. Recently, the use of deep eutectic solvents and ionic liquids (as opposed to aqueous solutions) have allowed widening the range of plateable metals and alloys to aluminium, cobalt-samarium, etc. [40]

The electrodeposition of metallic deposits from metal ions in an aqueous solution onto a conductive substrate is done by applying an electric field between the substrate and a counter electrode (CE), immersed in an electrolyte containing metal ions. The CE is either an inert electrode (Pt or graphite), or an electrode of the material to be plated, which keeps the concentration of metal ions in solution constant throughout the process (or multiple processes). A third electrode is usually employed as a reference electrode (RE) in order to measure (or apply) absolute potentials instead of potential differences. The deposition takes place by reduction of the metal cation, which collects electrons at the cathode (the substrate) according to its charge (Equation 2.16). While the described process is referred to as cathodic electrodeposition, non-metallic deposits such as metal oxides may also be deposited in anodic electrodeposition, using the substrate as anode [41]. Another alternative, which is commonly used for noble metals such as platinum, although also applicable to nickel, is electroless deposition, i.e. the spontaneous deposition of metal without an externally applied potential [42, 43].

The Nernst equation returns the reaction's equilibrium potential E_{eq} with respect to its standard electrode potential E_0 and the concentrations of both ions and reduced species (Equation 2.17). In Equation 2.17, the concentrations of the metal species ([Me] and [Me^{n+}]) can be exchanged for the respective species in any redox reaction equivalent to Equation 2.16. If applied to catalytic reactions in aqueous media, such as Equation 2.2 for HER, a logarithmic dependence on [H^+] is obtained, and therefore the equilibrium potential is pH dependent. In electrodeposition, this equilibrium potential is also denoted reduction potential. Notably, this equilibrium potential changes at the beginning of an electrodeposition process due to the creation of the reduced species. On the other hand, if the metal ion concentration in the solution is high, the changes in ion concentration due to the reduction can be neglected. Applying a potential below the equilibrium potential, i.e.

a more negative potential, enforces the reduction process, and the electro-deposition takes place. The difference between the applied potential and the equilibrium potential of a reaction, which shifts the reaction to one side or another, is referred to as overpotential, its symbol is η [44].

The kinetics of the reaction, i.e. the currents flowing in the redox reaction as a function of overpotential, are described by the Butler-Volmer equation, which is equally applicable to electrocatalytic redox reactions such as HER or ORR (Equation 2.18). The Tafel slope described above can be derived from the Butler-Volmer equation under the condition that the overpotential is sufficiently high so that either the anodic or the cathodic current can be disregarded. This leads to the Tafel equation as a simplification of the Butler-Volmer equation (Equation 2.19). Since the Tafel slope b was originally discovered experimentally, it is determined using the logarithm with base 10 (Figure 2.3), and obtains the physical term expressed in Equation 2.20 and whose only variables are the charge transfer coefficient a, and temperature.

$$Me^{n+}(aq)+ne^- \leftrightarrow Me(s) \tag{2.16}$$
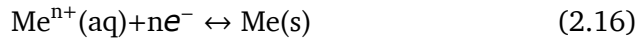
where Me is a metal, and n is the oxidation state of the metal ion determining the number of electrons exchanged in the reaction.

$$E_{eq} = E_0 - \frac{k_B T}{ne} \ln\left(\frac{[Me]}{[Me^{n+}]}\right) \tag{2.17}$$

where k_B is the Boltzmann constant, T the temperature, e the charge of an electron, and [Me] and [Me^{n+}] are the concentrations of the reduced metal and the metal anion, respectively.

$$j = j_0 \left(\exp\left(\frac{a_a ne}{k_B T}\eta\right) - \exp\left(\frac{a_c ne}{k_B T}\eta\right)\right) \tag{2.18}$$

where j_0 is the exchange current density, a_a and a_c are the dimensionless charge transfer coefficients of the anodic and cathodic current, respectively.

$$\eta = \frac{k_B T}{ane} \ln\left(\frac{j}{j_0}\right) \tag{2.19}$$

$$b = \frac{k_B T}{ane} \ln(10) \tag{2.20}$$

Electrodeposition can be performed in a variety of modes. The electric field is applied by imposing either potential or electric current between substrate and CE. The simplest and most common way is to either electrodeposit

using a constant current (galvanostatic electrodeposition) or a constant potential (potentiostatic electrodeposition), these are also referred to as direct current (DC) methods. Potentiostatic deposition has the advantage that it is independent of the substrate area, making it preferable especially when using complex substrate geometries such as metallic foams. For galvanostatic electrodeposition, a current density must be determined prior to the deposition in order to achieve reproducible results.

In principle any kind of waveform can be applied, though the most utilised form apart from the galvano- and potentiostatic (DC) methods is pulse electrodeposition [45, 46]. Likewise, this method can be run by applying either current or potential, which are applied periodically in the form of pulses of determined duration t_{on}. Between the pulses, during the relaxation time t_{off}, the applied electric field may be either switched off, set to another (lower) value, or reversed (Figure 2.5). The latter is referred to as pulse reverse electrodeposition.
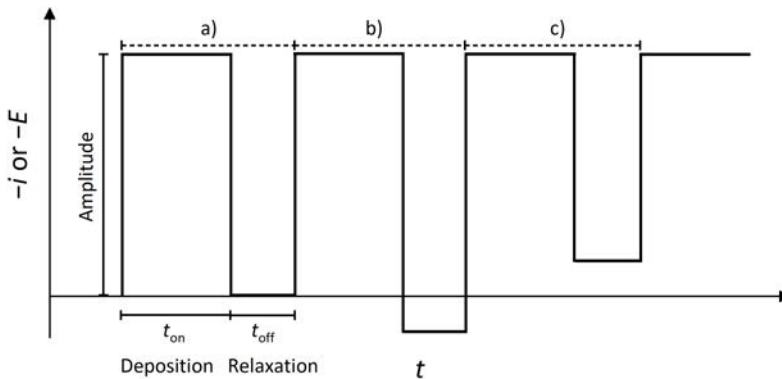
Figure 2.5: Typical periods for pulse electrodeposition: a) pulse deposition in on/off mode, b) pulse reverse electrodeposition using reversed polarity, c) pulse deposition with a fixed (non-zero) field during relaxation.

The variables for electrodeposition are therefore the amplitude of the electric field (in terms of current or potential) and the deposition time. The integration of current over time returns the transferred charge Q (Equation 2.21). The assumption that the entire amount of charge was transferred in the reduction process of the metal (Equation 2.16) is used to determine the maximum amount of deposited metal according to Faraday's law. If the actual mass of electrodeposited material is determined (e.g. by chemical analysis), the current efficiency of the electrodeposition process can be determined, i.e. what percentage of the total current contributed to the reduc-

tion of the metal (Equation 2.22). Besides the applied potential or current density, other important process parameters for the electrodeposition from aqueous electrolytes are the substrate material and its surface state, pH of the electrolyte, temperature, and electrolyte flow (agitation) [47].

$$Q \;=\; \int_0^{t_{end}} i(t)\, dt \tag{2.21}$$

$$\eta \;=\; m_{exp}\left(\frac{nF}{QM}\right) \tag{2.22}$$

where i is the measured (or applied) current, η is the current efficiency, m_{exp} the experimentally determined mass of the electrodeposit, F the Faraday constant, and M the molar mass of the deposited metal.

One of the competing reactions at the substrate, mostly in acidic media and at high negative potentials, is the reduction of protons leading to hydrogen formation. This can lead to incorporation of hydrogen into the deposit or to the evolution of hydrogen gas (Equation 2.2). In fact, hydrogen co-evolution was long considered a detrimental issue in coatings since it lead to unwanted porosity and embrittlement, but it has since been used intentionally to incorporate macroporosity with high S/V [48–50].

2.2.1 Binary alloy electrodeposition

By using salts of different metals in the electrolyte, multi-phase materials or alloys can be deposited. Each metal has its own reduction potential, i.e. in order to achieve the co-electrodeposition of more than one element their respective reduction potentials need to be sufficiently close together [51]. If this is not the case, complexing agents may be used to complex a metal, resulting in a complexed compound with a different reduction potential [52]. Another way to achieve closer proximity of the individual reduction potentials is by varying the ion concentrations in the electrolyte according to Equation 2.17. In turn, if the reduction potentials of the different elements are separated, it is possible to deposit those elements selectively and sequentially from the same electrolyte [53].

For each species, the deposition divides into different ranges: Close to the onset of the deposition, i.e. at low overpotential, the reduction current increases drastically with the overpotential. This is called the activation-controlled (or kinetic) regime. At larger overpotentials, the reduction current becomes limited by diffusion and will stay constant with overpotential.

16

This range is the mass-transfer or diffusion-controlled regime (Figure 2.6). For binary alloy electrodeposition, this leads to different scenarios; at a determined applied deposition potential, the reduction of both elements could be activation-controlled, diffusion-controlled, or a mix of both with either element reduced under activation control and the other under diffusion control.
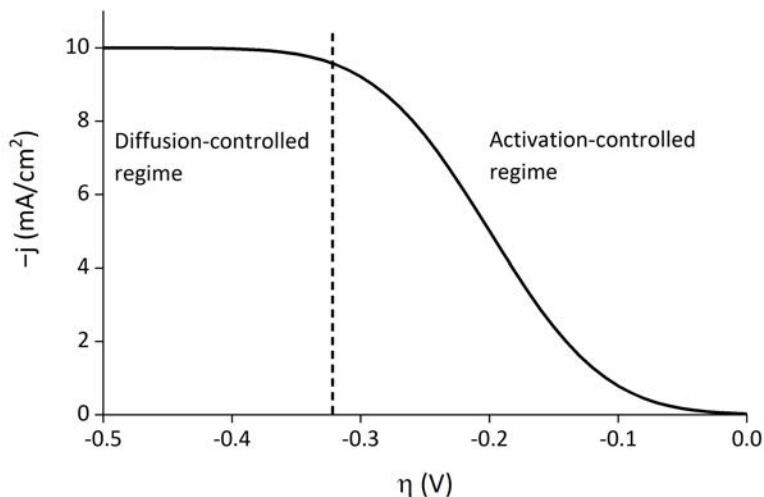
Figure 2.6: Cathodic current density as a function of overpotential showing activation-controlled and diffusion-controlled regime in metal electrodeposition.

Since under diffusion control there are no changes of the reduction current (and therefore of the deposition rate) with overpotential, the composition of the alloy will not change other than through the electrolyte composition. In the other cases (mixed or activation control), the resulting composition depends on the applied overpotential [54]. However, the different species may interact and an exact prevision of the electrodeposit's composition under given electrodeposition parameters, especially for less frequently investigated compounds, is usually not possible and remains to be determined experimentally and empirically.

Many different binary alloys have been successfully electrodeposited, most notably alloys of Ni, Cr, Sn, Zn, Ag, Au, Pd, and Pt, however, not any combination of those is feasible in electrodeposition [55]. Some elements, such as Mo or W, can only be deposited in metallic form in a multiple-step mechanism and in the presence of another electrodepositable element which is referred to as inductor metal [54].

2.2.2 Aqueous electrolytes

In the simplest case, the aqueous electrolyte contains only the dissolved metal salt in the form of Me^{n+} and its respective anion. However, the use of additives is inevitable in order to obtain reproducible results, a certain surface quality, or the codeposition of specific elements, as explained in the following [56]. However, in some cases—including micelle-assisted electrodeposition—the properties of the electrolyte, and, in consequence, those of the electrodeposit, do not depend exclusively on its composition but also on its preparation and ageing [57].

Acids and bases In any electrochemical process in aqueous media, the pH is one of the most important parameters which influences the species in equilibrium in solution, and the reaction products. It is therefore absolutely necessary to control the pH of an electrolyte, which can be adjusted by addition of any common acid or base.

pH buffer When a potential difference is imposed, a gradient in pH is easily established between the electrodes. Especially close to the substrate for electrodeposition, local changes in pH can be very high and lead to, for instance, the precipitation of metal hydroxides. The addition of a pH buffer can mitigate this effect [58, 59].

Complexing agent Especially when co-depositing different elements, a complexing agent may be needed to modify the deposition potential of the individual element. The complexing agent will bind the metal ions of a certain element and form a complexed ion, thus the deposition potential for this element is modified [60]. In general, a good co-deposition is achieved when the deposition potentials for both elements are identical. Some examples of common complexing agents are citrates, cyanides, ammoniates, and other organic acids.

Brightener Especially for decorative purposes, effort is made to achieve brilliant deposits, to this purpose there exist many different additives such as polymeric surfactants described below, and other organic and inorganic compounds, e.g. coumarin. Their principal function is to achieve that defects are preferentially filled during the deposition process, in this way levelling the surface [47].

Other additives Other additives of any kind depend very much on the material to be deposited and the issue to be targeted. There are strengtheners, which increase yield strength at the expense of ductility, such

as saccharin for Ni-deposits, where the yield strength is increased via grain refinement [61]. Sulphur-containing species can lower internal stresses of Ni deposits [38].

Surfactant A polymeric additive that can be used to lower the interfacial tension between electrolyte and electrodeposit, resulting in lower surface roughness and thus a better apparent finishing and higher brightness [62, 63]. Surfactants can also influence the structure of the electrodeposits, influence their grain size, and reduce their internal stress [61].

2.2.3 Physical properties of electrodeposited metals

As for most coating techniques, electrodeposition leads to the incorporation of internal stresses in the films. As a result of accumulating internal stress, cracking and delamination occur when the deposit thickness becomes too high [38]. Naturally, the critical thickness depends mostly on the deposit material, though, as mentioned above, certain additives can be used to reduce internal stress. For electrochemical applications, high coating thickness is only favourable if the deposit exhibits open porosity, otherwise an increase in thickness would not increase the accessible surface area.

One of the major properties of any kind of coatings is adhesion. The adhesion of a coating on a substrate mainly depends on the coating and substrate material and the kind of interface they establish. Coatings with good adhesion are usually established by diffusion, chemical binding, or mechanical interlock. Good adhesion depends on proper substrate preparation; if substrate and coating material are mutually soluble the creation of defects on the substrate, e.g. by etching, can enhance the diffusion [64]. In many electrodeposited films, the internal stress is elevated close to the interface, compromising their adhesion. In electrocatalytic applications, no mechanical loads are applied and thus there is no specific requirement for adhesion.

Metallic electrodeposits often exhibit low grain sizes in the nanometre range [65, 66]. This leads to a usually high yield strength of electrodeposited films according to the Hall-Petch relation, indicated by high hardness values due to dislocation pile-up at the grain boundaries [67]. However, there is an inversion of the Hall-Petch relation below a critical grain size of typically very few nanometres depending on the material, when deformation occurs by grain boundary sliding rather than dislocation motion [68, 69].

In the electrodeposition process, hydrogen can be easily incorporated into the deposits, which can be detrimental to materials susceptible to hydrogen

embrittlement, such as nickel, and even to steel substrates [38, 70]. For nickel, hydrogen also adds to the internal stress [47]. Post-deposition heat treatments can be used to remove hydrogen [56].

Since the ferromagnetic elements Fe, Co, and Ni are all electrodepositable, electrodeposits with different magnetic behaviour can be obtained, including ferromagnetic alloys. Ferromagnetic properties are most commonly evaluated by magnetic hysteresis loops, where the response of the material (magnetisation, M) to an externally applied magnetic field (H) is measured. The magnetisation can be seen as the sum of individual magnetic moments in a sample [71]. A means of normalisation is thus necessary for comparability, which is usually done by either volume or mass of the sample. In this work, the magnetisation is normalised by mass, taking into account that the determination of the volume is not straightforward for porous materials. Further, the magnetisation of a ferromagnet is not directly related to the external field but depends on the previous state of the material, leading to the well-known hysteresis. The most important magnetic properties obtained from a hysteresis loop are as follows (Figure 2.7).

Saturation magnetisation (M_s) The maximum magnetisation of the material when all magnetic moments are aligned in the direction of the applied field.

Remanent magnetisation (M_r) The retained magnetisation of a material at zero field, after being magnetised.

Coercive field or coercivity (H_c) The magnetic field strength required to reverse the orientation of the magnetisation of a material after being magnetised. Soft magnetic materials are characterised by a low H_c, as opposed to hard magnetic materials with high H_c. Soft magnetic materials require considerably less energy for reversal of magnetisation. For magnetic storage media, semi-hard magnetic materials are used in order to guarantee sufficient stability with respect to external magnetic thields or thermal effects.

Another major property of a ferromagnet is the temperature above which the ferromagnetic behaviour is lost and turns paramagnetic, its Curie temperature (T_C). This property can be measured at a fixed external field at which the material is saturated, by recording the temperature dependence of the magnetisation. Since there is no sharp transition between the ferromagnetic and paramagnetic state, there are different methods for the determination of T_C [72]. For example, T_C can be determined at the intersection of
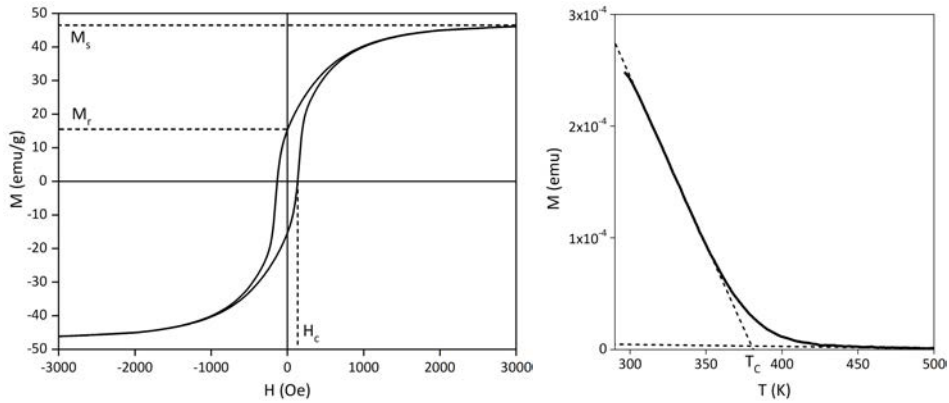
Figure 2.7: Magnetic hysteresis loop (left) and determination of Curie temperature from M-T curve using two-tangent method (right) of electrodeposited Ni–Pt thin film.

two tangents applied at the magnetic transition (Figure 2.7). This measurement is also useful to reveal if more than one ferromagnetic phase is present, this case would result in a multi-step transition between ferromagnetic and paramagnetic behaviour instead of a single step for a single ferromagnetic phase. Though multiple phases may also be revealed in a hysteresis loop, its interpretation is more complex.

In a three-dimensional ferromagnetic specimen, there are magnetic domains which are regions in which the individual magnetic moments are aligned in the same direction. In a demagnetised state, all domains are randomly aligned and the net magnetisation is 0. At saturation magnetisation, all magnetic moments align and a single domain is formed throughout the sample. When the external field is removed, the direction of magnetisation will change in those regions where another magnetisation direction is energetically more favourable while other regions will keep their previous state, and the net magnetisation reduces to remanence. Changes in the magnetisation are usually described by domain wall movement, i.e. the growth and shrinkage of domains, and the rotation of magnetisation which occurs close to saturation (Figure 2.8).

In electrodeposited materials, the ferromagnetic behaviour can be influenced by different factors. Fine-grained materials have a large amount of grain boundaries which can hinder domain wall movement and rotation of domains, resulting in a harder magnetic behaviour. Internal stress and dislocations can further hinder domain wall motion. Electrodeposited thin films will also show shape anisotropy: the magnetisation out of the plane, i.e. nor-
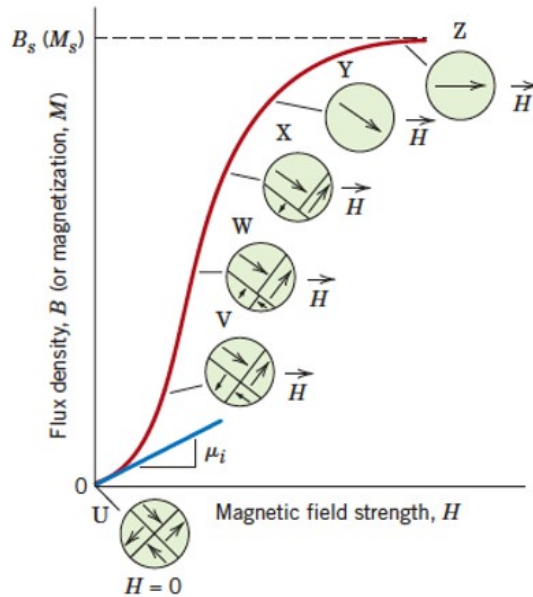
Figure 2.8: The magnetisation behaviour of an initially demagnetised ferromagnetic material as a function of magnetic field strength, described by domain growth and rotation [73]. Republished with permission of John Wiley & Sons, from Materials Science and Engineering, W. D. Callister Jr. and D. G. Rethwisch, 2011.

mal to the surface, requires much more energy (higher external field) than in-plane. This is due to the fact that an orientation of a magnetic domain is energetically more favourable if aligned parallel to the sample's surface [74].

2.2.4 Metal nanoparticle electrodeposition

Apart from nanoporous materials, which are discussed below, NP synthesis is another solution to obtain high S/V materials. One method for the synthesis of metallic NPs is by electrodeposition.

The metal electrodeposition process starts by nucleation and is then followed by growth of the nuclei (Figure 2.9) which eventually connect to form a metallic film [55]. As a consequence, NP deposition can be achieved by interrupting the electrodeposition process during the particle growth just after nucleation. The amount of NPs obtained is thus dependent on the number of nucleation sites. However, the exact process of NP formation by electrodeposition is still under discussion [75].
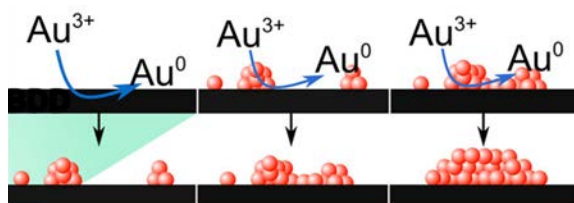
Figure 2.9: Nucleation and growth of Au NPs during electrodeposition on a diamond substrate [76]. Reprinted with permission from ACS Nano 2018, 12, 7388. Copyright 2018 American Chemical Society.

Since acidic fuel cells are one of the main applications of metallic NPs, research on metal NP electrodeposition focusses mostly on Pt and Pt alloy NPs. Electrodeposition often yields relatively large NPs, whereas small NPs of few nanometres are considered favourable for PEMFC. Hussein et al. employed pulsed laser heating in combination with potentiostatic deposition for 5 s and achieved smaller NPs with a porous structure in contrast to larger, dense NPs after room temperature (RT) electrodeposition [77]. Liu et al. proposed a synthesis route for Pt NPs via potentiodynamic electrodeposition onto WC substrates, resulting in well-dispersed NPs with average diameter below 10 nm [78].

Pulse electrodeposition is a method to achieve a high number of particle nucleation using short, high-current pulses. Ideally, each deposition pulse will generate additional nucleation instead of promoting particle growth. Egetenmeyer et al. studied the pulse electrodeposition of Pt, Pt–Ni and Pt–Cu NPs onto the GDL of a PEMFC, and the effects of the most important parameters such as eletrolyte composition, current amplitude (between 0.1 and 4 A/cm^2), t_{on} (between 1 and 100 ms), t_{off} (between 95 and 995 ms), and temperature [79]. The authors also studied an activation treatment of the GDL by Ar/O$_2$ plasma, increasing the wettability of the hydrophobic polytetrafluoroethylene (PTFE) containing surface prior to electrodeposition [80]. Huang et al. propose the seeding of a very low amount of Pt NPs onto the carbon substrate and a subsequent pulse electrodeposition process of Pt NPs [81].

Oshchepkov et al. electrodeposited Ni NPs using long (15–20 s) potentiostatic deposition pulses onto carbon substrates [82]. The group later adapted the process to openly porous Ni foam substrate material, where both the Ni NPs and the substrate contributed to the resulting catalytic properties [83]. An et al. synthesised Sn NPs using potentiostatic pulses where the system is at open circuit potential (OCP) during t_{off} [84].

Alternatively, additives such as polymeric surfactants can be used to sta-
bilise nanoparticles, i.e. to physically hinder agglomeration of NPs and film
formation. The successful formation of Ag NPs has been achieved using
polyethylene glycol (PEG) as an additive, whose concentration may be used
to control the NP size distribution. A very long deposition time of 30 min
was used in this case [85].

2.3 Nanoporous materials

Materials with a pore diameter between 0.1 nm and 100 nm are considered
nanoporous. According to IUPAC, nanoporosity itself divides into macropo-
rosity (above 50 nm), mesoporosity (between 2 nm and 50 nm), and micro-
porosity (below 2 nm) [86]. In general, porous materials find applications
in biomedical and energy applications [87–89]. Mesoporous materials are
of particular interest for catalytic applications, batteries, supercapacitors,
hydrogen storage, electrochemical sensors, water remediation, and drug de-
livery [90–97].

The strategies to synthesise porous materials by electrodeposition include
micelle-assisted deposition, the deposition using solid templates [98–100],
the controlled evolution of hydrogen during the deposition process [48–50],
selective (electro)chemical etching [101, 102], and the use of metallic foam
substrates [103–105] (Figure 2.10). Different methods may be combined to
achieve hierarchically porous structures [106].

Hard templating refers to any kind of solid template which can later be
selectively dissolved from the metal. Hard templates need to be deposited
onto a conductive substrate or metallised on one side prior to electrodeposi-
tion. One of the typically used hard templates is anodically oxidised alumina
(AAO) [107, 108]. A subdivision of hard templating is colloidal templat-
ing, where the template consists of spherical particles, which are usually
deposited onto a substrate by electrophoresis prior to film deposition [109].
Common substrates for colloidal templating are polystyrene (PS) or silica
spheres [110–114]. Hard templates are not only used for introduction of po-
rosity, but also in order to achieve defined nanostructures such as nanowires
or nanotubes [115, 116].

On the other hand, micelle-assisted electrodeposition is classified as a soft
templating method, where the template is dissolved in the solution and de-
posited on the substrate simultaneously with the metallic deposit. It is based
on the formation of micelles which can be formed in aqueous solutions by a
number of amphiphilic polymers which are mostly block copolymers [117,
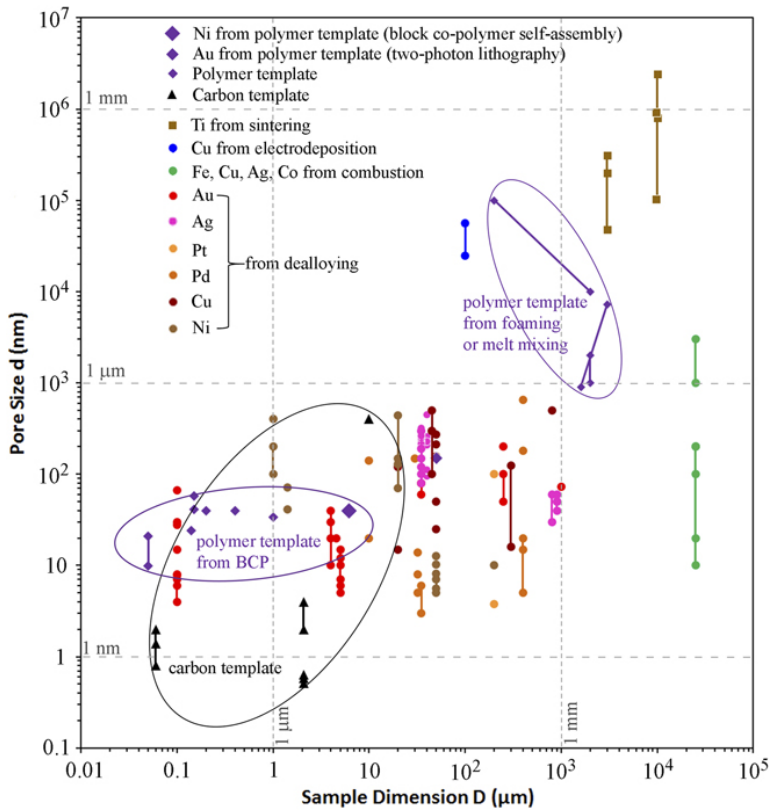
Figure 2.10: Pore size ranges in correlation with sample dimensions obtained by different strategies [98]. Reproduced from J. Mater. Res. 2018, 33, 1. Copyright 2017 Materials Research Society under CC BY 4.0.

118]. Above the critical micelle concentration (cmc), those micelles are formed spontaneously in aqueous solution [119]. At high concentrations, ordered lyotropic liquid crystal (LLC) phases can be formed [120, 121]. Amphiphilic polymers can usually form a number of different crystalline phases (Figure 2.11).

Micelle-assisted electrodeposition is often performed using commercially available amphiphilic polymers, such as Pluronic P-123, F-127, or Brij 58. These polymers contain hydrophobic parts such as polypropylene glycol (PPG) and hydrophilic parts such as PEG. In the literature, PPG and PEG are used equally to polypropylene oxide (PPO) and polyethylene oxide (PEO), respectively. Due to their amphiphilic nature, when in contact with water their hydrophobic parts minimise their energy by turning towards each other, and

Figure 2.11: The phase diagramme for an amphiphilic surfactant, showing its cmc
and the different potential crystalline phases [122]. Reproduced from
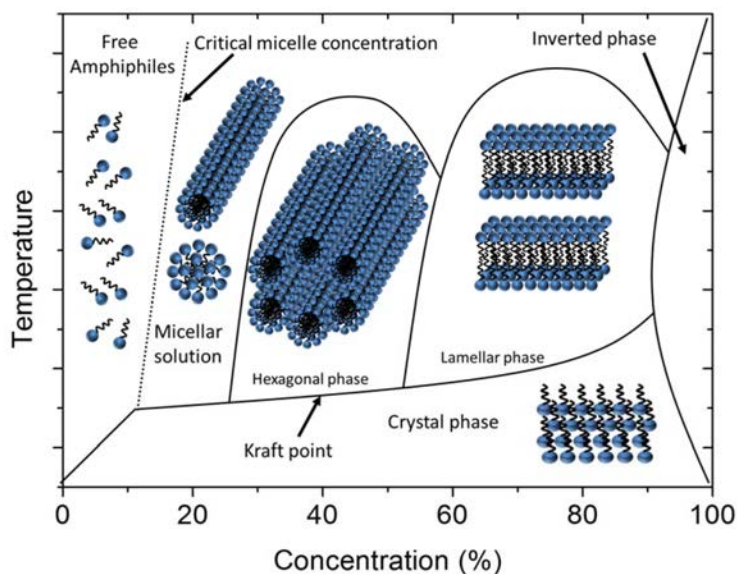Nanomaterials 2017, 7, 305. Copyright 2017 I. Dierking and S. Al-
Zangana under CC BY 4.0.

in this way form the core of the micelles whereas the hydrophilic chains are
oriented towards the aqueous media. In an electrolyte for electrodeposition,
the metal ions will interact and coordinate with the hydrophilic surface of
the micelles, which will be electrodeposited together with the metal(s) [90]
(Figure 2.12). After electrodeposition, the soft template is usually removed
by dissolution in an organic solvent to retain the porous deposit.

The first report of a metal electrodeposited using soft templating was
presented by Attard et al. in 1997, who prepared mesoporous Pt films from
an LLC phase containing hexachloroplatinic acid [123]. The approach was
then adopted to Pd [124], Ni [125] and a number of other metals and binary
alloys [126]. Zhang et al. combined electrodeposition (and electroless dep-
osition) of Pt from LLC with hard templating in order achieve hierarchically
nanoporous structures [127].

Later, Wang et al. showed that mesoporous Pt films could be obtained
at much lower surfactant concentrations, as long as the concentrations was
above the cmc. They compared the micelle-forming surfactants Pluronic
F-127, Brij 58, and another PEG-PPG-PEG block copolymer with higher mo-
lecular weight. The different surfactants led to different, yet homogeneous
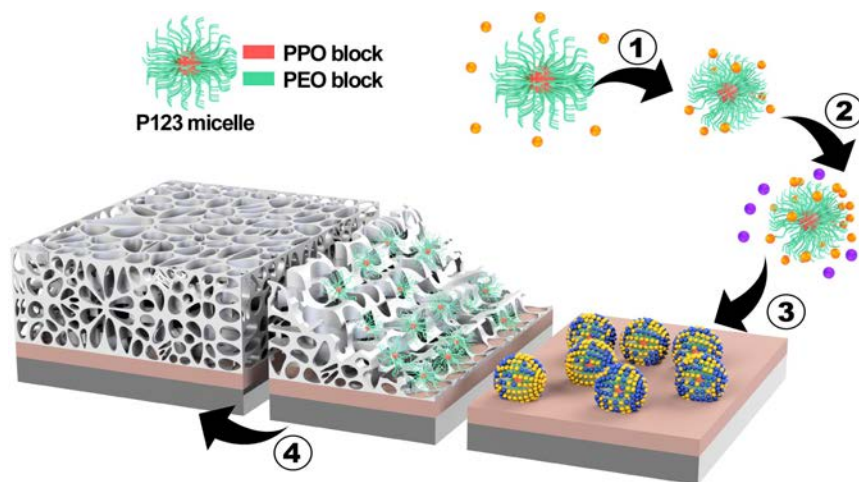
26

Figure 2.12: Scheme of micelle-assisted electrodeposition using Pluronic P-123, showing the coordination of Pt ions at the micelle surface (1), interaction of the micelles with different metal ion species (2), reduction of the metal species and simultaneous deposition of the micelles on a substrate (3), and the retention of a porous deposit after removal of the soft template (4). Courtesy of C. Navarro.

pore sizes between 5 and 20 nm, increasing with the molecular weight of the polymer. The authors also demonstrated increased catalytic activity at methanol oxidation due to the higher surface area [128]. The micelle-assisted synthesis was then also reported for a number of Pt alloys in large compositional ranges using Brij 58, such as Pt–Au [129], Pt–Cu [130], Pt–Pd [131], or Pt–Ru [132].

Up to present, the process has since been adopted to a number of different (electrodepositable) elements and alloys. For example, mesoporous Pd was synthesised using cetyltrimethylammonium chloride as surfactant, resulting in a very low pore size of 2 nm [133]. Mesoporous Ni and Ni–Cu alloys were electrodeposited using Pluronic P-123 from an acidic electrolyte, yielding films with a pore size of 5–30 nm [117]. P-123 was also used for electrodeposition of Fe–Pt with Fe ranging from 2 to 55 at% and pore size below 12 nm [134].

While most commercial block copolymers can form micelles spontaneously in aqueous solutions, they yield rather small pores at the lower end of the mesoporous range with pore sizes of 5–10 nm. In order to obtain larger pores which could be advantageous for electrolyte penetration in catalytic processes, more long-chained polymers can be used, however, those do

not form micelles spontaneously. They need to be assembled in a solvent replacement method using an organic solvent (most commonly tetrahydrofurane) and water [135, 136]. In this way, mesoporous Ni and Cu films with a pore size of 50 nm have been prepared using high molecular mass PS-*b*-PEO block copolymer [137, 138]. A pore size of 20–35 nm was obtained using the same PS-*b*-PEO block copolymer in electrodeposition of Ni–Pt alloy films [139]. This however does not necessarily imply that the resulting pore size is dependent on the metal species, since the micelle diameter of a polymer in water is also directly influenced by pH and temperature [140]. The direct effect of polymer chain length on the resulting pore size was shown for mesoporous Cu films [141].

Naturally, micelle-templated electrodeposition and NP deposition can be combined. Liang et al. electrodeposited mesoporous Pt–Ru NPs from an LLC phase of Brij 56 [142].

The magnetic behaviour of ferromagnetic materials is largely dependent on their morphology when it comes to nanostructures. Changes in the magnetic behaviour with respect to bulk materials, such as the transition from ferromagnetic to superparamagnetic behaviour, can be observed in ultrathin films or nanoparticles, where the particle size is too small to retain a large anisotropy energy compared to the thermal energy. The magnetic behaviour of such structures may also be manipulable by electric fields [143–145]. For mesoporous structures, those effects could be expected even to a larger extent if the wall thickness between the pores is in the same size range. Electrostatic charges accumulated at the surface of the pore walls can induce changes in the electronic band structure, especially in the 3d electron cloud of transition metals, and, consequently, in the magnetic anisotropy energy (thus resulting in changes in H_c).

This was shown in 2017 by Quintana et al., who studied the effect of voltage on $Ni_{80}Cu_{20}$ alloy films synthesised by micelle-assisted electrodeposition. The authors found that, indeed, the ultrathin pore walls of 600 nm thick mesoporous films contributed to voltage-induced changes in the magnetic anisotropy, resulting in a change of coercivity [146]. Later, they also showed tuneability of the saturation magnetisation through a reversible electrochemical redox process [147].

2.4 Ni- and Pt-based alloys

2.4.1 Ni–Pt alloys

Since both Ni and Pt crystallise in face-centred cubic (fcc) structure with similar lattice parameters and atomic radii, they are completely miscible, while certain ordered phases may be formed [148]. Attention should be given to the magnetic transition which occurs at the Curie temperature T_C and which shows a linear decrease with atomic percentage of Pt [149] (Figure 2.13). Due to the alloy's full miscibility, T_C can therefore be tuned by the Ni/Pt ratio.
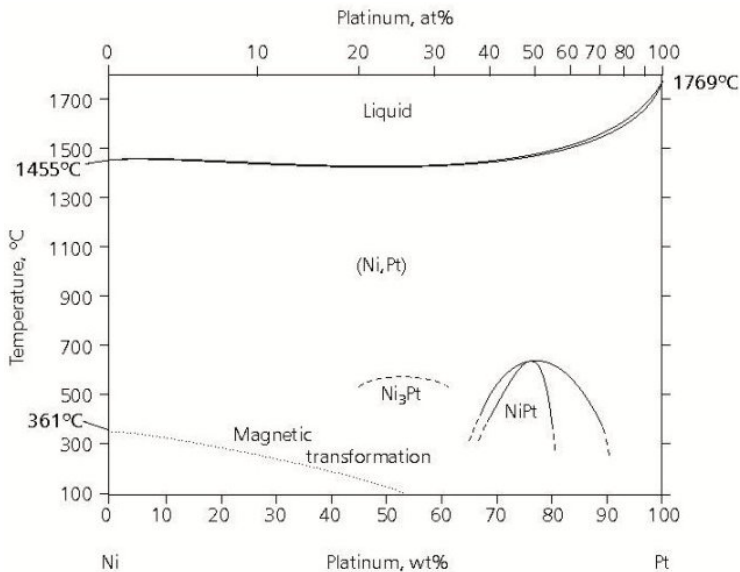
Figure 2.13: The Ni–Pt equilibrium phase diagramme [149]. Reprinted by permission from Springer Nature, Bull. Alloy Phase Diagr. 1989, 10, 258, Copyright 1989.

The electrodeposition of Ni has been widely studied, including the effect of different additives in the electrolyte on electrodeposited Ni [59, 150], and the magnetic behaviour of Ni and Ni–Fe nanostructures [151]. It dates back to the formulation of the Watt's bath in 1916 [152]. The electrodeposition of Pt is mostly done via hexachloroplatinates [153–155]. Furthermore, Pt may also be deposited by electroless deposition, where the metal reduces spontaneously on the substrate with the concurrent incorporation of phosphorous.

Yamauchi et al. synthesised mesoporous Pt-rich Pt–Ni electrodeposits by chemical redution from Brij-type LLC using nickel chloride, hexachloroplatinic acid, and sodium borohydride as reducing agent [156].

A process for electrodeposition of a dense, single-phase Ni–Pt alloy with tunable composition was demonstrated by Liu et al. from an acidic electrolyte containing potassium tetrachloroplatinate, nickel chloride and sodium chloride. By potentiostatic deposition in a potential window between –0.1 and –0.9 V vs saturated calomel electrode (SCE), covering the full compositional range. The authors showed that any of the alloy compositions outperformed a pure Pt electrode at ORR in acidic media; the best performance was reached with an alloy composition close to Ni_3Pt [157]. Mesoporous Pt–Ni was electrodeposited from hexachloroplatinic acid, nickel chloride, and LLC of Brij C10 surfactant, however, catalytic activity at ORR was unsatisfactory and the authors judged that the synthesis process was not optimal [158]. Remarkably, all synthesis routes of Ni–Pt electrodeposition imply the use of nickel chloride, although Ni can be deposited easily from both chloride, sulfate, or a mix of both. Since Pt salts or acids for electrodeposition are usually chloride-containing, it seems natural to use nickel chloride in the codeposition. However, there is no obvious limitation of Ni–Pt codeposition to the use of nickel chloride exclusively.

In contrast to the aforementioned synthesis routes via LLC, the combination of an electrodeposition process for Ni–Pt with micelle-assisted electrodeposition had not been documented before. The micelle-assisted electrodeposition provides a simpler, highly controllable and reproducible process for the synthesis of the mesoporous alloy.

Pt–Ni and its ternary alloys are being investigated for applications in PEM-FC [159–161], HER [162, 163], and other electrochemical applications [139, 164].

While Pt is the most efficient pure electrocatalyst for almost any catalytic reaction in acidic media [27, 29], Ni and its alloys are mainly applicable for HER in alkaline media, one of the most common alloys being Raney Ni (Ni–Al) [165]. Different Ni alloys have been investigated for HER in alkaline media, among them Ni–Mo–Al, Ni–W, Ni–Cu, but also Ni oxides, hydroxides and phosphides [166–172]. In fact, hydroxides are easily formed on Ni or Ni alloy surfaces in alkaline media [173], it is therefore probable that they are present on most Ni alloys used for HER in alkaline media. Other promising applications of Ni-based alloys are hydrogen storage and electrochemical supercapacitors [174].

2.4.2 Ni–Pt–Mo alloys

Molybdenum (Mo) may be used to improve the corrosion resistance of Ni-based alloys, especially in chloridic environments [175]. While up to 17 at% Mo can be dissolved into the Ni fcc phase, its solubility limit in Pt is approximately 20 at% (Figure 2.14). However, electrodeposition does not necessarily lead to the formation of the stable phases predicted by the phase diagramme, especially since both Ni–Mo and Mo–Pt phase diagrammes show a number of intermetallic and high-temperature phases which might be formed and stabilised by electrodeposition. The electrodeposition of Ni-Mo alloys is feasible from sodium molybdate with the use of a complexing agent such as sodium citrate [176, 177]. This electrodeposition is characterised by induced deposition, meaning that Mo requires the presence of an inductor metal in solution to secure full discharge of Mo(IV) to Mo(0) However, Mo may also be deposited in form of oxides [178–180]. The suitability of Ni-Mo for HER has been demonstrated [181–183]. Recently, it was further demonstrated that Mo oxide, in a compound with Ni, can enhance the kinetics of HER [184]. Pt containing Mo or Mo oxide may also improve ORR performance [185].

The direct synthesis of ternary Ni–Pt–Mo alloys is rarely reported. Mao et al. documented the synthesis of Pt–Mo–Ni alloy nanowires by thermal decomposition [188], but a syhthesis route via electrodeposition is lacking. Huang et al. investigated Mo doping of Pt–Ni NPs for ORR, which led to superior durability with respect to Pt–Ni NPs [189, 190].
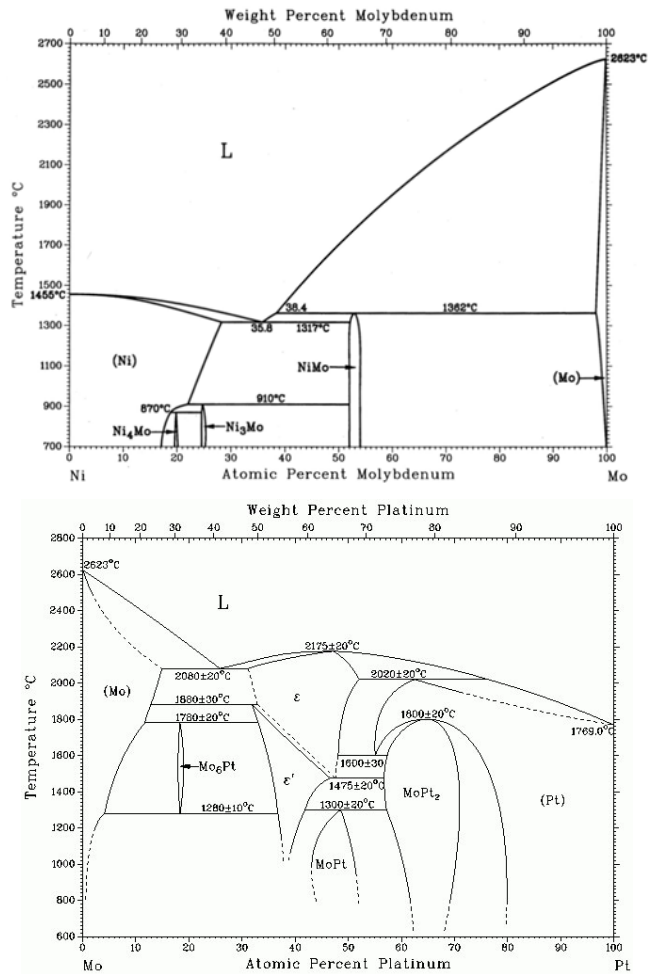
Figure 2.14: The equilibrium phase diagrammes of Ni–Mo [186] (top, republished with permission of McGraw Hill LLC, from F. A. Shunk, Constitution of binary alloys, 1969) and Mo–Pt [187] (bottom, Reprinted by permission from Springer Nature, Bull. Alloy Phase Diagr. 1980, 1, 89, Copyright 1969).

3 Objectives

This work is focussed mainly on the synthesis of nanostructured nickel-platinum based electrodeposits, and shall furthermore highlight their applicability in electrocatalysis and other potential applications. To this end, the following objectives are defined.

- Mesoporous Ni–Pt films
  - The successful synthesis by micelle-assisted electrodeposition of mesoporous Ni–Pt films through determination of the suitable electrolyte constituents (type of metal salts, type of micelle-forming surfactant, and other additives), optimisation of their concentrations, and determination of suitable parameters for electrodeposition.
  - The characterisation of the electrodeposited films in order to reveal the most important properties that can influence catalytic performance and durability: size and distribution of porosity, phase distribution, crystallite size, texture. Naturally, due to the targeted application in electrocatalysis, specific focus shall be laid on surface properties, such as nature (metallic or oxidic) of the surface and ECSA.
  - The demonstration of efficient performance at HER, including the relation of the observed catalytic activites with composition and the aforementioned properties, including evaluation of durability and degradation in acidic and alkaline media.
  - Exploitation of magnetic (vibrating sample magnetometry, VSM) and mechanical (nanoindentation) characterisation methods. Targeting the electrosynthesis of a series of Ni–Pt alloys with tuneable magnetic properties, in particular with variable T_C.

- Pt–Ni and Pt–Ni–Mo NPs
  - Elaboration of a pulse electrodeposition process to achieve the deposition of Pt–Ni NPs onto the GDL of a PEMFC and subsequent adaption to Pt–Ni–Mo.

- Structural and surface analysis with special focus to the effects and nature of Mo, and demonstration of ORR activity at electrochemical cell level. Relation of activity with NP composition and other properties.

- Implementation into PEMFC prototype, demonstration of functioning, and durability testing. Relation of durability with NP composition and other properties.

4 Experimental

The experimental techniques used for characterising the material are common, well known techniques which are described elsewhere. Instead, this chapter focuses on the material synthesis as one of the major foci of the thesis. Additionally, the electrochemical characterisation techniques and the PEMFC testing is described.

4.1 The electrochemical cell

The electrodeposition set-up is comprised of a three-electrode electrochemical cell with a thermalisation jacket in order to control the temperature, and an inlet for gas supply. The three electrodes are a counter electrode, the substrate, which serves as the working electrode, and a reference electrode. While a two-electrode set-up would only allow to measure potential differences, the RE allows to determine the absolute electrochemical potential with respect to the equilibrium potential of a redox reaction taking place inside of it. Here, the redox reaction between Ag and AgCl is employed in an Ag|AgCl electrode with an inner solution of 3 M KCl (Figure 4.1a). A potentiostat/galvanostat connected to the electrodes applies the deposition conditions.

4.1.1 The electrochemical microcell

The electrochemical microcell is a miniaturised version of an electrochemical cell, designed to study electrochemical properties such as corrosion behaviour on a sub-micrometre scale. In this way, the electrochemical microcell technique (EMT) can be used to study the corrosion behaviour of individual phases, inclusions, or grains in an alloy [191].

The electrochemical microcell has a reduced volume, where CE and RE are immersed. The WE is connected to the electrolyte via a microcapillary with a tip diameter of 50–200 µm, thus confining the area on the WE which is exposed to the electrolyte (Figure 4.1b). The electrochemical microcell is mounted on an optical microscope for selection of the zone to be studied (similar to a microindentation system).
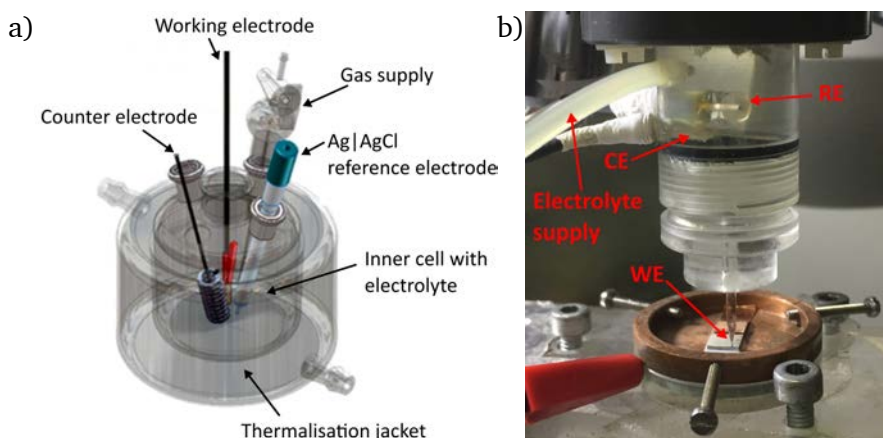
Figure 4.1: Electrochemical cell (a, courtesy of S. Pané) and electrochemical micro-cell (b) in comparison.

All electrochemical tests using EMT were performed at AGH University of Science and Technology, Kraków, at the Faculty of Foundry Engineering.

4.2 Synthesis by electrodeposition

4.2.1 Thin film synthesis

The micelle-assisted electrodeposition is performed in an electrochemical cell. The electrolyte for electrodeposition of mesoporous Ni-rich Ni–Pt films was developed empirically by changing electrolyte formulations, performing electrodeposition, and observing the electrodeposits by scanning electron microscopy (SEM) until satisfactory results were obtained. The conditions for those satisfactory results were high mesoporosity, continuous and defect-free morphology, the ability to electrodeposit over an ample potential range, the stability of the electrolyte, and the reproducibility of the results. The final electrolyte contained the salts of Ni and Pt, boric acid, ammonium chloride, and the block copolymer Pluronic P-123 (Table 4.1). This polymer has the structure PEG-PPG-PEG (Figure 4.2).

All other electrolyte formulations used were based on modification of this electrolyte, such as the removal of P-123 to synthesise dense thin films, the addition of sodium molybdate and citric acid for ternary Ni–Pt–Mo deposits, and the incrementation of Pt salt content for Pt-rich NPs. In all cases, HCl or NaOH were used for adjustment of the pH to 2.7.
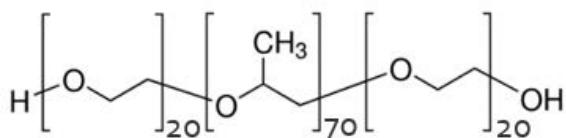
Figure 4.2: Chemical representation of Pluronic P-123.

Ternary Ni–Mo–Pt thin films were synthesised in an intermediate stage before starting with the more complex preparation of ternary Pt–Ni–Mo NPs. Aim of the Ni–Pt–Mo thin film electrodeposition was to determine if codeposition of Mo together with Ni and Pt is successful, to check if phase separation occurs, and to study the effect of deposition potential on the content of each element. For thin films, all of these aspects are easily controlled by SEM using energy-dispersive X-ray spectroscopy (EDX) but are not straightforward for NPs where the amount of electrodeposited material is much lower and often falls below the limit of detection. In addition, the ternary Ni–Mo–Pt thin films may be used for different studies such as HER.

Table 4.1: Electrolyte compositions for the deposition of thin films and nanoparticles presented in this work.

| | Thin films | | | Nanoparticles | |
	Ni–Pt		Ni–Pt–Mo	Pt–Ni	Pt–Ni–Mo
$NiCl_2$	200 mM	200 mM	200 mM	200 mM	200 mM
$Na_2PtCl_6 \cdot 6\,H_2O$	3 mM	3 mM	3 mM	5 mM	5 mM
H_3BO_3	200 mM	200 mM	200 mM	200 mM	200 mM
NH_4Cl	25 mM	25 mM	25 mM	25 mM	25 mM
P-123	10 g/l	—	—	—	—
$Na_2MoO_4 \cdot 2\,H_2O$	—	—	50 mM	—	50 mM
citric acid	—	—	100 mM	—	100 mM

All thin film electrodeposition was performed potentiostatically onto flat substrates. Those consisted of Si wafer metallised by sputter deposition of an intermediate Ti layer of approx. 10 nm and a Cu layer of approx. 200 nm in thickness as substrate for the electrodeposition. Preliminary experiments were also performed on Au and Ni surfaces instead of Cu.

4.2.2 Nanoparticle synthesis

The electrodeposition of NPs was performed in an electrochemical cell using pulse electrodeposition. Deposition parameters and galvanostatic control was chosen based on recent studies on Pt and Pt alloy NP electrodeposition for PEMFC [79–81]. In analogy to the tuneability of composition of Ni–Pt thin films, the electrodeposition current amplitude was varied in order to obtain NPs of different composition. At the same time, the number of cycles was adjusted in order to obtain identical deposition charges and therefore similar metal loadings. In between the cathodic pulses, no current was applied.

Since the GDL material which served as a substrate for electrodeposition has limited conductivity, the substrates were backed with a Cu sheet so that a homogeneous charge distribution over the entire substrate surface was guaranteed. However, exposition of the Cu sheet to the electrolyte was avoided by isolation with polyimide tape (Figure 4.3).
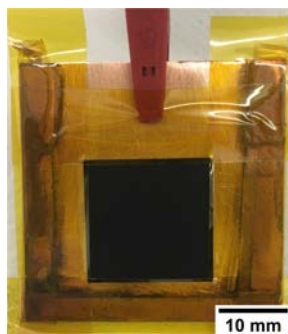
Figure 4.3: GDL as working electrode for nanoparticle electrodeposition backed by Cu sheet

In view of the acidic conditions of the PEMFC as targeted application and the oxidising conditions during ORR at the fuel cell cathode, it is clear that only electrocatalyst NPs with sufficient amount of noble metal qualify for adequate long-term durability. Therefore, during the preliminary studies consisting of optimising pulse electrodeposition parameters and electrolyte composition, NPs with 50 at% in Pt or higher were targeted. In parallel with the composition, NP particle size and catalyst loading were optimised. While at first small particle sizes were targeted, it should be noted that higher amounts of deposited material led to larger particle sizes and vice versa, so that a compromise between both parameters had to be found. This resulted in particle sizes of approx. 50 nm in diameter and catalyst loadings around

4 µg/cm^2. With respect to the deposition of Ni–Pt thin films, the amount of Pt salt in the electrolyte was increased (cf. Table 4.1).

Although feasible, the addition of a micelle-forming surfactant such as Pluronic P-123, which would allow the production of mesoporous particles, was discarded due to the objective of creating high amounts of TPB. Mesoporous NPs would theoretically show increased ECSA and therefore higher ORR activity in an electrochemical cell, but the density of TPB which would actually improve fuel cell performance should have a much higher dependency on particle size.

4.3 Electrochemical characterisation

4.3.1 Cyclic voltammetry

CV is used in order to determine the electrochemical processes of a given system within a chosen potential window. Similar to the electrodeposition process, potential range, scanning speed, agitation, and electrode materials influence the results of a CV. Thus, all of these parameters need to be controlled to ensure both reproducibility and comparability of the results.

In this work, CV is used for a number of purposes, the first of which is the characterisation of the electrodeposition electrolyte. Here, a vitreous carbon rod was employed as an inert WE, so that all observed currents could be related to metal reduction or oxidation of material deposited on the WE, without any contribution of the WE itself to oxidation and reduction currents. In this case, a scanning speed of 50 mV/s under static conditions was employed with the CV starting near OCP towards cathodic potentials.

CV was further used to study the oxidation and reduction behaviour of electrodeposited Ni–Pt thin films, focussing on the redox reaction between Ni(OH)$_2$ and NiOOH in alkaline media, a reaction exploited in electrochemical supercapacitors [192]. Both a conventional electrochemical cell and an electrochemical microcell were used, studying the effects of scanning speed and potential range in both 1 M NaOH and 0.5 M H$_2$SO$_4$.

4.3.1.1 ECSA

ECSA of both thin films and NPs were studied by hydrogen adsorption and desorption from CV as described in the previous chapter. The ECSA for Ni-rich Ni–Pt thin films was studied in 0.5 M NaOH alkaline solution according to Machado and Avaca by holding the potential at –1.35 V for 5 min and a subsequent CV starting from –1.05 V with an upper limit of –0.43 V vs

Ag|AgCl, and using 514 µC and 210 µC as the respective monolayer charge densities for Ni and Pt [173]. In contrast, the ECSA of Pt–Ni and Pt–Ni–Mo NPs was studied in 0.5 M H_2SO_4 after initial CVs to activate the electrocatalyst, in accordance with the method described by Wei et al. by performing CV between –0.2 V and –1.1 V vs Ag|AgCl, determining ECSA with respect to the Pt content using its corresponding monolayer charge of 210 µC [30]. In both cases, the scanning speed was 50 mV/s.

In case of the NPs, the double-layer capacitance needed for the determination of ECSA was determined by electrochemical impedance spectroscopy (EIS).

4.3.1.2 ORR

The determination of ORR behaviour is commonly performed by rotating disk electrode (RDE) measurements in order to eliminate mass-transport limitations [36]. Here, the ORR of carbon-supported NPs was measured in stagnant conditions. At first, a CV is recorded in N_2 saturated 0.1 M $HClO_4$ at 10 mV/s in the range of the ORR between 0 and 1.1 V vs RHE. Then, the electrolyte was saturated with O_2 for at least 30 min before conducting another CV in the same potential range. Due to the high ORR currents and limited conductivity of the carbon substrates, the curves were corrected for Ohmic drop [30]. The instrumentation resistance for this *iR* correction was determined by EIS. The final ORR curves are produced by subtraction of the CV recorded in N_2-saturated electrolyte.

4.3.2 EIS

EIS is a method to study an electrochemical system as a type of unknown circuit and to determine ohmic, capacitive, and inductive behaviour. In EIS, a small amplitude of either potential or current is applied as a sinusoidal waveform around a fixed potential or current, for example during HER. Here, all EIS measurements were performed at OCP after determining the OCP for 10 min. During the measurement, the frequency is varied from 100 kHz to 3 mHz, and the real and imaginary parts of the impedance are measured. Nyquist and Bode plots are used for graphic representation of the results. Using previously established models, such as the Randles circuit, an equivalent electrical circuit can be obtained for the electrochemical system. The components of the equivalent circuit correspond to electrochemical properties such as solution resistance, charge-transfer resistance, and double-layer

capacitance. Here, the fitting of the circuits for determination of the electro-chemical properties was performed using Dellis' Matlab function Zfit [193].

4.3.3 HER

While a Pt wire is employed as CE for all above-mentioned electrochemical experiments, a graphite rod is used as a CE in HER measurements. This is due to the fact that, when the WE is at high cathodic potentials, the CE is at high oxidising potentials where Pt, even if only in low amounts, can dissolve and redeposit on the WE [194]. Especially in long-term experiments, this can lead to noticeable improvement in performance at HER. The HER was studied by performing 200 cathodic-going LSVs at 50 mV/s from –0.15 to –0.5 V vs Ag|AgCl. Additional long-term experiments were performed by applying –10 mA/cm^2 for 24 h while monitoring the potential.

4.4 PEMFC testing

The electrodeposited Pt–Ni and Pt–Ni–Mo NPs supported on GDL substrates were hot-pressed with a Nafion 212 PEM and a commercial gas diffusion electrode (GDE) with a Pt loading of 0.3 mg/cm^2 serving as anode. Hot-pressing conditions were 0.5 MPa at 110 °C for 3 min.

The fuel cell testing was performed in a Greenlight G20 fuel cell test stand at the Research Institutes of Sweden (RISE), Borås, at the Department of Electrification and Reliability. The obtained MEA was mounted in a single cell fuel cell tester using (from the inside towards the outside) the MEA, a polymer sheet to avoid any electrical contact or short-circuiting outside of the active area, polymer gaskets, coated stainless steel flow plates, and bipolar plates. Uniform pressure was applied to the cell using four screws located at the corners and fixed with a torque of 0.5 Nm each. Electrical contacts for controlling the voltage were connected to the flow plates, and the contacts for applying the load were connected to the centre of the bipolar plates. A temperature sensor reads the temperature at the bipolar plates, and the gas inlets and outlets go through the bipolar planes to the MEA (Figure 4.4).

The fuel cell's active area was 2.9 cm^2. During the testing, the cell temperature was 80 °C. H$_2$ and air were used at anode and cathode with flows of 0.042 and 0.10 l/min, respectively.

An activation programme was run prior to testing, consisting of cycling between 0.9 V and 0.6 V for 2 000 cycles. After the activation, polarisa-

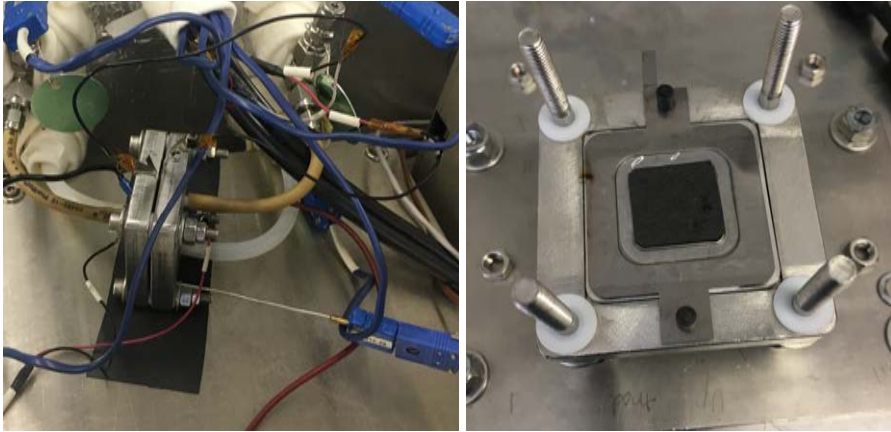Figure 4.4: Assembled PEMFC for testing (left) and open cell showing the MEA during assembly (right).

tion curves were recorded by taking points in steps of 0.05 V, first going towards lower voltages, and then up to open circuit voltage (OCV). ADT was performed by 20 000 cycles in the same range as the activation treatment, between 0.9 V and 0.6 V. Polarisation curves were obtained after 10 000 cycles and at the end of test.

Bibliography

[1] S. A. Sherif, F. Barbir, T. N. Veziroglu, *Solar Energy* **2005**, *78*, 647.

[2] K. T. Møller, T. R. Jensen, E. Akiba, H.-W. Li, *Prog. Nat. Sci.* **2017**, *27*, 34.

[3] J. Baxter, Z. Bian, G. Chen, D. Danielson, M. S. D. aund A. G. Fedorov, T. S. Fisher, C. W. Jones, E. Maginn, U. Kortshagen, A. Manthiram, A. Nozik, D. R. Rolison, T. Sands, L. Shi, D. Sholl, Y. Wu, *Energy Environ. Sci.* **2009**, *2*, 559.

[4] F. Orecchini, *Int. J. Hydrogen Energy* **2006**, *31*, 1951.

[5] S. P. S. Badwal, S. S. Giddey, C. Munnings, A. I. Bhatt, A. F. Hollenkamp, *Front. Chem.* **2014**, *2*, 79.

[6] *Hydrogen and Syngas Production and Purification Technologies*, (Eds.: K. Liu, C. Song, V. Subramani), Center for Chemical Process Safety of the American Institute of Chemical Engineers and John Wiley & Sons, Inc., NJ, **2010**.

[7] L. Mølmen, K. Eiler, L. Fast, P. Leisner, E. Pellicer, *APL Mater.* **2021**, *9*, 040702.

[8] B. G. Pollet, S. S. Kocha, I. Staffell, *Curr. Opin. Electrochem.* **2019**, *16*, 90.

[9] I. Roger, M. A. Shipman, M. D. Symes, *Nat. Rev. Chem.* **2017**, *1*, 0003.

[10] A. Kongkanand, M. F. Mathias, *J. Phys. Chem. Lett.* **2016**, *7*, 1127.

[11] R. Du, Q. Zhao, Z. Zheng, W. Hu, J. Zhang, *Adv. Energy Mater.* **2016**, *6*, 1600473.

[12] C. Navarro-Senent, A. Quintana, E. Menéndez, E. Pellicer, J. Sort, *APL Mater.* **2019**, *7*, 030701.

[13] K. Leistner, *Curr. Opin. Electrochem.* **2021**, *25*, 100636.

[14] *CRC Handbook of Chemistry and Physics*, (Eds.: R. C. Weast, M. J. Astle), CRC Press Inc., FL, 62nd ed., **1981**.

[15] S. Marini, P. Salvi, P. Nelli, R. Pesenti, M. Villa, M. Berrettoni, G. Zangari, Y. Kiros, *Electrochim. Acta* **2012**, *82*, 384.

[16] O. Khaselev, J. A. Turner, *Science* **1998**, *280*, 425.

[17] J. R. McKone, E. L. Warren, M. J. Bierman, S. W. Boettcher, B. S. Brunschwig, N. S. Lewis, H. B. Gray, *Energy Environ. Sci.* **2011**, *4*, 3573.

[18] P. Rodenas, T. Song, P. Sudhagar, G. Marzari, H. Han, L. Badia-Bou, S. Gimenez, F. Fabregat-Santiago, I. Mora-Sero, J. Bisquert, U. Paik, Y. S. Kang, *Adv. Energy Mater.* **2013**, *3*, 176.

[19] T. Yoshida, K. Kojima, *Interface* **2015**, *24*, 45.

[20] Fuel Cell Technologies Office in *Multi-Year Research, Development, and Demonstration Plan*, **2017**, Chapter 3.4 *Fuel Cells*.

[21] L. Mølmen, A. Alexandersson, P. Leisner, *Trans. IMF* **2019**, *97*, 112.

[22] X. Tian, X. Zhao, Y.-Q. Su, L. Wang, H. Wang, D. Dang, B. Chi, H. Liu, E. J. M. Hensen, X. W. Lou, B. Y. Xia, *Science* **2019**, *366*, 850.

[23] H. Cheng, Z. Cao, Z. Chen, M. Zhao, M. Xie, Z. Lyu, Z. Zhu, M. Chi, Y. Xia, *Nano Lett.* **2019**, *19*, 4997.

[24] J. Wang, G. Wu, W. Wang, W. Xuan, J. Jiang, J. Wang, L. Li, W.-F. Lin, W. Ding, Z. Wei, *J. Mater. Chem. A* **2019**, *7*, 19786.

[25] Z. Wang, X. Yao, Y. Kang, D. Xia, L. Gan, *Catalysts* **2019**, *9*, 569.

[26] W. Gong, Z. Jiang, R. Wu, Y. Liu, L. Huang, N. Hu, P. Tsiakaras, P. K. Shen, *Appl. Catal. B* **2019**, *246*, 277.

[27] J. K. Nørskov, J. Rossmeisl, A. Logadottir, L. Lindqvist, J. R. Kitchin, T. Bligaard, H. Jónsson, *J. Phys. Chem. B* **2004**, *108*, 17886.

[28] J. Shin, J.-H. Choi, P.-R. Cha, S. K. Kim, I. Kim, S.-C. Lee, D. S. Jeong, *Nanoscale* **2015**, *7*, 15830.

[29] J. Greeley, T. F. Jaramillo, J. Bonde, I. Chorkendorff, J. K. Nørskov, *Nat. Mater.* **2006**, *5*, 909.

[30] C. Wei, R. R. Rao, J. Peng, B. Huang, I. E. L. Stephens, M. Risch, Z. J. Xu, Y. Shao-Horn, *Adv. Mater.* **2019**, *31*, 1806296.

[31] D. Voiry, M. Chhowalla, Y. Gogotsi, N. A. Kotov, Y. Li, R. M. Penner, R. E. Schaak, P. S. Weiss, *ACS Nano* **2018**, *12*, 9635.

[32] J.-P. Diard, B. LeGorrec, S. Maximovitch, *Electrochim. Acta* **1990**, *35*, 1099.

[33] S. M. Alia, Y. S. Yan, B. S. Pivovar, *Catal. Sci. Technol.* **2014**, *4*, 3589.

[34] T. Shinagawa, A. T. Garcia-Esparza, K. Takanabe, *Sci. Rep.* **2015**, *5*, 13801.

[35] Y.-H. Fang, Z.-P. Liu, *ACS Catal.* **2014**, *4*, 4364.

[36] K. J. J. Mayrhofer, D. Strmcnik, B. B. Blizanac, V. Stamenkovic, M. Arenz, N. M. Markovic, *Electrochim. Acta* **2008**, *53*, 3181.

[37] V. G. Levich, *Physicochemical hydrodynamics*, Englewood Cliffs, N.J., Prentice-Hall, **1962**.

[38] M. Schlesinger in *Kirk-Othmer Encyclopedia of Chemical Technology*, American Cancer Society, **2004**, Chapter *Electroplating*.

[39] G. Zangari in *Modern electroplating* (Eds.: M. Schlesinger, M. Paunovic), John Wiley & Sons, Inc., NJ, 5th ed., **2010**, Chapter *Microelectromechanical systems*.

[40] B. D. Falola, I. I. Suni, *Curr. Opin. Solid State Mater. Sci.* **2015**, *19*, 77.

[41] L. Gu, Y. Wang, R. Lu, L. Guan, X. Peng, J. Sha, *J. Mater. Chem. A* **2014**, *2*, 7161.

[42] G. Kokkinidis, A. Papoutsis, D. Stoychev, A. Milchev, *J. Electroanal. Chem.* **2000**, *486*, 48.

[43] M. Schlesinger in *Modern electroplating* (Eds.: M. Schlesinger, M. Paunovic), John Wiley & Sons, Inc., NJ, 5th ed., **2010**, Chapter *Electroless deposition of nickel*.

[44] D. Li, C. Batchelor-McAuley, R. G. Compton, *Appl. Mater. Today* **2020**, *18*, 100404.

[45] M. S. Chandrasekar, M. Pushpavanam, *Electrochim. Acta* **2008**, *53*, 3313.

44

[46] E. Pellicer, E. Gómez, E. Vallés, *Surf. Coat. Technol.* **2006**, *201*, 2351.

[47] G. A. Di Bari in *Modern electroplating* (Eds.: M. Schlesinger, M. Paunovic), John Wiley & Sons, Inc., NJ, 5th ed., **2010**, Chapter *Electrodeposition of nickel*.

[48] S. Sengupta, A. Patra, S. Jena, K. Das, S. Das, *Metall. Mater. Trans. A* **2018**, *49A*, 920.

[49] H.-C. Shin, M. Liu, *Chem. Mater.* **2004**, *16*, 5460.

[50] X. Guo, X. Li, Y. Zheng, C. Lai, W. Li, B. Luo, D. Zhang, *J. Nanomater.* **2014**, 358312.

[51] M. Paunovic, M. Schlesinger in *Fundamentals of electrochemical deposition*, John Wiley & Sons, Inc., NJ, 2nd ed., **2006**, Chapter *Electrodeposition of Alloys*.

[52] S. Rode, C. Henninot, C. Vallières, M. Matlosz, *J. Electrochem. Soc.* **2004**, *151*, C405.

[53] N. Tsyntsaru, S. Belevsky, H. Cesiulis, A. Dikusar, J.-P. Celis, *Surf. Eng. Appl. Electrochem.* **2012**, *48*, 418.

[54] W. Plieth in *Electrochemistry for Materials Science*, Elsevier, NL, **2008**, Chapter Deposition of Alloys.

[55] Y. D. Gamburg, G. Zangari, *Theory and Practice of Metal Electrodeposition*, Springer, NY, **2011**.

[56] M. Paunovic, M. Schlesinger, D. D. Snyder in *Modern electroplating* (Eds.: M. Schlesinger, M. Paunovic), John Wiley & Sons, Inc., NJ, 5th ed., **2010**, Chapter *Fundamental considerations*.

[57] C. Navarro-Senent, S. Pané, J. Sort, E. Pellicer, *Electrochim. Acta* **2020**, *358*, 136940.

[58] J. Ji, C. Cooper, D. B. Dreisinger, E. Peters, *J. Appl. Electrochem.* **1995**, *25*, 642.

[59] X. Wu, Q. Gao, Z. Li, *Int. J. Electrochem. Sci.* **2015**, *10*, 8823.

[60] E. Dislaki, J. Sort, E. Pellicer, *Electrochim. Acta* **2017**, *231*, 739.

[61] M. Paunovic, M. Schlesinger in *Fundamentals of electrochemical deposition*, John Wiley & Sons, Inc., NJ, 2nd ed., **2006**, Chapter *Effect of Additives*.

[62] L. Oniciu, L. Mureşan, *J. Appl. Electrochem.* **1991**, *21*, 565.

[63] S. A. Watson, J. Edwards, *Trans. IMF* **1956**, *34*, 167.

[64] D. M. Mattox, *Interface Formation and the Adhesion of Deposited Thin Films*, Sandia Corporation, Albuquerque, NM Technical Report SC-R-65-852, **1965**.

[65] H. Li, F. Ebrahimi, *Mat. Sci. Eng. A* **2003**, *347*, 93.

[66] E. Pellicer, A. Varea, S. Pané, B. J. Nelson, E. Menéndez, M. Estrader, S. Suriñach, M. D. Baró, J. Nogués, J. Sort, *Adv. Funct. Mater.* **2010**, *20*, 983.

[67] J. Weertman, *Mat. Sci. Eng. A* **1993**, *166*, 161.

[68] C. Schuh, T. Nieh, T. Yamasaki, *Scr. Mater.* **2002**, *46*, 735.

[69] X. Shu, D. Kong, Y. Lu, H. Long, S. Sun, X. Sha, H. Zhou, Y. Chen, S. Mao, Y. Liu, *Sci. Rep.* **2017**, *7*, 13264.

[70] B. Craig in *ASM Handbook*, *Vol. 13A* (Eds.: S. Cramer, B. Covino, Jr.), ASM Intl., **2003**, Chapter *Hydrogen Damage*.

[71] *Magnétisme, Vol. 1 – Fondements*, (Ed.: É. du Trémolet de Lacheisserie), EDP Sciences, France, **2000**.

[72] K. Fabian, V. P. Shcherbakov, S. A. McEnroe, *Geochem. Geophys. Geosyst.* **2013**, *14*, 947.

[73] W. D. Callister, Jr., D. G. Rethwisch, *Materials Science and Engineering – An Introduction*, John Wiley & Sons, Inc., NJ, 8th ed., **2010**.

[74] C. Kittel, *Introduction to solid state physics*, *Vol. 8*, Wiley, NY, **1996**.

[75] J. Ustarroz, X. Ke, A. Hubin, S. Bals, H. Terryn, *J. Phys. Chem. C* **2012**, *116*, 2322.

[76] H. E. M. Hussein, R. J. Maurer, H. Amari, J. J. P. Peters, L. Meng, R. Beanland, M. E. Newton, J. V. Macpherson, *ACS Nano* **2018**, *12*, 7388.

[77] H. E. M. Hussein, H. Amari, J. V. Macpherson, *ACS Catal.* **2017**, *7*, 7388.

[78] Y. Liu, H. You, Y. C. Kimmel, D. V. Esposito, J. G. Chen, T. P. Moffat, *Appl. Surf. Sci.* **2020**, *504*, 144472.

[79] A. Egetenmeyer, M. Baumgärtner, T. Linckh, D. Durneata, H. Natter, R. Hempelmann, I. Radev, V. Peinecke, *Trans. IMF* **2017**, *95*, 9.

[80] A. Egetenmeyer, I. Radev, D. Durneata, M. Baumgärtner, V. Peinecke, H. Natter, R. Hempelmann, *Int. J. Hydrogen Energy* **2017**, *42*, 13649.

[81] C. Huang, C. B. Odetola, M. Rodgers, *Appl. Catal. A* **2015**, *499*, 55.

[82] A. G. Oshchepkov, G. Braesch, S. Ould-Amara, G. Rostamikia, G. Maranzana, A. Bonnefont, V. Papaefthimiou, M. J. Janik, M. Chatenet, E. R. Savinova, *ACS Catal.* **2019**, *9*, 8520.

[83] G. Braesch, A. G. Oshchepkov, A. Bonnefont, F. Asonkeng, T. Maurer, G. Maranzana, E. R. Savinova, M. Chatenet, *ChemElectroChem* **2020**, *7*, 1789.

[84] X. An, S. Li, A. Yoshida, Z. Wang, X. Hao, A. Abudula, G. Guan, *ACS Sustain. Chem. Eng.* **2019**, *7*, 9360.

[85] M. V. Roldán, N. Pellegri, O. de Santis, *J. Nanoparticles* **2013**, *2013*, 524150.

[86] *IUPAC. Compendium of Chemical Terminology*, (Eds.: A. D. McNaught, A. Wilkinson), Blackwell Scientific Publications, UK, 2nd ed., **1997**.

[87] O. V. Kharissova, H. V. R. Dias, B. I. Kharisov, *RSC Adv.* **2015**, *5*, 6695.

[88] F. J. Heiligtag, M. J. I. Airaghi Leccardi, D. Erdem, M. J. Süess, M. Niederberger, *Nanoscale* **2014**, *6*, 13213.

[89] Z. Yu, L. Tetard, L. Zhai, J. Thomas, *Energy Environ. Sci.* **2015**, *8*, 702.

[90] V. Malgras, H. Ataee-Esfahani, H. Wang, B. Jiang, C. Li, K.-W. Wu, J. Kim, Y. Yamauchi, *Adv. Mater.* **2016**, *28*, 993.

[91] N. Linares, A. M. Silvestre-Albero, E. Serrano, J. Silvestre-Albero, J. García-Martínez, *Chem. Soc. Rev.* **2014**, *43*, 7681.

[92] J. Kibsgaard, Z. Chen, B. N. Reinecke, T. F. Jaramillo, *Nat. Mater.* **2012**, *11*, 963.

[93] C. Hou, X.-Y. Lang, G.-F. Han, Y.-Q. Li, L. Zhao, Z. Wen, Y.-F. Zhu, M. Zhao, J.-C. Li, J.-S. Lian, Q. Jiang, *Sci. Rep.* **2013**, *3*, 2878.

[94] A. Prim, E. Pellicer, E. Rossinyol, F. Peiró, A. Cornet, J. R. Morante, *Adv. Funct. Mater.* **2007**, *17*, 2957.

[95] E. Rossinyol, A. Prim, E. Pellicer, J. Arbiol, F. Hernández-Ramírez, F. Peiró, A. Cornet, J. R. Morante, L. A. Solovyov, B. Tian, T. Bo, D. Zhao, *Adv. Funct. Mater.* **2007**, *17*, 1801.

[96] N. Chen, Q. Pan, *ACS Nano* **2013**, *7*, 6875.

[97] B. G. Trewyn, S. Giri, I. I. Slowing, V. S.-Y. Lin, *Chem. Commun.* **2007**, 3236.

[98] T. A. Rebbecchi Jr., Y. Chen, *J. Mater. Res.* **2018**, *33*, 1.

[99] I. Vukovic, G. ten Brinke, K. Loos, *Polymer* **2013**, *54*, 2591.

[100] H.-Y. Hsueh, Y.-C. Huang, R.-M. Ho, C.-H. Lai, T. Makida, H. Hasegawa, *Adv. Mater.* **2011**, *23*, 3041.

[101] X. Yan, F. Meng, Y. Xie, J. Liu, Y. Ding, *Sci. Rep.* **2012**, *2*, 941.

[102] S. Xie, M. Jin, J. Tao, Y. Wang, Z. Xie, Y. Zhu, Y. Xia, *Chem. Eur. J.* **2012**, *18*, 14974.

[103] N. Bai, Q. Li, D. Mao, D. Li, H. Dong, *ACS Appl. Mater. Interfaces* **2016**, *8*, 29400.

[104] X. Lu, C. Zhao, *Nat. Commun.* **2015**, *6*, 6616.

[105] R. Campbell, M. G. Bakker, *J. Porous Mater.* **2004**, *11*, 63.

[106] X.-Y. Yang, L.-H. Chen, Y. Li, J. C. Rooke, C. Sanchez, B.-L. Su, *Chem. Soc. Rev.* **2017**, *46*, 481.

[107] P.-C. Chen, Y.-M. Chang, P.-W. Wu, Y.-F. Chiu, *Int. J. Hydrogen Energy* **2009**, *34*, 6596.

[108] K. Nielsch, F. Müller, A.-P. Li, U. Gösele, *Adv. Mater.* **2000**, *12*, 582.

[109] K. M. Kulinowski, P. Jiang, H. Vaswani, V. L. Colvin, *Adv. Mater.* **2000**, *12*, 833.

[110] R. Zhu, M. McLachlan, S. Reyntjens, F. Tariq, M. P. Ryan, D. W. McComb, *Nanoscale* **2009**, *1*, 355.

[111] K. Nishikawa, K. Dokko, K. Kinoshita, S.-W. Woo, K. Kanamura, *J. Power Sources* **2009**, *189*, 726.

[112] E. Dislaki, J. Pokki, S. Pané, J. Sort, E. Pellicer, *Appl. Mater. Today* **2018**, *12*, 1.

[113] I. Golvano-Escobal, R. de Paz-Castany, C. C. J. Alcantara, S. Pané, E. García-Lecina, J. Sort, E. Pellicer, *Electrochim. Acta* **2019**, *313*, 211.

[114] Y. Yamauchi, K. Kuroda, *Electrochem. Commun.* **2006**, *8*, 1677.

[115] L. Zhang, L. Jin, B. Liu, J. He, *Front. Chem.* **2019**, *7*, 22.

[116] F. Mushtaq, M. Guerrero, M. S. Sakar, M. Hoop, A. M. Lindo, J. Sort, X. Chen, B. J. Nelson, E. Pellicer, S. Pané, *Nanoscale* **2015**, *3*, 23670.

[117] J. Zhang, A. Quintana, E. Menéndez, M. Coll, E. Pellicer, J. Sort, *ACS Appl. Mater. Interfaces* **2018**, *10*, 14877.

[118] H. Chen, L. Hu, Y. Yan, R. Che, M. Chen, L. Wu, *Adv. Energy Mater.* **2013**, *3*, 1636.

[119] G. Wanka, H. Hoffmann, W. Ulbricht, *Macromolecules* **1994**, *27*, 4145.

[120] C. Wang, D. Chen, X. Jiao, *Sci. Technol. Adv. Mater.* **2009**, *10*, 023001.

[121] F. Bender, R. K. Mankelow, D. B. Hibbert, J. J. Gooding, *Electroanalysis* **2006**, *18*, 1558.

[122] I. Dierking, S. Al-Zangana, *Nanomaterials* **2017**, *7*, 305.

[123] G. S. Attard, P. N. Bartlett, N. R. B. Coleman, J. M. Elliott, J. R. Owen, J. H. Wang, *Science* **1997**, *278*, 838.

[124] P. N. Bartlett, B. Gollas, S. Guerin, J. Marwan, *Phys. Chem. Chem. Phys.* **2002**, *4*, 3835.

[125] P. A. Nelson, J. M. Elliott, G. S. Attard, J. R. Owen, *Chem. Mater.* **2002**, *14*, 524.

[126] K. Ariga, A. Vinu, Y. Yamauchi, Q. Ji, J. P. Hill, *Bull. Chem. Soc. Jpn.* **2012**, *85*, 1.

[127] X. Zhang, W. Lu, J. Dai, L. Bourgeois, N. Hao, H. Wang, D. Zhao, P. A. Webley, *Angew. Chem.* **2010**, *49*, 10101.

[128] H. Wang, L. Wang, T. Sato, Y. Sakamoto, S. Tominaka, K. Miyasaka, N. Miyamoto, Y. Nemoto, O. Terasaki, Y. Yamauchi, *Chem. Mater.* **2012**, *24*, 1591.

[129] C. Li, H. Wang, Y. Yamauchi, *Chem. Eur. J.* **2013**, *19*, 2242.

[130] C. Li, Y. Yamauchi, *Chem. Eur. J.* **2014**, *20*, 729.

[131] H. Wang, Y. Yamauchi, *Chem. Asian J.* **2012**, *7*, 2133.

[132] H. Wang, M. Imura, Y. Nemoto, L. Wang, H. Y. Jeong, T. Yokoshima, O. Terasaki, Y. Yamauchi, *Chem. Eur. J.* **2012**, *18*, 13142.

[133] C. Li, B. Jiang, N. Miyamoto, J. H. Kim, V. Malgras, Y. Yamauchi, *J. Am. Chem. Soc.* **2015**, *137*, 11558.

[134] E. Isarain-Chávez, M. D. Baró, E. Pellicer, J. Sort, *Nanoscale* **2017**, *9*, 18081.

[135] R. Nagarajan, *J. Colloid Interface Sci.* **2015**, *449*, 416.

[136] S. Tanaka, B. P. Bastakoti, Y. L. S. Yusa, D. Ishii, K. Kani, A. Fatehmulla, W. A. Farooq, M. J. A. Shiddiky, Y. Bando, Y. V. Kaneti, Y. Yamauchi, M. S. A. Hossain, *Eur. J. Inorg. Chem.* **2017**, 1328.

[137] D. Baba, J. Kim, J. Henzie, C. Li, B. Jiang, Ö. Dag, Y. Yamauchi, T. Asahi, *Chem. Commun.* **2018**, *54*, 10347.

[138] C. Li, B. Jiang, Z. Wang, Y. Li, M. S. A. Hossain, J. H. Kim, T. Takei, J. Henzie, Ö. Dag, Y. Bando, Y. Yamauchi, *Angew. Chem.* **2016**, *128*, 12938.

[139] R. Artal, A. Serrà, J. Michler, L. Philippe, E. Gómez, *Nanomaterials* **2020**, *10*, 1435.

[140] B. Naskar, S. Ghosh, S. P. Moulik, *Langmuir* **2012**, *28*, 7134.

[141] H. Lim, D. Kim, Y. Kim, T. Nagaura, J. You, J. Kim, H.-J. Kim, J. Na, J. Henzie, Y. Yamauchi, *J. Mater. Chem. A* **2020**, *8*, 21016.

[142] Y.-C. Liang, Y.-W. Juan, K.-T. Lu, U.-S. Jeng, S.-A. Chen, W.-T. Chuang, C.-J. Su, C.-L. Liu, C.-W. Pao, J.-F. Lee, H.-S. Sheu, J.-M. Chen, *J. Phys. Chem. C* **2012**, *116*, 26649.
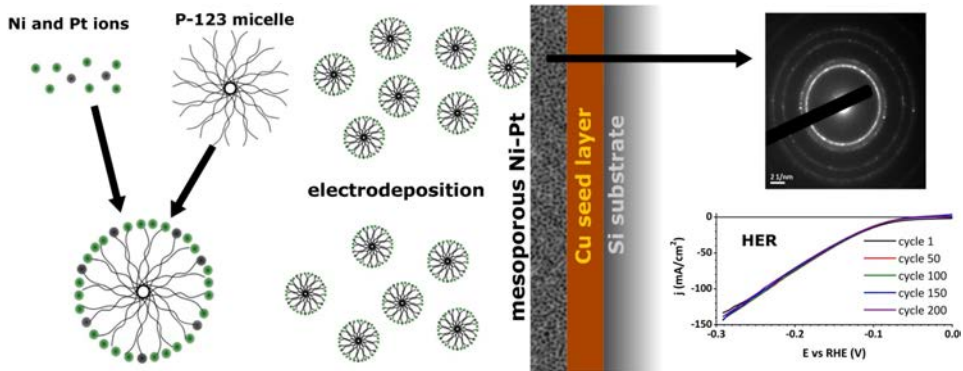
[143] H. K. D. Kim, L. T. Schelhas, S. Keller, J. L. Hockel, S. H. Tolbert, G. P. Carman, *Nano Lett.* **2013**, *13*, 884.

[144] I. V. Ovchinnikov, K. L. Wang, *Phys. Rev. B* **2009**, *80*, 012405.

[145] I. V. Ovchinnikov, K. L. Wang, *Phys. Rev. B* **2009**, *79*, 020402.

[146] A. Quintana, J. Zhang, E. Isarain-Chávez, E. Menéndez, R. Cuadrado, R. Robles, M. D. Baró, M. Guerrero, S. Pané, B. J. Nelson, C. M. Müller, P. Ordejón, J. Nogués, E. Pellicer, J. Sort, *Adv. Funct. Mater.* **2017**, *27*, 1701904.

[147] A. Quintana, E. Menéndez, E. Isarain-Chávez, J. Fornell, P. Solsona, F. Fauth, M. D. Baró, J. Nogués, E. Pellicer, J. Sort, *Small* **2018**, *14*, 1704396.

[148] G. Raykhtsaum, *Platin. Met. Rev* **2013**, *57*, 202.

[149] P. Nash, M. F. Singleton, *Bull. Alloy Phase Diagr.* **1989**, *10*, 258.

[150] R. Oriňáková, A. Turoňová, D. Kladeková, M. Gálová, R. M. Smith, *J. Appl. Electrochem.* **2006**, *36*, 957.

[151] P. Allongue, F. Maroun, H. F. Jurca, N. Tournerie, G. Savidand, R. Cortès, *Surf. Sci.* **2009**, *603*, 1831.

[152] O. P. Watts, *Trans. Am. Electrochem. Soc.* **1916**, *29*, 395.

[153] H. M. Yasin, G. Denuault, D. Pletcher, *J. Electroanal. Chem.* **2009**, *633*, 327.

[154] J. M. Elliott, G. S. Attard, P. N. Bartlett, N. R. B. Coleman, D. A. S. Merckel, J. R. Owen, *Chem. Mater.* **1999**, *11*, 3602.

[155] P. Garrido, E. Gómez, E. Vallés, *J. Electroanal. Chem.* **1998**, *441*, 147.

[156] Y. Yamauchi, S. S. Nair, T. Momma, T. Ohsuna, T. Osaka, K. Kuroda, *J. Mater. Chem.* **2006**, *16*, 2229.

[157] Y. Liu, C. M. Hangarter, U. Bertocci, T. P. Moffat, *J. Phys. Chem. C* **2012**, *116*, 7848.

[158] O. Sorsa, H. Romar, U. Lassi, T. Kallio, *Electrochim. Acta* **2017**, *230*, 49.

[159] E. Antolini, *Int. J. Energy Res.* **2018**, *42*, 3747.

[160] S. M. Alia, C. Ngo, S. Shulda, M.-A. Ha, A. A. Dameron, J. N. Weker, K. C. Neyerlin, S. S. Kocha, S. Pylypenko, B. S. Pivovar, *ACS Omega* **2017**, *2*, 1408.

[161] S. Grau, M. Montiel, E. Gómez, E. Vallés, *Electrochim. Acta* **2013**, *109*, 187.

[162] S. Fiameni, I. Herraiz-Cardona, M. Musiani, V. Pérez-Herranz, L. Vázquez-Gómez, E. Verlato, *Int. J. Hydrogen Energy* **2012**, *37*, 10507.

[163] J. Zheng, *Appl. Surf. Sci.* **2017**, *413*, 360.

[164] C. Xu, J. Wang, J. Zhou, *Sens. Actuators B* **2013**, *182*, 408.

[165] B. E. Conway, B. V. Tilak, *Electrochim. Acta* **2002**, *47*, 3571.

[166] A. Lasia in *Handbook of Fuel Cells – Fundamentals, Technology and Applications, Vol. 2* (Eds.: W. Vielstich, A. Lamm, H. A. Gasteiger), John Wiley & Sons, Ltd, UK, **2003**, Chapter *Hydrogen evolution reaction*.

[167] K. I. Siwek, S. Eugénio, D. M. F. Santos, M. T. Silva, M. F. Montemor, *Int. J. Hydrogen Energy* **2019**, *44*, 1701.

[168] L. Birry, A. Lasia, *J. Appl. Electrochem.* **2004**, *34*, 735.

[169] M. Metikoš-Huković, Z. Grubač, N. Radić, A. Tonejc, *J. Mol. Catal. A* **2006**, *249*, 172.

[170] Y. Ito, M. Izumi, D. Hojo, M. Wakisaka, T. Aida, T. Adschiri, *Chem. Lett.* **2017**, *46*, 267.

[171] J. Zhang, M. D. Baró, E. Pellicer, J. Sort, *Nanoscale* **2014**, *6*, 12490.

[172] Y.-J. Huang, C.-H. Lai, P.-W. Wu, L.-Y. Chen, *J. Electrochem. Soc.* **2010**, *157*, P18.

[173] S. A. S. Machado, L. A. Avaca, *Electrochim. Acta* **1994**, *39*, 1385.

[174] L. Zhang, D. Shi, T. Liu, M. Jaroniec, J. Yu, *Mater. Today* **2019**, *25*, 35.

[175] F. Cardarelli, *Materials Handbook*, Springer Intl. Publishing, Switzerland, 3rd ed., **2018**.

[176] E. Chassaing, N. Portail, A.-F. Levy, G. Wang, *J. Appl. Electrochem.* **2004**, *34*, 1085.

[177] K. Murase, M. Ogawa, T. Hirato, Y. Awakura, *J. Electrochem. Soc.* **2004**, *151*, C798.

[178] H. Ashassi-Sorkhabi, P. La'le Badakhshan, *Appl. Surf. Sci.* **2017**, *419*, 165–176.

[179] E. Gómez, E. Pellicer, E. Vallés, *J. Electroanal. Chem.* **2005**, *580*, 238.

[180] A. Quintana, A. Varea, M. Guerrero, S. Suriñach, M. D. Baró, J. Sort, E. Pellicer, *Electrochim. Acta* **2015**, *173*, 705.

[181] K. Hu, T. Ohto, L. Chen, J. Han, M. Wakisaka, Y. Nagata, J.-I. Fujita, Y. Ito, *ACS Energy Lett.* **2018**, *3*, 1539.

[182] G. Abuin, R. Coppola, L. Diaz, *Electrocatalysis* **2019**, *10*, 17.

[183] J. Halim, R. Abdel-Karim, S. El-Raghy, M. Nabil, A. Waheed, *J. Nanomater.* **2012**, 845673.

[184] X. Liu, K. Ni, C. Niu, R. Guo, W. Xi, Z. Wang, J. Meng, J. Li, Y. Zhu, P. Wu, Q. Li, J. Luo, X. Wu, L. Mai, *ACS Catal.* **2019**, *9*, 2275.

[185] Z. Liu, J. E. Hu, Q. Wang, K. Gaskell, A. I. Frenkel, G. S. Jackson, B. Eichhorn, *J. Am. Chem. Soc.* **2009**, *131*, 6924.

[186] F. A. Shunk, *Constitution of binary alloys*, McGraw-Hill, NY, **1969**.

[187] L. Brewer, R. H. Lamoreaux, R. Ferro, R. Marazza, *Bull. Alloy Phase Diagr.* **1980**, *1*, 89.

[188] J. Mao, W. Chen, D. He, J. Wan, J. Pei, J. Dong, Y. Wang, P. An, Z. Jin, W. Xing, H. Tang, Z. Zhuang, X. Liang, Y. Huang, G. Zhou, L. Wang, D. Wang, Y. Li, *Sci. Adv.* **2017**, *3*, 1603068.

[189] X. Huang, Z. Zhao, L. Cao, Y. Chen, E. Zhu, Z. Lin, M. Li, A. Yan, A. Zettl, Y. M. Wang, X. Duan, T. Mueller, Y. Huang, *Science* **2015**, *12*, 1230.

[190] Q. Jia, Z. Zhao, L. Cao, J. Li, S. Ghoshal, V. Davies, E. Stavitski, K. Attenkofer, Z. Liu, M. Li, X. Duan, S. Mukerjee, T. Mueller, Y. Huang, *Nano Lett.* **2018**, *18*, 798.

[191] H. Krawiec, V. Vignal, R. Oltra, *Electrochem. Commun.* **2004**, *6*, 655.

[192] N. Tokmak, M. Ürgen, *MRS Advances* **2017**, *2*, 3237.

[193] J.-L. Dellis, *Zfit*, **2020**, https://www.mathworks.com/matlabcentral/fileexchange/19460-zfit.

[194] R. Wei, M. Fang, G. Dong, J. C. Ho, *Sci. Bull.* **2017**, *62*, 971.

50

5 Results

The results are structured as a compilation of articles, presenting the published research works in chronological order, in addition to a manuscript prepared for publication. An additional work, which is not based on original research but on literature research, can be found in the Annex.

5.1 Mesoporous Ni-rich Ni–Pt thin films: Electrodeposition, characterization and performance toward hydrogen evolution reaction in acidic media

Konrad Eiler[a], Santiago Suriñach[a], Jordi Sort[a,b] and Eva Pellicer[a]

[a]Departament de Física, Universitat Autònoma de Barcelona, 08193 Bellaterra, Spain
[b]Institució Catalana de Recerca i Estudis Avançats (ICREA), Pg. Lluís Companys 23, 08010 Barcelona, Spain

The first published and initial work focusses on both the electrodeposition of mesoporous Ni-rich Ni–Pt thin films as well as their performance at HER. Therefore its main topics are the synthesis by electrodeposition including characterisation of the electrolyte, an initial compositional, structural and surface analysis, and an evaluation of the catalytic activity at HER in acidic media.

A tuneability of the composition is achieved by simple variation of the electrodeposition potential. Changes in morphology as a function of deposition potential are observed, while the porosity is homogeneously distributed in all three dimensions with identical, narrow size distribution irrespective of composition. The thin films, exhibiting a thickness around 200–300 nm, are of metallic nature and nanocrystalline. Hydroxide species are present on the surface, and are partially reduced during HER. Activity at HER is demonstrated to be more efficient for mesoporous thin films with respect to dense thin films, while the maximum electrocatalytic activity is found for $Ni_{84}Pt_{16}$. Above 8% of Pt content, excellent stability and reproducibility during 200 cathodic sweeps (LSV) is observed.

Mesoporous Ni-rich Ni–Pt thin films: Electrodeposition, characterization and performance toward hydrogen evolution reaction in acidic media

K. Eiler[a,*], S. Suriñach[a], J. Sort[a,b], E. Pellicer[a]

[a] *Departament de Física, Universitat Autònoma de Barcelona, 08193 Bellaterra, Spain*
[b] *Institució Catalana de Recerca i Estudis Avançats (ICREA), Pg. Lluís Companys 23, 08010 Barcelona, Spain*

ARTICLE INFO

ABSTRACT

Homogeneously mesoporous Ni–Pt thin films have been successfully synthesized by potentiostatic electrodeposition from an aqueous solution. The films are single-phase nanocrystalline Ni–Pt fcc solid solution and their composition can be adjusted with the deposition potential to a Ni content within 60-100 at%. The mesoporosity is constantly present, independent of the composition or microstructure, homogeneously distributed in all dimensions of the films with a pore diameter in the order of 10 nm. Film thickness is uniform and in the range of 200–300 nm. The films show improved performance over an electrodeposited Pt film at hydrogen evolution reaction (HER) and excellent stability in H_2SO_4 during 200 cycles. For the composition 84 at% Ni and 16 at% Pt, the overpotential required to reach a HER activity of $-10\,mA/cm^2$ is as low as -0.09 V vs. RHE. Meanwhile, the mesoporous alloy film with 95 at% Ni exhibits the highest activity with regard to the electrochemical surface area (ECSA).

1. Introduction

In order to move away from fossil fuels as a main energy source, renewable energies have to be made more accessible and affordable. Using hydrogen as an energy vector in fuel cell technology is entirely emission-free and due to the conversion cycle between water and hydrogen, a closed cycle of energy resource, this energy can theoretically be reused without compromising any resources [1]. Electrocatalysis is used to produce hydrogen gas directly from water. This catalysis is most efficient when performed in acidic media where H^+ concentration is high, this however usually requires the use of precious noble metals, commonly Pt [2]. In order to increase the affordability and accessibility of the technology, the material and component manufacturing cost needs to be minimized. Another crucial point for the success of fuel cell technology is the longevity of the components, related to their corrosion resistance.

For electrocatalytic processes used for water splitting, such as the hydrogen evolution reaction (HER), the surface-to-volume ratio of the catalyst is one of the most important factors. A highly porous material possesses an increased surface-to-volume ratio with respect to a dense material and thus the active surface available for the reaction is increased [3]. At the same time, an induced porosity reduces the amount of material needed, making it more cost-effective. The improvement of the HER activity on a porous structure has been shown, for example, on

MoS_2 [4]. Additionally, porous materials are of general interest in several fields such as in biomedical applications, sensors, water remediation, and many others [5].

By partially substituting platinum as one of the most active materials for HER with another more abundant, yet electrocatalytically active material, the cost-effectiveness may be further increased. Nickel has been chosen for this purpose due to its high abundancy, well-documented electrodeposition process [6,7] and its reliable HER performance in alkaline solution [8,9]. Among the iron group metals, it is the most active material toward HER [10]. Many Ni alloys have been studied extensively as potential catalysts for HER [2,11], though only few studies on Ni–Pt are reported. So far, HER of Ni–Pt materials has been studied for nanostructures such as nanowires [12] and more sophisticated architectures like nano-multipods [13], however those works are generally focused on HER in alkaline media.

The alloying of Ni with the noble metal Pt may allow to perform HER in acidic media, making the reaction more efficient due to a high concentration of H^+. Co-electrodeposition, both in general and of Ni alloys in particular, as well as the mechanism of micelle-assisted electrodeposition, has been well documented [14–16]. This method makes use of a polymeric surfactant forming spherical micelles in the electrolyte and being deposited together with the metals, leaving a mesoporous structure when the polymer is dissolved. Furthermore, Ni and Pt are fully miscible under equilibrium conditions, where ordered fcc

---

phases are possible for certain compositions [17].

Ni–Pt is therefore a promising material for different catalytic processes and has been synthesized through wet chemistry by various means involving multiple steps, creating different architectures such as thin films, nanoparticles, nanowires and foam structures. One way is the spontaneous deposition of Pt onto previously electrodeposited porous Ni or onto Ni foam to maximize the surface area, and leading to Pt enrichment only at the surface, where it is needed [18]. The subsequent deposition of Ni and Pt may also be used for producing nanoparticles to obtain a high surface-to-volume ratio [19].

Another method is the direct reduction from solution containing a reducing agent, creating Ni–Pt nanoparticles [20–22]. Ni–Pt may also be produced via lyotropic liquid crystal media formed by high concentrations of a surfactant, which is able to induce mesoporosity [23,24].

Finally, a one-step method is available to produce homogeneous single-phase Ni–Pt, as has been shown for a dense film [25]. In this work, that procedure is combined with the use of an amphiphilic surfactant in order to induce mesoporosity, which has not been documented for Ni-rich alloy electrodeposits so far. Advantages of this method are the one-step co-deposition of the alloy, where only the removal of the surfactant is necessary after the deposition.

2. Experimental

The electrodeposition was carried out using an aqueous solution with the following contents:

- 200 mM NiCl$_2$
- 3 mM Na$_2$PtCl$_6$·6 H$_2$O
- 200 mM H$_3$BO$_3$
- 25 mM NH$_4$Cl
- 10 g/l Pluronic P-123 with an average molecular weight M_n of 5800.

All chemicals were of analytical grade and used as-received without purification. Additionally, HCl was added to adjust the pH to 2.7. This pH had been determined as stable; it was experienced that when using the electrolyte at a higher pH, the pH dropped during usage.

In the aqueous solution, the triblock copolymer Pluronic P-123 forms micelles above its critical micelle concentration [26], which—together with the metal cations—migrate toward the cathode and account for the mesoporosity. Boric acid serves as a pH buffer, i.e. to prevent the local rise of pH at the cathode during electrodeposition [27]. Ammonium chloride also buffers the pH and the ammonium ion complexes both Ni [28] and Pt [29], which is intended to provide a better co-deposition of Pt and Ni.

A three-electrode set-up was used, with an Ag|AgCl 3 M KCl reference electrode and a platinum wire as counter electrode. The three electrodes were connected to an Autolab 302N potentiostat/galvanostat. A jacketed cell was used to keep the solution at 30 °C during deposition and the solution was de-aerated with nitrogen gas before each deposition. A volume of 50 ml of solution was used for deposition.

For characterization of the electrolyte, vitreous carbon was used as the working electrode and cyclic voltammetries (CVs) were conducted with a lower limit between −0.9 and −1.3 V and an upper limit of 1.3 V vs. Ag|AgCl at a scan rate of 50 mV/s. Vitreous carbon is commonly chosen because it does not undergo any oxidation or reduction within the applied potential range. The CVs were recorded for a series of different concentrations of NiCl$_2$ in the electrolyte, namely 0, 50, 100, 150 and 200 mM. The potential was scanned from −0.2 V vs. Ag|AgCl toward the negative cathodic limits and afterwards reversed toward the positive direction.

For deposition of the thin films, the substrate functioning as working electrode was a Cu-coated Si wafer with a Ti adhesion layer, both grown by sputter deposition, with a working area of 0.2 cm^2. Layer thicknesses were about 10 nm for Ti and 200 nm for Cu. The deposition

was carried out potentiostatically while stirring the solution at 200 rpm, applying a potential in a range between −1.3 and −0.6 V, with deposition times ranging from 30 s (−1.3 V) to 180 s (−0.6 V). Since the current density decreased when moving toward less negative deposition potentials, the deposition time was scaled up in order to obtain similar deposition charges and therefore similar film thicknesses for all samples. After the deposition, the remaining polymer was removed from the deposited film by ultrasonic cleaning in ethanol for 10 min. The films were then rinsed with acetone, ethanol, and water.

Since the deposition was easily performed, replicas were fabricated whenever needed for a specific analysis, so that effects of aging due to oxidation could be minimized.

In order to study the effects of the porosity, dense Ni-Pt films were electrodeposited by preparing the identical electrolyte with the exception of the P-123 triblock copolymer. Films were deposited under identical conditions at deposition potentials of −1.2 V (30 s), −1.0 V (30 s), −0.9 V (60 s) and −0.7 V vs. Ag|AgCl (120 s). During ultrasonic cleaning in ethanol after the electrodeposition, it was witnessed that, unlike the porous films, the dense films detached from the substrate in many cases. Since in this case it was not necessary to dissolve any polymer, the ultrasonic cleaning was omitted for the dense films which were only rinsed in ethanol.

Dense and mesoporous pure Pt films were electrodeposited to compare their HER activity with that of the Ni–Pt films. The electrolyte for the deposition of dense Pt contained 3 mM Na$_2$PtCl$_6$·6H$_2$O, 200 mM H$_3$BO$_3$ and 200 mM NaCl, with a pH of 3.4. The same contents were used for the deposition of mesoporous Pt, adding 10 g/l of Pluronic P-123, and the pH was 2.8 in this case. As for all other deposits, the electrodeposition was done at 30 °C while stirring. Dense Pt films were deposited at −0.7 V vs. Ag|AgCl for 600 s whereas mesoporous Pt films were grown at −0.6 V vs. Ag|AgCl for 2400 s.

HER characterization was conducted in the same set-up, using 0.5 M H$_2$SO$_4$ as electrolyte, an Ag|AgCl reference electrode filled with 3 M Na$_2$SO$_4$ in the outer jacket and a graphite rod as counter electrode. The temperature was adjusted to 25 °C and the solution was de-aerated before each HER process. This process was set to 200 cycles from −0.15 to −0.5 V vs. Ag|AgCl with a scan rate of 50 mV/s for a series of Ni–Pt samples with different Ni to Pt ratios, the pure Pt films, and a bare substrate (with the Cu seed layer). In the case of the Cu layer, only 50 sweeps were performed.

The measured potentials vs. Ag|AgCl were converted to RHE scale according to the following equation (Eq. (1)):

$$E_{RHE} = E_{Ag|AgCl} + 0.059\,pH + E^0_{Ag|AgCl} \tag{1}$$

where E_{RHE} is the converted potential vs. RHE, $E^0_{Ag|AgCl}$ is 0.210 V at 25 °C, and $E_{Ag|AgCl}$ is the experimentally measured potential against the Ag|AgCl reference electrode.

For determination of the electrochemical surface area (ECSA), preliminary measurements performed in 0.5 M H$_2$SO$_4$ have provoked the oxidation and dissolution of the Cu seed layer, and thus did not lead to meaningful results. In order to avoid this problem, the measurements were performed in 0.5 M NaOH. Since the mechanism of hydrogen adsorption on Ni–Pt in alkaline media might be different from that in acidic media, the results have to be treated with caution, however the general trend should persist for alkaline as for acidic media. The ECSA of the samples subjected to HER was determined by cycling the potential between −1.05 to −0.43 V vs. Ag|AgCl in 0.5 M NaOH starting in positive direction after polarization for 5 min at −1.35 V, integrating the positive current density related to the adsorption of hydrogen [9]. The charge densities of a monolayer related to hydrogen were taken as 514 μC/cm^2 for Ni and 210 μC/cm^2 for Pt. The charge density of a monolayer was therefore calculated for each Ni/Pt ratio by multiplying the atomic fraction of each element with their corresponding charge density.

The thin films were analyzed as-deposited and after HER by scanning electron microscopy (SEM) coupled with energy-dispersive X-ray

56

spectroscopy (EDX) on a Zeiss Merlin electron microscope to prove mesoporosity and to obtain the Ni to Pt ratio of the films, as well as to observe potential surface modification due to HER testing. Imaging was performed using the InLens detector with an acceleration voltage of 1–2 kV, while an acceleration voltage of 20 kV was used for EDX, where two different areas of roughly 300 µm by 200 µm (at a magnification of 1000) per sample were analyzed.

Cross-sections for transmission electron microscopy (TEM) were prepared by mechanical grinding, polishing, and subsequent ion polishing with a 5 keV Ar ion beam for a total of 5 h. Analysis of the cross sections was performed on a JEOL JEM-2011 TEM using an acceleration voltage of 200 kV in both bright field and diffraction mode.

As-deposited thin films were dissolved in aqua regia consisting of HNO_3 (100%, v/v) and HCl (37%, v/v) in a ratio of 1:3 in volume and subsequently analyzed by inductively coupled plasma optical emission spectroscopy (ICP-OES) to determine the absolute mass of both Ni and Pt in the films, disregarding other elements such as oxygen. The equipment used was a Perkin-Elmer model Optima 4300DV. A blank of the solution, as well as the solution where an uncoated substrate had been immersed in, were added to the ICP-OES analyses. In addition, an aliquot of the sulfuric acid solution used in HER experiments was analyzed for one of the thin films to determine whether Ni or Pt are dissolved after cathodic polarization.

Grazing incidence X-ray diffraction (GIXRD) was conducted for phase analysis of the films in a 2θ range from 38° to 62° on a Malvern-PANalytical X'pert Pro MRD diffractometer. A Rietveld refinement was performed using the software MAUD for phase determination [30].

X-ray photoelectron spectroscopy (XPS) was performed on a PHI 5500 spectrometer on samples with three different Ni to Pt ratios (Ni contents of 98, 84, and 61 at%) as well as on a sample after HER, initially containing 84 at% Ni. The measurements were performed without any surface preparation and after Ar ion sputtering for 30 s. For each measurement, a survey spectrum was recorded as well as the detail spectra for the line positions of C1s, O1s, Ni2p and Pt4f. The energy calibration was done by setting the binding energy of the $Pt4f_{7/2}$ line to 71.3 eV. Monochromated Al-K_α radiation with an incident angle of 45° was used as source. The fitting was done using the software XPSPEAK, applying a Shirley background and a Lorentzian–Gaussian ratio of 30% in all cases.

Contact angle measurements were performed in a Femtobiomed Smartdrop surface analyzer using the sessile drop method on all mesoporous samples previously subjected to HER. Droplets of ultrapure water of 3 µl each were used.

3. Results and discussion

3.1. Characterization of the electrolyte

All CVs were scanned at first toward negative potential to reduce metal ions in solution at the working electrode and then toward positive potential to oxidize the deposit. Effects of the $NiCl_2$ concentration in the electrolyte are investigated while all other concentrations are kept constant (Fig. 1).

For the deposition of the coatings, the zone of reduction is important for defining the range of deposition potentials. When comparing the CVs for the solutions containing Ni(II) and Pt(IV) to the one containing only Pt(IV), the large reduction peak at negative potential can be attributed to Ni(II) discharge. With increasing Ni(II) concentration, the reduction current density increases and the deposition onset for Ni–Pt (i.e. simultaneous reduction of Pt and Ni ions) shifts toward more positive values. At a $NiCl_2$ concentration of 200 mM, the cathodic current seems to be split into three cathodic waves. The existence of multiple peaks for each element may be caused by Pt and Ni reducing to different oxidation states, e.g. metallic Pt and Ni as well as oxides or hydroxides which are detected in XPS (as shown later). Additionally, the evolution of hydrogen contributes to the cathodic
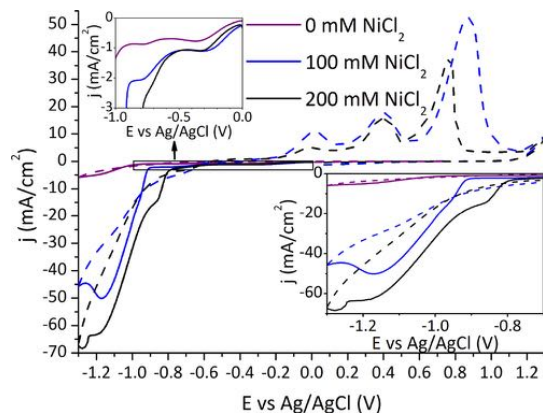

Fig. 1. CV of the electrolyte on a vitreous carbon electrode as a function of $NiCl_2$ concentration under stagnant conditions. Electrolyte contains (0–200) mM $NiCl_2$, 3 mM $Na_2PtCl_6\cdot6H_2O$, 200 mM H_3BO_3, 25 mM NH_4Cl, and 10 g/l Pluronic P-123. The initial sweep toward negative potential is displayed by continuous lines while the subsequent sweep toward positive potential is displayed by dashed lines. Insets show the regions of initial (upper left) and ongoing reduction (lower right).

current.

If the CV of the Ni-free solution is zoomed in the region of the onset of deposition, two reduction peaks are observed, located between −0.3 and −0.4 V as well as around −0.8 V vs. Ag/AgCl (Fig. 1, upper inset). These peaks can be attributed to Pt deposition and the reduction of protons on deposited Pt, respectively [31]. The potentials for deposition were therefore chosen in the range where the reduction takes place, roughly between −1.3 and −0.6 V vs. Ag|AgCl. Due to the agitation during deposition, reduction starts at slightly more positive potentials than in the CV which was recorded under stationary conditions. More negative potentials were excluded due to disturbance by intense hydrogen co-evolution.

In the zone of oxidation toward positive potentials, three separate oxidation peaks are observed for the Ni-containing solutions (Fig. 1). Oxidation currents at negative potential are assigned to the formation of $Ni(OH)_2$ [32]. The peak at 0 V vs. Ag|AgCl is attributed to hydrogen adsorption [33]. At 0.4 V vs. Ag|AgCl, $Ni(OH)_2$ is oxidized to NiOOH [32]. The oxidation at 0.8 V vs. Ag|AgCl may be attributed to the superficial oxidation of Pt [34]. The absence of oxidation peaks in the CV of the Ni-free electrolyte may be related to its significantly lower conductivity. For a $NiCl_2$ concentration of 200 mM, a detachment of the deposited film at the working electrode was observed by the naked eye at around 0.8 V vs. Ag|AgCl, resulting in an abrupt decrease of oxidation current density at this potential, otherwise the oxidation peak should reach at least the charge of the one for 100 mM $NiCl_2$.

Except for the CV with lower limit at −0.9 V showing only an oxidation peak around 0 V vs. Ag|AgCl, all other CVs show a combination of at least three oxidation peaks, with slightly varying position (Fig. 2). Assuming that—despite the shift in position—the oxidation peaks belong to identical oxidation processes, there are no new phases created from −1.05 to −1.3 V vs. Ag|AgCl. The shifts in position and differences in oxidation charge may be the result of varying composition of a Ni–Pt phase. The presence of multiple peaks may be due to oxidation to hydroxides or oxides with different oxidation levels of the metal. At positive potentials, Pt can oxidize to PtOH and PtO around 0.8 V and more positive [34], while Ni already oxidizes to $Ni(OH)_2$ at negative potentials and further to NiOOH at a potential of 0.4 V [32].

Preliminarily, the constituents and concentrations of the electrolyte had been changed until the quality of the deposited thin films had been satisfactory from which point the composition had not been altered
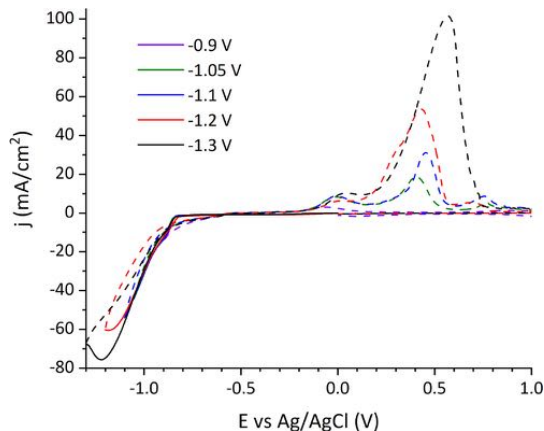
3

Fig. 2. CV of the electrolyte on a vitreous carbon electrode as a function of the applied cathodic limit for the electrolyte used for electrodeposition containing 200 mM $NiCl_2$. The initial sweep toward negative potential is displayed by continuous lines while the subsequent sweep toward positive potential is displayed by dashed lines.

further.

The CV of the electrolyte used for deposition of dense Ni–Pt films, where the triblock copolymer Pluronic P-123 was omitted from the bath, shows only little difference to that of the electrolyte used for preparation of the porous films (Fig. 3). The only significant difference is the onset of reduction—apparent as a shoulder—which occurs at a more positive potential when the triblock copolymer is not present. Here, the surfactant may hinder the reduction initially, causing the observed shift.

3.2. Deposition of mesoporous Ni–Pt films

During electrodeposition, the current density was recorded over time. Since higher negative potential produced higher current densities (j, Fig. 4) and therefore higher deposition charges, the deposition times were adjusted accordingly to prepare thin films with comparable thickness which resulted around 200–300 nm. Current efficiencies were
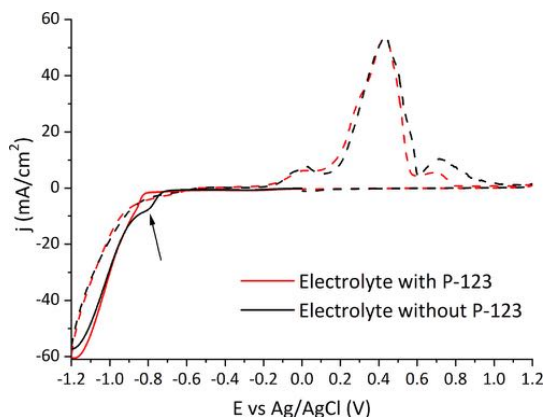

Fig. 3. CV of the electrolytes with Pluronic P-123 for preparation of porous films and without the triblock copolymer for preparation of dense films, on a vitreous carbon electrode. The initial sweep toward negative potential is displayed by continuous lines while the subsequent sweep toward positive potential is displayed by dashed lines.
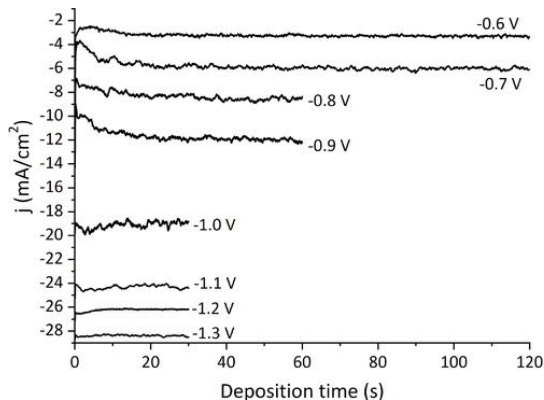

Fig. 4. Current densities recorded at different deposition potentials during potentiostatic electrodeposition of mesoporous Ni–Pt films on Si/Ti/Cu substrates from the optimized electrolyte under stirring conditions.

determined by comparing the theoretical mass of the deposits according to Faraday's laws of electrolysis, using the deposition charge (integrated current), with the mass determined by ICP-OES. The average current efficiency was 70 ± 5% while showing no dependence on the applied deposition potential, inferring that hydrogen co-evolution was kept low during the deposition. Between the deposition potentials of −1.1 and −0.9 V, the current density changes significantly, attributed to the high slope in the CV between these potentials (cf. Fig. 2).

3.3. Chemical composition of the Ni–Pt films

By changing the deposition potential, the Ni/Pt ratio in the films can be adjusted. The more negative the deposition potential, the more Ni-rich is the resulting thin film, indicating that Ni discharge proceeds under charge-transfer control (Fig. 5). Dense and mesoporous films deposited under identical conditions lead to comparable Ni/Pt ratios. The atomic percentages of Ni and Pt were calculated from their masses obtained by ICP, disregarding any other possible contents such as O or H. The level of oxygen was monitored by EDX; it is observed that the content of oxygen is slightly higher for films deposited at less negative potentials. In any case, the overall oxygen level is generally low (Fig. 5).
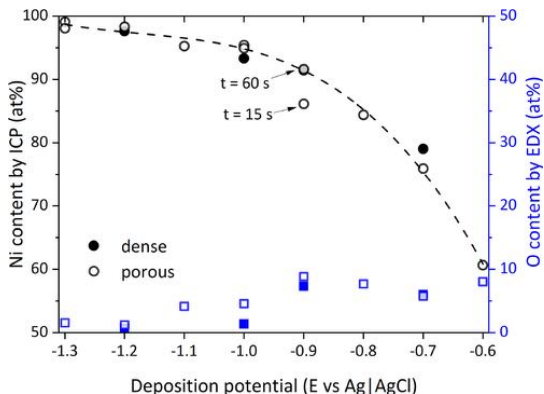

Fig. 5. Variation of Ni and O content with deposition potential in dense and mesoporous Ni–Pt films as determined by ICP (Ni) and EDX (O). Deposition times were 30 s for deposition potentials between −1.3 and −1.0 V, 60 s for −0.9 and −0.8 V, and 120 s for −0.7 and −0.6 V vs. Ag|AgCl. The effect of a reduced deposition time of 15 s is shown for the deposition potential of −0.9 V.
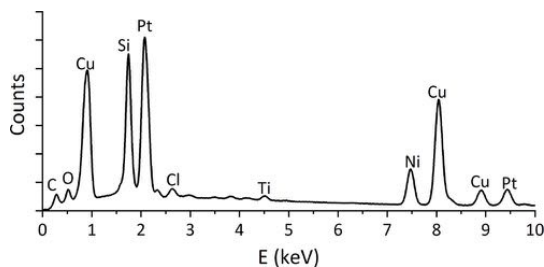
Fig. 6. EDX spectrum for mesoporous Ni–Pt film deposited at −0.6 V vs. Ag|AgCl on Si/Ti/Cu substrate.

The chemical composition is not exclusively a result of the deposition potential but also the deposition time. For a deposition potential of −0.9 V vs. Ag|AgCl, the Pt content was 14 at% after 15 s and 8 at% after 60 s of deposition time. Thus lower deposition times lead to higher fractions of Pt in the films, indicating that the fraction of Pt in the alloy is higher close to the substrate, i.e. a gradient of composition is established throughout the thickness of the coating. However, this effect has only been observed for deposition potentials of −0.9 V and more positive.

The oxygen content measured by EDX is not limited to the film due to the low film thickness and the high information volume of characteristic X-rays. The overall oxygen content reaches from 1 at% for Ni-rich films up to ca 10% for the films with lower Ni content. In EDX, all elements of the substrate (Si, Ti and Cu) are detected as well as C, O, and Cl in low quantities (Fig. 6).

3.4. Morphology

The observable morphology of the mesoporous Ni–Pt films changes with the deposition potential; therefore the deposition potential determines not only the composition but also the morphology of the films. A homogeneously distributed mesoporosity with globular pores in the order of 10 nm is clearly observable for all applied deposition potentials (Fig. 7).

The films deposited between −1.3 and −1.2 V vs. Ag|AgCl feature polyhedral grains, leading to higher surface roughness. In addition, the micrographs of the rougher films give an idea of the grain size, which is of the order of 50–100 nm. At −1.1 V the polyhedral grain morphology tends to vanish and for deposition potentials from −1.0 V and less negative, the grain size cannot be resolved and the surface roughness is very low.

The dense Ni–Pt films show homogeneous microstructures. Those deposited at more negative potential exhibit coarser grains and thus a higher roughness (Fig. 8). Therefore it is clear that the change from coarse, polyhedral grains to fine grains observed on the mesoporous Ni–Pt films is related to the applied potential rather than an effect imposed by the P-123 block copolymer.

From the TEM cross-section, the homogeneously porous character throughout the thickness of the thin film is observed (Fig. 9a). Toward the interface of the film with the substrate, the contrast decreases due to increasing thickness of the cross-section. By SEM, the layered structure with the Si substrate, the Cu layer and the Ni–Pt film is observed, together with the uniform film thickness which was determined as 280 ± 8 nm (Fig. 9b).

3.5. Phase analysis

The XRD patterns show the {111} and {200} reflections for a single fcc phase, along with the reflections of the fcc-Cu seed layer (Fig. 10a). The formation of a single phase for Ni–Pt can be understood on the basis of its negative heat of mixing [35]. With increasing Pt content, the
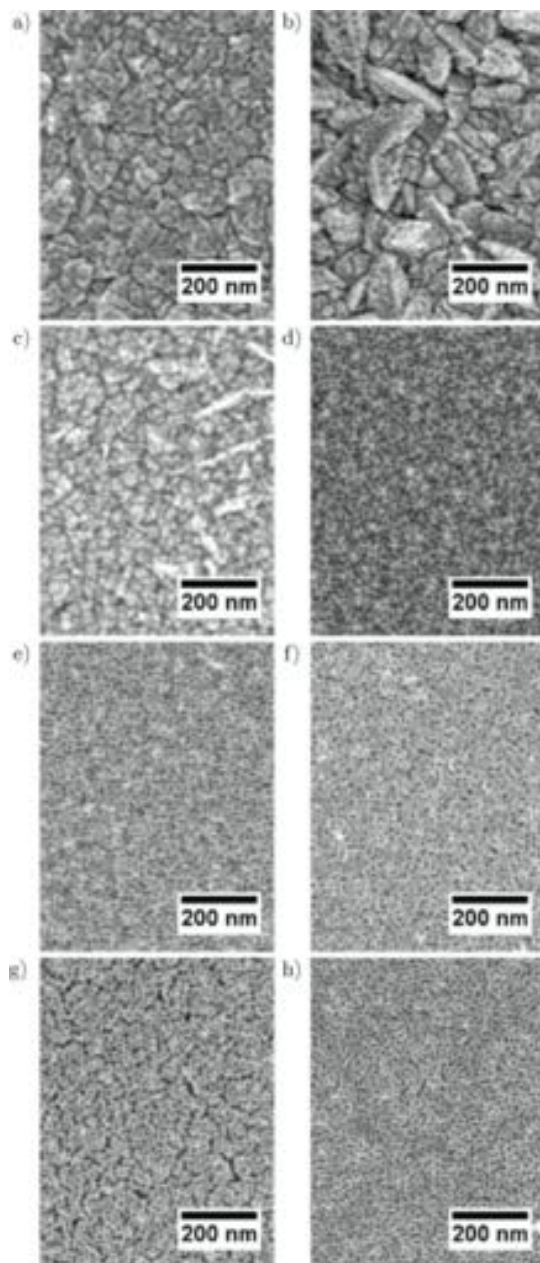
Fig. 7. SEM micrographs of mesoporous Ni–Pt thin films deposited at (a) −1.3 V, (b) −1.2 V, (c) −1.1 V, (d) −1.0 V, (e) −0.9 V, (f) −0.8 V, (g) −0.7 V, (h) −0.6 V vs. Ag|AgCl.

peaks shift toward lower angles, i.e. higher cell parameter, due to the higher cell parameter of Pt with respect to Ni. At a Ni content around 80 at%, the peaks of the Ni–Pt phase are superposed on those of the Cu seed layer.

The existence of a single phase should be beneficial for HER, especially when intended for use in acidic media. A two-phase alloy would immediately act as a galvanic cell when subjected to an
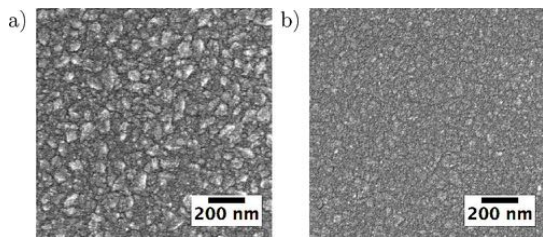
Fig. 8. SEM micrographs of dense Ni–Pt thin films deposited at (a) −1.0 V and (b) −0.7 V vs. Ag|AgCl.
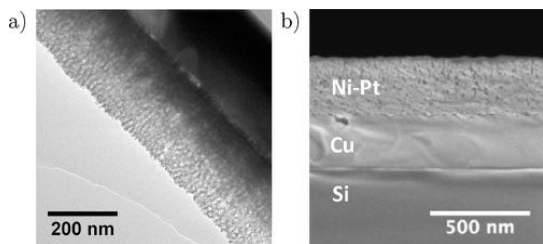
Fig. 9. (a) TEM and (b) SEM micrograph of cross-section of mesoporous Ni–Pt thin film deposited at −0.9 V vs. Ag|AgCl.
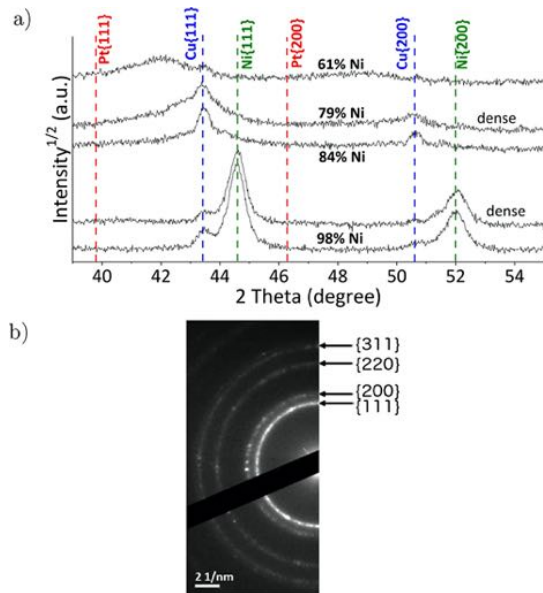
Fig. 10. (a) XRD patterns of mesoporous and dense Ni–Pt films as a function of Ni percentage with the fcc peak positions of {111} and {200} reflections for pure Ni, Pt, and Cu indicated by dashed lines, and (b) SAED diffraction pattern taken at cross-section of mesoporous 92 at% Ni thin film.

electrolyte, leading to the dissolution of the less noble phase. In the case of separate deposition of Ni and Pt, the former would be dissolved preferentially.

In the selected area electron diffraction (SAED) pattern obtained by TEM, rings attributed to {220} and {311}-planes are observed, confirming the existence of the fcc phase (Fig. 10b). The occurrence of continuous rings demonstrates the nanocrystallinity of the Ni–Pt phase,
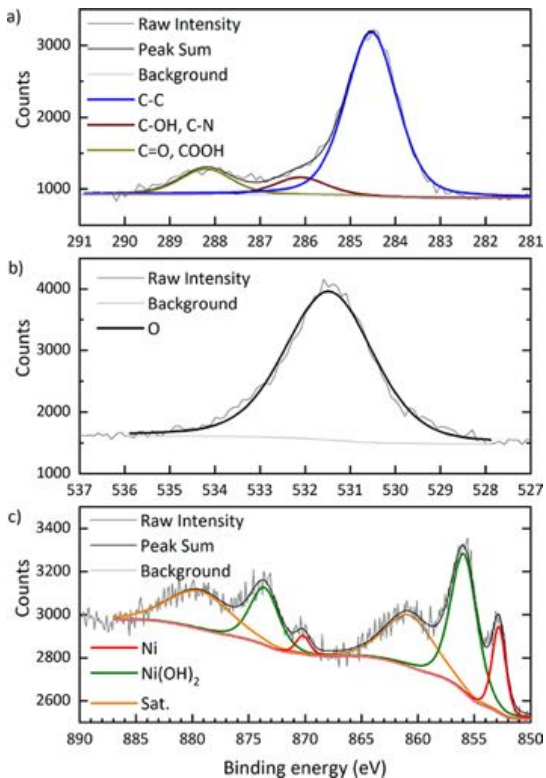
Fig. 11. XPS core-level spectra for 84 at% Ni mesoporous Ni–Pt thin film as-prepared on (a) C1s, (b) O1s, (c) Ni2p position.

in agreement with the very broad peaks present in the XRD patterns with exception of the thin film with 98 at% Ni, which shows narrower peaks caused by a bigger crystallite size in accordance with the microstructure (Fig. 7b).

3.6. XPS analysis

3.6.1. Initial surface state of the films

XPS was carried out on mesoporous Ni–Pt films containing 61, 84 and 98 at% Ni. The XPS survey spectra of the thin films are dominated by the emissions of C and O, indicating the surfaces' covering by organics. The C1s emission is split into three contributions (Fig. 11a), while the O1s emission appears as a single line (Fig. 11b).

The majority of C is attributed to covalent C−C bonds at 284.5 eV. The line at 286 eV is primarily attributed to alcohols, but may as well originate from C−N bonds. The emission at 288 eV may originate from ketones or carboxyl groups [36,37]. The presence of alcohols and ketones may be due to remnants of ethanol and acetone used for cleansing the surfaces.

The Ni2p core-level spectrum shows a contribution of metallic Ni (852.5 eV), and Ni(OH)$_2$ (856 eV), which accounts for the majority of Ni present at the surface (Fig. 11c) [38,39]. The Pt4f emissions at the surface show both metallic Pt and platinum hydroxide (as shown later).

3.6.2. Chemical state after sputtering

After sputtering, the emissions of C1s and O1s are significantly reduced on all samples (not shown).

The Ni2p emissions for the three different film compositions increase with the Ni content (Fig. 12). In all cases, the majority of Ni is

Fig. 12. Ni2p core-level XPS spectra for mesoporous Ni–Pt films containing (a) 61 at% Ni, (b) 84 at% Ni, (c) 98 at% Ni after Ar ion sputtering.

Fig. 13. Pt4f and Ni3p core-level XPS spectra for mesoporous Ni–Pt films containing (a) 61 at% Ni, (b) 84 at% Ni, (c) 98 at% Ni after Ar ion sputtering.

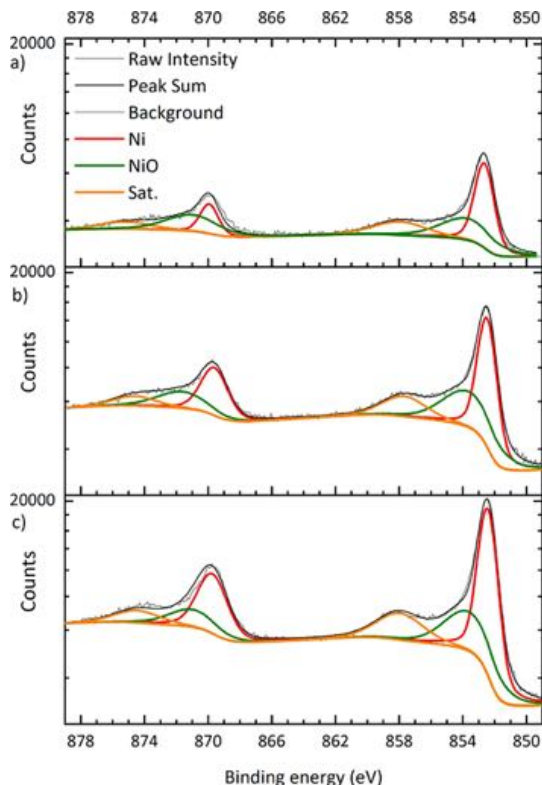**Fig. 14.** 200th cycle of HER in 0.5 M H_2SO_4 at a scan rate of 50 mV/s for all tested samples. The current has been normalized by the geometrical area.

metallic, as shown by the origin of the emission line at 852.5 eV. A second emission line is observed with its center around 854 eV, attributed to NiO [38]. The $Ni(OH)_2$ detected before sputtering is therefore exclusively present on the surface, i.e. a natural surface hydroxide due to exposure to normal atmosphere or the contact with water. In contrast, the NiO present after sputtering may have been produced during electrodeposition, or due to an oxidation through the porosity with limited access to oxygen. In any case, the results prove that the films are mostly metallic.

Regarding the Pt4f emission lines, an expected increase in intensity with increasing Pt content is observed (Fig. 13). Additionally, the emission lines of Ni3p are apparent for all three samples. The emission lines of the Cu3p doublet at 75 and 78 eV, respectively, complicate the interpretation for the sample containing 61 at% Ni. The presence of Cu on this sample is indicated by the Cu2p emission of the survey spectrum, which was significantly higher than for the other samples thus indicating a lower film thickness for this composition. The emission at 72 eV is attributed to platinum hydroxide [37]. The fraction of Pt bound in hydroxides increases with increasing Pt content of the sample.

3.7. HER performance

After the first cycles of HER, the sweeps recorded overlap until the end of the experiment at cycle 200. As a general trend, the HER activity with regard to the geometric area increases with increasing Pt content. The difference between porous and dense films is not as significant as could be expected, though porous films show higher activity than dense films with similar composition. However, the influence of the composition is dominant. Most notably, all Ni–Pt films show a better behavior
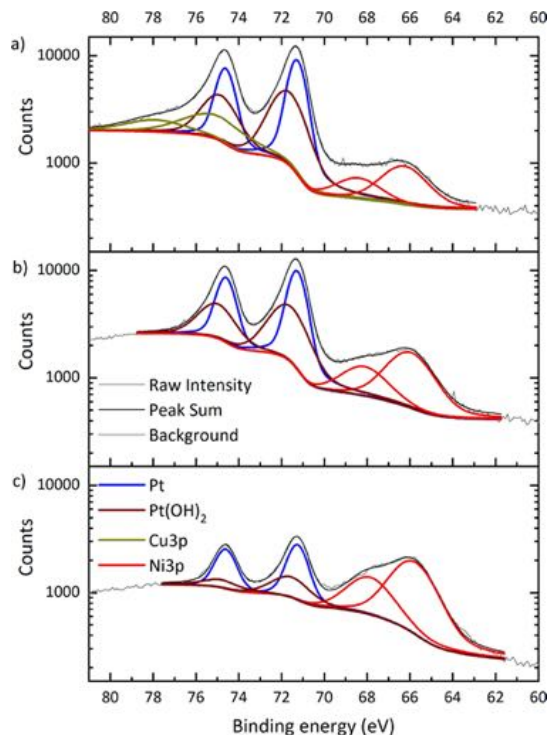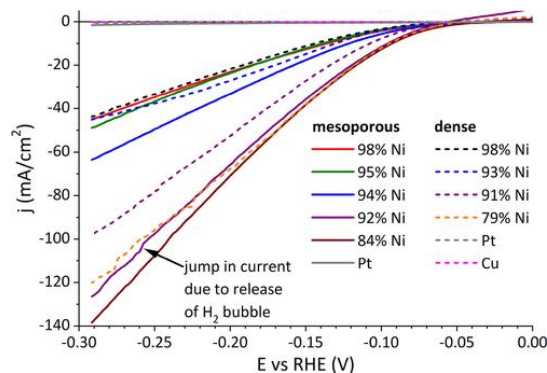
than the films containing only Pt (Fig. 14). The HER activity of the pure Pt films is lowest of all, the porous Pt film showing slightly higher activity than the dense one. It must be noted that no effort was made in order to optimize the electrodeposition of pure Pt; and it is reported that chemically prepared Pt can yield very different and poorer behavior at HER when compared to Pt prepared by vacuum methods [40]. An advantage of dense Ni–Pt alloy over a pure Pt film is not expected. On the substrate (Cu layer), the activity was one order of magnitude lower than on the Pt films.

The Tafel slopes of the mesoporous Ni–Pt films obtained from the HER polarization curves exhibit Tafel slopes between 49 and 63 mV/dec (Fig. 15), showing that the process is not limited by the Volmer
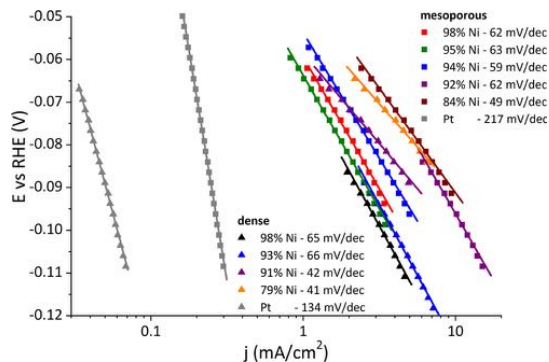
Fig. 15. Tafel slopes for mesoporous and dense Ni–Pt and Pt films obtained from the HER polarization curves.

reaction but by one of the possible desorption steps. The lowest slope of 41 mV/dec is reached by a dense film with 79 at% Ni. The Tafel slope is with 217 mV/dec (mesoporous) and 134 mV/dec (dense) significantly higher for the Pt films.

The overpotential required to obtain a current density of -10 mA/cm^2 is with -0.09 V vs. RHE lowest for the mesoporous film with 84 at% Ni and the dense film with 79 at% Ni (Table 1). For the pure Pt films, -10 mA/cm^2 was not reached within the measured potentials.

For HER in acidic media, mostly Pt has been investigated, and a commercial Pt/C catalyst is a common reference, exhibiting $\eta_{10} \leq 50$ mV with a Tafel slope of $b = 30$ mV/dec [41]. Other pure metals have been investigated in acidic media, including iridium, silver, copper and cobalt [2]. Generally, the other noble metals show good activity at HER, such as iridium, reaching $\eta_{10} = 56$ mV and $b = 35$ mV/dec [42]. Several heterogeneous materials, especially phosphides, are gaining interest at HER in acidic media, often reaching η_{10} below 100 mV [43] and generally showing comparable performance to the Ni–Pt films reported here.

The electrochemical surface area is related to the charge consumed in the hydrogen adsorption peak up to 0.55 V vs. RHE [9]. This adsorption peak changes its form with the Ni/Pt ratio of the films. In comparison with the ECSA of the pure Pt film, most mesoporous films do not show a higher ECSA (Fig. 16). Similar curves were obtained for the dense films, also indicating that the ECSA of the mesoporous films is not higher compared to those obtained for the dense films. Comparing the values of the obtained roughness factors R_f, it can be concluded that the electrochemical activity of the Ni–Pt films is mostly determined by their Pt content (Table 1).

Table 1
Overpotential η_{10} required for HER activity of -10 mA/cm^2, roughness factors R_f for determination of ECSA and Tafel slopes b for mesoporous and dense Ni–Pt and Pt films.

Ni (at%)	η_{10} (V vs. RHE)	R_f	b (mV/dec)
Mesoporous			
98	-0.14	6	62
95	-0.14	4	63
94	-0.12	16	59
92	-0.10	71	62
84	-0.09	83	49
0 (Pt)	–	13	217
Dense			
98	-0.14	29	65
93	-0.13	18	66
91	-0.11	29	42
79	-0.09	94	41
0 (Pt)	–	6	134
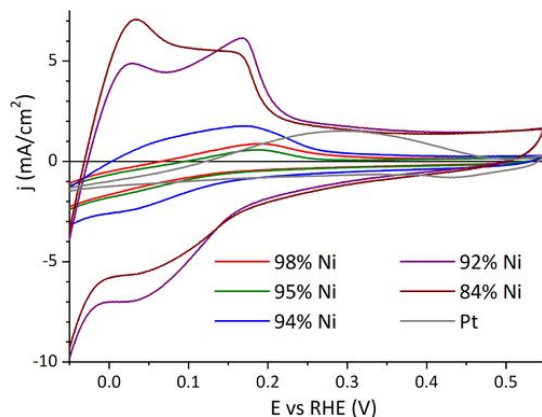
**Fig. 16.** Cyclic voltammetries of mesoporous Ni–Pt and Pt films recorded at 50 mV/s in 0.5 M NaOH for determination of ECSA.
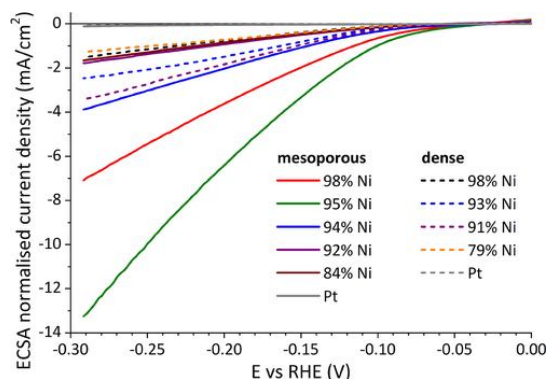
Fig. 17. 200th cycle of HER in 0.5 M H$_2$SO$_4$ at a scan rate of 50 mV/s for all tested samples normalized by the ECSA.

A normalization of the HER activity by the ECSA shows that the highest efficiency at HER with regard to the ECSA is reached for the mesoporous film containing 95 at% Ni (Fig. 17). The dense Ni–Pt films show similar activities for HER between 1 mA/cm^2 and 4 mA/cm^2 at -0.3 V.

Although the mesoporous Ni–Pt films with 95 at% Ni and 94 at% Ni are nominally very similar in composition, their difference in electrocatalytic performance results mainly from the fact that they have been synthesized at different electrodeposition potentials, i.e. -1.1 and -1.0 V vs. Ag|AgCl, respectively. A pronounced difference in the microstructure is observed between these two compositions with a higher grain size for 95 at% Ni, leading to changes in the ECSA (cf. Fig. 7c and d). Furthermore, the thickness of the 95 at% Ni film is slightly higher due to the higher deposition current (cf. Fig. 4).

Again, the pure Pt films exhibit by far the poorest behavior when the ECSA is taken into account. Compared to the results obtained by XPS, it is seen that the fraction of Pt(OH)$_2$ is lower when the Ni content is higher, and large for high Pt contents (Fig. 13). The poor performance of the Pt thin film may be the result of a large fraction of hydroxides of this film, which may block catalytic activity [44].

Regarding the Ni–Pt films, superficial Ni(OH)$_2$ is reported to show improved HER activity in comparison with purely metallic Ni [45], i.e. the HER activity of the Ni–Pt films may be influenced by different fractions of Ni oxides on the surfaces. An increase of catalytic activity due to Ni(OH)$_2$ is not observed here; the effect of Pt hydroxides is
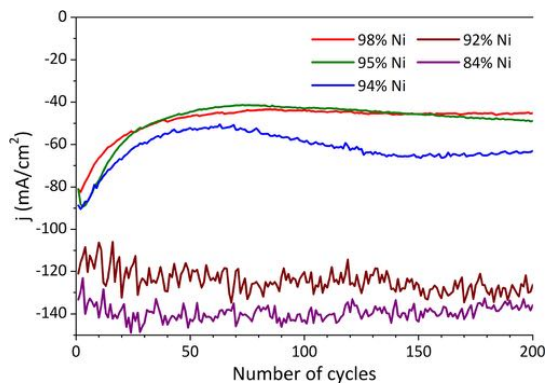
Fig. 18. Variation of HER current at -0.3 V in 0.5 M H_2SO_4 with the number of cycles for mesoporous Ni–Pt films with varying Ni content.

Fig. 20. Morphology of mesoporous Ni–Pt film with (a) 95 at% Ni and (b) 84 at % after 200 cycles of HER in 0.5 M H_2SO_4.

apparently predominant.

Pure Pt and Pt-rich Ni–Pt nanowires have been reported to show activities of over 60 mA/cm^2 at -0.10 V vs. RHE and an η_{10} of -0.03 V vs. RHE [12].

In view of the maximum current reached at each cycle, the films with Ni contents from 94 to 98 at% show an initial decrease of activity, and a stabilization of the current density thereafter (Fig. 18). For 84 at % and 92 at% Ni, the performance is rather steady, with a slight improvement over the first cycles. This activation may be related to the removal of superficial organics observed in XPS (cf. Fig. 11). Also, the samples show very different magnitudes of variation in the current reached: for the lower Ni contents (and higher HER activities), the variation is much larger. The observed variations in current may be related to the high hydrogen production, where the produced hydrogen gas partially blocks the surface from the electrolyte. A measurement of the contact angles with water did not reveal any significant differences; the contact angle was 110° for 98 at% Ni and 96° for 84 at% Ni, the other films exhibiting contact angles in between those two. Thus, the differences in behavior at HER cannot be related with the wettability of the mesoporous films.

The high reproducibility of HER on the mesoporous alloy films is exemplarily shown for the film with 84 at% Ni by comparing different cycles; the recorded curves overlap almost perfectly and show very little variations (Fig. 19). The high reproducibility is observed for all Ni–Pt films.

3.8. Post-HER analysis

Upon microstructural analysis, the morphology of the films remains unchanged after the HER tests. The porosity is conserved as before
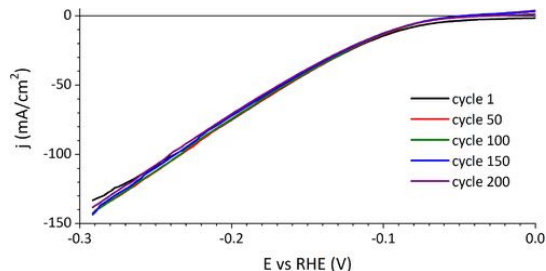
Fig. 19. HER cycles in 0.5 M H_2SO_4 at a scan rate of 50 mV/s for mesoporous Ni–Pt film with 84 at% Ni. The current has been normalized by the geometrical area.
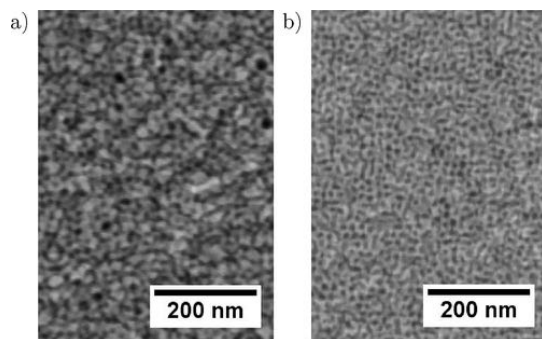
(Fig. 20).

In EDX, a decrease of a few atomic percent Ni in relation to Pt is observed for the samples with Ni contents of 94 at% and below. From the solution used for HER of a film of 84 at% Ni, an aliquot was withdrawn for ICP analysis and both Ni and Pt were detected in the solution at 7% of the mass of the film, in a relation close to the composition of the film. Thus, some leaching of material into the solution occurs, however, there is no significant change in the Ni/Pt ratio, indicating that Ni is not preferentially etched in relation to Pt. Due to the fact that HER is reproducible over 200 cycles, this leaching is either limited to the initial cycles during HER, or an extremely slow process. The stability of the Ni–Pt films is critical when immersed into H_2SO_4 without any polarization, where selective etching of Ni was detected (around 20% of the Ni in the films was dissolved). The exposure of Ni–Pt films to H_2SO_4 without polarization should therefore be limited to a minimum.

The core-level XPS spectrum of Ni2p of a sample with 84 at% after HER exhibits a lower fraction of Ni(OH)$_2$ in comparison to the as-prepared state (Fig. 21). Relating the area of the peaks for Ni(OH)$_2$ to those for metallic Ni, the fraction of oxide on the surface without any sputtering is 60% after HER and 75% in the as-prepared state.

By analogy, the Pt4f emission line shows a reduced fraction of Pt (OH)$_2$ after HER (Fig. 22). The fractions of Pt bound in hydroxide are
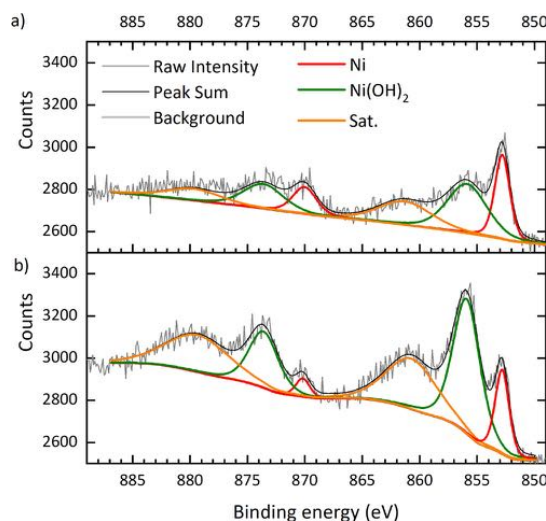
Fig. 21. Ni2p core-level XPS surface spectra for mesoporous Ni–Pt thin film with 84 at% Ni (a) subjected to HER, (b) in the as-prepared state.
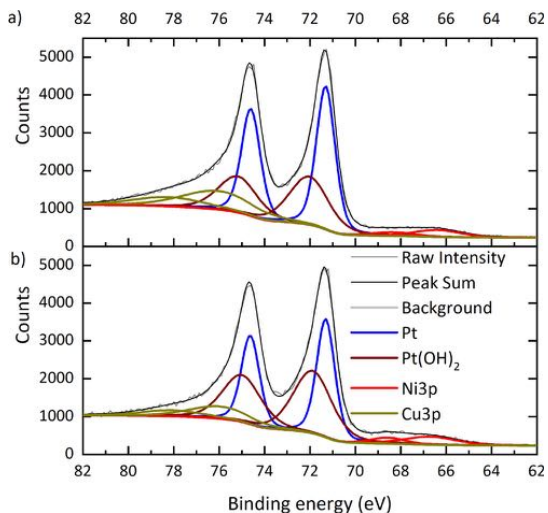
Fig. 22. Pt4f core-level XPS surface spectra for mesoporous Ni–Pt thin film with 84 at% Ni (a) subjected to HER, (b) in the as-prepared state.

41% after HER and 53% as-prepared. The lower emissions of Pt(OH)$_2$ and Ni(OH)$_2$ indicate a reduction of the metal hydroxides on the surface during HER, and the reduced amount of Pt hydroxide may be responsible for the increasing current over the initial cycles of HER. Especially PtOH has been reported to block the activity of catalytical processes [44]. On Ni surfaces, NiH formation has been observed to limit HER in alkaline solution [46]. It is also possible that Ni(OH)$_2$ has reformed after HER under atmospheric conditions.

C1s and O1s emissions do not show any significant differences before and after HER. However, it is possible that—analogous to Ni (OH)$_2$—organics are removed during initial cycles of HER and subsequently re-establish on the surface since XPS analyses were conducted ex situ after HER tests.

4. Conclusion

Mesoporous Ni–Pt thin films have been successfully deposited using a one-step micelle-assisted electrodeposition process from a reproducible and stable electrolyte. The films are single phase (Ni–Pt solid solution) as determined by GIXRD. The composition is easily adjustable in a range of 100–60 at% (or 30 wt%) Ni by adjusting the deposition potential and time. Especially in the range of low Pt contents, the composition can be adjusted very accurately. The mesoporosity on the order of 10 nm is homogeneously distributed independent of the composition in a nanocrystalline microstructure with higher crystallite sizes and roughness for films with Ni contents close to 100%. The films' thickness is on the order of 200–300 nm.

All produced Ni-rich thin films yield reproducible HER activity in 0.5 M H$_2$SO$_4$ over 200 cycles, showing increasing activity by geometric area following the Pt content of the films up to a maximum Pt content of 26 at%. The mesoporosity does increase the activity with regard to dense films, however the effect is only moderate and a significant increase in the ECSA is not observed. Through the normalization by ECSA, effects of porosity and surface passivation are eliminated, allowing a better comparison of the electrocatalytic performance of the material. The most effective mesoporous film composition with respect to ECSA was found to be of 95 at% Ni, i.e. containing only 5 at% Pt, showing that an optimum performance is already reached with a very low amount of Pt. However, the ECSA is low for 95 at% Ni and must be further improved in order to fully exploit the limits of the material. A

better performance, i.e. a higher ECSA, may be reached with a higher pore size, or a hierarchically porous structure. Chemical analysis after HER indicated some leaching of both Ni and Pt which will be investigated by corrosion measurements, since it is not clear if this process is only initial or constantly ongoing. Due to the reproducibility of the HER measurements, the leaching of Ni and Pt is either initial or a very slow process which does not influence the performance. If leaching needs to be absolutely avoided, it may be necessary to execute HER in less acidic or alkaline media. Nevertheless, HER in acidic media proved to be feasible and reliable for all compositions, even when the thin film contained only 1 at% Pt.

Conflict of interest

None declared.

References

[1] F. Orecchini, The era of energy vectors, Int. J. Hydrogen Energy 31 (2006) 1951.
[2] A. Lasia, Hydrogen evolution reaction, in: W. Vielstich, A. Lamm, H.A. Gasteiger (Eds.), Handbook of Fuel Cells – Fundamentals, Technology and Applications, vol. 2, John Wiley & Sons, UK, 2003, pp. 416–440.
[3] G. Leofanti, M. Padovan, G. Tozzola, B. Venturelli, Surface area and pore texture of catalysts, Catal. Today 41 (1998) 207.
[4] J. Kibsgaard, Z. Chen, B.N. Reinecke, T.F. Jaramillo, Engineering the surface structure of MoS$_2$ to preferentially expose active edge sites for electrocatalysis, Nat. Mater. 11 (2012) 963.
[5] V. Malgras, H. Ataee-Esfahani, H. Wang, B. Jiang, C. Li, K.-W. Wu, J. Kim, Y. Yamauchi, Nanoarchitectures for mesoporous metals, Adv. Mater. 28 (2015) 993.
[6] R. Oriňáková, A. Turoňová, D. Kladeková, M. Gálová, R.M. Smith, Recent developments in the electrodeposition of nickel and some nickel-based alloys, J. Appl. Electrochem. 36 (2006) 957.
[7] S. Sengupta, A. Patra, S. Jena, K. Das, S. Das, A study on the effect of electro-deposition parameters on the morphology of porous nickel electrodeposits, Metall. Mater. Trans. A 49A (2018) 920.
[8] N. Krstajić, M. Popović, B. Grgur, M. Vojnović, D. Šepa, On the kinetics of the hydrogen evolution reaction on nickel in alkaline solution. Part I. The mechanism, J. Electroanal. Chem. 512 (2001) 16.
[9] S. Machado, L. Avaca, The hydrogen evolution reaction on nickel surfaces stabilized by H-absorption, Electrochim. Acta 39 (1994) 1385.
[10] W. Sheng, M. Myint, J. Chen, Y. Yan, Correlating the hydrogen evolution reaction activity in alkaline electrolytes with the hydrogen binding energy on monometallic surfaces, Energy Environ. Sci. 6 (2013) 1509.
[11] F. Safizadeh, E. Ghali, G. Houlachi, Electrocatalysis developments for hydrogen evolution reaction in alkaline solutions – a review, Int. J. Hydrogen Energy 40 (2015) 256.
[12] P. Wang, K. Jiang, G. Wang, J. Yao, X. Huang, Phase and interface engineering of platinum-nickel nanowires for efficient electrochemical hydrogen evolution, Angew. Chem. Int. Ed. 55 (2016) 12859.
[13] Z. Cao, Q. Chen, J. Zhang, H. Li, Y. Jiang, S. Shen, G. Fu, B. Lu, Z. Xie, L. Zheng, Platinum–nickel alloy excavated nano-multipods with hexagonal close-packed structure and superior activity towards hydrogen evolution reaction, Nat. Commun. 8 (2017) 15131.
[14] J. Zhang, A. Quintana, E. Menéndez, M. Coll, E. Pellicer, J. Sort, Electrodeposited Ni-based magnetic mesoporous films as smart surfaces for atomic layer deposition:

an "all-chemical" deposition approach toward 3D nanoengineered composite layers, ACS Appl. Mater. Interfaces 10 (2018) 14877.

[15] D. Baba, J. Kim, J. Henzie, C. Li, B. Jiang, Ö. Dag, Y. Yamauchi, T. Asahi, Electrochemical deposition of large-sized mesoporous nickel films using polymeric micelles, Chem. Commun. 54 (2018) 10347.

[16] C. Li, Y. Yamauchi, Synthesis of mesoporous platinum-copper films by electrochemical micelle assembly and their electrochemical applications, Chem. Eur. J. 20 (2014) 729.

[17] G. Raykhtsaum, Platinum alloys: a selective review of the available literature, Platin. Met. Rev. 57 (2013) 202.

[18] S. Fiameni, I. Herraiz-Cardona, M. Musiani, V. Pérez-Herranz, L. Vázquez-Gómez, E. Verlato, The HER in alkaline media on Pt-modified three-dimensional Ni cathodes, Int. J. Hydrogen Energy 37 (2012) 10507.

[19] M. Li, Y. Lei, N. Sheng, T. Ohtsuka, Preparation of low-platinum-content platinum-nickel, platinum-cobalt binary alloy and platinum–nickel–cobalt ternary alloy catalysts for oxygen reduction reaction in polymer electrolyte fuel cells, J. Power Sources 294 (2015) 420.

[20] W. Wang, D. Wang, X. Liu, Q. Peng, Y. Li, Pt–Ni nanodendrites with high hydrogenation activity, Chem. Commun. 49 (2013) 2903.

[21] Y. Hu, Q. Shao, P. Wu, H. Zhang, C. Cai, Synthesis of hollow mesoporous Pt–Ni nanosphere for highly active electrocatalysis toward the methanol oxidation reaction, Electrochem. Commun. 18 (2012) 96.

[22] X. Huang, E. Zhu, Y. Chen, Y. Li, C.-Y. Chiu, Y. Xu, Z. Lin, X. Duan, Y. Huang, A facile strategy to Pt₃Ni nanocrystals with highly porous features as an enhanced oxygen reduction reaction catalyst, Adv. Mater. 25 (2013) 2974.

[23] Y. Yamauchi, S.S. Nair, T. Momma, T. Ohsuna, T. Osaka, K. Kuroda, Synthesis and characterization of mesoporous Pt-Ni (H₁-Pt/Ni) alloy particles prepared from lyotropic liquid crystalline media, J. Mater. Chem. 16 (2006) 2229.

[24] O. Sorsa, H. Romar, U. Lassi, T. Kallio, Co-electrodeposited mesoporous PtM (M = Co, Ni, Cu) as an active catalyst for oxygen reduction reaction in a polymer electrolyte membrane fuel cell, Electrochim. Acta 230 (2017) 49.

[25] Y. Liu, C.M. Hangarter, U. Bertocci, T.P. Moffat, Oxygen reduction reaction on electrodeposited Pt₁₀₀₋ₓNiₓ: influence of alloy composition and dealloying, J. Phys. Chem. C 116 (2012) 7848.

[26] G. Wanka, H. Hoffmann, W. Ulbricht, Phase diagrams and aggregation behavior of poly(oxyethylene)–poly(oxypropylene)–poly(oxyethylene) triblock copolymers in aqueous solutions, Macromolecules 27 (1994) 4145.

[27] J. Ji, C. Cooper, D. Dreisinger, E. Peters, Surface pH measurements during nickel electrodeposition, J. Appl. Electrochem. 25 (1995) 642.

[28] I. Rodriguez-Torres, G. Valentin, F. Lapicque, Electrodeposition of zinc–nickel alloys from ammonia-containing baths, J. Appl. Electrochem. 29 (1999) 1035.

[29] M. Baumgärtner, C. Raub, The electrodeposition of platinum and platinum alloys, Platin. Met. Rev. 32 (1988) 188.

[30] L. Luterotti, Total pattern fitting for the combined size-strain-stress-texture determination in thin film diffraction, Nucl. Instrum. Methods Phys. Res. B 268 (2010) 334.

[31] S. Grau, M. Montiel, E. Gómez, E. Vallés, Ternary PtCoNi functional films prepared by electrodeposition: magnetic and electrocatalytic properties, Electrochim. Acta 109 (2013) 187.

[32] M. Vuković, Voltammetry and anodic stability of a hydrous oxide film on a nickel electrode in alkaline solution, J. Appl. Electrochem. 24 (1994) 878.

[33] P. Garrido, E. Gómez, E. Vallés, Simultaneous electrodeposition and detection of platinum on silicon surfaces, J. Electroanal. Chem. 441 (1998) 147.

[34] K.R. Rasmi, S.C. Vanithakumari, R.P. George, C. Mallika, U.K. Mudali, Development and performance evaluation of nano platinum coated titanium electrode for application in nitric acid medium, Mater. Chem. Phys. 151 (2015) 133.

[35] S. Divi, A. Chatterjee, Generalized nano-thermodynamic model for capturing size-dependent surface segregation in multi-metal alloy nanoparticles, RSC Adv. 8 (2008) 10409.

[36] G. Arteaga, L. Rivera-Gavidia, S. Martínez, R. Rizo, E. Pastor, G. García, Methanol oxidation on graphenic-supported platinum catalysts, Surfaces 2 (2019) 16.

[37] J.F. Moulder, W.F. Stickle, P.E. Sobol, K.D. Bomben, Handbook of X-ray Photoelectron Spectroscopy, Physical Electronics, Inc., MI, 1995.

[38] L. Salvati, L. Makovsky, J. Stencel, F. Brown, D. Hercules, Surface spectroscopic study of tungsten-alumina catalysts using X-ray photoelectron, ion scattering, and Raman spectroscopies, J. Phys. Chem. 85 (1981) 3700.

[39] H.-W. Hoppe, H.-H. Strehblow, XPS and UPS examinations of the formation of passive layers on Ni in 1 M sodium hydroxide and 0.5 M sulphuric acid, Surf. Interface Anal. 14 (1989) 121.

[40] J. McKone, E.L. Warren, M.J. Bierman, S.W. Boettcher, B.S. Brunschwig, N.S. Lewis, H.B. Gray, Evaluation of Pt, Ni, and Ni–Mo electrocatalysts for hydrogen evolution on crystalline Si electrodes, Energy Environ. Sci. 4 (2011) 3573.

[41] Z. Lei, S. Xu, P. Wu, Ultra-thin and porous MoSe₂ nanosheets: facile preparation and enhanced electrocatalytic activity towards the hydrogen evolution reaction, Phys. Chem. Chem. Phys. 18 (2016) 70.

[42] E. Lamy-Pitara, J. Barbier, The electrocatalytic reactions of oxidation and evolution of hydrogen on iridium electrodes modified by sulphur adsorption, J. Electroanal. Chem. 416 (1996) 47.

[43] M. Zeng, Y. Li, Recent advances in heterogeneous electrocatalysts for the hydrogen evolution reaction, J. Mater. Chem. A 3 (2015) 14942.

[44] S. Ghosh, S. Mondal, R. Raj, Carbon nanotube-supported dendritic Pt-on-Pd nanostructures: growth mechanism and electrocatalytic activity towards oxygen reduction reaction, J. Mater. Chem. A 2 (2014) 2233.

[45] J.-P. Diard, B. LeGorrec, S. Maximovitch, Étude de l'activation du dégagement d'hydrogène sur électrode d'oxyde de nickel par spectroscopie d'impédance, Electrochim. Acta 35 (1990) 1099.

[46] D.M. Soares, O. Teschke, I. Torriani, Hydride effect on the kinetics of the hydrogen evolution reaction on nickel cathodes in alkaline media, J. Electrochem. Soc. 139 (1992) 98.
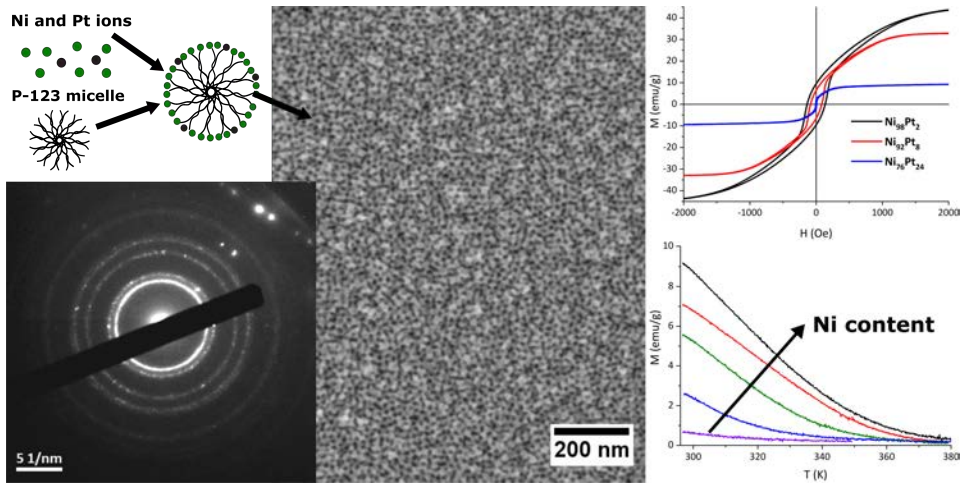
5.2 Tailoring magnetic and mechanical properties of mesoporous single-phase Ni–Pt films by electrodeposition

Konrad Eiler[a], Jordina Fornell[a], Cristina Navarro-Senent[a], Eva Pellicer[a] and Jordi Sort[a,b]

[a]Departament de Física, Universitat Autònoma de Barcelona, 08193 Bellaterra, Spain
[b]Institució Catalana de Recerca i Estudis Avançats (ICREA), Pg. Lluís Companys 23, 08010 Barcelona, Spain

In this work, the mechanical and magnetic properties of the previously developed Ni–Pt thin films are studied. Rietveld refinement is used to determine the crystallite sizes which are in the lower nanometre range and account for high hardness of the thin films. Furthermore, the synthesis is extended to thin films with higher Pt contents with the aim to synthesise a series of thin films with different Curie temperatures below, near to, and above RT.

The demonstrated single-phase nature of both mesoporous and dense thin films leads to linear relations of T_C, M_s, and—in the case of mesoporous films—H_c with the composition. Therefore, the magnetic properties of the alloy films can be directly tuned by the electrodeposition potential, making the system attractive for application in magnetically actuated MEMS where specific magnetic properties are required.

Check for updates

Tailoring magnetic and mechanical properties of mesoporous single-phase Ni–Pt films by electrodeposition

Konrad Eiler, [ID] *[a] Jordina Fornell, [ID] [a] Cristina Navarro-Senent, [ID] [a] Eva Pellicer [ID] [a] and Jordi Sort [ID] *[a,b]

Homogeneous mesoporous Ni-rich Ni–Pt thin films with adjustable composition have been synthesised by one-step micelle-assisted electrodeposition. The films exhibit a face-centred cubic solid solution (single phase) and their magnetic and mechanical properties can be tuned by varying the alloy composition. In particular, the Curie temperature (T_C) is shown to decrease with the Pt content and thin films with a T_C close to room temperature (*i.e.* $Ni_{58}Pt_{42}$) and below can be produced. Hysteresis loops show a decrease of saturation magnetisation (M_s) and coercivity (H_c) with decreasing Ni content. A comparison of porous and dense films reveals significantly lower saturation magnetic field strength for porous films. Concerning mechanical properties, mainly two trends can be observed: a decrease of the Young's modulus of the nanoporous films with respect to dense films by 10% in average and a progressive increase of Young's modulus with the Ni content from 4.2 GPa to 5.7 GPa in both types of films. The tunability of properties and facility of synthesis make this alloy a promising material for microelectromechanical systems (MEMS).

1 Introduction

The ability to adjust the magnetic properties of a system without drastically changing other physical properties—such as electrical, mechanical or thermal properties—is beneficial for application in magnetic micro- and nanoelectromechanical systems (MEMS/NEMS), where para- and ferromagnetic phases need to be in electrical contact while ensuring mechanical compatibility between different components.[1] If there is a low difference in composition between the paramagnetic and the ferromagnetic phase, there will be only little difference in electrical conductivity—thus avoiding local heating—, a low mismatch in thermal expansion—avoiding excessive thermally induced interfacial stresses—and good mechanical integrity.[2] Single-phase alloys have the potential to prevent these problems from occurring intrinsically, and—in the case of full miscibility—do not undergo phase transition and avoid temperature-induced formation of secondary phases.[3] Additionally, an electrical contact between two phases of similar composition is less susceptible to atmospheric corrosion caused by humidity.

Electrodeposited soft magnetic alloys are widely used as writing heads for hard disks, where the main requirements include corrosion resistance, low stress and thermal stability.[4] For many applications, soft ferromagnetic materials with Curie temperature (T_C) close to room temperature (RT) are of interest in order to reduce energy consumption during storage and access of data.

A T_C close to RT also allows to study the magnetic behaviour in this temperature region without applying heat, helping to advance in the theoretical models to understand the magnetic phase transition effects. In general, T_C can be tailored by varying the content of a ferromagnetic element in a solid solution comprising ferromagnetic and paramagnetic elements. In this work, Ni–Pt is used to that purpose. While Pt is an excellent corrosion resistant material, Ni provides ferromagnetic properties. Moreover, Ni has a high abundance and provides mechanical stability and electrical conductivity. This makes Ni–Pt a multifunctional alloy whose properties can be tuned by the composition, rendering it ideal for application in magnetic MEMS or NEMS. Ni and Pt promote the formation of single-phase alloys due to their full miscibility, given their identical lattice structure (fcc) and their comparable atomic radii.[5]

Compared to coarse-grained materials, nanocrystalline metals and alloys exhibit larger yield stress and hardness due to enhanced dislocation pile-up at grain boundaries (Hall–

[a]Departament de Física, Universitat Autònoma de Barcelona, 08193 Bellaterra (Cerdanyola del Vallès), Spain. E-mail: konrad.eiler@uab.cat, jordi.sort@uab.cat
[b]Institució Catalana de Recerca i Estudis Avançats (ICREA), 08010 Barcelona, Spain

Petch strengthening).[6] Using suitable conditions for electrode-position, nanocrystalline films can be readily obtained, thus improving the mechanical properties without compromising any other properties.[7,8]

Mesoporous materials, due to their high surface-to-volume ratio, are generally of interest in biomedicine, water remediation, catalysis, and energy storage and conversion devices such as batteries and fuel cells.[9–13] In the case of nanoporous magnetic materials, the coercivity can be reduced by applying voltage, due to large electric charge accumulation effects on the surface (converse magnetoelectric effect).[14] Again, this can reduce the energy consumption during writing of information in magnetic storage media and other magnetically actuated devices.[15]

Furthermore, the interest in the biomedical field and bio-MEMS is growing.[4] Here, mesoporous materials are appealing for application in drug delivery since the pores may act as reservoirs for the drugs to be delivered.[16]

Nanoporous materials are often superhydrophobic (and oleophilic), a property that may be utilised in water remediation (*i.e.* oil decontamination). If the material is at the same time ferromagnetic, it can easily be retrieved from the water and thereby recycled for multiple usage.[17,18]

The formation of a single-phase alloy generally depends on the thermodynamics of the system; the phase diagram and the mixing enthalpy for the element pair being suitable indicators as to whether a single-phase alloy can be obtained. The Ni–Pt phase diagram shows full miscibility with the existence of ordered phases, and an approximately linear dependence of T_C on composition, reaching 373 K (100 °C) at 26 at% Pt.[19] Ni–Pt exhibits a negative mixing enthalpy,[20] favouring the formation of a single phase. However, especially by electrodeposition the stabilisation of metastable phases is possible.

Another requirement for alloy electrodeposition is that the deposition potentials of the two elements need to be sufficiently close together; complexing agents are commonly used to shift the deposition potential for one of the elements in order to approach the deposition potential of the other and thus achieve their co-deposition.[7] The use of a polymeric surfactant to introduce nanoporosity can interfere with the crystal growth of the metallic film,[21] eventually changing the microstructure and leading to phase separation. A general issue in the electrodeposition of metallic films is also the incorporation of oxygen and hydrogen, leading to the formation of oxide/hydroxide phases[22,23] and hydrogen embrittlement, to which Ni is rather susceptible.[24]

Single-phase dense Ni–Pt films have already been electrodeposited from K_2PtCl_4 containing solution at acidic pH for the purpose of oxygen reduction reaction in the full compositional range.[25]

Here, the synthesis of Ni–Pt thin films is accomplished using the well-described mechanism of micelle-assisted electrodeposition to introduce porosity.[26–28] In this one-step deposition process, a block copolymer forms micelles when its concentration in water is above the critical micellar concentration (cmc), and the metal ions assemble at the exterior (hydro-philic) part of the micelles. The latter are thus co-deposited when the metal ions are reduced at the working electrode. The polymer can later be easily dissolved, leaving a mesoporous metallic film behind.

Since mostly magnetic properties of the Ni–Pt system are investigated here, this work focuses on Ni-rich alloys of the Ni–Pt system. A dependence of T_C, M_s and H_c on the composition ($Ni_xPt_{1−x}$) is observed, as well as progressive variation in their mechanical properties. The nanocrystalline, single-phase material is characterised for both mesoporous and dense morphology, revealing that the mesoporosity influences both the magnetic and mechanical behaviour.

2 Experimental

The electrodeposition of mesoporous Ni–Pt films was carried out using an aqueous solution containing 200 mM $NiCl_2$, 3 mM $Na_2PtCl_6·6H_2O$, 200 mM H_3BO_3, 25 mM NH_4Cl, and 10 g $l^{−1}$ Pluronic P-123 (average molecular mass M_n = 5800). HCl was added to adjust the pH to 2.7. For the deposition of dense films, the block copolymer P-123 was omitted while keeping the concentration of all other chemicals constant.

A three-electrode set-up with an Ag|AgCl 3 M KCl reference electrode and a platinum wire as counter electrode was used while the temperature during deposition was kept at 30 °C. All given potentials refer to the Ag|AgCl electrode. De-aeration with nitrogen gas was performed before each deposition, and the deposition was performed while stirring the electrolyte at 100 rpm.

For electrodeposition, silicon substrates were metallised with a 10 nm Ti adhesion layer and a 200 nm Cu seed layer, both deposited by sputter deposition. The back of the substrates was insulating due to the presence of SiO_2. Potentiostatic deposition, using potentials between −1.3 V and −0.6 V and deposition times from 30 s to 180 s, were applied using an Autolab 302N potentiostat/galvanostat to deposit films with different Ni to Pt ratios. Since the deposition rate was higher for more negative potentials, the deposition time was adjusted for each deposition potential in order to obtain similar film thickness for all compositions. In practice, this meant increasing the deposition time when moving towards more positive potentials (Fig. 1). After deposition of the porous
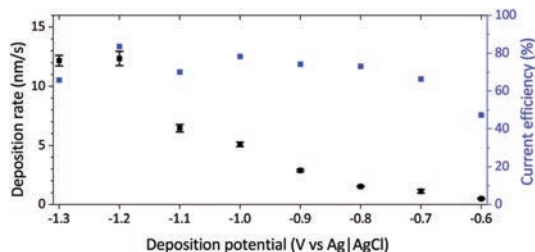

Fig. 1 Deposition rate and faradaic efficiency of mesoporous Ni–Pt films as a function of the applied deposition potential.

70

films, the block copolymer was removed by ultrasonic cleaning in ethanol for 10 min.

In order to determine the faradaic current efficiency, the theoretical mass ($m_{\text{theoretical}}$) of a $\text{Ni}_x\text{Pt}_{(1-x)}$ film was determined assuming that all current measured during the deposition process corresponds to the reduction of the metal ions (eqn (1)).

$$m_{\text{theoretical}} = \frac{1}{F}\left(x\frac{M(\text{Ni})}{z(\text{Ni})} + (1-x)\frac{M(\text{Pt})}{z(\text{Pt})}\right)\int_0^t i \cdot dt \quad (1)$$

where F is the Faraday constant, x is the atomic fraction of Ni in the deposit, $M(\text{Ni})$ and $M(\text{Pt})$ are the molar masses of Ni and Pt, $z(\text{Ni}) = 2$ and $z(\text{Pt}) = 4$ are the numbers of electrons supplied for the reduction of a Ni, and a Pt ion, respectively. i is the measured current and t is the deposition time.

Together with the real masses of the deposits determined by ICP-MS (see below for the procedure), which also allowed the determination of the atomic fractions of Ni and Pt, the faradaic efficiency is determined by the ratio of the real and the theoretical mass $m_{\text{real}}/m_{\text{theoretical}}$.

For determination of the deposition rates, the real masses of the deposits were used to estimate their density, from which the total thickness was calculated. Thus the deposition rates reported show the total thickness divided by the deposition time.

The synthesised Ni–Pt thin films were analysed by scanning electron microscopy (SEM) coupled with energy-dispersive X-ray spectroscopy (EDX) on a Zeiss Merlin electron microscope. Imaging was done at an acceleration voltage of 1–2 kV using an InLens detector to reveal the existence of mesoporosity.

Transmission electron microscopy (TEM) was performed on a Jeol JEM-2011 electron microscope with an acceleration voltage of 200 kV working in bright field and diffraction mode. Sample preparation for TEM was performed by making a cross-cut of a mesoporous sample with a diamond saw. By grinding and polishing with a final diamond polish of 1 μm particle size, the thickness was reduced to about 30 μm. Finally, Ar ion milling with an energy of 5 keV was performed at an angle of 8° for several hours to reduce the thickness locally to a few nanometers. For the preparation of the cross-section of a dense Ni–Pt film, a lamella was cut using a focused ion beam SEM (FIB-SEM).

Grazing incidence X-ray diffraction (GIXRD) was conducted on a Malvern-PANalytical Xpert Pro MRD diffractometer using Cu-K$_\alpha$ radiation for phase analysis of the films in a 2θ range from 38° to 62°. Rietveld refinement was performed using the software MAUD[29] in order to determine the lattice parameter and crystallite size for each composition.[30]

The mechanical properties of the films, i.e. hardness (H) and reduced Young's modulus (E_r), were evaluated by nanoindentation. The continuous stiffness measurement (CSM) technique was used since it allows the assessment of depth-dependent properties of materials in a single step. The method involves applying a dynamic (oscillatory) load on top of a static load while the material is penetrated in order to determine the continuous stiffness, which is then further processed to calculate H and E_r.[31]

E_r can be seen as a combined modulus of the tested sample and the indenter (eqn (2)).[32]

$$\frac{1}{E_r} = \frac{1 - \nu_s^2}{E_s} + \frac{1 - \nu_i^2}{E_i} \quad (2)$$

where ν is the Poisson's ratio and the indices r, s and i stand for reduced, sample and indenter, respectively.

The nanoindentation tests were carried out with a Nanoindenter XP from MTS using a Berkovich-shaped diamond tip with $E_i = 1140$ and $\nu_i = 0.07$. Due to the large Young's modulus of the indenter in comparison with most metals, the difference between E_r and E_s is usually within a few per cent. The CSM mode was applied with a harmonic displacement of 2 nm and a harmonic frequency of 45 Hz. The experiments were performed in displacement control mode, with a strain rate of 0.05 s^{-1} up to a maximum penetration depth of 100 nm. The Poisson's ratio ν was assumed to be 0.3. Sixteen indents, separated by 10 μm each, were performed on each sample from on top (on the films' surfaces).

Magnetic hysteresis loops were recorded at RT in-plane and out-of-plane by vibrating sample magnetometry (VSM) on an LOT-QuantumDesign MicroSense VSM up to 20 000 Oe. VSM was also used for measuring the temperature dependence of the magnetisation in the saturated regime at 1000 Oe in order to determine T_C, using nitrogen gas flow to control the temperature. After first measurements of T_C, the deposition potential was refined in the range between −0.70 V and −0.60 V to obtain films with a T_C in the desired range. All thin films were subsequently dissolved in aqua regia for chemical analysis by ICP-MS using an Agilent 7500ce spectrometer to obtain the exact compositions of the Ni–Pt films, and to normalise the measured magnetic moment by the total mass of Ni and Pt for each sample. T_C was determined by the two-tangent method, applying tangents to the linear parts of the M–T (magnetisation over temperature) curve both below and above the magnetic transition and taking T_C at the point of their intersection.[33]

3 Results and discussion

3.1 Chemical composition

The composition of the synthesised thin films is determined by the electrodeposition parameters, mainly the deposition potential. Since Pt(IV) deposits at less negative potentials than Ni(II), the Ni content increases when the potential is more negative (Table 1). The same trend was observed by Liu et al. during the electrodeposition of dense Ni–Pt films from a different bath formulation.[25] Progressive enrichment in Ni as the applied potential was made more negative was accompanied by an increase in the deposition rate up to −1.2 V (Fig. 1). The compositions of the dense thin films are similar to their porous counterparts deposited under the same con-

71

Table 1 Composition of dense and mesoporous Ni–Pt films produced at given deposition potentials and determined by ICP-MS

	Composition	
Deposition potential [V]	Porous	Dense
−1.3	$Ni_{99}Pt_1$	
−1.2	$Ni_{98}Pt_2$	$Ni_{98}Pt_2$
−1.0	$Ni_{95}Pt_5$	$Ni_{93}Pt_7$
−0.9	$Ni_{92}Pt_8$	$Ni_{91}Pt_9$
−0.8	$Ni_{84}Pt_{16}$	
−0.7	$Ni_{76}Pt_{24}$	$Ni_{79}Pt_{21}$
−0.6	$Ni_{61}Pt_{39}$	

ditions, *i.e.* the composition is not influenced by the presence of the P-123 triblock copolymer for a given potential. All percentages of Ni and Pt in this work, ranging from 61 at% Ni to 99 at% Ni, are given in atomic percentage. For the film compositions, oxygen or other impurities are not taken into account, however those were monitored by EDX and the oxygen content never exceeded 10 at% (note that in EDX, it is not possible to discriminate whether the oxygen originates from the film or the substrate layers). Current efficiencies determined for the mesoporous Ni–Pt films were between 65% and 85% for all deposition potentials except −0.6 V, where the current efficiency was 47% (Fig. 1).

3.2 Microstructure

All films deposited from the electrolyte containing P-123 exhibit a homogeneously distributed mesoporosity (Fig. 2). The thin films containing 99% and 98% Ni have a clearly visible grain structure with an appreciable roughness (Fig. 2a and b). For 95% Ni, a rough surface without perceptible grain structure is observed (Fig. 2c), while the films ranging from 94% to 61% Ni are smoother, since no topographic contrast other than the one caused by the porosity is visible. Furthermore, those films do not show any apparent grain structure on the nanoscale, and they are highly mesoporous with a narrowly distributed pore size on the order of 10 nm. The microstructures of the dense films show the continuous surfaces with an appreciable, low roughness (Fig. 3).

On a cross-section of a $Ni_{92}Pt_8$ thin film, the porosity over the full film thickness is observed by TEM, together with the Cu seed layer (Fig. 4a). Underneath the Cu layer, the Ti layer and Si substrate are visible. The irregular shape of the film suggests that the film surface has been partially removed during ion polishing. SEM micrographs of this cross-section reveal the film's homogeneity at surface level and the film thickness is around 280 nm (Fig. 4b).

At high resolution, crystal planes become visible and indicate the nanocrystalline structure of the thin film (Fig. 5). A few nanometre thick layer covers the surface of the thin film, which may be a surface oxide, or a damaged layer caused by amorphisation of the metal due to the ion beam polishing during preparation.

In the cross-section of the dense $Ni_{91}Pt_9$ film, a film thickness of *ca.* 250 nm is observed (Fig. 6a). Similar to the meso-
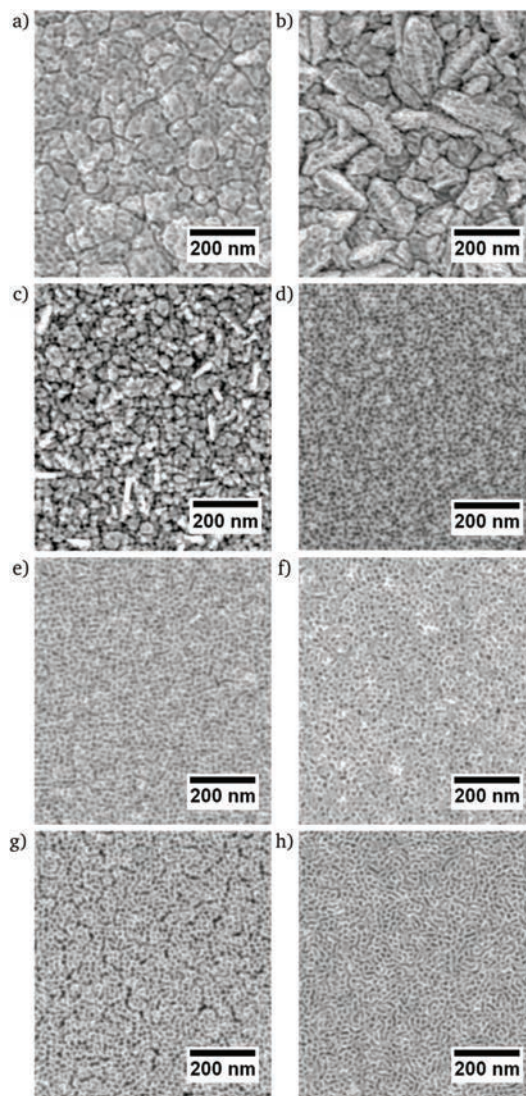
Fig. 2 SEM micrographs of mesoporous Ni–Pt thin films (a) $Ni_{99}Pt_1$, (b) $Ni_{98}Pt_2$, (c) $Ni_{95}Pt_5$, (d) $Ni_{94}Pt_6$, (e) $Ni_{92}Pt_8$, (f) $Ni_{84}Pt_{16}$, (g) $Ni_{76}Pt_{24}$, (h) $Ni_{61}Pt_{39}$ acquired by InLens detector.

porous film (Fig. 5), its nanocrystalline morphology is revealed in high resolution conditions (Fig. 6b).

3.3 Phase analysis

The diffraction patterns obtained by GIXRD show an fcc single-phase solid solution with a cell parameter between those for fcc Ni and fcc Pt (as indicated by the discontinuous lines in Fig. 7) for all compositions. The diffraction patterns of the Ni–Pt films are superposed on the reflections of the fcc Cu seed layer (Fig. 7).
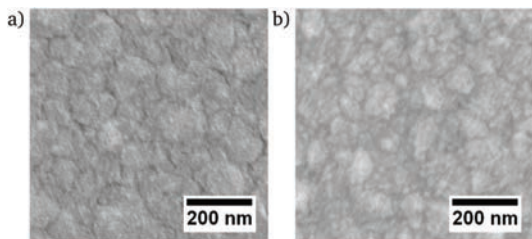
Fig. 3 SEM micrographs of dense Ni−Pt thin films (a) $Ni_{98}Pt_2$, (b) $Ni_{91}Pt_9$ acquired by InLens detector.
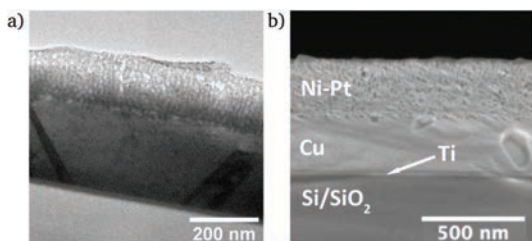
Fig. 4 (a) TEM and (b) SEM micrograph of a cross-section of mesoporous $Ni_{92}Pt_8$ thin film.
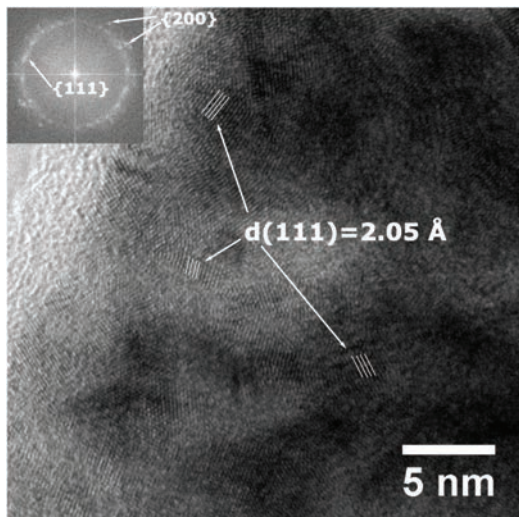
Fig. 5 High resolution TEM micrograph of a cross-section of mesoporous $Ni_{92}Pt_8$ thin film with selected crystal planes indicated. The corresponding fast Fourier transform (FFT) image for the entire zone is shown as an inset on the top left.

Fig. 6 TEM micrographs of dense $Ni_{91}Pt_9$ thin film (a) over the full cross-section and (b) under high-resolution conditions.
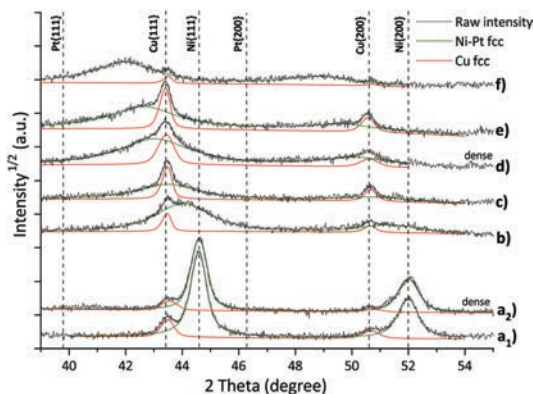
Fig. 7 GIXRD diffraction patterns of Ni−Pt thin films showing the deconvolution of the Ni−Pt (green) and Cu (red curve) phases after Rietveld refinement for (a_1) $Ni_{98}Pt_2$, (a_2) dense $Ni_{98}Pt_2$, (b) $Ni_{92}Pt_8$, (c) $Ni_{84}Pt_{16}$, (d) dense $Ni_{79}Pt_{21}$, (e) $Ni_{76}Pt_{24}$, (f) $Ni_{61}Pt_{39}$. With exception of (a_2) and (d) all films are mesoporous.

the structure (*cf.* Fig. 7, by comparing curves a_1 and a_2 or d and e).

Upon increasing Pt content in the alloy, the diffraction peaks shift towards lower diffraction angles, indicating a progressive increase in the cell parameter. The cell parameter of the Pt–Ni phase obtained by Rietveld refinement scales linearly with the alloy composition, thus following Vegard's law.[34] However, there is a tendency towards cell parameters slightly higher than expected (Fig. 8). This effect was also observed by Kumar *et al.*,[35] and related to the size mismatch due to the different atomic radii of Ni and Pt. Similar deviations, ascribed to the presence of tensile microstrain, have been documented for electrodeposited Ni films.[36]

With the exception of the film containing 98 at% Ni, the reflections of the Ni–Pt phase are significantly broadened due to the small crystallite size. The Rietveld refinement returned crystallite sizes on the order of 5 nm for Ni contents between 61% and 92%, and 50 nm in the case of $Ni_{98}Pt_2$. Similar values are obtained for dense films, hence the nanocrystallinity resulted entirely from the electrodeposition parameters

Remarkably, there is no apparent difference in the diffraction patterns between dense and porous films of identical composition, *i.e.* the porosity has very little or no influence on
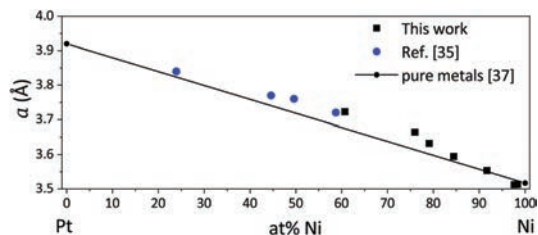
Fig. 8 Dependence of cell parameter *a* on composition of Ni–Pt thin films as determined in this work as well as by Kumar *et al.*[35] Values for pure Ni and Pt are included as a reference.[37]

Table 2 Crystallite sizes of representative Ni–Pt thin films obtained by Rietveld refinement of their respective GIXRD patterns

Composition	Morphology	Crystallite size [nm]
$Ni_{98}Pt_2$	Porous	41
$Ni_{98}Pt_2$	Dense	53
$Ni_{92}Pt_8$	Porous	7
$Ni_{84}Pt_{16}$	Porous	6
$Ni_{79}Pt_{21}$	Dense	5
$Ni_{76}Pt_{24}$	Porous	5
$Ni_{61}Pt_{39}$	Porous	6

and electrolyte composition (Table 2). The presence of the P-123 surfactant did not provoke or influence the formation of a nanocrystalline structure. It can be concluded that differences in behaviour between mesoporous and dense films are entirely related to effects of porosity, since there are no other structural differences apparent.

The nanocrystalline nature of the films is also demonstrated by TEM under diffraction conditions, showing that crystals are oriented in all possible directions within the cross-section (Fig. 9).

3.4 Mechanical properties

Representative curves obtained from nanoindentation tests display the dependences of E_r and H on the penetration depth

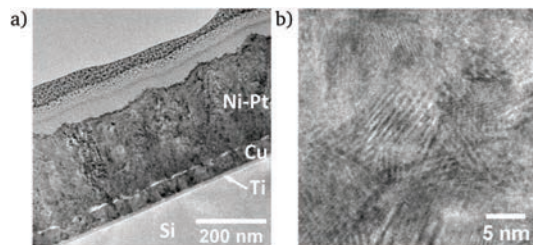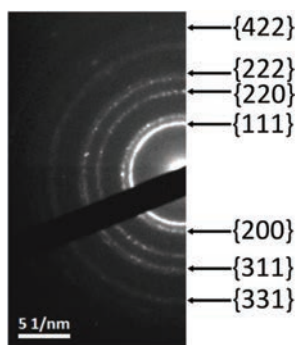Fig. 9 Selected area electron diffraction pattern taken at a cross-section of mesoporous $Ni_{92}Pt_8$ with the Miller indices of the diffraction rings indicated.
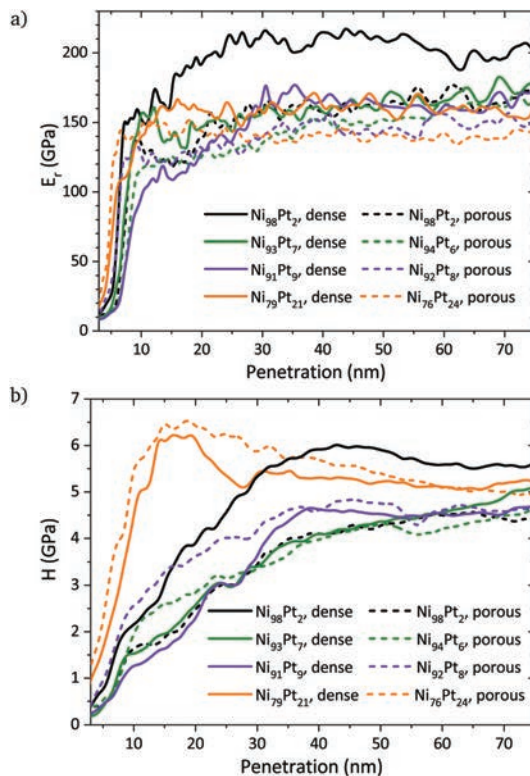
Fig. 10 Representative curves of (a) the reduced Young's modulus and (b) hardness as a function of the nanoindenter's penetration into the surface for selected dense and porous thin films.

into the surface for selected samples (Fig. 10). Nanoindentation measurements may have some influence from the substrate. It is commonly accepted that if the maximum penetration depth is kept lower than one tenth of the overall film thickness, the contribution of the substrate can be disregarded.[31] Considering the experimentally determined film thickness of approximately 280 nm for the Ni–Pt films, the contribution of the substrate may not be neglected for penetration depths higher than 30 nm. Nevertheless, since the film thickness is similar for all compositions, the influence of the substrate on the obtained mechanical properties may be considered similar for all samples, and thus the observed trends in E_r and H are representative of the films' properties.

For a given composition, the dense films show a higher Young's modulus than their porous counterparts, as expected due to their higher density (Fig. 10a). The decrease of hardness and Young's modulus with porosity is a well-documented effect.[38–40] The relation between the Young's moduli of the porous and bulk materials is given by

$$E_{porous} = C_1 E_{bulk} \left(\frac{\rho_{porous}}{\rho_{bulk}} \right)^2 \qquad (3)$$

74

where C_1 is a geometry constant close to 1.[41] In turn, hardness is directly related to the yield stress σ according to $H = 3\sigma$ for metals, which has been confirmed to hold for a nanoporous, single-phase metallic material.[42] The relation between the yield stress of the porous and dense counterparts is the following

$$\sigma_{\text{porous}} = C_2 \sigma_{\text{bulk}} \left(\frac{\rho_{\text{porous}}}{\rho_{\text{bulk}}} \right)^{\frac{3}{2}} \quad (4)$$

where C_2 is equal to 0.3.[41] Therefore, porosity has a more drastic influence on the Young's modulus than on hardness since, as shown in the equations above, $E_{\text{porous}}/E_{\text{bulk}}$ is proportional to $(\rho_{\text{porous}}/\rho_{\text{bulk}})^2$ (where $\rho_{\text{porous}}/\rho_{\text{bulk}}$ is the relative density of the material), whereas hardness is proportional to $(\rho_{\text{porous}}/\rho_{\text{bulk}})^{3/2}$. Comparing the results for mesoporous and dense Ni–Pt films, the Young's modulus shows a stronger influence of porosity than the hardness (Fig. 11). Indeed, the decrease in hardness due to the occurrence of porosity is only apparent for the $Ni_{98}Pt_2$ film. For the rest of compositions, the hardness of the porous films is equal or slightly higher than for their dense counterparts.

Comparing the reduced Young's moduli of porous and non-porous films with similar composition using eqn (3), the relative density is different for each composition. From the microstructures it can be assumed that the mesoporosity introduced
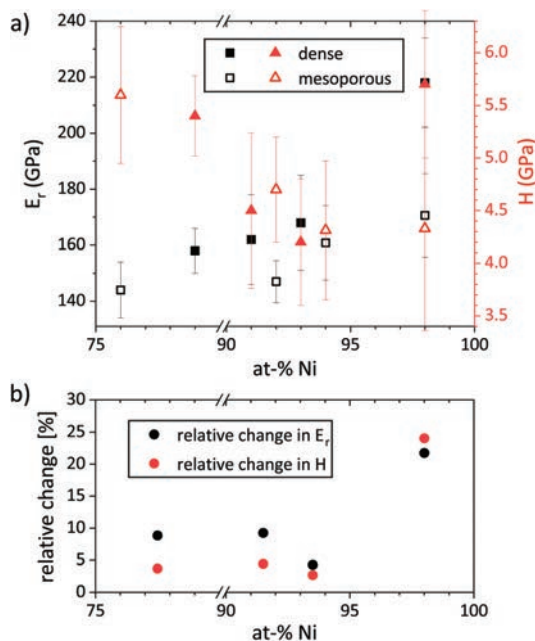
Fig. 11 Averaged reduced Young's modulus and hardness of porous and dense Ni–Pt thin films (a) and the relative changes in E_r and H introduced by porosity, in percentage of the values determined for the dense films (b), at a penetration depth of 40 nm.

by the surfactant is constant over all compositions, however, $Ni_{98}Pt_2$ may have some additional porosity due to voids in-between the grains (cf. Fig. 2). For $Ni_{98}Pt_2$, the relative density yields 61%, i.e. a porosity of 39%. Contrarily, for the pair $Ni_{94}Pt_6$ (porous) and $Ni_{93}Pt_7$ (dense), the determined relative density is 92% (and thus corresponding to a porosity of 8%). The relative densities of the two remaining porous/non-porous pairs ($Ni_{92}Pt_8/Ni_{91}Pt_9$ and $Ni_{76}Pt_{24}/Ni_{79}Pt_{21}$) are 82% and 83%, respectively.

An interplay between porosity, Ni/Pt ratio and grain size may be appreciated in the Young's modulus. As observed, E is always larger in bulk solid films than in their porous counterparts. Also, the Young's modulus tends to increase with the Ni content in agreement with the rule of mixture of two different elements where $E_{\text{Ni}} = 200$ GPa and $E_{\text{Pt}} = 172$ GPa.[5] Grain size might also have an influence on E but its effect should be negligible compared to the other two.

Depending on the state of annealing, the hardness of a pure metal can vary significantly from a metallurgical viewpoint. Generally, Ni bulk metal can reach a Vickers hardness of 1.7 GPa in an annealed state, and 6.3 GPa in a hardened state.[5] Concerning electrodeposited pure Ni, nanocrystalline films with grain sizes (d) between 12 nm and 22 nm exhibit hardness values between 3.9 ($d = 22$ nm) and 6.4 GPa ($d = 14$) nm (ref. 43)—in this case, the high hardness is a result of the nanocrystallinity. For Pt bulk material, the hardness values vary between 0.4 GPa (annealed) and 2.1 GPa (hardened).[5] The inversion of the Hall–Petch relationship due to a change in the mechanism of plastic deformation was determined for nanocrysytalline Pt for grain sizes lower than 10 nm.[44]

The Ni–Pt films possess hardness values lying between 4 GPa and 6 GPa. The generally high values are a result of the nanocrystallinity, however, internal stresses may also contribute to an increased hardness. In the compositional range between 75% and 95% Ni, where the grain size is constant, a trend of increasing hardness with increasing Pt content is observed, which may be related to a solid solution strengthening. For $Ni_{98}Pt_2$, this trend is not continued and its higher hardness may be the result of the difference in grain size (cf. Fig. 2b and Table 2). It has been shown that below a grain size of 14 nm, the breakdown of the Hall–Petch relationship is reached for Ni.[43] Thus, apart from the $Ni_{98}Pt_2$ films, all other Ni–Pt films are subject to an inverse Hall–Petch effect, resulting in lower hardness values for those films.

An effect of the porosity on the hardness of the films in the compositional range between 75% and 95% Ni lies within the measurement uncertainty and cannot be observed (Fig. 10b and 11a). Only for the composition $Ni_{98}Pt_2$, the hardness is significantly lower when porosity is present.

3.5 Magnetic properties

In-plane hysteresis loops conducted by VSM show highest saturation magnetisation M_s and coercivity H_c for Ni-rich films, both decreasing with Pt content (Fig. 12). A change of slope (the orientation of magnetic domains is increasingly hindered) occurring between the coercivity field and the saturation mag-
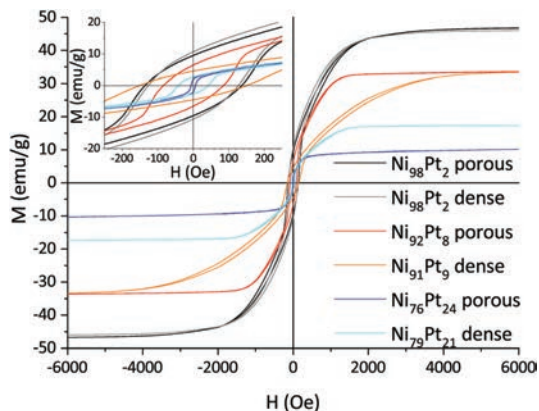
Fig. 12 In-plane magnetic hysteresis loops for porous and dense Ni–Pt thin films with different compositions.

cally hard axis lies out of plane, where the loops are strongly tilted with respect to the in-plane direction. Therefore, the hysteresis loops of dense and porous films are dominated by shape anisotropy. Here, the orientation of magnetic domains normal to the plane is energetically unfavourable, and an increased energy input (applied field) is needed to fully magnetise the films normal to the plane (Fig. 14). The out-of-plane coercivity is lower, i.e. it is easier to demagnetise the material in this mode compared to in-plane. Contrarily to the in-plane mode, the out-of-plane hysteresis loops show a widening when approaching saturation. This effect is generally observed in Ni-rich alloy films—permalloy in particular—as the so-called transcritical state.[46] When the film thickness is sufficiently high, magnetic stripe domains form by part of the magnetisation orienting out of the plane (when applying an external magnetic field in plane) due to an anisotropy caused by in-plane internal stresses.[46]

netisation is observed for both mesoporous and dense films. This effect is generally stronger for dense films—with the exception of $Ni_{98}Pt_2$ which shows the same behaviour as its porous counterpart—indicating that the observed behaviour may be caused by internal stresses which are less pronounced in the porous films. In the case of $Ni_{98}Pt_2$, it is assumed that internal stresses are minimised due to the fact that the material is almost pure Ni and therefore the effect of stresses due to dissolution of Pt (with a higher atomic radius) into the Ni lattice is smaller.

The saturation magnetisation M_s follows a linear trend with the composition for all films. For a given composition, the mass-normalised M_s is identical for both dense and porous films. The same is true for the coercivity of the porous films (Fig. 13). For $Ni_{98}Pt_2$, M_s reaches 46 emu g^{-1}, approaching the value for pure Ni of 54 emu g^{-1} (ref. 45) and thus confirming again that the oxygen content is negligible.

Comparing the behaviour along in-plane and out-of-plane measuring directions, it is clearly observed that the magneti-

Fig. 14 In-plane and out-of-plane magnetic hysteresis loops for two selected dense and porous Ni–Pt thin films with similar composition.

Fig. 13 Dependence of saturation magnetisation M_s and coercivity H_c on composition of Ni–Pt thin films, taken from in-plane hysteresis measurements. The linear trends for the mesoporous films are displayed as dotted lines.

Fig. 15 Dependence of magnetisation on temperature of mesoporous Ni–Pt thin films at 1000 Oe.

76
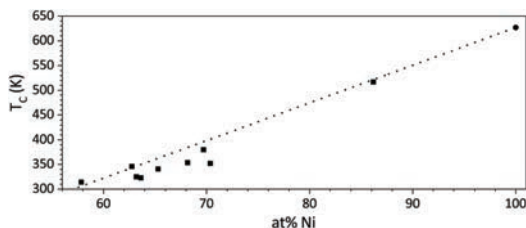
Fig. 16 Curie temperature T_C as a function of composition of meso-porous Ni–Pt thin films. T_C for pure Ni is shown for reference. The general trend is indicated by a dotted line.

The temperature scans reveal a phase transition of the Ni–Pt alloys from ferromagnetic to paramagnetic state (Fig. 15). The fact that a single transition is observed consolidates that the structure of the films is indeed single-phase.

As a general trend, the magnetic transition and therefore the Curie temperature shifts to lower temperatures for films with higher Pt content. The magnetisation curve for $Ni_{58}Pt_{42}$ shows only the final part of the phase transition, indicating that its T_C is very close to RT (Fig. 15, violet curve).

The resulting values for T_C show a linear relationship with the percentage of Ni (Fig. 16). The T_C was only determined for those films where the magnetic transition appeared sufficiently above the start of the measurement range (298 K).

4   Conclusions

Mesoporous and dense Ni–Pt thin films have been synthesised by electrodeposition from aqueous media, achieving the meso-porosity through micelle-assisted deposition with a block copolymer. The composition of the thin films can be tuned in a large range between $Ni_{98}Pt_2$ and $Ni_{61}Pt_{39}$ by varying the deposition potential, resulting in a sin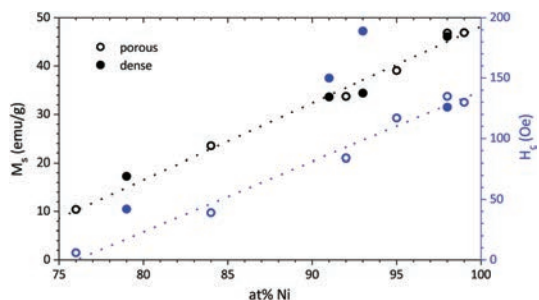gle-phase Ni–Pt solid solution in all cases. The porosity is homogeneously distributed for all compositions and the nanocrystallinity is not affected by the porosity. Crystallite sizes are around 50 nm for the most Ni-rich composition $Ni_{98}Pt_2$, and between 5–7 nm for the other compositions. The mechanical properties are strongly dependent on both porosity and composition. The ratio of the reduced Young's moduli suggests a porosity of around 18% for Pt contents of 8 at% and more, whereas a porosity of 39% is obtained for $Ni_{98}Pt_2$. Apart from the effect of porosity, the reduced Young's modulus shows a strong compositional dependence, increasing with the Ni content. The measured hardness shows the effect of solid solution strengthening, and an effect of the microstructure in the case of $Ni_{98}Pt_2$, due to the significantly different morphology and grain size at this particular composition. The single-phase character also makes it possible to tune the magnetic properties with the composition; T_C can be adjusted to a desired value reaching from the T_C of Ni (630 K) down to RT and below. Adjusting T_C to RT may allow to study the magnetic behaviour close to T_C, and

other possible effects such as a voltage-dependency of T_C. Apart from T_C, the saturation magnetisation and—in the case of the mesoporous films—also the coercivity scales with the composition, thus facilitating to predict the magnetic behaviour for a certain composition and to easily select a suitable composition in order to obtain the desired magnetic properties.

Conflicts of interest

There are no conflicts to declare.

Acknowledgements

Notes and references

1 G. Schiavone, M. P. Y. Desmulliez and A. J. Walton, *Micromachines*, 2014, **5**, 622.

2 *MEMS: A practical guide to design, analysis, and applications*, ed. J. Korvink and O. Paul, William Andrew, NY and Springer-Verlag, Germany, 2006.

3 R. Coutu Jr., P. Kladitis, K. Leedy and R. Crane, *J. Micromech. Microeng.*, 2004, **14**, 1157.

4 D. Niarchos, *Sens. Actuators, A*, 2003, **106**, 255.

5 F. Cardarelli, *Materials Handbook*, Springer Intl. Publishing AG, Switzerland, 3rd edn, 2018.

6 J. Weertman, *Mater. Sci. Eng., A*, 1993, **166**, 161.

7 E. Pellicer, A. Varea, S. Pané, B. J. Nelson, E. Menéndez, M. Estrader, S. Suriñach, M. D. Baró, J. Nogués and J. Sort, *Adv. Funct. Mater.*, 2010, **20**, 983.

8 H. Li and F. Ebrahimi, *Mater. Sci. Eng., A*, 2003, **347**, 93.

9 Z. Li, J. Barnes, A. Bosoy, J. F. Stoddart and J. Zink, *Chem. Soc. Rev.*, 2012, **41**, 2590.

10 N. Linares, A. Silvestre-Albero, E. Serrano, J. Silvestre-Albero and J. García-Martínez, *Chem. Soc. Rev.*, 2014, **43**, 7681.

11 L. Zhang, L. Jin, B. Liu and J. He, *Front. Chem.*, 2019, **7**, 22.
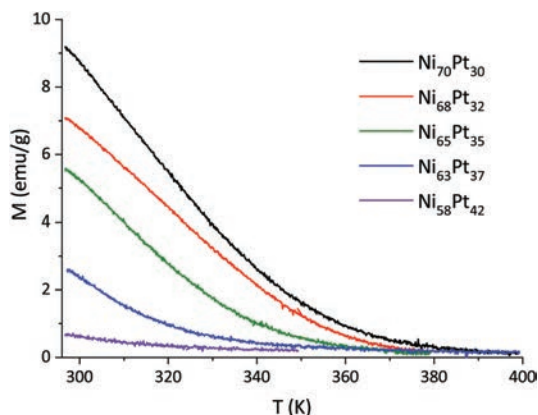
12 A. L. Wang, H. Xu, J. X. Feng, L. X. Ding, Y. X. Tong and G. R. Li, *J. Am. Chem. Soc.*, 2013, **135**, 10703.

13 L. X. Ding, A. L. Wang, G. R. Li, Z. Liu, W. X. Zhao, C. Su and Y. X. Tong, *J. Am. Chem. Soc.*, 2012, **134**, 5730.

14 A. Quintana, J. Zhang, E. Isarain-Chávez, E. Menéndez, R. Cuadrado, R. Robles, M. D. Baró, M. Guerrero, S. Pané,

B. J. Nelson, C. M. Müller, P. Ordejón, J. Nogués, E. Pellicer and J. Sort, *Adv. Funct. Mater.*, 2017, **27**, 1701904.

15 C. Navarro-Senent, A. Quintana, E. Menéndez, E. Pellicer and J. Sort, *APL Mater.*, 2019, **7**, 030701.

16 B. G. Trewyn, S. Giri, I. I. Slowing and V. S.-Y. Lin, *Chem. Commun.*, 2007, **31**, 3236.

17 R. Du, Q. Zhao, Z. Zheng, W. Hu and J. Zhang, *Adv. Energy Mater.*, 2016, **6**, 1600473.

18 O. Kharissova, H. V. R. Dias and B. I. Kharisov, *RSC Adv.*, 2015, **5**, 6695.

19 P. Nash and M. F. Singleton, *Bull. Alloy Phase Diagrams*, 1989, **10**, 258p.

20 R. A. Walker and J. B. Darby Jr., *Acta Metall.*, 1970, **18**, 1261.

21 A. Gomes and M. I. da Silva Pereira, *Electrochim. Acta*, 2006, **51**, 1342.

22 C. Navarro-Senent, J. Fornell, E. Isarain-Chávez, A. Quintana, E. Menéndez, M. Foerster, L. Aballe, E. Weschke, J. Nogués, E. Pellicer and J. Sort, *ACS Appl. Mater. Interfaces*, 2018, **10**, 44897.

23 E. Isarain-Chávez, M. D. Baró, E. Pellicer and J. Sort, *Nanoscale*, 2017, **9**, 18081.

24 B. Craig, *ASM Handbook, Volume 13A: Corrosion: Fundamentals, Testing, and Protection*, ASM Intl., 2003, pp. 367–380.

25 Y. Liu, C. M. Hangarter, U. Bertocci and T. P. Moffat, *J. Phys. Chem. C*, 2012, **116**, 7848–7862.

26 V. Malgras, H. Ataee-Esfahani, H. Wang, B. Jiang, C. Li, K.-W. Wu, J. Kim and Y. Yamauchi, *Adv. Mater.*, 2015, **28**, 993.

27 H. Wang, L. Wang, T. Sato, Y. Sakamoto, S. Tominaka, K. Miyasaka, N. Miyamoto, Y. Nemoto, O. Terasaki and Y. Yamauchi, *Chem. Mater.*, 2012, **24**, 1591.

28 J. Zhang, A. Quintana, E. Menéndez, M. Coll, E. Pellicer and J. Sort, *ACS Appl. Mater. Interfaces*, 2018, **10**, 14877–14885.

29 Materials analysis using diffraction, http://maud.radiogra-phema.com/, (accessed Dec. 2019).

30 L. Luterotti, *Nucl. Instrum. Methods Phys. Res., Sect. B*, 2010, **268**, 334.

31 A. C. Fischer-Cripps, *Nanoindentation*, Springer, NY, 1st edn, 2002.

32 W. C. Oliver and G. M. Pharr, *J. Mater. Res.*, 1992, **7**, 1564.

33 C. S. Grommé, T. L. Wright and D. L. Peck, *J. Geophys. Res.*, 1969, **74**, 5277.

34 L. Vegard, *Z. Phys.*, 1921, **5**, 17.

35 U. Kumar, K. G. Padmalekha, P. K. Mukhopadhyay, D. Paudyal and A. Mookerjee, *J. Magn. Magn. Mater.*, 2005, **292**, 234–240.

36 S. Sengupta, A. Patra, S. Jena, K. Das and S. Das, *Metall. Mater. Trans. A*, 2018, **49A**, 920–937.

37 A. W. Hull, *Phys. Rev.*, 1921, **17**, 571–588.

38 F. Tancret and F. Osterstock, *Philos. Mag.*, 2003, **83**, 125.

39 S. Cariou, F.-J. Ulm and L. Dormieux, *J. Mech. Phys. Solids*, 2008, **56**, 924.

40 J. Biener, A. M. Hodge, A. V. Hamza, L. M. Hsiung and J. H. Satcher Jr., *J. Appl. Phys.*, 2005, **97**, 024301.

41 L. J. Gibson and M. F. Ashby, *Cellular solids: structure and properties*, Cambridge University Press, UK, 2nd edn, 1997.

42 H. J. Jin, L. Kurmanaeva, J. Schmauch, H. Rösner, Y. Ivanisenko and J. Weissmüller, *Acta Mater.*, 2009, **57**, 2665.

43 C. Schuh, T. Nieh and T. Yamasaki, *Scr. Mater.*, 2002, **46**, 735.

44 X. Shu, D. Kong, Y. Lu, H. Long, S. Sun, X. Sha, H. Zhou, Y. Chen, S. Mao and Y. Liu, *Sci. Rep.*, 2017, **7**, 13264.

45 B. Cullity and C. Graham, *Introduction to magnetic materials*, John Wiley & Sons, Inc., NJ, 2nd edn, 2009.

46 A. V. Svalov, I. R. Aseguinolaza, A. Garcia-Arribas, I. Orue, J. M. Barandiaran, J. Alonso, M. L. Fernández-Gubieda and G. V. Kurlyandskaya, *IEEE Trans. Magn.*, 2010, **46**, 333.

78

$Ni(OH)_2 \rightleftharpoons NiOOH$ **Mesoporous Ni-Pt alloy** $2H + 2e^- \rightleftharpoons H_2$

200 nm

NaOH H_2SO_4
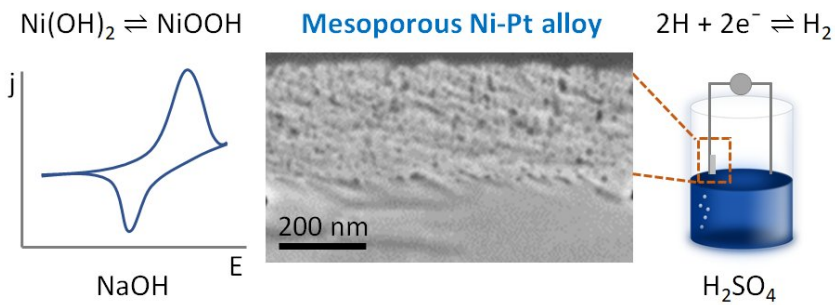
5.3 Electrochemical characterisation of multifunctional electrocatalytic mesoporous Ni-Pt thin films in alkaline and acidic media

Konrad Eiler[a], Halina Krawiec[b], Iryna Kozina[b], Jordi Sort[a,c] and Eva Pellicer[a]

[a]Departament de Física, Universitat Autònoma de Barcelona, 08193 Bellaterra, Spain
[b]Faculty of Foundry Engineering, AGH University of Science and Technology, 30-059 Kraków, Poland
[c]Institució Catalana de Recerca i Estudis Avançats (ICREA), Pg. Lluís Companys 23, 08010 Barcelona, Spain

This work is the result of a collaboration and research stay at AGH University of Science and Technology, Kraków, and focusses on electrochemical characterisation and durability of Ni–Pt thin films in view of potential applications in both acid and alkaline environments. The article is centred on the exploitation of the EMT, backed up by studies in a regular electrochemical cell.

In 0.5 M H_2SO_4 acidic media, 24 h of continuous HER leads to an initial drop in overpotential, followed by a stabilisation. Failure of the system is observed when the thin films are anodically polarised, so that reliable application can only be guaranteed if cathodic potential is constantly applied. In acidic media, the range of application is wider and only limited by an irreversible surface passivation at 1.0 V vs Ag|AgCl. In addition, a redox reaction is observed at lower anodic potentials between nickel hydroxide and oxyhydroxide. This fully reversible redox reaction is enhanced with the Pt content acting as an intrinsic catalyst and reveals another potential application in the field of electrochemical (super)capacitors.

Electrochemical characterisation of multifunctional electrocatalytic mesoporous Ni-Pt thin films in alkaline and acidic media

Konrad Eiler [a,*], Halina Krawiec [b], Iryna Kozina [b], Jordi Sort [a,c], Eva Pellicer [a]

[a] Departament de Física, Universitat Autònoma de Barcelona, 08193 Bellaterra, Spain
[b] Faculty of Foundry Engineering, AGH University of Science and Technology, 30-059 Kraków, Poland
[c] Institució Catalana de Recerca i Estudis Avançats (ICREA), Pg. Lluís Companys 23, 08010 Barcelona, Spain

ARTICLE INFO

ABSTRACT

Reliability and long-term performance are the key features of modern energy storage and conversion devices. The long-term stability depends entirely on the electrochemical and corrosion properties of device components. Single-phase mesoporous Ni-rich Ni-Pt thin films have shown to be a promising electrocatalyst for hydrogen evolution reaction (HER) and therefore with potential application in fuel cells, water electrolysers or similar devices. The HER activity of the mesoporous Ni-Pt films is reliable and stable in 0.5 M H_2SO_4 up to 200 linear sweep voltammetry cycles, however leaching of Ni occurs in absence of cathodic polarisation. Long-term electrolysis measurements at a HER current of –10 mA/cm^2 reveal an increase in potential over time, which is minimised when the Pt content is increased. In 1 M NaOH, the material is stable up to an applied anodic limit of 1.5 V vs. Ag|AgCl although surface passivation takes place at 1.0 V. If the anodic limit does not exceed 0.6 V vs. Ag|AgCl, a fully reversible redox reaction is observed by cyclic voltammetry, with redox charges increasing with Pt content and scan speed. In addition, significantly higher current densities are recorded for mesoporous films compared to dense counterparts. This charge/discharge behaviour of the redox reaction indicates that the mesoporous Ni-Pt films may as well be used as an electrochemical supercapacitor. As a HER catalyst, the material is safely applicable in alkaline media.

1. Introduction

Efficient and sustainable electrocatalysts are needed to increase the competitivity of hydrogen energy over conventional, polluting power generation. Especially in acidic environments, such as proton exchange membrane fuel cells (PEMFC), where the stability of the catalyst is critical, material selection and design is very important [1]. Since Pt is the most active but also expensive catalyst, efforts are made in order to find a compromise between cost and performance of the catalyst [2]. Alternatively, water electrolysis and fuel cells can operate in alkaline media as a less aggressive environment for the catalyst [3].

Apart from the selection of a catalyst material, the structure of catalysts is optimised in order to maximise their surface area while minimising the amount of material [4]. This can be achieved by synthesising materials with high surface-to-volume ratios such as porous structures, nanoparticles, or nanotubes. Thin films, in spite of their lower surface area, typically show higher specific electrochemical activity compared to nanoparticles [5].

Ni is a good candidate to partially replace Pt via alloying. Several features related to the Gibbs free energy, electronegativity and lattice mismatch point to a good electrocatalytic activity of Ni-Pt alloys towards HER [6]. Ni is commonly used for the protection of electrical contacts, and electrodeposited Ni coatings are often used for corrosion protection [7,8]. For example, electrodeposited Ni-based Ni-Co-B coatings have shown to improve the corrosion resistance in a fuel cell environment compared to uncoated stainless steel and Al 6061 alloy [9]. Many Ni-based compounds have been investigated for HER, however almost exclusively in alkaline media [10–13].

A critical issue for Ni-rich alloys is hydrogen embrittlement, which can occur especially in environments containing H_2S, and even during the hydrogen evolution reaction [14]. Electrodeposited

* Corresponding author.
E-mail addresses: konrad.eiler@uab.cat, konrad.eiler@gmx.de (K. Eiler), krawiec@agh.edu.pl (H. Krawiec), eva.pellicer@uab.cat (E. Pellicer).

Ni films are especially susceptible to hydrogen embrittlement due to interstitial, monoatomic hydrogen dissolved in the crystal lattice [15]. However, this form of hydrogen embrittlement is reversible [16].

Single-phase mesoporous Ni-Pt thin films exploit both the increase of surface area provided by the porous structure, as well as a reduced usage of Pt via alloying with Ni. In a previous study, Ni-rich films were produced by electrodeposition and thoroughly characterised, showing excellent performance at HER in 0.5 M H_2SO_4 [17]. A good stability over 200 cycles of HER was reported for Ni-Pt films with different compositions, ranging from 99 at% Ni (1 at% Pt) to 61 at% Ni (39 at% Pt). Yet, their electrochemical behaviour in acidic and alkaline media remains to be explored. In view of their potential integration in PEMFCs, their long-term stability must be further assessed by corrosion studies to determine if the mesoporous Ni-Pt thin films can be safely used in acidic media, or if an alkaline electrolyte is more favourable for long-term stability instead.

Also, the effect of the composition on the electrochemical behaviour must be investigated. The selective dissolution in acidic media, also known as leaching, is a common issue for Pt alloyed with a transition metal [18], but may be hindered in single-phase alloys, where the noble metal can protect the transition metal atoms if its content is sufficiently high. Other strategies with the intent to minimise the leaching of Ni include the synthesis of core-shell structures with a Pt-rich surface protecting the Ni-rich core [19]. The corrosion resistance of Ni-Pt alloys is expected to increase with the Pt content. However, any effect of the mesoporosity on the electrochemical behaviour needs to be investigated. For instance, the porosity may lead to crevice corrosion due to differential aeration inside the pores [20].

This work focusses on the effect of composition (Ni and Pt contents) and mesoporosity on the observed electrochemical behaviour, corrosion properties, and long-term stability of Ni-Pt alloy thin films. In order to assess the electrochemical properties of Ni-rich Ni-Pt alloy thin films, the behaviour is studied both in acidic (0.5 M H_2SO_4) and alkaline (1 M NaOH) electrolytes, two media which are commonly used to study materials for acidic and alkaline fuel cells. The studies were conducted by cyclic voltammetry (CV) and with the use of the electrochemical microcell technique (EMT), which allows for multiple measurements on a single sample, with the aim to identify the oxidation and reduction reactions occurring. In addition, electrochemical impedance spectroscopy (EIS) was used to provide an understanding of the corrosion resistance of the Ni-Pt films in acidic media. Although cathodic potentials, which are usually not critical in terms of corrosion, are applied during HER, the electrode potential can rise well into the range of oxidising potentials when not in operation [21].

2. Experimental

All electrochemical tests were performed on single-phase, nanocrystalline Ni-Pt thin films with varying composition, both with and without mesoporosity, which had been structurally characterised elsewhere [17,22]. A series of dense and mesoporous Ni-Pt films, ranging from 61 at% to 99 at% Ni, are investigated in the present study (Table 1).

The samples consisted of a Si wafer sputter-deposited with a Ti adhesion layer and a Cu seed layer, onto which Ni-Pt films were grown (Fig. 1). The films were potentiostatically deposited from an aqueous electrolyte, using a micelle-forming surfactant in the case of the mesoporous films [17]. TEM analyses were performed on a Jeol JEM-2011 at 200 kV acceleration voltage. Sample preparation was done by grinding, polishing and Ar ion milling (for mesoporous $Ni_{92}Pt_8$) as well as by cutting with a focused ion beam (FIB, for dense $Ni_{91}Pt_9$).

Table 1
Composition and morphology of electrochemically studied Ni-Pt thin films.

porous	dense
$Ni_{99}Pt_1$	
$Ni_{98}Pt_2$	$Ni_{98}Pt_2$
$Ni_{95}Pt_5$	$Ni_{93}Pt_7$
$Ni_{92}Pt_8$	$Ni_{91}Pt_9$
$Ni_{84}Pt_{16}$	
$Ni_{76}Pt_{24}$	$Ni_{79}Pt_{21}$
$Ni_{61}Pt_{39}$	
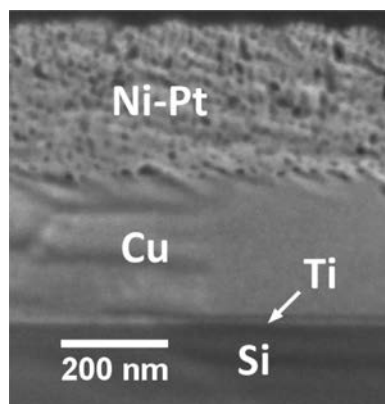
Fig. 1. Representative cross-sectional SEM micrograph of a Si/Ti/Cu substrate coated with mesoporous Ni-Pt.

An Autolab 302N potentiostat/galvanostat was used to perform all electrochemical tests. Initial CVs were performed in a conventional three-electrode set-up using an Ag|AgCl reference electrode (RE) and a platinum spiral as counter electrode (CE). HER in 0.5 M H_2SO_4 was investigated by linear sweep voltammetry (LSV), sweeping the potential from –0.15 V to –0.5 V vs. Ag|AgCl in an identical set-up but with the use of a graphite rod as CE. For evaluation of the long-term stability at HER in 0.5 M H_2SO_4, a 24 h long electrolysis was performed at a geometric current density of –10 mA/cm^2. Results obtained from these methods, which deal with the characterisation of the whole films (as opposed to local measurements) are hereafter denoted as global scale tests.

The EMT was used to study the electrochemical behaviour of the Ni-Pt thin films in detail. Contrarily to its usual scope to study single inclusions, grains, phases etc. [23], and due to the homogeneous, single-phase and nanocrystalline character of the Ni-Pt thin films, this method was used here to study the overall representative behaviour of the films locally, and, moreover, allowed to perform multiple measurements on the same sample. Results from this method are further denoted as local technique, local scale or EMT.

The set-up consists of an optical microscope, into which the electrochemical cell is mounted, and the sample functioning as working electrode (WE) is placed on a conductive sample holder, all placed inside a Faraday cage (Fig. 2). The samples' surfaces were electrically connected to the sample holder via copper tape. The electrochemical microcell is filled with the electrolyte, a Pt wire is used as CE and an Ag|AgCl electrode as RE. The electrolyte is connected to the WE through a glass microcapillary with a tip diameter of 50–200 μm. The tip is covered with a silicone gasket to protect the capillary and facilitate the contact with the WE [24]. Using the objectives of the optical microscope, the area to be measured
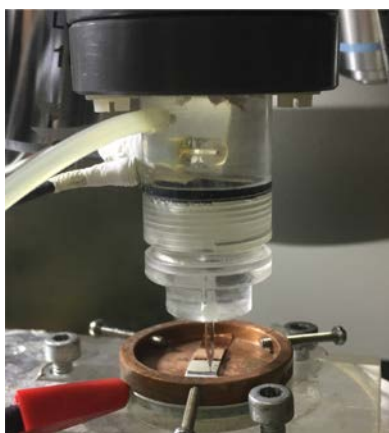
Fig. 2. Set-up of the electrochemical microcell. The tip of the glass microcapillary is in contact with the metallic mesoporous Ni-Pt film.

was checked before each measurement in order to confirm that it was homogeneous and free of defects or surface pollution.

The EMT was used in the following studies:

- CVs
  - in NaOH from −0.5 V to 0.6 V and 1.5 V vs. Ag|AgCl
  - in H_2SO_4 from −0.5 V to 0.5 V vs. Ag|AgCl
- EIS in H_2SO_4

EIS in NaOH did not yield any valid data since the currents were below the detection limit. EIS was conducted in a frequency range from 100 kHz to 3 mHz, after an equilibration time of 5 min at open circuit potential (OCP), with an amplitude of 10 mV.

The thin films were analysed before and after electrochemical measurements by scanning electron microscopy (SEM) coupled with energy-dispersive X-ray spectroscopy (EDX) on a Zeiss Merlin electron microscope to study the effects of exposure to acidic and alkaline media on the microstructure and composition. Imaging was performed using the InLens detector with an acceleration voltage of 1–2 kV, while an acceleration voltage of 20 kV was used for EDX.

For quantification of dissolution or leaching of the mesoporous Pt-Ni thin films in sulfuric acid, the surfaces of $Ni_{95}Pt_5$, $Ni_{92}Pt_8$, and $Ni_{84}Pt_{16}$ films were immersed in 0.5 M H_2SO_4 at OCP for 10 min and the solution was then analysed by inductively coupled plasma mass spectrometry (ICP-MS) using an Agilent 7500ce spectrometer to determine the amount of dissolved Ni and Pt.

3. Results and discussion

3.1. Microstructural analysis

The TEM cross-sections of the mesoporous $Ni_{92}Pt_8$ (Fig. 3a) and dense $Ni_{91}Pt_9$ (Fig. 3b) films are shown for comparison. While the latter shows its fully dense appearance, a homogeneous distribution of pores can be observed in the mesoporous counterpart. Film thickness lies between 200 nm and 300 nm, which holds for all compositions.

At high resolution, the nanocrystallinity of the films is revealed (Fig. 3c) and further confirmed by the selected area electron diffraction (SAED) pattern, where the existence of arbitrary crystal orientations of the single-phase fcc Ni-Pt alloy is shown (Fig. 3d).

3.2. HER performance at global scale

The performance of the Ni-rich Ni-Pt thin films at HER in 0.5 M H_2SO_4 (Eq. (1)) shows that hydrogen production is highly reproducible, with very little changes up to 200 sweeps. Representa-
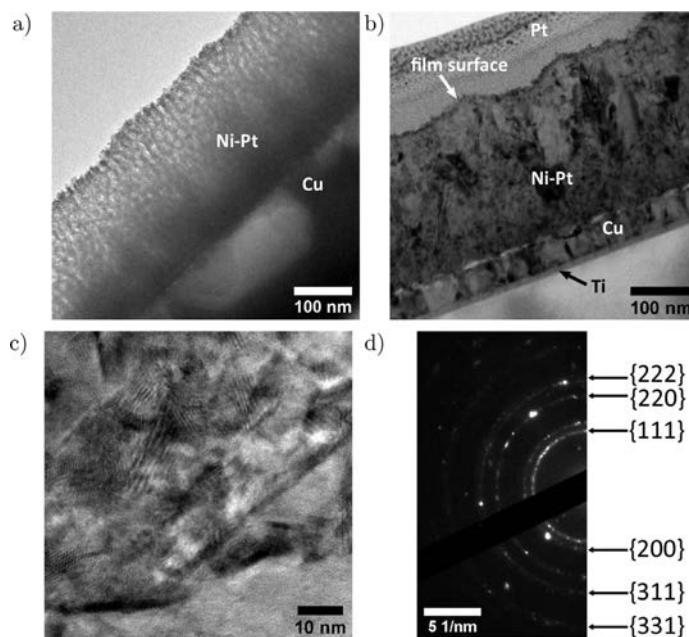
Fig. 3. TEM micrographs of the full cross-section of (a) mesoporous $Ni_{92}Pt_8$ and (b) dense $Ni_{91}Pt_9$ films; (c) high-resolution TEM micrograph and (d) SAED pattern of dense $Ni_{91}Pt_9$ film with the corresponding planes of the fcc lattice indicated. The additional Pt layer visible in panel (b) results from the sample preparation by FIB.
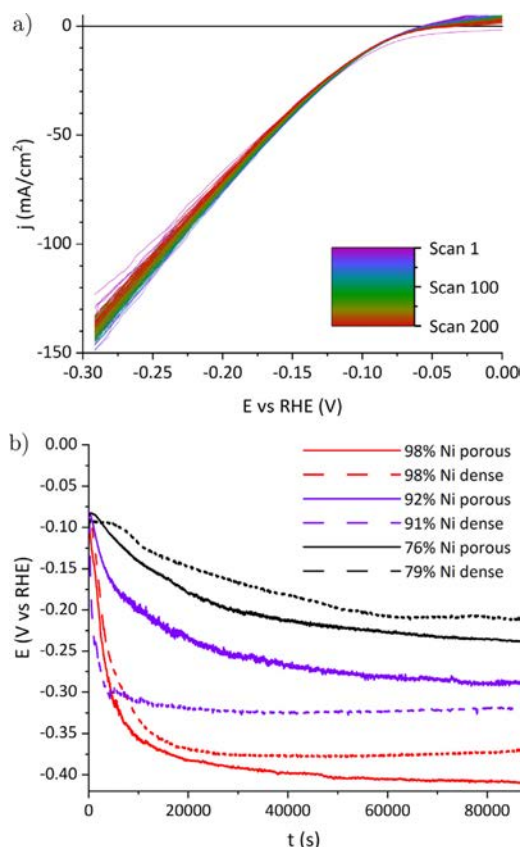
Fig. 4. Exemplary HER performance during 200 sweeps in 0.5 M H_2SO_4 at a scan rate of 50 mV/s for mesoporous $Ni_{84}Pt_{16}$ film (a). Evolution of potential over time at constant HER current density of −10 mA/cm² for dense and mesoporous Ni-Pt films (b). The current density values correspond to the current normalized by the geometric area of the film.

Fig. 5. (a) Mesoporous microstructure of $Ni_{84}Pt_{16}$ before and (b) after 200 sweeps of HER in 0.5 M H_2SO_4; (c) micrograph of the surface of mesoporous $Ni_{76}Pt_{24}$ after 24 h at −10 mA/cm² with cracks indicated by arrows.

tively for all compositions, the $Ni_{84}Pt_{16}$ alloy film shows the HER during LSV, reaching current densities of up to 150 mA/cm² at − 0.3 V vs. reversible hydrogen electrode (RHE, Fig. 4a). A certain deviation between individual sweeps is always obtained due to the temporary blocking of the surface by hydrogen bubbles being formed [17]. Comparable activity at HER in the same media has been reported for mesoporous Pt-rich Fe-Pt films [25]. Thus, the Ni-Pt films reported here are able to achieve the same activity at HER with a significantly lower Pt content.

$$2H^+ + 2e^- \xrightarrow{Ni\text{-}Pt} H_2 \qquad (1)$$

Long-term electrolysis experiments indicate that the recorded potential changes over time. Specifically, at constant operation at −10 mA/cm², it is observed that an increasingly cathodic potential is needed to maintain the HER current (Fig. 4b). However, irrespective of composition or the presence of porosity in the alloy, this potential stabilises over time and indicates that no further degradation in performance is expected. The higher the Pt content in the films, the lower is the resulting change in potential. An increase in the overpotential required for HER and oxygen evolution reaction (OER) at constant current density in macroporous electrodeposited Ni has also been observed in alkaline media [26]. Contrarily, the constant operation of Ni foam at HER in 0.5 M H_2SO_4 at a fixed

potential for 15 h revealed a shift of the current density towards more negative values, which was related to a surface roughening of the Ni foam [27].

3.2.1. Microstructural analysis after HER

The microstructure of the films after 200 sweeps of HER appears unaltered compared to the as-deposited state (Fig. 5a, b). Upon closer examination, the size of the mesopores appears slightly bigger after HER experiments, suggesting the removal of material such as oxides, hydroxides or other contaminants from the surface. A comparison of EDX spectra before and after HER did not reveal significant differences in the Ni/Pt ratios.

After the 24 h long electrolysis, cracking was observed in dense and mesoporous Ni-Pt films (Fig. 5c). In all cases, a slight decrease in Ni content after the electrolysis was observed, in addition to particles containing nickel and sulfur formed on the surface (possibly nickel sulfate), visible as white particles in Fig. 5c. Both these effects are likely to be the origin of the potential increase observed during electrolysis.

3.3. Verification of the applicability of the EMT

Although the Ni-Pt films are targeted for application in acidic media, application in alkaline media is a possible alternative. Since alkaline media is far less aggressive, it allows for non-destructive electrochemical characterisation, and for validation of the set-up and measurement parameters before the behaviour of the Ni-Pt films in acidic media is studied. As aforementioned, a period of in-operation of electrolysers may transiently cause the application of oxidising potentials to the cathode and it is therefore important to evaluate the electrochemical response of the catalyst in the anodic range [21].

Fig. 7. Exemplary CV of a dense $Ni_{93}Pt_7$ film in 1 M NaOH at a scan rate of 100 mV/s and anodic limit of 1.5 V vs Ag|AgCl determined by EMT. The inset shows a zoomed detail of the low current region where the redox reaction $Ni(OH)_2 \rightleftharpoons NiOOH$ is expected.

peaks can be explained by both the oxidation of α- and β-$Ni(OH)_2$ at different potentials [29] as well as the formation of NiOOH with different crystallographic structures [30]. Indeed, a shoulder to the right of the main peak was already observed using EMT at 100 mV/s (Fig. 6a).

3.4. Electrochemical behaviour in NaOH determined by EMT

The behaviour of the Ni-Pt films was studied in the potential range between −0.5 V and 1.5 V vs Ag|AgCl. When the anodic potential was as high as 1.5 V, a large oxidation peak centred around 1 V was observed for all samples (Fig. 7). After this large oxidation peak was recorded, no further major oxidation or reduction currents were observed within the entire potential window in the subsequent cycles. However, microscopic analyses confirmed that the Ni-Pt film was still intact and no dissolution had taken place. Therefore, the large oxidation peak observed in the first cycle can be attributed to a passivation of the film's surface which could not be reversed within the applied potential window and may be related to an irreversible oxidation of Pt [31,32]. In order to avoid the effect of passivation on the redox reaction $Ni(OH)_2 \rightleftharpoons NiOOH$, the anodic limit was set to 0.6 V, resulting in a stabilisation of the redox reaction (Fig. 8).

3.4.1. Characterisation of redox reaction $Ni(OH)_2 \rightleftharpoons NiOOH$ by EMT

The characteristics of the redox reaction (Eq. (2)) resolved by the CVs show dependencies on the film composition, porosity, and the scan rate. Although the redox reaction is determined to involve the formation of Ni hydroxides/oxyhydroxides, the reaction is enhanced by the incorporation of higher amounts of Pt in the films (Fig. 9). This may be related to the fact that Pt as an excellent electrocatalyst is able to enhance electrochemical reactions on neighbouring Ni atoms due to synergistic effects. In this way, the reaction enhances while increasing the Pt content while the amount of Ni atoms available on the surface decreases. As a result, there should be a certain Pt content for which the maximum effect is obtained.

In absence of porosity, the measured currents are significantly lower. This difference is not as high as might be expected from the difference in surface area between mesoporous and dense films, but correlates well with the fact that the ECSA determined in a

Fig. 6. CVs of mesoporous $Ni_{84}Pt_{16}$ in NaOH on global (green) and local scale (blue) in 1 M NaOH at a scan rate of (a) 100 mV/s and (b) 20 mV/s. (For interpretation of the references to colour in this figure legend, the reader is referred to the web version of this article.)

In the CVs obtained from both global scale and local measurements in NaOH, a redox reaction is observed within the potential window from −0.5 V and 0.6 V (Fig. 6a). The oxidation and reduction peaks correspond with the redox reaction between $Ni(OH)_2$ and NiOOH (Eq. (2)) [28].

$$Ni(OH)_2 + OH^- \rightleftharpoons NiOOH + H_2O + e^- \qquad (2)$$
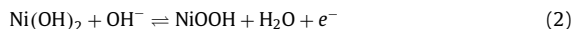
Both methods reveal the same redox reaction at similar current densities, confirming that—due to the homogeneity of the Ni-Pt thin films—the EMT technique is able to capture the films' global electrochemical properties. Using the local technique, the oxidation and reduction peaks are wider with respect to the global technique, and the peaks are more separated. This observation is made for all film compositions, and applies especially at higher scanning speeds. This is probably due to the very small volume of the electrochemical microcell, where the availability of species such as OH^- is reduced and the kinetics are thus slowed and limited by the diffusion of those species through the capillary as a very constrained path. This effect is more significant at high scanning speeds, where the depletion of species available at the electrode is even faster.

At low scan rates with the local technique (i.e. 10 mV/s and 20 mV/s), progressive widening of the peaks makes it possible to discriminate between two oxidation peaks which were not resolved on the global scale (Fig. 6b). The split into two oxidation

Fig. 8. Exemplary CV of a dense $Ni_{93}Pt_7$ film in 1 M NaOH at a scan rate of 100 mV/s and anodic limit of 0.6 V vs Ag|AgCl.
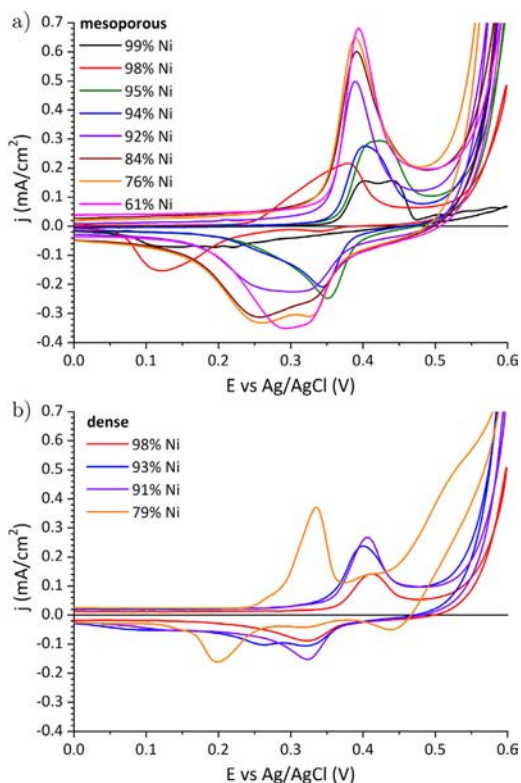
Fig. 9. CVs of (a) mesoporous and (b) dense Ni-Pt films with varying composition in 1 M NaOH at a scan rate of 10 mV/s.

Fig. 10. Peak oxidation and reduction current densities of the redox reaction $Ni(OH)_2 \rightleftharpoons NiOOH$ determined by CV in 1 M NaOH versus square root of the scan rate for dense and mesoporous Ni-Pt thin films.
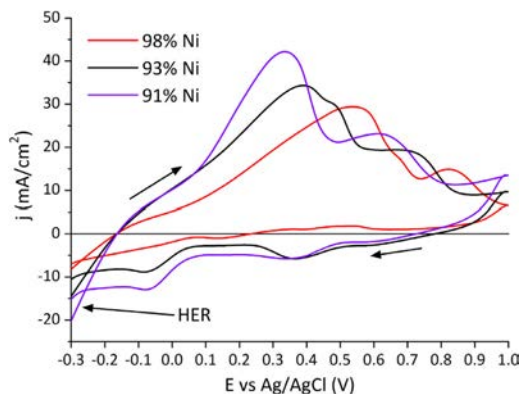
Fig. 11. CVs of dense Ni-Pt films in 0.5 M H_2SO_4 at a scan rate of 100 mV/s. The scan direction is indicated by arrows.

previous study did not reveal significant differences between the different film morphologies [17].

For the mesoporous Ni-Pt films with Ni contents of 84% and lower (i.e. 61%, 76% and 84% Ni), a square root dependency is appreciated between the peak oxidation (and reduction) current density and the scan rate (Fig. 10). The peak current densities were taken from the peaks corresponding to Eq. (2) at approx. 0.4 V (oxidation peak) and 0.3 V (reduction peak). In those cases where

the relationship is linear, the redox reaction is diffusion-controlled by the diffusion of OH^- in solution (cf. Eq. (2)). The highest activity is observed for 76% Ni, the films containing 84% and 61% Ni follow with similar activities. This observation consolidates the assumption that Pt acts as an electrocatalyst for the reaction, and thus there is a certain Pt content at which the electrochemical activity of the surface towards the observed redox reaction between $Ni(OH)_2$ and NiOOH is the most active.

For higher Ni contents, the trend is not linear. Above a certain scan rate of about 80–100 mV/s, the current stagnates, indicating that the kinetics of the redox reaction becomes limited by another factor. The peak reduction currents are generally lower than the corresponding oxidation currents due to the generally wider reduction peaks (cf. Fig. 9). Nevertheless, the trends observed on the reduction part of the reaction are equal to those on the oxidation.

The observed characteristics of the Ni-Pt films may be exploited in application as an electrochemical supercapacitor. Although the current densities are not comparable to those reported for Ni-based electrochemical supercapacitors [33,34], an appropriate anodic oxidation treatment may achieve superior performance, taking advantage of the enhancement provided by the addition of Pt.
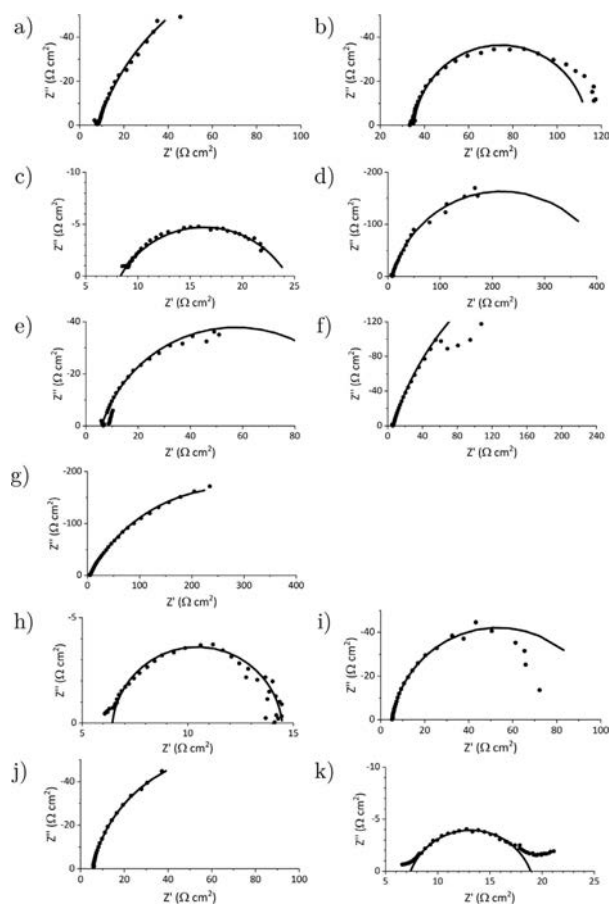
Fig. 12. Nyquist plots for mesoporous (a) $Ni_{99}Pt_1$, (b) $Ni_{98}Pt_2$, (c) $Ni_{95}Pt_5$, (d) $Ni_{94}Pt_6$, (e) $Ni_{92}Pt_8$, (f) $Ni_{76}Pt_{24}$, (g) $Ni_{61}Pt_{39}$, and dense (h) $Ni_{98}Pt_2$, (i) $Ni_{93}Pt_7$, (j) $Ni_{91}Pt_9$, (k) $Ni_{79}Pt_{21}$ thin films in 0.5 M H_2SO_4 at OCP.

3.5. Electrochemical behaviour in H_2SO_4 determined by EMT

Due to the high Ni contents in all films, a dissolution of Ni takes place in sulfuric acid when anodic potentials are applied. In the CVs of the dense films, this dissolution is predominant in the first anodic sweep (Fig. 11). A similar observation had been made during LSV experiments of electrodeposited Ni-P [21]. The observed oxidation is most likely not exclusively the dissolution of Ni (Eq. (3)), which is attributed to the highest oxidation peak for all compositions, but also that of the underlying Cu, which has its standard potential in this potential range and may thus be assigned to the smaller oxidation peak which appears as a shoulder at 0.48 V for 93% Ni and at 0.66 V for 98% Ni [35]. The third, most anodic oxidation peak can be referred to the oxidation or dissolution of Pt [35]. At the very beginning of the anodic sweep, negative currents related to proton reduction (i.e. HER) are clearly observed, suggesting that hydrogen adatoms form on the surface and are subsequently oxidised (Eq. (4)), thus contributing to the oxidation current as well, especially at very low anodic potentials.

$$Ni \longrightarrow Ni^{2+} + 2e^- \qquad (3)$$

$$H_{ad} \longrightarrow H^+ + e^- \qquad (4)$$

Interestingly, the oxidation waves shift to more anodic potentials with increasing Ni content of the films. Hence, the alloying of higher amounts of Pt with Ni increases the surface activity for electrochemical reactions, as seen before, but also accelerates the dissolution of the material in acidic media under anodic polarisation. For the mesoporous films, the dissolution processes were faster and immediately exposed the Cu seed layer which was dissolved simultaneously. This prevented a detailed analysis of the anodic processes taking place in sulfuric acid. In any case, an anodic polarisation of the Ni-Pt films in sulfuric acid leads to dissolution and failure of the films and must be avoided in application.

3.6. EIS analyses by EMT

Fig. 12 shows the Nyquist plots for both mesoporous and dense Ni-Pt films after EIS at OCP in acidic media. In general, the impedance increases with the Pt content.

The fitting for the EIS spectra was done by simulating an electrical equivalent circuit with the solution resistance R_s, in series with a parallel circuit of the charge-transfer resistance R_{ct} and the double-layer capacitance C_{dl}, whose behaviour is modelled by a constant phase element (CPE), and represents a simplified Randles circuit (Fig. 13) [36]. This model was used for the fitting of the
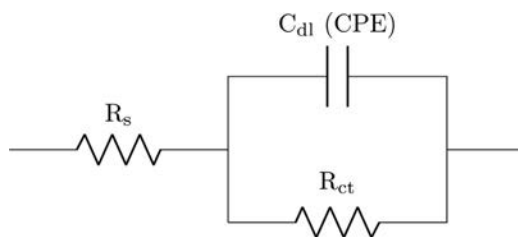
Fig. 13. Electrical equivalent circuit used for the fitting of EIS spectra of the Ni-Pt films.

Table 2
Solution resistance R_s, charge-transfer resistance R_{ct} and double-layer capacitance C_{dl} determined by fitting of the EIS spectra for mesoporous and dense Ni-Pt films.

composition	R_s Ω cm^2	R_{ct} Ω cm^2	C_{dl} mF/cm^2
mesoporous			
$Ni_{99}Pt_1$	8.2 ± 1.5	200 ± 40	3.5 ± 0.6
$Ni_{98}Pt_2$	35 ± 2	79 ± 5	27 ± 2
$Ni_{95}Pt_5$	8.3 ± 0.5	16 ± 1	31 ± 2
$Ni_{94}Pt_6$	8.4 ± 0.3	420 ± 20	12 ± 1
$Ni_{92}Pt_8$	6.0 ± 0.3	100 ± 10	46 ± 2
$Ni_{76}Pt_{24}$	6.1 ± 0.1	650 ± 10	41 ± 1
$Ni_{61}Pt_{39}$	4.9 ± 0.1	550 ± 20	40 ± 1
dense			
$Ni_{98}Pt_2$	6.4 ± 0.3	8.0 ± 0.3	15 ± 1
$Ni_{93}Pt_7$	5.3 ± 0.1	96 ± 2	17 ± 1
$Ni_{91}Pt_9$	5.4 ± 0.2	130 ± 10	26 ± 1
$Ni_{79}Pt_{21}$	7.4 ± 0.3	12 ± 1	4.6 ± 0.2

spectra acquired in 0.5 M H_2SO_4 at OCP of all mesoporous and dense Ni-Pt films.

The results of the fitting show that, expectably, the solution resistance is similar in all cases, except for $Ni_{98}Pt_2$ (Table 2). The determined charge-transfer resistance is generally higher for the mesoporous films, indicating that those are more resistant to corrosion than the dense films. This is a counter-intuitive result, suggesting that an increase in the surface area does not lower the corrosion resistance of the Ni-Pt thin films. The highest charge-transfer resistances is found for mesoporous $Ni_{76}Pt_{24}$ and $Ni_{61}Pt_{39}$. The double-layer capacitance, which depends mainly on the surface area and the surface composition, indicates an increase with the Pt content and is generally higher for mesoporous the films, although this difference is relatively low and may be related to the minor differences in ECSA observed [17].

The Bode plots show that the general behaviour of the mesoporous Ni-Pt films is very similar, the main differences lying in the magnitude of both impedance and phase (Fig. 14).

At high frequencies, the impedance follows a composition dependence, increasing with Ni content. The frequency dependence of the phase angle shows a shift of the maximum phase angle towards lower frequencies with the Pt content, indicating an increase in capacitance.

Metikoš-Huković et al. compared sputter-deposited nanocrystalline Ni with electrodeposited Ni by EIS during HER in alkaline media, finding that the electrodeposited Ni films exhibited higher Faradaic resistance and significantly lower double-layer capacitance in the order of 1 μF/cm^2 [37]. Krstajić et al. investigated the impedance of Ni at HER in NaOH and found that the impedance decreased when the HER potential was made more negative, reaching impedance values much lower than those reported here, and thus indicate that the impedance at potentials where HER takes place is significantly lower than at corrosion potential. The observed C_{dl} was in the order of 100 μF/cm^2 [38]. Perez
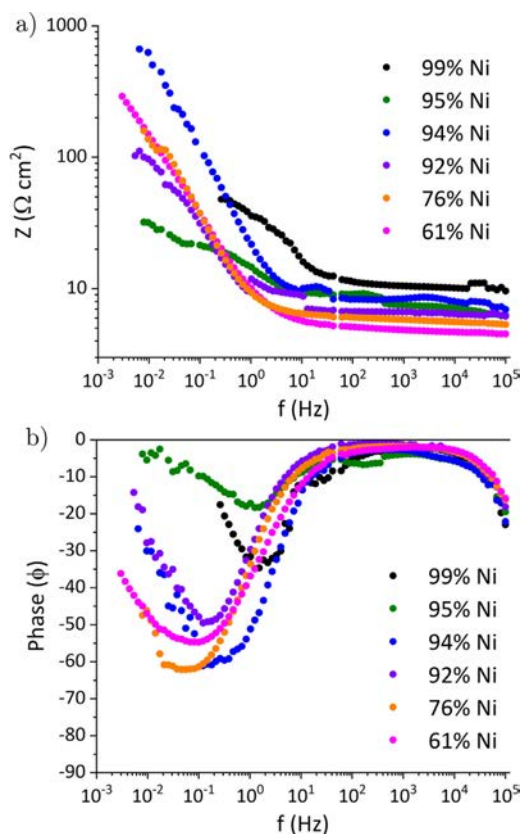
Fig. 14. Impedance (a) and phase angle (b) as a function of the frequency in EIS for mesoporous Ni-Pt films.

et al. conducted a similar study when investigating the oxygen reduction reaction (ORR) on Pt both in NaOH and H_2SO_4. A minimum of the impedance at a certain ORR potential was observed, again showing that impedance is lower when the material is employed in its function as a catalyst [39]. Juskowiak-Brenska et al. found that for electrodeposited Ni coatings the charge-transfer resistance in acidic media decreased significantly when the coating thickness was decreased, yielding 20 Ω cm^2 for thickness of 1 μm [40]. In comparison, the mesoporous Ni-Pt films presented here show superior R_{ct} considering their thickness of 200–300 nm.

SEM/EDX analyses after EIS show that the Ni/Pt ratio decreased, i.e. a leaching of Ni has taken place in all Ni-Pt films, and indicate that the electrochemical process observed in EIS is dominated by the dissolution of Ni. A good stability of the Ni-Pt films in absence of external polarisation can therefore not be guaranteed, i.e. the Ni-Pt films may only be able to serve reliably at HER in 0.5 M H_2SO_4 as long as it is cathodically polarised, i.e. under cathodic protection.

Indeed, a parallel experiment which consisted in an incubation of the mesoporous Ni-Pt films in 0.5 M H_2SO_4 resulted in the leaching of Ni, which was less pronounced when the Pt content was higher. For $Ni_{95}Pt_5$, the leaching of Ni was 23 ± 3% in mass with respect to the total mass of the Ni-Pt film, while this value amounted to 17 ± 3% for both $Ni_{92}Pt_8$ and $Ni_{84}Pt_{16}$. Alia et al. found that Ni-Pt nanowires did not present any leaching of

Ni when the Pt content was above 75% in mass, corresponding to about 47 at% [41].

4. Conclusions

The investigated electrodeposited Ni-Pt is a multifunctional alloy which may serve both in alkaline and acidic environments, provided that a reducing potential is applied when working in acidic conditions.

Due to the observed reversible redox reaction $Ni(OH)_2 \rightleftharpoons NiOOH$ in NaOH, the Ni-Pt thin films with Ni contents of 84% and lower may be used in the charge and discharge of batteries as well as supercapacitors, where electrical charge can be stored in the form of chemical bonds, and very high currents can be retrieved [33,34,42].

On the other hand, it was observed that the HER in 0.5 M H_2SO_4 is stable and reproducible up to 200 LSV cycles, however, anodic polarisation as well as an absence of polarisation at OCP will lead to leaching of Ni into the sulfuric acid. In long-term HER operation at -10 mA/cm^2, an increase in potential is recorded, although stabilising over time. The higher the Pt content of the alloy, the lower was the resulting increase in potential. Interestingly, the mesoporous Ni-Pt films seem more resistant to corrosion, the corrosion resistance increasing roughly with the Pt content. The films showing the highest resistance to corrosion in sulfuric acid, and at the same time a very high activity at the redox reaction $Ni(OH)_2 \rightleftharpoons NiOOH$, are mesoporous $Ni_{76}Pt_{24}$ and $Ni_{61}Pt_{39}$.

Since in an application such as a PEMFC, the leaching of Ni will most likely lead to a degradation in the fuel cell performance, two approaches may be used to overcome this phenomenon: using a higher Pt-content alloy to minimise the dealloying effect, or, secondly, a dual-layer structure of the catalyst with a Pt-Ni alloy catalyst layer stacked onto a Pt catalyst layer [43].

Declaration of Competing Interest

The authors declare that they have no known competing financial interests or personal relationships that could have appeared to influence the work reported in this paper.

CRediT authorship contribution statement

Konrad Eiler: Conceptualization, Validation, Formal analysis, Investigation, Data curation, Writing - original draft, Writing - review & editing, Visualization. **Halina Krawiec:** Conceptualization, Methodology, Resources, Writing - review & editing, Supervision, Funding acquisition. **Iryna Kozina:** Conceptualization, Validation, Resources. **Jordi Sort:** Resources, Writing - review & editing, Supervision, Funding acquisition. **Eva Pellicer:** Conceptualization, Methodology, Validation, Resources, Writing - review & editing, Supervision, Project administration, Funding acquisition.

Acknowledgement

References

[1] Y. Nie, L. Li, Z. Wei, Recent advancements in Pt and Pt-free catalysts for oxygen reduction reaction, Chem. Soc. Rev. 44 (2015) 2168.

[2] S.A. Sherif, F. Barbir, T.N. Veziroglu, Wind energy and the hydrogen economy—review of the technology, Solar Energy 78 (2005) 647.

[3] S. Marini, P. Salvi, P. Nelli, R. Pesenti, M. Villa, M. Berrettoni, G. Zangari, Y. Kiros, Advanced alkaline water electrolysis, Electrochim. Acta 82 (2012) 384.

[4] M. Zeng, Y. Li, Recent advances in heterogeneous electrocatalysts for the hydrogen evolution reaction, J. Mater. Chem. A 3 (2015) 14942.

[5] S.M. Alia, Y.S. Yan, B.S. Pivovar, Galvanic displacement as a route to highly active and durable extended surface electrocatalysts, Catal. Sci. Technol. 4 (2014) 3589.

[6] J. Zheng, Seawater splitting for high-efficiency hydrogen evolution by alloyed PtNi$_x$ electrocatalysts, Appl. Surf. Sci. 413 (2017) 360.

[7] J.D. Guttenplan, Corrosion in the electronics industry, ASM Handbook, 13, ASM Intl., 1987.

[8] J. Mazia, D.S. Lashmore, Electroplated coatings, ASM Handbook, 13, ASM Intl., 1987.

[9] S.A. Gamboa, J.G. Gonzalez-Rodriguez, E. Valenzuela, B. Campillo, P.J. Sebastian, A. Reyes-Rojas, Evaluation of the corrosion resistance of Ni-Co-B coatings in simulated PEMFC environment, Electrochim. Acta 51 (2006) 4045.

[10] W. Wang, L. Yang, F. Qu, Z. Liu, G. Du, A.M. Asiri, Y. Yao, L. Chen, X. Sun, A self-supported NiMoS$_4$ nanoarray as an efficient 3D cathode for the alkaline hydrogen evolution reaction, J. Mater. Chem. A 5 (2017) 16585.

[11] L. Zhang, X. Ren, X. Guo, Z. Liu, A.M. Asiri, B. Li, L. Chen, X. Sun, Efficient hydrogen evolution electrocatalysis at alkaline pH by interface engineering of Ni$_2$P–CeO$_2$, Inorg. Chem. 57 (2018) 548.

[12] L. Xie, F. Qu, Z. Liu, X. Ren, S. Hao, R. Ge, G. Du, A.M. Asiri, X. Sun, L. Chen, In situ formation of a 3D core/shell structured Ni$_3$N@Ni–Bi nanosheet array: an efficient non-noble-metal bifunctional electrocatalyst toward full water splitting under near-neutral conditions, J. Mater. Chem. A 5 (2017) 7806.

[13] C. Tang, R. Zhang, W. Lu, Z. Wang, D. Liu, S. Hao, G. Du, A.M. Asiri, X. Sun, Energy-saving electrolytic hydrogen generation: Ni$_2$P nanoarray as a high-performance non-noble-metal electrocatalyst, Angew. Chem. Int. Ed. 56 (2017) 842.

[14] B. Craig, Hydrogen damage, in: S. Cramer, B. Covino, Jr. (Eds.), ASM Handbook, 13A, ASM Intl., 2003, p. 367.

[15] J. Fidelle, R. Bernardi, R. Broudeur, C. Roux, M. Rapin, Disk pressure testing of hydrogen environment embrittlement, in: L. Raymond (Ed.), Hydrogen Embrittlement Testing, ASTM Intl., 1974, p. 221.

[16] L. Raymond, Evaluation of hydrogen embrittlement, ASM Handbook, 13, ASM Intl., 1987.

[17] K. Eiler, S. Suriñach, J. Sort, E. Pellicer, Mesoporous Ni-rich Ni-Pt thin films: Electrodeposition, characterization and performance toward hydrogen evolution reaction in acidic media, Appl. Catal. B 265 (2020) 118597.

[18] S. Sui, X. Wang, X. Zhou, Y. Su, S. Riffat, C. Liu, A comprehensive review of Pt electrocatalysts for the oxygen reduction reaction: Nanostructure, activity, mechanism and carbon support in PEM fuel cells, J. Mater. Chem. A 5 (2017) 1808.

[19] J.-L. Shui, J.-W. Zhang, J.C.M. Li, Making Pt-shell Pt$_{30}$Ni$_{70}$ nanowires by mild dealloying and heat treatments with little Ni loss, J. Mater. Chem. 21 (2011) 6225.

[20] B.C. Syrett, S. Begum, Corrosion, crevice, Reference Module in Materials Science and Materials Engineering, Elsevier Inc., 2016.

[21] A.R.J. Kucernak, V.N. Naranammalpuram Sundaram, Nickel phosphide: the effect of phosphorus content on hydrogen evolution activity and corrosion resistance in acidic medium, J. Mater. Chem. A 2 (2014) 17435.

[22] K. Eiler, J. Fornell, C. Navarro-Senent, E. Pellicer, J. Sort, Tailoring magnetic and mechanical properties of mesoporous single-phase Ni-Pt films by electrodeposition, Nanoscale 12 (2020) 7749.

[23] H. Krawiec, Z. Szklarz, Combining the electrochemical microcell technique and the electron backscatter diffraction method to study the electrochemical behaviour of polycrystalline aluminium in sodium chloride solution, Electrochim. Acta 203 (2016) 426.

[24] H. Krawiec, V. Vignal, R. Oltra, Use of the electrochemical microcell technique and the svet for monitoring pitting corrosion at MNS inclusions, Electrochem. Commun. 6 (2004) 655.

[25] E. Isarain-Chávez, M.D. Baró, E. Pellicer, J. Sort, Micelle-assisted electrodeposition of highly mesoporous Fe-Pt nodular films with soft magnetic and electrocatalytic properties, Nanoscale 9 (2017) 18081.

[26] Y.-J. Huang, C.-H. Lai, P.-W. Wu, L.-Y. Chen, Ni inverse opals for water electrolysis in an alkaline electrolyte, J. Electrochem. Soc. 157 (2010) P18.

[27] J. Lu, T. Xiong, W. Zhou, L. Yang, Z. Tang, S. Chen, Metal nickel foam as an efficient and stable electrode for hydrogen evolution reaction in acidic electrolyte under reasonable overpotentials, ACS Appl. Mater. Interfaces (8) (2016) 5065.

[28] A. Seghiouer, J. Chevalet, A. Barhoun, F. Lantelme, Electrochemical oxidation of nickel in alkaline solutions: a voltammetric study and modelling, J. Electroanal. Chem. 442 (1998) 113.

[29] W. Visscher, E. Barendrecht, Investigation of thin-film α- and β-Ni(OH)$_2$ electrodes in alkaline solutions, J. Electroanal. Chem. 154 (1983) 69.

[30] M. Vuković, Voltammetry and anodic stability of a hydrous oxide film on a nickel electrode in alkaline solution, J. Appl. Electrochem. 24 (1994) 878–882.

[31] K.A. Striebel, F.R. McLarnon, E.J. Cairns, Oxygen reduction on Pt in aqueous K$_2$CO$_3$ and KOH, J. Electrochem. Soc. 137 (1990) 3351.

[32] R.K. Ahluwalia, D.D. Papadias, N.N. Kariuki, J.-K. Peng, X. Wang, Y. Tsai, D.G. Graczyk, D.J. Myers, Potential dependence of Pt and Co dissolution from platinum-cobalt alloy PEFC catalysts using time-resolved measurements, J. Electrochem. Soc. 165 (2018) F3024.

[33] N. Tokmak, M. Ürgen, Production and characterization of electroactive nickel oxides grown on nickel foam by anodic oxidation in KOH melts for supercapacitor applications, MRS Advances 2 (2017) 3237.

[34] H. Ashassi-Sorkhabi, P. La'le Badakhshan, Electrochemical synthesis of three-

-dimensional porous networks of nickel with different micro-nano structures for the fabrication of Ni/MnO$_x$ nanocomposites with enhanced supercapacitive performance, Appl. Surf. Sci. 419 (2017) 165.

[35] D.C. Harris, Quantitative Chemical Analysis, 7th, W. H. Freeman and Company, NY, 2007.

[36] A. Lasia, A. Rami, Kinetics of hydrogen evolution on nickel electrodes, J. Electroanal. Chem. 294 (1990) 123.

[37] M. Metikoš-Huković, Z. Grubač, N. Radić, A. Tonejc, Sputter deposited nanocrystalline Ni and Ni-W films as catalysts for hydrogen evolution, J. Mol. Catal. A Chem. 249 (2006) 172.

[38] N. Krstajić, M. Popović, B. Grgur, M. Vojnović, D. Šepa, On the kinetics of the hydrogen evolution reaction on nickel in alkaline solution. Part I. The mechanism, J. Electroanal. Chem. 512 (2001) 16–26.

[39] J. Perez, E.R. Gonzalez, E.A. Ticianelli, Oxygen electrocatalysis on thin porous coating rotating platinum electrodes, Electrochim. Acta 44 (1998) 1329.

[40] A. Juskowiak-Brenska, J. Lapinski, D. Pletcher, F.C. Walsh, Porosity of nickel electrodeposits on mild steel using electrochemical impedance spectroscopy, Transactions of the IMF 90 (2012) 156.

[41] S.M. Alia, C. Ngo, S. Shulda, M.-A. Ha, A.A. Dameron, J. Nelson Weker, K.C. Neyerlin, S.S. Kocha, S. Pylypenko, B.S. Pivovar, Exceptional oxygen reduction reaction activity and durability of platinum-nickel nanowires through synthesis and post-treatment optimization, ACS Omega 2 (2017) 1408.

[42] U. Falk, Alkaline storage batteries, in: M. Barak (Ed.), Electrochemical Power Sources: Primary & Secondary Batteries, Institution of Engineers and Peter Peregrinus Ltd., UK and NY, 1980.

[43] W. Li, R. Lin, Y. Yang, One simple method to mitigate the structure degradation of alloy catalyst layer in PEMFC, Electrochim. Acta 323 (2019) 134823.

90

5.4 Oxygen reduction reaction and PEM fuel cell performance of pulse electrodeposited Pt–Ni and Pt–Ni–Mo nanoparticles

Konrad Eiler[a], *Live Mølmen*[b,c], *Lars Fast*[b], *Peter Leisner*[c], *Jordi Sort*[a,d] *and Eva Pellicer*[a]

[a]Departament de Física, Universitat Autònoma de Barcelona, 08193 Bellaterra, Spain

[b]Department of Electrification and Reliability, RISE Research Institutes of Sweden, Borås, Sweden

[c]Department of Materials and Manufacturing, Jönköping University, Sweden

[d]Institució Catalana de Recerca i Estudis Avançats (ICREA), Pg. Lluís Companys 23, 08010 Barcelona, Spain

The following manuscript, which is the result of a joint work on the electrodeposition of Pt alloy NPs at UAB and PEMFC testing during a research stay at RISE, Sweden, is the second work of this collaboration after the review article shown in the Annex. The manuscript is at preparation stage, to be submitted to a suitable journal.

The electrodeposition of Pt–Ni and Pt–Ni–Mo NPs directly onto the carbon cloth electrode of a PEMFC is demonstrated as an approach to simplify the production of ORR electrocatalysts for PEMFC. The electrodeposition on the hydrophobic substrate takes place automatically on its most active spots, leading to very high mass efficiency of the electrocatalyst. The formation of NPs is achieved by pulse electrodeposition using high-current pulses to obtain high amounts of particle nucleation. By variation of the current amplitude, different compositions of Pt–Ni and Pt–Ni–Mo are obtained. The activity at ORR for all compositions is validated at electrochemical cell level, and PEMFC testing including ADT is performed. A very efficient catalyst utilisation is determined, although a higher amount of deposited catalyst is desirable for industrial application.

Oxygen reduction reaction and PEM fuel cell performance of pulse electrodeposited Pt–Ni and Pt–Ni–Mo nanoparticles

K. Eiler[a,1], L. Mølmen[b,c,1], L. Fast[b], P. Leisner[c], J. Sort[a,d], E. Pellicer[a]

[a]*Departament de Física, Universitat Autònoma de Barcelona, 08193 Bellaterra, Spain*
[b]*Department of Electrification and Reliability, RISE Research Institutes of Sweden, Borås, Sweden*
[c]*Department of Materials and Manufacturing, Jönköping University, Sweden*
[d]*Institució Catalana de Recerca i Estudis Avançats (ICREA), Pg. Lluís Companys 23, 08010 Barcelona, Spain*

Abstract

Proton exchange membrane fuel cells (PEMFCs), based on hydrogen energy, are an important alternative to fossil fuels and a complement to batteries for the electrification of vehicles. However, their high cost obstructs commercialisation, and the catalyst material, including its synthesis, constitutes one of the major cost components. In this work, Pt–Ni and Pt–Ni–Mo nanoparticles (NPs) with different compositions have been synthesised in a single step by pulse electrodeposition onto a PEMFC's gas diffusion layer. Both Pt–Ni and Pt–Ni–Mo catalysts exhibit very high mass activities at oxygen reduction reaction (ORR) with very low Pt loadings of around 4 $\mu g/cm^2$. Particle sizes of 40–50 nm and 40–80 nm are obtained for Pt–Ni and Pt–Ni–Mo, respectively. The highest ORR mass activities were found for $Pt_{67}Ni_{33}$ and $Pt_{66}Ni_{32}Mo_2$ NPs.

Keywords: Electrodeposition, oxygen reduction reaction, PEM fuel cell, electrocatalysis, nanoparticle synthesis

1. Introduction

The market for proton exchange membrane fuel cells (PEM-FCs) is growing as the EU has highlighted hydrogen as a key factor in the energy market in their Green Deal plan [1]. One of the ways in which hydrogen shall be used is to power heavy duty vehicles, where large storage capacity and fast refuelling is crucial. To increase the competitivity of such fuel cell electric vehicles (FCEV), the production cost of fuel cells needs to be reduced. The platinum-based electrocatalysts are one of the main cost-determining components, leading to an enormous research interest in the reduction of Pt content. The alloying of Pt is among the different strategies towards this goal [2].

Along with the strive for cost reduction, the durability of the electrocatalysts is a major issue to be tackled. The widely used, commercially available Pt/C catalysts show a number of disadvantages with respect to oxygen reduction reaction (ORR) performance at the cathode of the PEMFC. Apart from their poor efficiency with respect to the Pt loading, their limited durability is a major drawback for reliable long-term application and sustainability. The most investigated and most promising Pt alloy nanoparticles (NPs) tackling these issues are Pt–Co and Pt–Ni NPs [3]. Further improvements are sought by investigation of ternary alloy NPs.

One of the challenges, and an important factor influencing the fuel cell performance, is the synthesis route of the catalyst, which also adds up to the production cost. In most approaches,

the catalyst NPs are synthesised on a carbon support, mixed with a binder and ionomer, and sprayed onto the membrane, which leads to NPs being deposited in locations where they are not accessible for the catalytic reactions [4]. Using direct electrodeposition of Pt alloy NPs onto the gas diffusion layer (GDL) of the PEMFC, the NPs are deposited on the most active sites of the carbon support. Furthermore, this approach combines both synthesis and application (or distribution) of NPs into a single step, providing a cost reduction of the synthesis route [5].

While synthesis of Pt–Ni NPs for ORR [6, 7], as well as the electrodeposition of Pt–Ni alloys in general [8, 9] is well advanced, Mo-containing Pt alloys have been little investigated. Huang et al. showed that the doping of Pt_3Ni NPs with Mo led to extraordinary ORR performance, making the ternary Pt–Ni–Mo system an interesting candidate for ORR studies [10]. The electrochemical co-deposition of Mo, which is usually achieved using sodium molybdate [11], may lead to the formation of intermediate Mo oxide species due to partial reduction of Mo(VI) [12]. However, even NPs containing Mo oxide may eventually show improved electrocatalytic properties [13].

An extensive study on the pulse electrodeposition of Pt NPs for ORR was carried out by Huang et al. [14]. Li et al. deposited Pt-Ni on glassy carbon substrates in a two-step electrochemical process by first electrodepositing Ni, Co, and Ni–Co and then submerged the deposits in a Pt-containing acid to achieve spontaneous galvanic replacement. The highest ORR activity was found for the ternary Pt–Ni–Co catalyst [15]. Sorsa et al. electrodeposited Pt–Ni from liquid crystalline solution onto GDL substrates. In this study, however, no significant improvement of the electrodeposited Pt–Ni over commercial Pt/C was observed [16].

Email addresses: `konrad.eiler@uab.cat` (K. Eiler),
`live.molmen@ri.se` (L. Mølmen), `eva.pellicer@uab.cat` (E. Pellicer)
[1]These authors contributed equally to this work.

In this work, pulse electrodeposition is used to deposit Pt–Ni and Pt–Ni–Mo particles directly onto the microporous layer of a commercial GDL. In this way, all particles are deposited on the most active sites of the carbon support's surface where they guarantee excellent contact with both the support and the proton exchange membrane (PEM) in the fuel cell. The Pt–Ni and Pt–Ni–Mo NPs with different compositions are chemically and structurally characterised, and ORR in acidic media is performed. Finally, fuel cell performance and durability tests in a PEMFC prototype are carried out after hot-pressing the obtained cathodes with the PEM and a commercial Pt/C electrode as anode.

2. Experimental

NP synthesis. The synthesis of Pt–Ni and Pt–Ni–Mo NPs was performed by pulse electrodeposition from aqueous solution in a three-electrode electrochemical cell. An Autolab PGSTAT204 potentiostat/galvanostat was used with a Pt wire as counter electrode (CE), an Ag|AgCl (3 M KCl) reference electrode (RE) and a working electrode (WE). The WE consisted of a 2 cm by 2 cm GDL, supplied by Freudenberg, mounted on a Cu support in order to ensure electrical connection and a homogeneous charge distribution over the entire area of the GDL during electrodeposition. The excessive area of the Cu support was isolated with polyimide tape (Fig. 1).
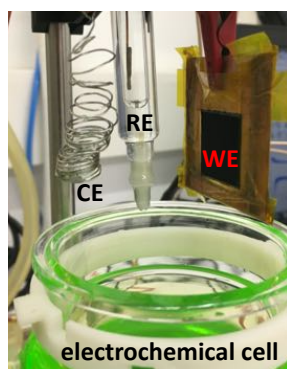
Figure 1: Set-up of the three-electrode electrochemical cell with the Pt counter electrode (CE), Ag|AgCl reference electrode (RE), and the GDL mounted on a Cu plate at the working electrode (WE).

The aqueous electrolytes were loaded with nickel chloride, sodium hexachloroplatinate, boric acid, and ammonium chloride, based on an earlier study [8]. For the deposition of Pt–Ni–Mo, sodium molybdate as well as citric acid as complexing agent were added (Tab. 1).

The electrolytes were studied using vitreous carbon as WE and performing a cyclic voltammetry (CV) between –1.3 V and 1.3 V with respect to the RE in order to determine the regions of reduction and oxidation of all species.

The electrodeposition was carried out in stagnant conditions with pulses of varying current densities in order to obtain different alloy compositions. The choice of pulse deposition pa-

Table 1: Electrolyte composition for the deposition of Pt–Ni and Pt–Ni–Mo NPs

	Pt–Ni	Pt–Ni–Mo
200 mM	$NiCl_2$	$NiCl_2$
5 mM	$Na_2PtCl_6 \cdot 6\,H_2O$	$Na_2PtCl_6 \cdot 6\,H_2O$
200 mM	H_3BO_3	H_3BO_3
25 mM	NH_4Cl	NH_4Cl
50 mM		$Na_2MoO_4 \cdot 2\,H_2O$
100 mM		citric acid

rameters was orientated on the study on the electrodeposition of Pt–Ni NPs carried out by Egetenmeyer et al. [17]. Pulse on-time and off-time were kept constant at 5 ms and 70 ms, respectively, while the number of cycles was changed with the current density in order to obtain identical deposited charges and, assuming similar Faradaic current efficiencies for each electrolyte, similar catalyst loading (Tab. 2). The total charge was increased for the Pt–Ni–Mo deposition due to the addition of citric acid which was observed to compromise the current efficiency. It was also observed during initial studies that higher current densities were needed for the ternary NPs in order to obtain the desired particle size and composition.

Table 2: Conditions for pulse electrodeposition of Pt-Ni and Pt-Ni-Mo NPs

Cathodic peak current density [mA/cm^2]	Number of cylces	Composition
31	240	$Pt_{79}Ni_{21}$
37	200	$Pt_{67}Ni_{33}$
43	170	$Pt_{80}Ni_{20}$
49	150	$Pt_{73}Ni_{27}$
54	920	$Pt_{78}Ni_{21}Mo_1$
77	640	$Pt_{66}Ni_{32}Mo_2$
100	490	$Pt_5Ni_{71}Mo_{24}$
123	440	$Pt_5Ni_{74}Mo_{21}$

For all NPs, the amplitude of the deposition potential increases with the amplitude of the current density (Fig. 2). During pulse deposition of Pt–Ni NPs, the amplitude ranges initially between –1.4 and –2.0 V vs Ag|AgCl depending on the applied current density. This potential drops towards the end of the deposition to within –1.0 to –1.3 V. The potential established during off-time changes from just below 0 V to slightly positive potential. In turn, the potential amplitudes for the deposition of ternary Pt–Ni–Mo NPs ranges from –2.0 V to –4.0 V due to the higher current densities applied. This potential does not change significantly until the end of deposition, while the potential during off-time changes to –0.6 V towards the end, showing a trend which is inverse to the one observed for binary NPs.

Electrochemical characterisation. The identical three-electrode set-up was also used for CV studies of the NP/C assemblies in H_2SO_4 in order to activate the catalysts and to determine their electrochemically active surface area (ECSA). To this end, 30 cycles at 200 mV/s and 5 cycles at 50 mV/s were
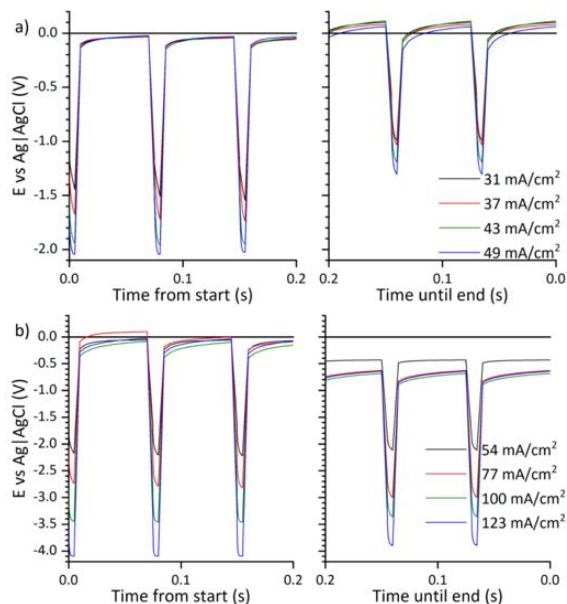
Figure 2: Initial and final pulses for pulse deposition of Pt–Ni (a) and Pt–Ni–Mo (b) NPs.

recorded in a potential window between 0 and 1.3 V vs RHE. ORR was performed by CV in O_2-saturated 0.1 M $HClO_4$ after recording a background CV in N_2-saturated electrolyte, both at 10 mV/s between 0 and 1.1 V vs RHE and in static conditions. The curves were corrected for Ohmic drop (iR-correction) after determination of the instrumentation resistance by electrochemical impedance spectroscopy (EIS) [18]. A Pt/C GDE with a Pt loading of 0.3 mg/cm^2 was tested as a reference.

SEM. All deposited NPs, as well as the unloaded GDL substrate, were analysed by scanning electron microscopy (SEM) on a Zeiss Merlin electron microscope in order to evaluate particle size, distribution, and loading of the substrates, using an acceleration voltage of 1 kV. Particle sizes were determined by image analysis of the SEM micrographs using ImageJ, taking the average of 100–200 particles per sample. SEM was also used for post analysis after PEMFC testing on a TESCAN LYRA3, after the cathode was delaminated from the membrane electrode assembly (MEA). For cross-sectional observation, one MEA was cut, embedded in epoxy resin, mechanically ground and polished and subsequently ion milled by Ar ions on a Gatan PECS II.

TEM. Transmission electron microscopy (TEM) was conducted on a JEOL JEM-2011 for all compositions in high resolution and diffraction mode in order to study the crystalline structure of the nanoparticles. Samples for TEM were prepared by scratching the catalyst NPs, together with part of the carbon support off the electrodes, dispersing the samples in ethanol, and dropping them onto the carbon film of a TEM copper grid.

Chemical analysis. For determination of both composition and loading of the substrates, NPs were dissolved in aqua regia, consisting of hydrochloric acid and nitric acid in a ratio of 3:1 in volume, and the concentration of Pt, Ni and Mo in the solution was determined by ICP-MS on an Agilent 7500ce spectrometer for each variation of electrodeposition parameters. In addition, the Faradaic current efficiency was determined by relating the total charge during electrodeposition to the absolute masses of Pt, Ni, and Mo, and assuming that all metals were fully reduced.

XPS. X-ray photoelectron spectroscopy (XPS) was performed on a PHI 5500 spectroscope to study the surface state of the NPs, recording the core spectra for C1s, Ni2p, Pt4f, and Mo2p, before and after Ar ion sputtering for 30 s. Peak fitting of the spectra was done by the software XPSPEAK.

Fuel cell testing. For the PEMFC testing, the cathodes containing the electrodeposited Pt–Ni and Pt–Ni–Mo NPs were hot-pressed together with a Nafion 212 membrane and a commercial GDE with a Pt loading of 0.3 mg/cm^2 as anode using a pressure of 0.5 MPa at 110 for 3 minutes to form the MEA.

All MEAs were tested in a single cell fuel cell tester using coated stainless steel flow plates. The active area of the fuel cell was 2.9 cm^2. A Greenlight G20 test station was used for PEMFC tests, with a temperature of 80 °C for both gases and a dewpoint temperature of 65 °C. The flow of H_2 and air were 0.042 and 0.10 l$_n$/min, respectively.

The cells were activated by cycling between 0.9 V and 0.6 V for 2 000 cycles before a polarisation curve was obtained. For durability testing, an accelerated stress test (AST) consisting of 20 000 additional cycles were performed, with polarisation curves obtained after 10 000 cycles and at end of test (EoT).

3. Results and discussion

3.1. Characterisation of the as-deposited NPs

Microstructural analysis. The GDL substrates show the typical homogeneous microporous layer, consisting of aggregates of globular carbon particles (Fig. 3a). Fluorine emissions in EDX confirmed the presence of PTFE (not shown).

After the pulse electrodeposition, Pt–Ni and Pt–Ni–Mo NPs are homogeneously distributed on the surface and near-surface region of the microporous layer (Fig. 3). All Pt-Ni NPs show a uniform, spherical shape with an average particle size between 40 nm and 50 nm independent of composition or process parameters (Tab. 3), and are agglomerated in very few cases (Fig. 3b-e). The Pt–Ni–Mo NPs have the tendency to a spherical structure, although less defined and with higher roughness than the Pt–Ni NPs. While the particle size of $Pt_{78}Ni_{21}Mo_1$ is around 80 nm (Fig. 3f), the other ternary alloy NPs lie between 40 nm and 50 nm. For $Pt_5Ni_{74}Mo_{21}$, a mixture of large (>100 nm) and small (<50 nm) NPs is appreciated (Fig. 3i). This observation is in agreement with the large error in particle size determined for this composition (Tab. 3). All other compositions show relatively narrow size distributions (Fig. 4). While commercial Pt/C has significantly smaller particle size, Fouda-Onana et al. electrodeposited Pt particles with a size of 50 nm and found that

despite the larger particle size, the utilisation rate was high due to all particles having triple phase boundaries (TPB) [19].
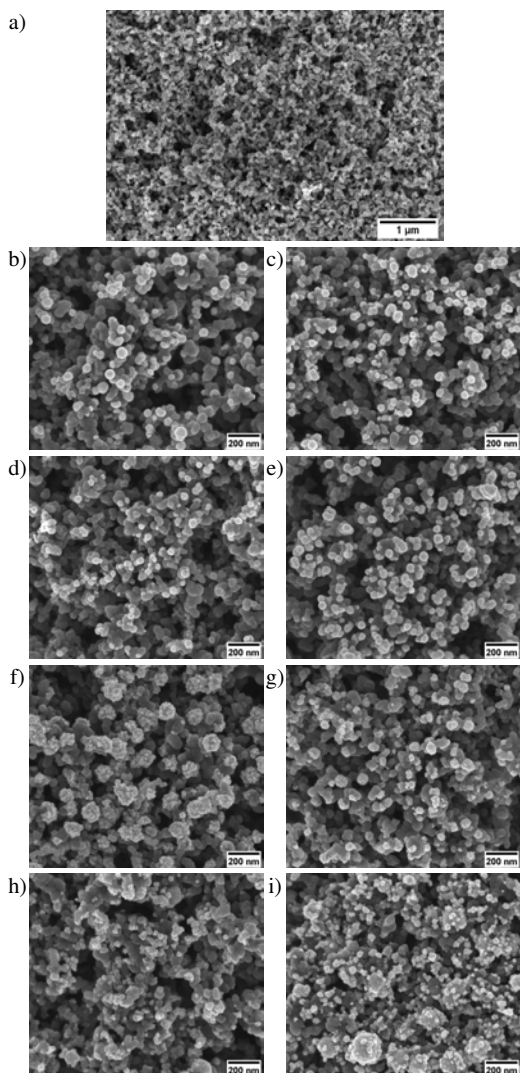
Figure 3: SEM micrographs of GDL substrate (a), electrodeposited binary $Pt_{79}Ni_{21}$ (b), $Pt_{67}Ni_{33}$ (c), $Pt_{80}Ni_{20}$ (d), $Pt_{73}Ni_{27}$ (e), and ternary $Pt_{78}Ni_{21}Mo_1$ (f), $Pt_{66}Ni_{32}Mo_2$ (g), $Pt_5Ni_{71}Mo_{24}$ (h), $Pt_5Ni_{74}Mo_{21}$ (i) NPs on the GDL. In the micrographs, the metallic NPs appear brighter than the microporous carbon.

In TEM observations, the Pt–Ni and Pt–Ni–Mo NPs are clearly distinguished from the C support by phase contrast (Fig. 5a,e). The binary NPs are of well-defined, globular form, while the ternary NPs are more irregular (Fig. 5b,f). The high resolution mode reveals the nanocrystalline structure of Pt–Ni NPs, indicated by diffraction planes with different orientations (Fig. 5c). This nanocrystallinity is also clearly observed in the selected area electron diffraction (SAED) pattern of a single NP with a diameter (ø) <50 nm, where almost any diffraction di-

rection is present, confirmed by the quasi-continuous rings observed in the pattern (Fig. 5d). The corresponding d-spacings match the face-centred cubic (fcc) phase for a Pt–Ni alloy.

The Pt–Ni–Mo NPs, even those with very low Mo content, show more diffuse diffraction rings of the fcc solid solution than the Pt–Ni NPs, and some additional diffraction spots which were not identified and may indicate the presence of a Mo oxide species (Fig. 5h). Diffraction planes are only appreciated at the NPs' surfaces (Fig. 5g).

XPS. The Pt4f spectra of the surfaces of the deposited Pt–Ni NPs, exemplary shown for $Pt_{73}Ni_{27}$, show emissions of metallic Pt at 71.4 eV and of Pt(I) at 72.3 eV, wich can be assigned to platinum hydroxide [20]. In the Ni2p spectra, no contribution of metallic Ni is observed and most superficial Ni is bound in $Ni(OH)_2$ (Fig. 6a, b).

After Ar ion sputtering, the XPS spectra show a contribution of metallic Ni, as well as a higher fraction of metallic Pt with respect to the hydroxide species. It must be noted that, in contrast to bulk material, the contribution of the NPs' surface cannot be eliminated by sputtering. The fractions of the metallic species of both Pt and Ni in the NP cores should therefore be higher than those represented in the XPS spectra before Ar ion sputtering.

For the ternary Pt–Ni–Mo NPs, very similar observations are made with respect to the Pt4f and Ni2p emissions (Fig. 6c, d). The Mo3d detail spectra do not show any evidence of metallic Mo at 228.0 eV [20]. The initial surface state shows the occurrence of Mo(VI) exclusively, which points to the presence of MoO_3. After sputtering, the lower oxidation state Mo(IV) is found, which may correspond to MoO_2 (Fig. 6e). Therefore, Mo(VI) was not fully reduced to Mo(0) in spite of the presence of Ni(II) and citrate in the electrolyte.

3.2. Half-cell electrochemical tests

The GDL substrates exhibit a rather low electric conductivity, leading to a relatively high double-layer capacitance observed in CV. Nevertheless, the hydrogen adsorption (H_{ads}) and desorption peaks (H_{des}) used for the determination of ECSA are well-defined, as shown exemplarily for $Pt_{73}Ni_{27}$ (Fig. 7).

The ECSA of both the Pt–Ni and Pt–Ni–Mo is comparable to what is found in literature (Tab. 3) [2], showing that despite the electrodeposited catalysts having a large particle size, the Pt utilisation is high.

The electrodeposited Pt–Ni and Pt–Ni–Mo NPs all show lower reduction potentials at ORR as compared to the Pt/C (Fig. 8a). Among them, the Mo-containing NPs are inferior to the binary alloy NPs with comparable Pt/Ni ratio. Interestingly, the best performance among the electrodeposited NPs is observed for $Pt_{67}Ni_{33}$.

The advantage of electrodeposited Pt–Ni and Pt–Ni–Mo NPs becomes apparent when the Pt mass activity at ORR is observed (Fig. 8b). $Pt_{67}Ni_{33}$ shows the highest Pt mass activity among the binary NPs. In addition, the Ni-rich ternary NPs, which also have significantly higher amounts of Mo, show the highest mass activity with respect to Pt content. This shows that the addition of Mo does not compromise the catalytic activity and may indeed lead to improvement, however, the stability at
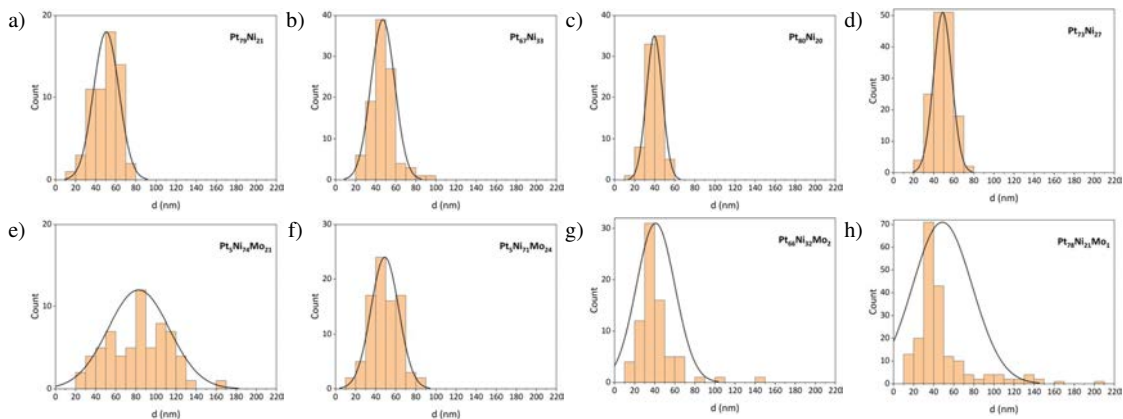
Figure 4: Particle size distribution of $Pt_{79}Ni_{21}$ (a), $Pt_{67}Ni_{33}$ (b), $Pt_{80}Ni_{20}$ (c), $Pt_{73}Ni_{27}$ (d), $Pt_{78}Ni_{21}Mo_1$ (e), $Pt_{66}Ni_{32}Mo_2$ (f), $Pt_5Ni_{71}Mo_{24}$ (g), and $Pt_5Ni_{74}Mo_{21}$ (h) NPs.
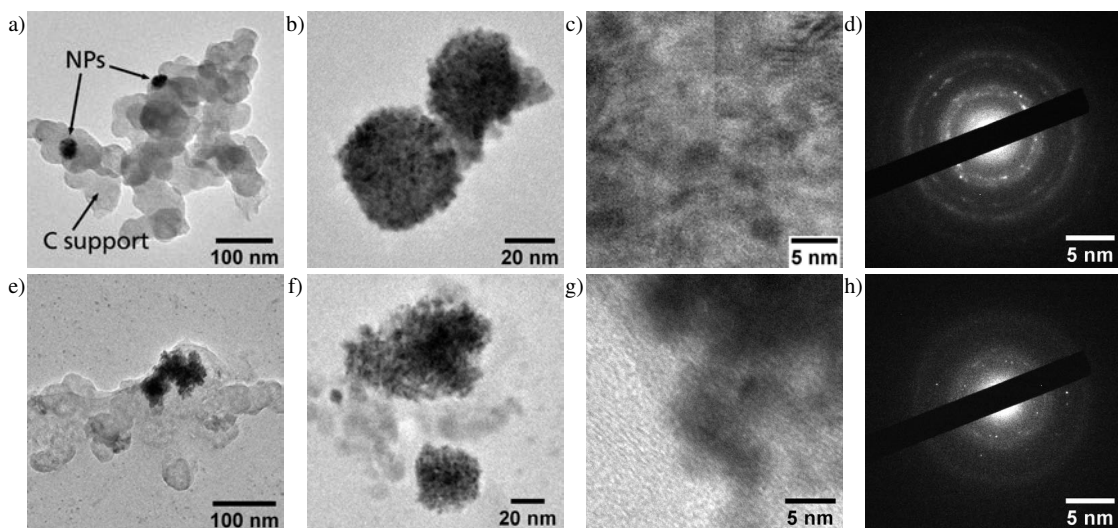
Figure 5: TEM micrographs of C-supported $Pt_{67}Ni_{33}$ (top, a–c) and $Pt_{78}Ni_{21}Mo_1$ (bottom, e–g) NPs (a, b, e, f), in high resolution (c, g) and SAED pattern for a single NP (d, h).

ORR in acidic conditions remains doubtful at this point. Among the Pt-rich ternary NPs, $Pt_{66}Ni_{32}Mo_2$ shows the highest Pt mass activity, corresponding to the Ni/Pt ratio of the binary $Pt_{67}Ni_{33}$.

An increase in total load of electrodeposited NPs on the GDL is expected to increase the half-wave potential at ORR. However, the electrodeposition of higher amounts of catalyst could easily lead to NP growth rather than nucleation of more particles.

Another way of improving the ORR of the electrodeposited NPs is by addition of an ionomer such as Nafion, which can lead to a significant increase in ECSA and ORR performance [21].

In terms of kinetics, the determined Tafel slopes (b) show a significant improvement with respect to the commercial Pt/C electrode, for which a Tafel slope of 103 mV is obtained. In-

terestingly, all binary Pt–Ni binary alloy NPs exhibit an almost identical Tafel slope of 65–66 mV (cf. Tab. 3). The ternary Pt–Ni–Mo alloys show a higher spread in b, where $Pt_{66}Ni_{32}Mo_2$ has the lowest Tafel slope of 62 mV (Fig. 9).

3.3. PEMFC testing

The cross-sectional image of a hot-pressed MEA prior to testing in the fuel cell shows that the catalyst layer (CL) is homogeneous and well adhered to the membrane, ensuring proton conductivity (Fig. 10).

The polarisation curves show that the low catalyst loading results in low current density (not shown). However, the catalysts activity is similar independent of composition, both initially and after AST. Interestingly, the $Pt_{67}Ni_{33}$ and $Pt_{66}Ni_{32}Mo_2$ again

Table 3: Summary of the determined parameters for Pt–Ni and Pt–Ni–Mo NPs. NP size at beginning of test (BoT) and end of test (EoT), total metal catalyst and Pt loadings, and electrochemically active surface area (ECSA) calculated with respect to mass of Pt

Composition	Mean ⌀ BoT	Mean ⌀ EoT	Catalyst loading	Pt loading	Current efficiency	ECSA	b
	nm	nm	$\mu g/cm^2$	$\mu g/cm^2$	%	m^2/g_{Pt}	mV
$Pt_{79}Ni_{21}$	50±13	46±19	4.0	3.7	23	36	66
$Pt_{67}Ni_{33}$	47±12	44±20	4.6	4.0	26	19	65
$Pt_{80}Ni_{20}$	40±8	46±20	4.4	4.1	25	40	65
$Pt_{73}Ni_{27}$	49±9	38±17	4.4	4.0	25	34	66
$Pt_{78}Ni_{21}Mo_1$	83±30	45±24	8.1	7.4	7	28	66
$Pt_{66}Ni_{32}Mo_2$	49±14	26±14	2.5	2.2	2	18	62
$Pt_5Ni_{71}Mo_{24}$	41±19	24±12	7.2	0.9	12	25	72
$Pt_5Ni_{74}Mo_{21}$	49±30	17±9	5.6	0.8	8	88	82
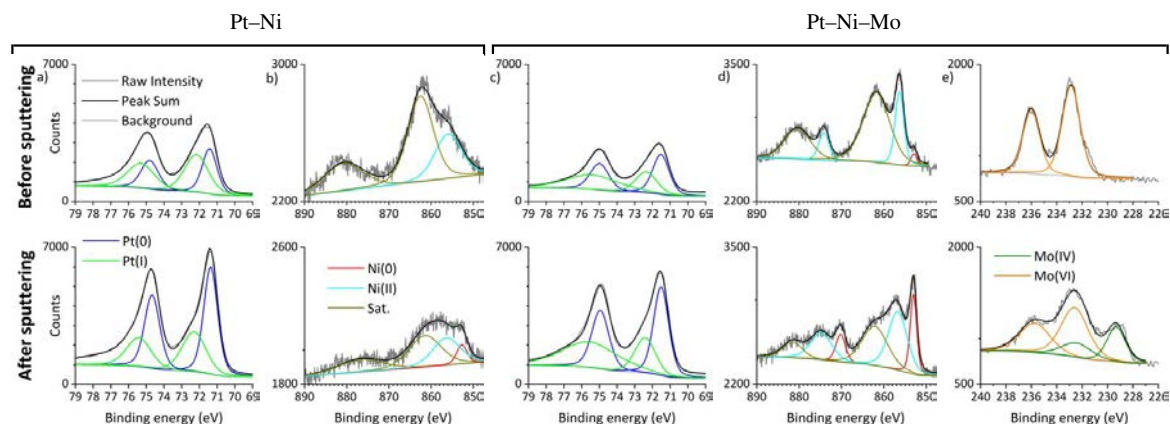
Figure 6: XPS detail spectra of Pt4f (a) and Ni2p (b) of $Pt_{73}Ni_{27}$ NPs and of Pt4f (c), Ni2p (d) and Mo3d (e) of $Pt_5Ni_{71}Mo_{24}$ NPs before (top) and after sputtering (bottom)
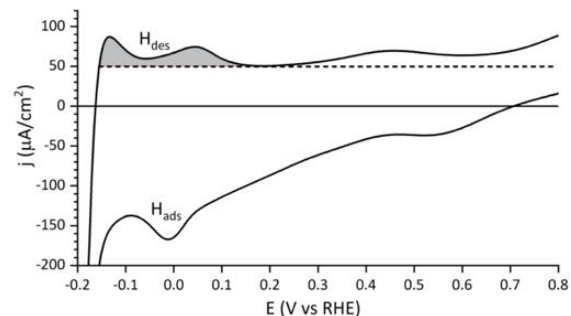
Figure 7: Representative CV of GDL-supported $Pt_{73}Ni_{27}$ in 0.5 M H_2SO_4 for the determination of ECSA. The integrated area of the hydrogen desorption peak is displayed in grey.

show the highest activity. The major drop in PEMFC performance takes place during the first 10 000 cycles, while there is not as significant drop from 10 000 to 20 000 AST cycles (Fig. 11). This is in accordance with literature [2], and can be explained by the dissolution of unstable catalytic sites, such as surface Ni and Mo in the initial half of the AST, leaving the particles more stable in the second half of the AST.

The SEM micrographs of the NPs after AST in the PEMFC show that the particle size in general is reduced (Fig. 12). The exception is $Pt_{80}Ni_{20}$, where the particle size is slightly increased (Tab. 3). The particle size increase can be explained by Pt dissolution from smaller, less stable particles, and re–deposition onto larger particles. It should be noticed that some particles are attached to the membrane after disassembling the MEA. The Pt–Ni samples have kept their spherical morphology, while the Pt–Ni–Mo have increased roughness after testing. It is also clear that the two samples with very low Pt loading experience the most severe dissolution of catalyst material. However, the PEMFC performance at EoT is similar to the other samples. This may be due to the high surface area endowed by the rough morphology of these NPs.

4. Conclusions

Binary Pt–Ni and ternary Pt–Ni–Mo NPs were successfully synthesised by pulse electrodeposition from aqueous media di-
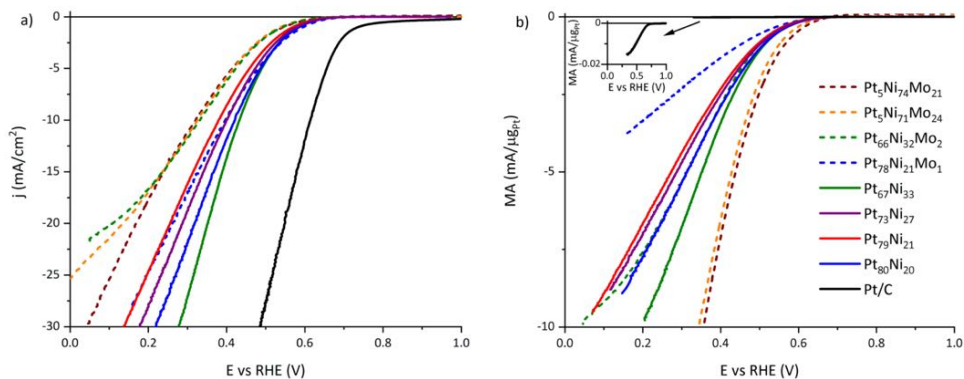
Figure 8: ORR of Pt–Ni and Pt–Ni–Mo NPs deposited on GDL in comparison with Pt/C, by geometric current density (a) and by Pt mass activity (b). The inset in (b) shows the mass activity for the Pt/C electrode.
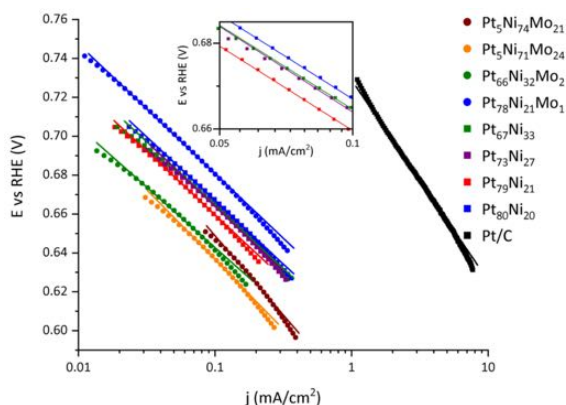
Figure 9: Tafel slopes for the GDL-supported Pt–Ni and Pt–Ni–Mo NPs, and for commercial Pt/C. The inset shows a zoom for the closely-placed Pt–Ni NP electrocatalysts.

rectly onto the GDL for a PEMFC. The so-prepared carbon-supported catalysts show high specific activities and the applicability in PEMFC was demonstrated in a single–cell, with $Pt_{67}Ni_{33}$ and $Pt_{66}Ni_{32}Mo_2$ showing the highest activity both in ORR measurements and in the PEMFC. However, a higher total amount of catalyst is needed for practical applications, either by increasing the Pt load in electrodeposition or by increasing the fuel cell's active area. Further optimisation is possible by tuning particle size.

With respect to the ternary alloy NPs, an obvious advantage over binary Pt–Ni NPs is not observed. Since Mo was mostly found in an oxidised state and the crystallinity of the ternary NPs as observed by SAED was lower, the question remains open as to whether a true, metallic ternary alloy would yield superior ORR activity.

Overall, the demonstrated electrodeposition process provides a promising alternative to the conventional methods of ORR electrocatalyst synthesis. In addition to the facile synthesis
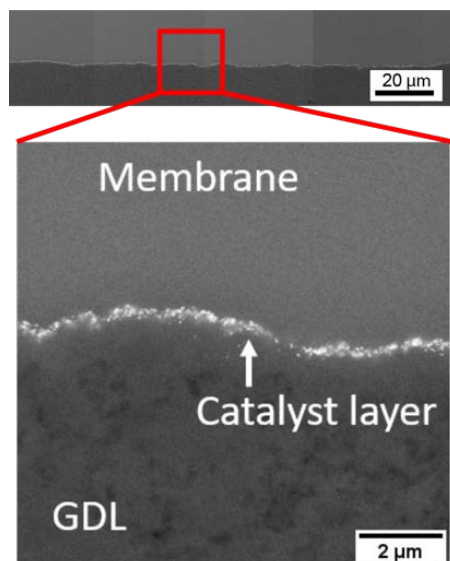
Figure 10: Back-scattered electron micrograph of a cross section of hot-pressed $Pt_{66}Ni_{32}Mo_2$ MEA prior to PEMFC testing.

which applies the catalyst NPs directly onto the GDL, the utilisation of the metal electrocatalyst can be seen as close to 100%.
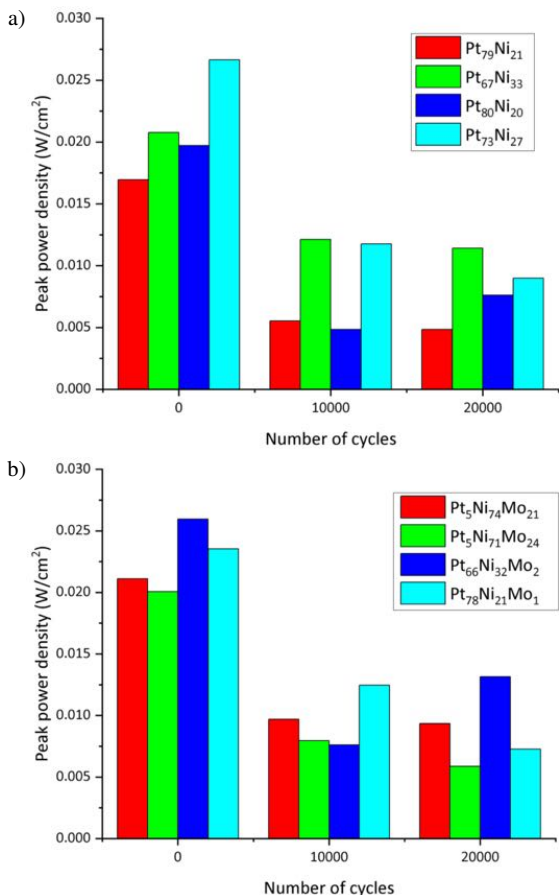
Figure 11: Peak power density of Pt–Ni (a) and Pt–Ni–Mo catalysts (b) after activation, 10 000, and 20 000 AST cycles.

Figure 12: SEM micrographs of $Pt_{79}Ni_{21}$ (a), $Pt_{67}Ni_{33}$ (b), $Pt_{80}Ni_{20}$ (c), $Pt_{73}Ni_{27}$ (d), $Pt_{78}Ni_{21}Mo_1$ (e), $Pt_{66}Ni_{32}Mo_2$ (f), $Pt_5Ni_{71}Mo_{24}$ (g), and $Pt_5Ni_{74}Mo_{21}$ (h) NPs on the GDL after AST in the PEMFC.

References

[1] European Commission, A hydrogen strategy for a climate-neutral Europe, COM(2020) 301 final (2020).

[2] L. Mølmen, K. Eiler, L. Fast, P. Leisner, E. Pellicer, Recent advances in catalyst materials for proton exchange membrane fuel cells, APL Mater. 9 (2021) 040702.

[3] K. Kodama, T. Nagai, A. Kuwaki, R. Jinnouchi, Y. Morimoto, Challenges in applying highly active Pt-based nanostructured catalysts for oxygen reduction reactions to fuel cell vehicles, Nat. Nanotechnol. 16 (2021) 140.

[4] J. Hou, M. Yang, C. Ke, G. Wei, C. Priest, Z. Qiao, G. Wu, J. Zhang, Platinum-group-metal catalysts for proton exchange membrane fuel cells: From catalyst design to electrode structure optimization, EnergyChem 2 (2020) 100023.

[5] A. Egetenmeyer, I. Radev, D. Durneata, M. Baumgärtner, V. Peinecke, H. Natter, R. Hempelmann, Pulse electrodeposited cathode catalyst layers for pem fuel cells, Int. J. Hydrog. Energy 42 (2017) 13649.

[6] E. Antolini, The oxygen reduction on Pt-Ni and Pt-Ni-M catalysts for low-temperature acidic fuel cells: A review, Int. J. Energy Res. 42 (2018) 3747.

[7] X. Tian, X. Zhao, Y.-Q. Su, L. Wang, H. Wang, D. Dang, B. Chi, H. Liu, E. J. M. Hensen, X. W. Lou, B. Y. Xia, Engineering bunched Pt-Ni alloy nanocages for efficient oxygen reduction in practical fuel cells, Science 366 (2019) 850.

[8] K. Eiler, S. Suriñach, J. Sort, E. Pellicer, Mesoporous Ni-rich Ni-Pt thin films: Electrodeposition, characterization and performance toward hydrogen evolution reaction in acidic media, Appl. Catal. B 265 (2020) 118597.

[9] Y. Liu, C. M. Hangarter, U. Bertocci, T. P. Moffat, Oxygen reduction reaction on electrodeposited $Pt_{100-x}Ni_x$: influence of alloy composition and dealloying, J. Phys. Chem. C 116 (2012) 7848.

[10] X. Huang, Z. Zhao, L. Cao, Y. Chen, E. Zhu, Z. Lin, M. Li, A. Yan, A. Zettl, Y. M. Wang, X. Duan, T. Mueller, Y. Huang, High-performance transition metal-doped Pt₃Ni octahedra for oxygen reduction reaction, Science 12 (2015) 1230.

[11] E. Chassaing, N. Portail, A.-F. Levy, G. Wang, Characterisation of electrodeposited nanocrystalline Ni–Mo alloys, J. Appl. Electrochem. 34 (2004) 1085.

[12] E. Gómez, E. Pellicer, E. Vallés, Intermediate molybdenum oxides involved in binary and ternary induced electrodeposition, J. Electroanal. Chem. 580 (2005) 238.

[13] Z. Liu, J. E. Hu, Q. Wang, K. Gaskell, A. I. Frenkel, G. S. Jackson, B. Eich-

horn, PtMo alloy and MoO_x@Pt core-shell nanoparticles as highly CO-tolerant electrocatalysts, J. Am. Chem. Soc. 131 (2009) 6924.

[14] C. Huang, C. B. Odetola, M. Rodgers, Nanoparticle seeded pulse electrodeposition for preparing high performance Pt/C electrocatalysts, Appl. Catal. A 499 (2015) 55.

[15] M. Li, Y. Lei, N. Sheng, T. Ohtsuka, Preparation of low-platinum-content platinum-nickel, platinum-cobalt binary alloy and platinum-nickel-cobalt ternary alloy catalysts for oxygen reduction reaction in polymer electrolyte fuel cells, J. Power Sources 294 (2015) 420.

[16] O. Sorsa, H. Romar, U. Lassi, T. Kallio, Co-electrodeposited mesoporous PtM (M=Co, Ni, Cu) as an active catalyst for oxygen reduction reaction in a polymer electrolyte membrane fuel cell, Electrochim. Acta 230 (2017) 49.

[17] A. Egetenmeyer, M. Baumgärtner, T. Linckh, D. Durneata, H. Natter, R. Hempelmann, I. Radev, V. Peinecke, Pulse electrodeposition of catalyst nanoparticles for application in PEM fuel cells, Trans. IMF 95 (2017) 9.

[18] C. Wei, R. R. Rao, J. Peng, B. Huang, I. E. L. Stephens, M. Risch, Z. J. Xu, Y. Shao-Horn, Recommendation practices and benchmark activity for hydrogen and oxygen electrocatalysis in water splitting and fuel cells, Adv. Mater. 31 (2019) 1806296.

[19] F. Fouda-Onana, N. Guillet, A. M. Almayouf, Modified pulse electrodeposition of Pt nanocatalyst as high-performance electrode for PEMFC, J. Power Sources 271 (2014) 401.

[20] J. F. Moulder, W. F. Stickle, P. E. Sobol, K. D. Bomben, Handbook of X-ray photoelectron spectroscopy, Physical Electronics, Inc., MI, 1995.

[21] P. Mardle, G. Thirunavukkarasu, S. Guan, Y.-L. Chiu, S. Du, Comparative study of PtNi nanowire array electrodes toward oxygen reduction reaction by half-cell measurement and PEMFC test, ACS Appl. Mater. Interfaces 12 (2020) 42832.

6 General discussion

In the following, the main strengths and weaknesses of the work are highlighted. Since the discussion of the individual results is found in the respective articles, this chapter is intended to discuss the overall results in a broader perspective including thoughts on upscaling and industrial application.

In electrocatalysis in general, the main requirements for a new catalyst are its energy efficiency, its durability, and its initial cost. The latter is composed of the material cost and the cost of the synthesis process. Electrodeposition is a generally facile and cost-efficient synthesis method, which in this work is kept highly efficient due to very short electrodeposition times at the minute scale, a high reusability of the electrolyte which can be stored and reused multiple times, and a low amount of additives which are necessary to provide high quality and reproducibility. Another cost-reducing factor in electrodeposition is the direct deposition of the catalyst onto a suitable substrate which can be readily adapted to the respective application, and is advantageous especially for the PEMFC where the catalyst NPs are, in addition, deposited onto the most active sites of the substrate. In the case of HER, the use of flat substrates can easily be extended to macroscopically porous substrates such as commercial metallic foams in order to multiply the electrocatalyst's surface area. For this purpose, the employment of potentiostatic deposition, which is independent of the not easily determinable substrate area, becomes especially valuable.

In the case of pulse deposition, however, which was employed for the synthesis of Pt alloy NPs, a potentiodynamic control in combination with pulses in the millisecond range does not seem fully reliable. For potential control, the potential needs to be read with the use of a RE and may lead to delays in the same time range. In fact, most published works where pulse deposition with millisecond pulses is performed rely on current control. The same was thus employed in this work in order to apply the electrodeposition conditions with higher accuracy. Although the carbon substrates used are openly porous, their reasonably high two-dimensional electrode area provides good repeatability between individual samples. A determination of the actual current density passed through the substrates is, however, not possible.

While the pulse electrodeposited Pt–Ni particles are single-phase, the Mo species in Pt–Ni–Mo NPs are not fully reduced and hint to the existence of a Mo(IV) oxide. The more irregular, rougher shape of Pt–Ni–Mo NPs, and their lower crystallinity with respect to Pt–Ni NPs, can be attributed to the occurrence of amorphous Mo species. A noticeable improvement of the catalytic properties or durability due to the addition of Mo, as documented by literature, was not observed. Since Mo is known to increase the corrosion resistance of Ni in acidic media, it may be more beneficial for Ni-rich alloys, such as in ternary Ni–Pt–Mo thin films for HER in acidic media.

The variation of the current amplitude in pulse electrodeposition does not result in a coherent trend in composition of the NPs, although the composition is altered by the current amplitude. Yet, the targeted compositional range was readily obtained for Pt–Ni NPs. The pulse electrodeposition of the ternary system Pt–Ni–Mo is more complex and does not follow the same trends as the binary Pt–Ni system, which is primarily seen in the much lower Faradaic current efficiency of the ternary system. With stepwise alteration of the current amplitude, a sudden increase of Mo content is observed, coinciding with a drastic change in Ni (increase) and Pt content (decrease). In conclusion, the activation-controlled regime for Mo seems to be very narrow and almost directly passes on to diffusion control when the current density is increased. In addition, since the electrodeposition of Mo is only possible together with Ni as inductor metal, an effective co-deposition of Mo may only be possible for alloys with high contents of Ni. Electrodeposition of a Pt-rich alloy with targeted composition below 30 at% Ni and 5–10 at% Mo seems therefore little promising.

The reduction of material cost is effectively tackled by two factors: on the one hand, a low amount of Pt is used, by synthesising Ni–Pt thin films with low Pt content for HER, and by electrodeposition of extremely low amounts of electrocatalyst for ORR in PEMFC. Considering the thin films, the cost reduction of the binary Ni–Pt alloy with respect to pure Pt can be estimated by the cost of the precursors used for electrodeposition. If $Ni_{84}Pt_{16}$ is considered as the optimum composition, its cost reduction with respect to the same amount of pure Pt would be of just over 60%. Secondly, an increase in surface area is targeted by synthesising two kinds of nanostructures which should lead to higher mass-specific catalytic activities: mesoporous thin films for HER and NPs for ORR.

Concerning the mesoporous thin films, an improvement in HER over dense thin films was found, however not as high as could be expected due to the large increase in surface area as a result of the porosity. Their main advantage results from the lower density and therefore lower utilisation of Pt

and Ni with respect to the dense thin films. The question remains whether the pore size of around 10 nm is suitable for water electrolysis, whether hydrogen gas is able to be created and to escape freely from inside a pore, and whether the electrolyte effectively penetrates the mesopores. In fact, the mesoporous structure of the surface could give rise to the lotus effect, where the water is repelled from the surface, which would lead to a negative effect with respect to catalytic activity. However, contact angle measurements could not reveal any differences in wettability between dense and mesoporous thin films, thus the wetting of the surface is neither improved nor compromised by the nanostructure. The electrocatalytic activities and ECSA of materials with higher pore sizes in the mesoporous range should be investigated to study the effect of pore size.

Although mass activities of the NPs for ORR are very high, the power output obtained from a PEMFC prototype is rather low. A higher amount of deposited NPs is preferable, however the amount of nucleation cannot be fully decoupled from NP growth. The low wettability of the carbon substrates' surface due to their PTFE content may also suggest that the substrates were not wetted below the first few hundred nanometers of the substrates. An activation treatment of the substrate surface, such as by oxygen or argon plasma, could favour the deposition of NPs in deeper regions of the surface, but would most probably harm the PTFE layer and the wetting properties needed in the PEMFC in order to drain the produced water. A less aggressive solution is the pressurisation of the electrolyte during deposition in order to force its penetration into the substrate. Another—hypothetical—solution could be the re-design of the MEA which would allow larger electrode areas, such as a foldable MEA. Electrodeposited NPs can be applied to a much thinner GDL, in turn they need a higher area for higher power output.

The durability of mesoporous Ni–Pt thin films in 0.5 M H_2SO_4 is guaranteed as long as the applied potential is cathodic, although an initial decrease of activity at HER is observed, ascribed to the leaching of Ni. For practical applications such as electrolysers, this leaching can be provoked in a pretreatment in order not to contaminate the device during operation. In 1 M NaOH the durability is much higher, without any observable degradation, and is only limited by an irreversible passivation at higher anodic potentials (1.0 V vs Ag|AgCl). An application in alkaline media is therefore more straightforward compared to acidic media, where more precautionary measures need to be taken in order not to expose the electrocatalyst to anodic or open circuit potential for too long.

Both Pt–Ni and Pt–Ni–Mo NPs suffer from significant loss of activity after ADT in a PEMFC. However, the mass efficiencies at ORR are extremely high,

so that even after a 50% loss in activity, a mass activity significantly higher than the one of commercial Pt/C is retained. The activity loss of NPs at ORR takes place during the first 10 000 cycles of ADT. After the full 20 000 cycles, only little additional change in activity is observed for most compositions. It is presumable that the activity loss is only initial and then stabilises, similar to the behaviour of the Ni–Pt thin films in acidic media, though further tests are needed to validate this.

In terms of energy efficiency, the Ni–Pt thin films have shown very low overpotentials at HER, thus the electrical energy needed to trigger the production of hydrogen is low. In addition, the kinetics determined by the Tafel slope are close to the theoretically achievable maximum for Pt. In contrast to the electrodeposition of Pt alloy NPs, where further development is needed in order to satisfy all demands of their application in PEMFC, the electrodeposited Ni–Pt thin films are readily employable at HER. The electrodeposition process, taking into account the rather simple composition of the electrolyte and the high repeatability of the results, should be upscalable to industrial standards with little effort. In this way, the production of green hydrogen can be further facilitated. As a form of energy storage, its production can be combined with other renewable energy sources such as solar, wind or hydro energy, which are in need of energy storage solutions since they cannot run simply on demand.

The energy efficiency also plays a major role in applications where magnetic properties are exploited. The Ni–Pt thin films are soft magnetic and require low energy for switching the magnetisation. Additionally, the successful synthesis of alloys with a Curie temperature close to RT implies that a low amount of (thermal) energy allows to switch between ferromagnetic and paramagnetic states. While the practical applicability of thermally actuated magnetism is questionable, other effects on T_C can be investigated, such as the manipulation of the T_C of a thin film with applied voltage. Attempts to achieve this behaviour have been made in the frame of this work, but were not successful.

The investigation of possible magnetoelectric effects of mesoporous Ni–Pt films did not yield any significant results, suggesting that the thin film criterion to observe such effects is not fulfilled, i.e. the pore walls are not sufficiently thin. Thinner pore walls could potentially be achieved by lower metal salt concentrations and/or higher surfactant concentration, which may lead to lower amounts of metal ions coordinated with the micelles and a more close-packed porosity.

While Pt plays a key role in the electrocatalytic properties of the alloys, the observed tuneability of magnetic properties is basically a result of the single-

phase character and structure of an alloy constituted by a ferromagnet and a paramagnet. In order to reduce the cost for magnetic applications, the rather expensive Pt may therefore be substituted, and another (electrodepositable) binary system with complete miscibility, such as Ni–Cu, may exhibit similar tuneability of magnetic properties at lower production cost.

7 Conclusions

The synthesis and characterisation of Ni–Pt thin films leads to the following conclusions:

- The synthesis of homogeneous Ni–Pt alloy thin films was successfully demonstrated by potentiostatic electrodeposition from aqueous media.

- Micelle-assisted electrodeposition using Pluronic P-123 leads to the formation of homogeneously mesoporous Ni–Pt alloy thin films with narrow pore size distribution of ca. 10 nm pore size. The induced mesoporosity does not cause any compositional or structural differences with respect to dense thin films.

- The composition of both mesoporous and dense thin films is tunable in a wide compositional range between 50–99 at% of Ni (1–50 at% Pt) by variation of the deposition potential.

- All Ni–Pt thin films are single-phase fcc solid solution, prohibiting corrosion by galvanic coupling.

- Saturation magnetisation, coercivity and Curie temperature of the mesoporous thin films are linearly dependent on their Ni content, and therefore manipulable by the electrodeposition parameters. Tuneability of M_s and T_C are a consequence of the single-phase character, while the tuneability of H_c is assigned to both single-phase character and mesoporosity.

- All Ni–Pt thin films are nanocrystalline, accounting for high mechanical properties in accordance with the Hall-Petch relation.

- The HER activity of mesoporous Ni–Pt thin films in acidic media is composition dependant. The geometric current density at HER increases with the Pt content of the thin films, however, when ECSA is taken into account, the Ni-rich alloy $Ni_{95}Pt_5$ shows the highest efficiency. In consequence, there seems to be an optimum alloy composition for the HER with low Pt content.

- The higher efficiency of mesoporous thin films at HER with respect to dense films is mainly due to the lower density, i.e. lower amount of material in the porous films.

- In acidic media, thin films of all compositions exhibit good durability as long as cathodic potential is applied, though an initial activity decrease occurs.

- In alkaline media, thin films of all compositions are stable in a wide potential range up to 1.0 V vs Ag|AgCl.

- The reversible redox reaction between NiOOH and $Ni(OH)_2$ in alkaline media is improved by the Pt content acting as a catalyst and making the system interesting for application in electrochemical supercapacitors.

For Pt–Ni and Pt–Ni–Mo NPs, the following conclusions are deduced.

- Pulse electrodeposition successfully yields Pt–Ni and Pt–Ni–Mo NPs, deposited directly onto the GDL of a PEMFC.

- While the electrodeposited Pt–Ni particles are single-phase, the Mo species in Pt–Ni–Mo NPs are not fully reduced and hint to the existence of a Mo(IV) oxide, responsible for more irregular, rougher NPs with lower crystallinity with respect to Pt–Ni NPs.

- Variation of the current densities in pulse electrodeposition does not result in a coherent trend in composition of the NPs, although the composition is altered by the current amplitude. For Pt–Ni NPs, the targeted compositional range was readily obtained.

- The pulse electrodeposition of the ternary system Pt–Ni–Mo is more complex and does not follow the same trends as the binary Pt–Ni system. Obtention of Pt-rich alloy NPs was only possible with relatively low Mo contents around 1 at%.

- ORR activity on electrochemical cell level is successfully demonstrated, including on the rather Ni-rich Pt–Ni–Mo NPs.

- The ECSA of electrodeposited NPs is in the same range as for common Pt/C electrocatalysts for ORR.

- PEMFC testing shows very high utilisation of the electrocatalyst NPs, due to the concentration of NPs at the topmost layer of the GDL and their location at the most active sites of the GDL.

- ADT shows significant loss in activity, however, a stabilisation is observed over time and the loss of activity seems to be only initial.

- The best performance, considering both mass activity and durability, is found for $Pt_{67}Ni_{33}$ and $Pt_{66}Ni_{32}Mo_2$.

8 Outlook

For mesoporous Ni–Pt thin films, the electrodeposition process is optimised, however, a number of possibilities exist in order to boost electrocatalytic efficiency and durability, as stated in the following.

- Establishment of hierarchical porosity as a combination of mesoporosity with an approach to obtain a co-existing macroporous structure, such as colloidal templating.
- Obtention of larger mesopores by micelle-assisted electrodeposition using a surfactant with larger molecular mass.
- Template-assisted electrodeposition of the mesoporous material in more sophisticated high-surface area structures such as nanowires or nanotubes, e.g. using AAO or track-etched polymeric membrane templates. Such structures are also favourable for application in electrochemical supercapacitors.
- Study of magnetic field-enhanced electrocatalysis.
- Incorporation of a third element to create a ternary system in an attempt to increase stability in acidic media, such as Mo.
- Study of possible magnetoelectric effects in the alloy, such as voltage-modulated changes in magnetisation, coercivity, or T_C (especially when T_C is close to RT).

For the Pt–Ni and Pt–Ni–Mo ORR electrocatalyst NPs, the principal functioning of the presented approach was validated. Further optimisation is needed for full applicability in PEMFC, and the following points should be studied.

- Deposition of higher amounts of electrocatalyst onto the GDL in order to achieve higher power output of the PEMFC. The results presented here show that the mass activity of all NPs is high despite their relatively high particle size with respect to common Pt/C electrocatalysts. Although higher amounts of pulse electrodeposited material leads to even higher particle sizes, those may still show higher activity than commercial ORR electrocatalysts.

- Substitution of Mo of the ternary system with another element such as Co or Fe.

- Adaption of the synthesis process in order to deposit material in higher depths of the GDL.

List of Figures

List of Tables

116

Glossary

AAO	Anodic aluminium oxide (Anodically oxidised alumina)
ADT	Accelerated degradation test
BET	Brunauer-Emmett-Teller method
CE	Counter electrode
cmc	Critical micelle concentration
CV	Cyclic voltammetry
DC	Direct current
DFT	Density functional theory
DoE	U.S. Department of Energy
ECSA	Electrochemically active surface area
EIS	Electrochemical impedance spectroscopy
EMT	Electrochemical microcell technique
fcc	Face-centred cubic
GDE	Gas diffusion electrode
GDL	Gas diffusion layer
HER	Hydrogen evolution reaction
HOR	Hydrogen oxidation reaction
LLC	Lyotropic liquid crystal
LSV	Linear sweep voltammetry
MA	Mass activity
MEA	Membrane electrode assembly
MEMS	Microelectromechanical system
NP	Nanoparticle
OCP	Open circuit potential
OCV	Open circuit voltage

OER	Oxygen evolution reaction
ORR	Oxygen reduction reaction
PEG	Polyethylene glycol
PEM	Proton exchange membrane
PEMFC	Proton exchange membrane fuel cell
PEO	Polyethylene oxide (equivalent to PEG)
PPG	Polypropylene glycol
PPO	Polypropylene oxide (equivalent to PPG)
PS	Polystyrene
PTFE	Polytetrafluoroethylene
RDE	Rotating disk electrode
RE	Reference electrode
RHE	Reversible hydrogen electrode
RISE	Research Institutes of Sweden
RT	Room temperature
S/V	Surface-to-volume ratio
SA	Specific activity
SCE	Saturated calomel electrode
SEM	Scanning electron microscopy
SHE	Standard hydrogen electrode
TPB	Triple phase boundary
VSM	Vibrating sample magnetometry

Appendix
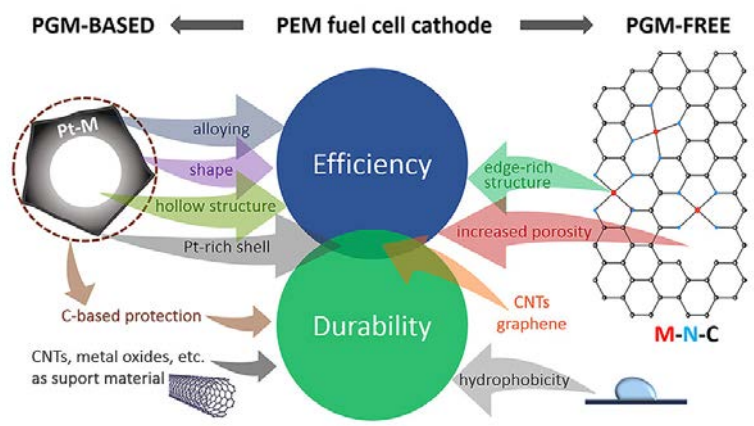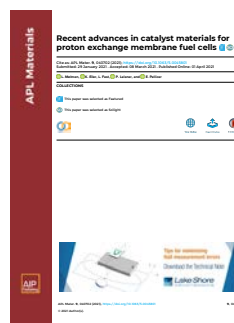
Recent advances in catalyst materials for proton exchange membrane fuel cells

Live Mølmen[a,b]*, Konrad Eiler*[c]*, Lars Fast*[a]*, Peter Leisner*[b] *and Eva Pellicer*[c]

[a]Department of Electrification and Reliability, RISE Research Institutes of Sweden, Borås, Sweden
[b]Department of Materials and Manufacturing, Jönköping University, Sweden
[c]Departament de Física, Universitat Autònoma de Barcelona, 08193 Bellaterra, Spain

This research update, which is similar to a review article, is the first co-production in collaboration with RISE. It introduces all approaches for ORR electrocatalysts for PEMFC presented in the last two years, covering not only Pt-based catalysts but also single-atom catalysts based on transition metal atoms in a carbonic structure. The most important properties of ORR and PEMFC testing are listed in tables, facilitating direct compatibility. Emphasis is placed on those works which present not only results from ORR but also from PEMFC testing, especially ADT. The number of recent publications on the topic is extremely high and represents the global effort towards emission-free energy technologies such as the PEMFC. The most promising candidates for ORR electrocatalysis are certainly Pt-based, combining different approaches for the maximisation of efficiency and durability, such as alloying with transition metals, shape optimisation, hollow NP structures, and a carbon-based protection. In addition, carbon corrosion of the catalyst support can be tackled by the use of optimised support structures.

Recent advances in catalyst materials for proton exchange membrane fuel cells SCI F

View Online   Export Citation   CrossMark

L. Mølmen,[1,2] (iD) K. Eiler,[3] (iD) L. Fast,[1] P. Leisner,[2] (iD) and E. Pellicer[3,a] (iD)

AFFILIATIONS

[1] Department of Electrification and Reliability, RISE Research Institutes of Sweden, Borås, Sweden
[2] Department of Materials and Manufacturing, Jönköping University, Jönköping, Sweden
[3] Departament de Física, Universitat Autònoma de Barcelona, 08193 Bellaterra, Spain

[a] Author to whom correspondence should be addressed: eva.pellicer@uab.cat

ABSTRACT

Research on fuel cell technology is constantly gaining importance, while global emission requirements are becoming more and more restrictive. For environmentally neutral proton exchange membrane fuel cells (PEMFCs) to become a competitive technology, sustainable infrastructures need to be established. One of the main showstoppers is the utilization of the rare and therefore costly precious metal Pt as the key element in the electrocatalysis of hydrogen and oxygen. A huge amount of research is done on immensely reducing or even replacing Pt for future PEMFC technology. In this research update, the progress on oxygen reduction reaction catalysts in acidic media over the past two years is reviewed, with special attention to their durability.

NOMENCLATURE

ADT	accelerated degradation test	MA	mass activity
AEM	anion exchange membrane	MEA	membrane electrode assembly
AEMFC	anion exchange membrane fuel cell	MOF	metal–organic framework
ALD	atomic layer deposition	NG	nanographene
b	Tafel slope	NP	nanoparticle
CB	carbon black	NT	nanotube
CNT	carbon nanotube	NW	nanowire
CNW	carbon nanowire	OCV	open circuit voltage
CV	cyclic voltammetry	ORR	oxygen reduction reaction
DFT	density functional theory	PANI	polyaniline
DOE	U.S. Department of Energy	PEM	proton exchange membrane
$E_{1/2}$	half-wave potential	PEMFC	proton exchange membrane fuel cell
ECSA	electrochemically active surface area	PGM	platinum group metal
FC	fuel cell	RDE	rotating disk electrode
GDL	gas diffusion layer	RGO	reduced graphene oxide
HOR	hydrogen oxidation reaction	RHE	reversible hydrogen electrode
IL	ionic liquid	SA	specific activity
j_k	kinetic current density	SAC	single-atom catalyst
LSV	linear sweep voltammetry	STEM	scanning transmission electron microscopy
		TEM	transmission electron microscopy
		ZIF-8	zeolitic imidazolate framework

121

I. INTRODUCTION

Proton exchange membrane fuel cell (PEMFC) vehicles are emerging into the commercial market as the drive for zero-emission vehicles increases.[1] However, the cost of the PEMFC is still high, with one of the major cost components being the noble metal catalyst. The rather sluggish oxygen reduction reaction (ORR) at the cathode requires catalysts with a higher surface area and optimized structure in order to minimize the use of platinum group metals (PGMs).

Today, Pt and its alloys are the most commonly used catalysts for PEMFCs at both the anode and the cathode. In 2017, the U.S. Department of Energy (DOE) set the technical target of reaching a total loading of platinum group metals below 0.125 mg/cm^2 by 2020. Their target activities at 0.9 V vs reversible hydrogen electrode (RHE) are a PGM mass activity (MA) of 0.44 A/mg$_{PGM}$ for PGM catalysts and a current density of 44 mA/cm^2 for PGM-free catalysts.[2] While the Pt loading can easily be reduced below 0.05 mg/cm^2 at the anode,[3] the stability and performance of the electrocatalyst at the cathode is critical. In the acidic and oxidizing conditions at the cathode, Pt nanoparticles (NPs) tend to agglomerate and grow, thus losing the surface area. Although some research papers have reached the 2020 goals, commercial fuel cells still operate with around 0.35 mg$_{Pt}$/cm^2 when used in vehicles.[1]

There are several strategies for improving the cathode catalyst in terms of efficiency and durability (Fig. 1). The size of commercial Pt NPs has already been minimized to 3–6 nm. To further reduce the cost and/or improve the catalytic activity of Pt, research groups are aiming at the shape control of Pt NPs, alloying of Pt, core–shell NP structures with Pt-rich surfaces, and the synthesis of hollow NP structures. The durability can be improved by confining the PGM NPs in a carbon based structure, as well as by making use of different support materials. Recycling of membrane electrode assemblies (MEA) containing PtCo has also shown that the global impact of the catalyst can be reduced by extracting the metals from the aged MEA and synthesizing new catalysts.[4]

On the other hand, Pt-free catalysts such as single-atom catalysts (SAC) are the focus of investigations (Fig. 1). These are most commonly of M–N–C type, where M is a metal, most commonly Fe or Co.[3] Optimization of these catalysts is currently followed up by creating edge-rich and porous structures, making use of favorable structures such as graphene or carbon nanotubes (CNTs), and by increasing the catalyst's hydrophobicity. Additionally, transition metal dithiolenes (M–S–C structures) comprising Fe or Co have been recently proposed by density functional theory (DFT).[5] A number of different compounds have likewise been determined by DFT as sufficiently stable two-dimensional materials for ORR,[6] although experimental demonstration is yet to be performed.

In the following, the most recently investigated electrocatalysts for ORR will be discussed for each strategy, being split into PGM-based catalysts on the one hand and PGM-free catalysts on the other hand. The focus is on their synthesis, performance, and durability. Due to the vast number of publications in the past years, the focus lies on those works providing membrane electrode assembly (MEA) tests in fuel cells. Additionally, works on catalyst materials that have not been tested at this level but in the view of the authors present promising performance and applicability in the PEMFC have also been considered. The goal of this work is to give a brief overview of the latest developments and to point out the most promising approaches for future research.

While ORR studies in alkaline media are currently very popular, the focus of this work is on the research dedicated to ORR in acidic media in order to identify suitable materials and synthesis processes for the successful development of PEMFCs. The primary objective does not necessarily lie in outperforming commercial Pt/C, but in achieving high reliability and durability of the catalyst in a cost-efficient synthesis process.

II. PGM-BASED CATALYSTS

Four different approaches are mainly pursued on PGM-based catalysts: the alloying of Pt or other PGM, the optimization of the pure Pt catalyst, an optimization of the supporting substrate, and the protection of the catalyst in an organic structure. Naturally, these approaches are often combined to acquire superior results.

A. PGM alloys

PGM alloys allow for reducing the use of the PGM, and electronic properties improving the catalytic activity of the PGM can be
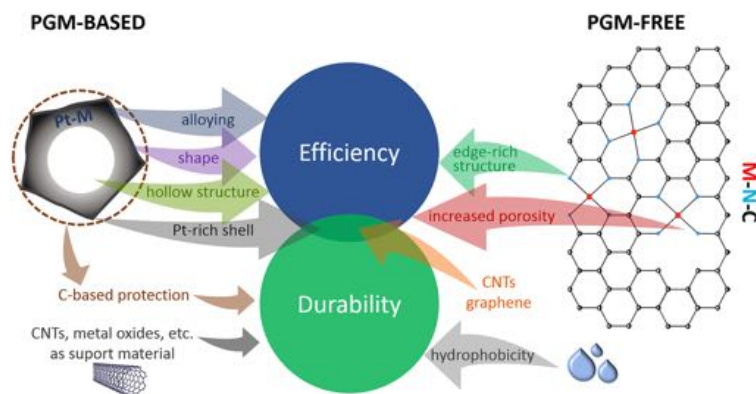
FIG. 1. Current strategies for improving the efficiency and durability of PGM-based (left) and PGM-free (right) ORR catalysts for PEMFCs.

122

obtained. The alloying elements may also contribute with their own catalytic activity.

One of the most popular approaches is the alloying of Pt with transition metals such as Fe, Co, Ni, and Cu, which are usually employed in the form of NPs with a Pt-rich surface. The Pt-rich and electrochemically stable surface is usually formed by either a specific etching process or the dissolution of transition metal atoms during operation; the result is often referred to as a core–shell structure. Several of these catalysts are already being used commercially, such as Pt–Co, which serves in Toyota's fuel cell car;[7] however, research on different Pt–Co NP structures is still ongoing.[8–11] Current research focuses a lot on the development of Pt–Ni alloys,[12–15] where several works report the synthesis of octahedral NPs.[16–20]

Gong et al. successfully synthesized Pt–Ni as dumbbell-shaped particles, which did not show increased electrochemically active surface area (ECSA) but were able to achieve both higher ORR MA and higher retention of activity after accelerated degradation testing (ADT) when compared to globular Pt–Ni NPs[21] (Fig. 2).

A neural-like network of Pt–Co NPs connected by CNTs (Fig. 3) developed by Wang et al. was able to show outstanding performance at both H₂/O₂ and H₂/air fueled PEMFCs while being completely free from degradation after both ADT in an electrochemical half-cell and continuous operation of PEMFC.[22]

Several other binary alloys investigated involve Pt–Ag,[23] Pt–Bi,[24] Pt–Cu,[25,26] Pt–Fe,[27–30] Pt–Ir,[31–35] Pt–Se,[36] Pt–Te,[37] and Pt–Zn.[38] In addition, several ternary[39–48] and quaternary alloys[49,50] have been investigated. A Pt-rare earth catalyst is proposed by Chu et al.;[51] however, such a catalyst is questionable in terms of large-scale application due to its low abundance.

Apart from alloying, a few works concentrated on the phosphorization[52,53] or nitrogenation[54] of Pt.

Dionigi et al. and Cao et al. reported further improvement in the durability of octahedral Pt–Ni by introducing additional alloying elements in a second synthesis step, such as Mo[39] or Cu,[40] respectively.
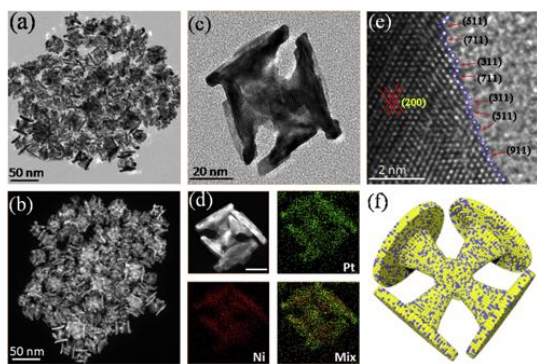
Wang et al. investigated ternary alloys of Pt with the three transition metals Fe, Ni, and Co, finding that the Pt–Co–Fe alloy was the most favorable among the possible combinations in terms of both activity and durability.[43]

The non-platinum containing PGM alloys recently reported for acidic ORR are Pd-based[55,56] or Ir-based.[57] Pd–Mo nanosheets investigated by Luo et al. showed extremely high ORR activity in alkaline media and also have superior performance in acidic media; however, the authors considered that the stability in acidic media was insufficient for practical applications.[55] More frequently, Pd is also alloyed with Pt in a variety of nanostructures.[35,58–63] Several works reported ternary alloys including both Pt and Pd.[64–69] Nan et al. investigated different Pd–M/Pt core–shell catalysts with Ni, Co, and Fe as alloying elements. The Pd–Fe core provided the best ORR activity, while all alloy cores outperformed the catalyst containing a pure Pd core.[68] A ternary alloy of exclusively noble metals (Pt–Pd–Ir) was investigated by Deng et al.[70]

For most reported alloy catalysts, an improvement due to alloying with additional elements is reported. Deng et al. found that binary Pt–Pd on carbon nanowires (CNWs) outperformed ternary Pt–Pd–Au, however, the Au phase was mostly segregated so that the effect of alloying could not be studied.[59]

B. Optimization of pure Pt catalysts

The optimization of pure Pt focuses on shape-tuning, to optimize ECSA and to expose the most active crystal planes, and on the tuning and control of the particle size. In terms of shape, rhombic dodecahedral NPs show the highest activity in perchloric acid, while the cubic shape is the least favorable[71] (Fig. 4).

Dong et al. studied the mechanism of ORR on Pt(100), Pt(110), and Pt(111) facets and were able to monitor the intermediates in situ by Raman spectroscopy. On Pt(111), where ORR is improved, the reaction takes place via the formation of HO₂ radicals, whereas OH radicals are formed on Pt(100) as well as Pt(110).[72] Chen et al. synthesized NPs in a multipod structure showing good performance; however, degradation was still an issue.[73]

Cheng et al. used an Se film on the carbon support in order to seed Pt NPs smaller than 2 nm, resulting not only in superior performance but also in much improved durability.[74] Another approach was pursued by Chen et al., who synthesized supramolecular Pt-containing structures with promising results for ORR.[75]

C. Optimization of the supporting layer

The interface between the PGM catalyst and its supporting layer is crucial since poor adhesion can lead to catalyst detachment. In addition, the support must provide an electrical connection to the catalyst and may influence the density of states in the d-band of the catalyst. Carbon black (CB) is the most commonly used support for the PEMFC catalyst. Current research includes the use of CNTs,[22,76–80] CNWs,[9,59,81] metal oxides,[82–86] a combination of those,[87] and various other compounds.[88–91] Those can be used to either replace CB or act as an intermediate support between the catalyst and CB.

Doping of CB with N, as well as the use of Mn as a precursor results in more graphitic and corrosion-resistant carbon.[92,93] As reported by Yang et al., Pt particles deposited on N–CB were smaller and better dispersed, resulting in an increase in ECSA and

FIG. 2. Dumbbell-shaped Pt–Ni NPs for ORR captured by TEM [(a), (c), and (e)], STEM [(b) and (d)], and their 3D structure model (f). The Pt–Ni/C catalyst reached an ORR MA of over 1.3 A/mg$_{Pt}$.[21] Reprinted with permission from Gong et al., Appl. Catal. B **246**, 277 (2019). Copyright 2019 Elsevier.
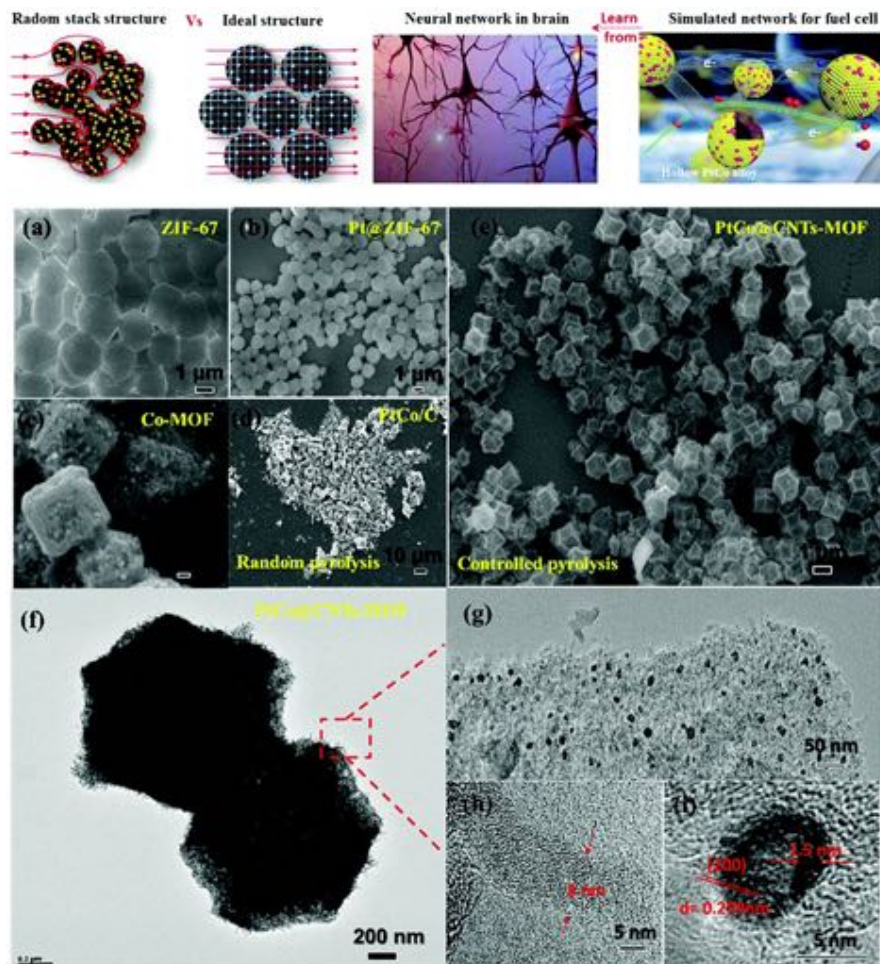
FIG. 3. Scheme of hollow Pt–Co NPs in an organic network connected by CNTs inspired by the neural network (top). SEM micrographs of the intermediate products during synthesis [(a)–(c)] and the products after pyrolysis [(d) and (e)]. TEM micrographs of the obtained Pt–Co/CNT/C catalyst [(f)–(i)], which reached a peak power density of over 1 W/cm^2 in a H$_2$/O$_2$ PEMFC at a Pt loading as low as 60 μg/cm^2 at the cathode.[22] Republished with permission from Wang et al., J. Mater. Chem. A **7**, 19786 (2019). Copyright 2019 Royal Society of Chemistry.

PEMFC performance.[92] Increased graphitization is also achieved by N-doping along with increased porosity of the carbon support.[93,94] N-doping is proposed to also give a more homogeneous ionomer distribution.[94] Coalescence of Pt and Pt–Co particles was suppressed by utilizing a porous carbon support, resulting in improved performance and durability.[95]

D. Protection of the PGM catalyst in an organic matrix

The most promising approach in order to limit degradation and increase the durability of PGM catalysts is their protection in a carbon-based matrix, where the PGM catalyst is not in direct contact with the polymer membrane.[96,97] Zhao et al. successfully "confined" Pt$_3$Co NPs in mesoporous carbon derived from the zeolitic imidazolate framework (ZIF-8). With the NPs trapped in the mesoporous structure, both detachment and agglomeration of NPs could be largely avoided, while the catalytic activity was not compromised.[98] Li et al. used an ionic liquid (IL) film to cover Pt/C NPs. In addition to the protective effect of those films, their electronic properties also improved ORR activity with respect to the bare Pt/C.[99] Zhou et al. created a carbon-based shell for Pt derived from Nafion,

124
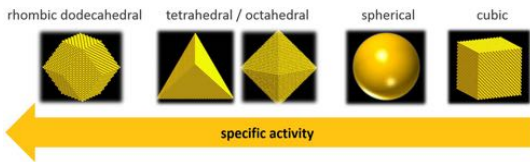
FIG. 4. Shape dependency of ORR activity for pure Pt NPs in perchloric acid.

FIG. 6. SEM micrographs of Pt–Co mesoporous NTs synthesized using Te NWs and F127 block copolymer as templates. The inset in (b) shows the cross section of a NT. Interestingly, the Pt–Co NTs outperformed Pt–Ni NTs synthesized through the same route.[106] Reprinted with permission from Yin *et al.*, ACS Sustainable Chem. Eng. **7**, 7960 (2019). Copyright 2019 American Chemical Society.

improving the PEMFC performance at a low Pt loading of 0.07 mg/cm^2; however, the durability was not studied.[96]

Choi *et al.* synthesized Pt–Fe NPs in a block copolymer matrix and achieved the formation of a carbon shell around the NPs. This catalyst achieved extremely high Pt mass activity in a half cell of 9 A/mg, and in PEMFC, an extremely low Pt loading of 0.01 mg/cm^2 was used to achieve a performance comparable to commercial Pt/C.[30]

Xiao *et al.* investigated the ORR of the noble metals Ir and Ru in a PGM–N–C configuration as SACs, reporting extraordinarily high ORR MAs including promising results at the PEMFC level.[100,101] Liu *et al.* determined that Ir and Rh showed favorable performance when applied as SAC, in contrast to Pt and Pd.[102]

E. Synthetic strategies

The most common approach for the synthesis of PGM-based catalysts is the solvothermal reduction method in autoclave. Meanwhile, alternative synthesis routes include pyrolysis, galvanic replacement, selective etching, and electrodeposition (Fig. 5). Moreover, the synthesis may comprise those multiple synthesis steps.

FIG. 5. Main strategies for the synthesis of PGM electrocatalysts.

In the solvothermal reduction method, metal precursors (usually acetyl acetates) are dissolved and mixed with a reducing agent and other additives. Carbon is often mixed in before the reduction process, which takes place in an autoclave at elevated temperatures. The product is then dried. For application in an MEA, the catalyst is usually dispersed in a solvent and sprayed onto the electrode.

Zhao *et al.* studied the size dependence of icosahedral Pt NPs synthesized using tetraethylene glycol as both the solvent and reductant and were able to synthesize the catalyst within 20 min. Interestingly, the highest kinetic current was reached for the largest NPs (14 nm), which also exhibited the best durability.[103]

Lei *et al.* demonstrated the synthesis of Pt–Co, Pt–Fe, and Pt–Ni NPs through the same route, allowing a direct comparison between their ORR activities, finding that Pt–Co was the most active at the ORR between them.[104] A similar observation was made by Wang *et al.*[105]

Yin *et al.* reported a room temperature synthesis for mesoporous Pt–Co and Pt–Ni nanotubes (NTs).[106] Here, the reduction of Pt–M (M = Co, Ni) takes place using ascorbic acid as a reducing agent and by galvanic replacement of the previously synthesized Te nanowires (NWs). In addition, a polymeric surfactant introduces mesoporosity in the material (Fig. 6). The same approach is used by the group to prepare mesoporous Pt–Te NTs.[37]

Yang *et al.* proposed a silica-assisted pyrolysis method for the reduction of Fe–Pt NPs.[27] After pyrolysis, the silica is removed and the Pt–Fe NPs are etched to obtain a hollow structure (Fig. 7). Alternative synthesis routes for Pt–Fe NPs are the
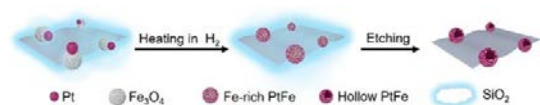
FIG. 7. Scheme for the formation of hollow Pt–Fe NPs from Pt and Fe$_3$O$_4$ precursors by silica-assisted pyrolysis. SiO$_2$ prevents the agglomeration of NPs during the heat treatment at 900 °C at which formation of Pt–Fe NPs takes place. Subsequent etching in HF removes SiO$_2$ and dealloys the NPs to obtain an electrochemically stable composition of Pt–Fe. The Pt–Fe/C catalyst reached a MA of over 1 A/mg$_{Pt}$ and 91% retention of MA after ADT.[27] Reprinted with permission from Yang *et al.*, Chem. Eur. J. **26**, 4090 (2020). Copyright 2019 Wiley-VCH Verlag GmbH & Co. KGaA, Weinheim.
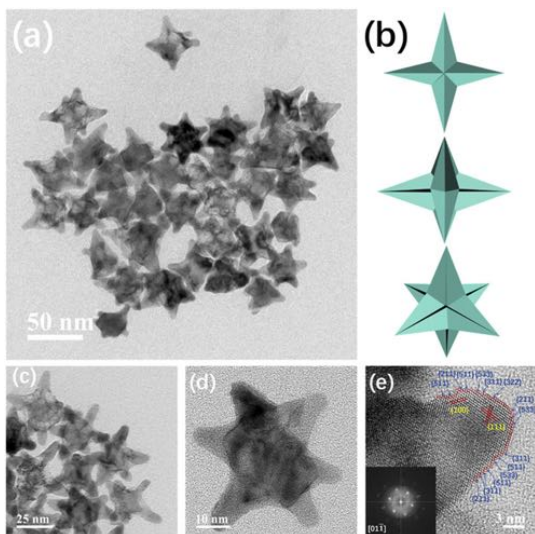
FIG. 8. TEM micrographs [(a) and (c)–(e)] and 3D model (b) of hexapod Pt–Pd–Cu NPs, which reached an ORR MA of 1.17 A/mg$_{Pt}$.[64] Reprinted with permission from Chen *et al.*, ACS Sustainable Chem. Eng. **8**, 1520 (2020). Copyright 2020 American Chemical Society.

impregnation–reduction method[28] and pyrolysis from a single precursor.[29] Higher process temperatures lead to the formation of an ordered structure, more favorable for ORR activity.[28,29]

Chen *et al.* achieved the synthesis of ternary Pt–Pd–Cu alloy NPs in a hexapod shape (Fig. 8). The formation of this unique shape was triggered by a combination of etching and selective growth.[64]

Mesoporous structures are reported in many cases, and their catalytic activity is certainly promising due to their generally higher

ECSA and MA.[17,37,65,67,69,70,106] However, their applicability in a PEMFC is questionable, as its performance depends on the number of triple points, which do not necessarily increase due to mesoporosity of the catalyst. In these cases, high ORR activities at the rotating disk electrode (RDE) level need to be backed up by PEMFC testing to prove the effect of a mesoporous structure on the FC. Otherwise, porous structures can still lead to improved MAs due to a decrease in the amount of non-surface material and can be ultimately optimized by the synthesis of hollow structures, as long as the stability is not compromised.[12,27,69]

A more promising approach is the combination of the catalyst with a mesoporous support layer, where the catalyst is confined within the mesopores.[94,98,107]

An alternative for the synthesis of PGM NPs is through pulse electrodeposition onto the carbon support.[11,108] Wang *et al.* successfully deposited Pt NPs within a desirable particle size of 3–10 nm after determining the optimum deposition parameters. The electrodeposited Pt/C showed higher half-wave potential E$_{1/2}$, kinetic current density j$_k$, and stability with substantially lower Pt loading in comparison to commercial Pt/C.[108]

Hussain *et al.* produced an Nb–Ti oxide substrate by atomic layer deposition (ALD), followed by the deposition of Pt by magnetron sputtering, and high ORR activity at a very low Pt loading of 9 μg/cm^2 was reached.[86] A sputter deposition approach was also followed by Ergul-Yilmaz *et al.* for the deposition of Pt.[109]

F. Durability issues

Many PGM-based catalysts suffer from constant performance degradation.[12] For pure Pt, this generally refers to the dissolution and redeposition of Pt, leading to particle growth and thus loss of the total catalyst area.[110] For alloys, leaching of non-noble metals can cause compositional and structural changes. A detailed *in situ* examination of the degradation of octahedral Pt–Ni was performed by Beermann *et al.*, identifying coalescence and particle motion as the main degradation mechanisms.[111] Another considerable problem of pure Pt is its methanol-dependent performance.
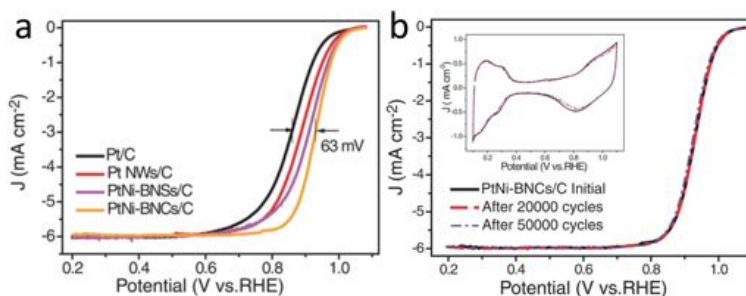
FIG. 9. Comparison of linear sweep voltammograms (LSVs) of C-supported Pt–Ni bunched nanocages (PtNi–BNCs/C), Pt–Ni bunched nanospheres (PtNi-BNSs/C), Pt NWs, and commercial Pt/C, where the Pt–Ni nanocages demonstrate an improvement of 63 mV in E$_{1/2}$ with respect to commercial Pt/C (a). LSVs of C-supported Pt–Ni nanocages including cyclic voltammograms (inset) initially and after 20 000 and 50 000 cycles of ADT, showing that neither ORR nor ECSA is significantly affected by the ADT (b).[12] Reprinted with permission from Tian *et al.*, Science **366**, 850 (2019). Copyright 2019 AAAS.

TABLE I. Characteristics of ORR for different PGM-based electrocatalysts in 0.1 M HClO$_4$. j$_k$, MA, and SA are given at 0.9 V vs RHE. ADT refers to 10 000 potential cycles between 0.6 and 1.0 V unless stated otherwise. MA and ECSA usually refer to Pt mass only. All potentials refer to RHE.

Catalyst	Kinetic current density j$_k$ (mA/cm^2)	Half-wave potential E$_{1/2}$ (V)	Tafel slope b (mV/dec)	Mass activity MA (mA/mg)	Specific activity SA (mA/cm^2)	Electrochemical surface area ECSA (m^2/g)	Retained mass activity after ADT (%)	Loss in E$_{1/2}$ after ADT (mV)	References
Ir–N–C	9.8	0.86	41	12 200[a]				n/a[b]	100
Ir–N–C		0.83	48				97[c]		102
Na–Pt–R/C		0.71	118					35[d]	75
Pd–Mo/C				660[a]	0.47	139			55
Pt/C		0.95		2 070	3.1	70	97		114
Pt/C				870	1.49				119
Pt/C				370	0.55	69	58		73
Pt/C				860	0.99	87	83[e]		115
Pt/C	3.4	0.91							108
Pt/C		0.88				44		27	81
Pt/C				260	0.43	69			96
Pt/C				260	0.65	40	74[f]		109
Pt(N)/C		0.93		102		69	96[g]		54
Pt/C–N	3.13	0.87	98					5[h]	120
Pt/C/PANI				63	0.09				121
Pt/Co–N/C		0.89		227		48	85[h]	4[h]	10
Pt/Ir/C	2.9	0.86		373	1.30		84[b]		33
Pt/Mn/C		0.88		300	0.57	67		31[h]	93
Pt/Se/C		0.96		750	0.32	231	93		74
Pt/IL/C				800	1.32				99
Pt/Nb–O/C		0.92	64	560	0.85	66	100		84
Pt/Nb–O/C				429	0.52	83	80[i]		83
Pt/Nb–O/CNT[j]	1.1	0.86	59	57		82	93[h]	6[h]	87
Pt/Nb–Ti–O/C[j]		0.77	52	56	0.32			20	86
Pt/Pd/C				750	1.01		60		62
Pt/Pd–Co/C				160[a]	0.58	130			68
Pt/Pd–Fe/C				260[a]	0.88	129	89		68
Pt/Pd–Ni/C				110[a]	0.69	125			68
Pt/Ti–C		0.82		80	0.13		88	1	88
Pt/Ti–N		0.85		140	0.27		79	7	88
Pt/Ti–Nb–O				150	0.35	43			82
Pt/Ti(N,C)O				115		41	n/a		85
Pt/Ti–C–O(F)/CNT		0.90		210	0.32	64			79
Pt/Ti–C–O(F)/CNT		0.88		163	0.26	63		19[k]	80
Pt/Pd/W–Ni/C		0.90		370[a]			n/a[h]	1[h]	90
Pt–Ag/C	2.17	0.88		316	3.46	91	n/a		23
Pt–Au–Cu/C		0.92	78	750[a]	0.49	153		n/a	48
Pt–Bi/C		0.84		1 040			87[c]		24
Pt–Co/C		0.97		2 260	8.6	27	94[i]		8
Pt–Co/C			151	128		30	78[d]		26
Pt–Co/C		0.89		640	1.29	49	86		104
Pt–Co/C				740	1.74		91	5	105
Pt–Co/C		0.91	62	950	0.99	50			106
Pt–Co/Nb–O/C				449	0.63	71	n/a		83
Pt$_3$Co/C		0.93	62	830	1.44	58	87[b]	5[b]	98
Pt–Co/CNT		0.94		852	1.38	62	103	n/a	22
Pt–Co–Fe/C		0.90		650		26	84	6	43
Pt–Co–Ni–Mo/C				450		49	78		49
Pt–Cu/C				2 570	2.82	91			25

TABLE I. (*Continued.*)

Catalyst	Kinetic current density j_k (mA/cm^2)	Half-wave potential $E_{1/2}$ (V)	Tafel slope b (mV/dec)	Mass activity MA (mA/mg)	Specific activity SA (mA/cm^2)	Electrochemical surface area ECSA (m^2/g)	Retained mass activity after ADT (%)	Loss in $E_{1/2}$ after ADT (mV)	References
Pt–Cu–Ni/C				1 290	1.7	73	93[m]	10[m]	46
Pt–Cu–Ni–W/C				2 020		126	66[g]		50
Pt–Cu–W/C		0.93	56	750	1.43	53	96[h]		42
Pt–Fe/C		0.92	58	680	2.23	30	73		28
Pt–Fe/C				300		54			29
Pt–Fe/C			48	1 020	2.73	37	91		27
Pt–Fe/C		0.88		470	0.92	51	74		104
Pt–Fe/C						50			92
Pt–Fe/C				9 000			69		30
Pt–Fe/TiCrN				674	1.28		90[b]	6[b]	107
Pt–Fe–Mo/C		0.92		780	0.56	133	67[m]	26[m]	47
Pt–Ir/C		0.87			1.18	32		23	32
Pt–Ir/C		0.91	65	522[a]	1.56	33		30[b]	35
Pt–Ir@Pd/C				1 880	1.27	122[n]	84		31
Pt–Ni/C				1 640		38	63		39
Pt–Ni/C		0.94		1 676	5.84	29			16
Pt–Ni/C		0.93		1 330		27	73		21
Pt–Ni/C				914	2.45	37	75[o]	14[o]	17
Pt–Ni/C			58	1 900	7.7	25	91[b]	5[b]	18
Pt–Ni/C				790		30	58[p]		19
Pt–Ni/C			54	3 520	5.16	68	99[e]		12
Pt–Ni/C	2.84	0.87	26	268	14.3	19			13
Pt–Ni/C		0.87		400	0.77	52	70		104
Pt–Ni/C		0.90	61	900	0.89	49			106
Pt–Ni/C						45			92
Pt–Ni/C				14		29			14
Pt$_3$Ni(Au)/C				3 080	5.74	35	95[g]		113
Pt–Ni/Nb–O/C				539	0.50	107	n/a		83
Pt–Ni–Cu/C				3 700	6.2	60	82[m]		40
Pt–Ni–In/C				760	1.96	39	98[q]		41
Pt–Ni–Ir/C				409		85	86[b]		45
Pt–Ni–Mo/C				3 430		38	72		39
Pt–P/C		0.93		915	1.86	52	93		52
Pt–Pd/C						70			92
Pt–Pd/C				920[r]	1.04	72[r]	91[p]	9[p]	58
Pt–Pd/C		0.87		411	0.43	93	88[b]		59
Pt–Pd/C		0.92		850[a]	1.33	54	73	14	60
Pt–Pd/C				480[a]	1.93	45	54[m]	30[m]	61
Pt–Pd/C		0.90	65	410[a]	0.91	52		20[b]	35
Pt–Ir/C				31[a]		57			34
Pt–Pd–Ag/C		0.90	59	610	1.11	55		11[b]	65
Pt–Pd–Cu/C		0.93		1 170	2.20	53	63	12	64
Pt–Pd–Ir/C		0.95	63	1 030	2.08	48	78	7	70
Pt–Pd–Ni/C		0.94	68	1 140	1.52	56		n/a	69
Pt–Pd–Ni/C			77	1 170	3.8	32	84		66
Pt–Pd–Ni–P/C		0.93	61	450	0.89	51	84	6[b]	67
Pt–Te/C		0.92	65	400	0.9	45	92[s]		37
Pt–Y–O/C				108	0.20	53	83[o]		51
Pt–Zn/C		0.94		1 020	1.68	61		n/a	38
Rh–N–C		0.68	51						102

128

TABLE I. (*Continued.*)

Catalyst	Kinetic current density j_k (mA/cm²)	Half-wave potential $E_{1/2}$ (V)	Tafel slope b (mV/dec)	Mass activity MA (mA/mg)	Specific activity SA (mA/cm²)	Electrochemical surface area ECSA (m²/g)	Retained mass activity after ADT (%)	Loss in $E_{1/2}$ after ADT (mV)	References
Ru–N–C		0.82	54	4 780[a]	11.95			17[g]	101
Se/Pt/C		0.82[i]	58		1.7				36

[a]Normalised by total PGM mass.
[b]After 5000 potential cycles of ADT.
[c]After 10 000 seconds of chronoamperometry.
[d]After 1000 potential cycles of ADT.
[e]After 50000 potential cycles of ADT.
[f]After 3000 potential cycles of ADT.
[g]After 20000 potential cycles of ADT.
[h]After 30000 potential cycles of ADT.
[i]After 25000 potential cycles of ADT.
[j]In H_2SO_4.
[k]After 2000 potential cycles of ADT.
[l]At 60 °C.
[m]After 15000 potential cycles of ADT.
[n]Normalized by mass of Pt and Ir.
[o]After 6000 potential cycles of ADT.
[p]After 8000 potential cycles of ADT.
[q]After 4000 potential cycles of ADT.
[r]Normalized by total catalyst mass.
[s]After 5 h of chronoamperometry.
[t]Recalculated from Ag/AgCl assuming a pH of 1.

Mom *et al.* investigated the oxidation behavior of Pt under PEMFC conditions and found that oxidation of Pt was favored under wet conditions at oxidizing potentials, especially on Pt NPs. Furthermore, the authors showed that the use of a Br-containing membrane instead of a regular Nafion membrane could suppress oxide formation.[112]

Outstanding durability has been reported by Tian *et al.* on bunched Pt–Ni nanocages, with only marginal decrease in MA after 50 000 cycles of ADT (Fig. 9). This performance has been related to the protective Pt skin structure of the catalyst.[12] Wu *et al.* improved the durability of Pt₃Ni NWs by Au doping, while the ORR activity was unaffected by the addition of Au.[113] Corroborated by DFT studies, the authors suggest that Au occupies surface defects of the Pt₃Ni matrix and immobilizes Ni atoms. A similar observation was made by Shen *et al.* using In in order to limit the diffusion of Ni.[41] Although the initial performance was inferior to that of a Pt–Ni alloy, an improved durability of Pt–Ni–In was found, and the optimum In content is the result of a trade-off between activity and durability.

Feng *et al.* produced Pt–Te nanosheets, which were then submitted to electrochemical dissolution of Te. The so-obtained porous Pt nanosheets showed very high MA and durability even after 30 000 potential cycles.[114] Similar observations were made by Kong *et al.* after dealloying Pt–Ni NWs[115] and referred to the higher defect density of dealloyed Pt, leading to improved ORR performance.[116]

In a different approach, a significant improvement was made by Guo *et al.* to Pt/C by applying a phosphorization treatment, leading to the formation of Pt₂P.[52]

Tu *et al.* found that the addition of W to Pt–Cu led to the outstanding stability of the catalyst after 30 000 potential cycles, even though the performance has been notably decreased after 5000 cycles.[42] This example shows that sufficiently long durability tests are indispensable for the evaluation of an ORR catalyst and 10 000 potential cycles, as suggested by the DOE, should be the absolute minimum.[2]

The fact that MA of the PGM-based catalysts is often reported with respect to Pt mass leads to the questionable assumption that ORR solely takes place on Pt atoms. Especially, if other PGM-metals such as Pd or Ir are involved, but also in the case of alloying of Pt with non-noble elements, their contribution to ORR activity is neglected and unrealistically high MA are reported. Although the Pt MA is therefore little meaningful from a scientific viewpoint, it can give a good estimation on the required amount of Pt and therefore the cost efficiency. From a purely electrochemical view, the ECSA-normalized specific activity (SA) should provide better comparability (Table I). A sound guidance for measuring and reporting the catalytic activity was produced by Wei *et al.*[117]

Zalitis *et al.* targeted the issue that although Pt alloys often show higher activity around the half-wave potential, they often do not exhibit as high current densities at higher ORR overpotential, close to the working potential of the PEMFC.[118] It is therefore important to document the MA at a higher potential such as 0.9 V vs RHE.

Ir-based catalysts[57] and Pt–Pd alloys[35] show very good CO tolerance in contrast to Pt. Bak *et al.* further found that carbon corrosion was suppressed when Ir was present.[34]

III. PGM-FREE CATALYSTS

Research on PGM-free catalysts for the ORR in acidic media includes ceramic catalysts such as CoS_2,[122] NiN[123] and Fe_3C;[124] however, the majority of the PGM-free catalysts are carbon-based. Carbon-based electrocatalysts profit from the huge abundance of carbon as well as from the highly advanced existing technologies able to tune carbon to the desired electronic properties. Carbon doped with elements such as nitrogen,[125,126] sulfur, phosphorous, and their combinations[127–129] has proven to work as ORR catalysts in both half-cell and PEMFC experiments. However, the current densities of these catalysts are not comparable to their PGM counterparts yet. Therefore, co-doping carbon with nitrogen and a transition metal to form SAC M–N–C structures where M=(Fe, Co, Cr, Ni, Mn, Ti, Zn)[130–135] is the focus of current PGM-free research.
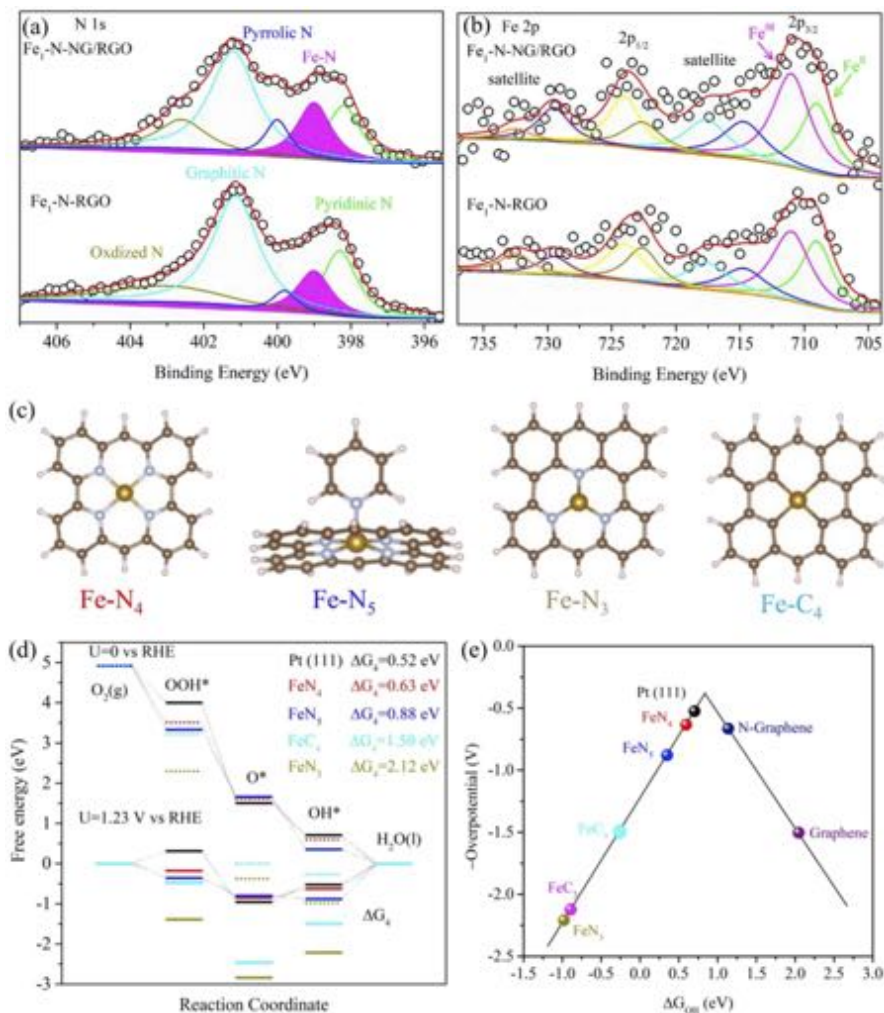
FIG. 10. X-ray photoelectron spectra of single-atom Fe anchored to nanographene (NG) and reduced graphene oxide [(RGO, (a) and (b)] and schematic of the Fe–N_4, Fe–N_5, Fe–N_3, and Fe–C_4 active sites where Fe is indicated in gold, N is indicated in gray, and C is indicated in dark orange (c). The free-energy diagram of these sites also at the Pt(111) facet in acidic media from DFT calculations (d) and a volcano plot of the ORR activity by plotting the overpotential as a function of the binding energy of OH of these sites, Pt(111), nitrogen-doped graphene, and graphene (e).[146] Reprinted with permission from Chen *et al.*, Nano Energy **66**, 104164 (2019). Copyright 2019 Elsevier.

130
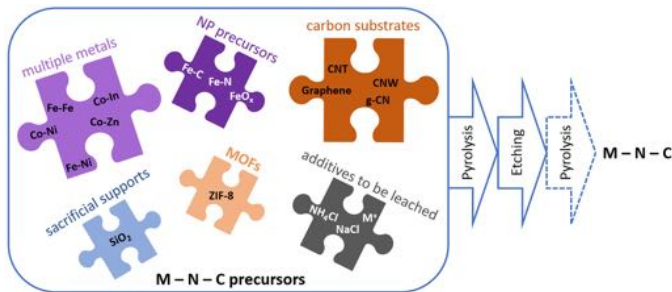
FIG. 11. Scheme for the synthesis of SAC electrocatalysts.

These SACs utilize abundant materials and thus have the potential to significantly reduce the cost of PEMFCs. The electrocatalytic activity of these materials is highly dependent on the type of metal and is reported to follow the order Fe > Co > Mn > Cu > Ni.[136] Fe has therefore been studied extensively.[130,137–144] To facilitate the optimization of SACs, studies to understand which are the active sites have been performed. Zhang et al. found pyrrole-type FeN$_4$ to be most active through both DFT calculations and from high open circuit voltage (OCV) and peak power density from tests in PEMFC. Chen et al. reached the same conclusion[145] (Fig. 10). Mun et al. investigated the effect of the carbon support on the activity of FeN$_4$ and found that the activity can be tuned by adding electron-withdrawing/donating groups.[146]

A. Synthetic strategies

The synthesis of M–N–C catalysts is most commonly done through pyrolysis, where nitrogen containing the organic precursor and metal precursor are mixed and subsequently heated in an inert atmosphere.[138,147,148] Some research groups add sulfur to the M–N–C to improve catalyst activity.[149–152] To ensure porosity, a sacrificial support may be added[147,153–157] or a metal–organic framework (MOF) such as ZIF-8 can be used as the organic precursor.[148,158–163] In principle, several different precursors may be combined (Fig. 11). Zhu et al. combined the use of a sacrificial polystyrene template and ZIF-8 to obtain a hierarchically porous structure.[164] The first pyrolysis step is followed by

etching to remove the support, surface oxides, and unstable metal clusters[138,147,148] (Fig. 12). An additional pyrolysis step ensures carbonization and yields a more uniform morphology.[147,148] Several groups have added excess Fe to form NPs of iron carbides or nitrides within the Fe–N–C.[141,165,166]

Gao et al. combined the pyrolysis and etching step by adding H$_2$ to atmosphere during pyrolysis of a MOF-based catalyst. Tunable hierarchical porosity was obtained.[131] Li et al. added additional metal ions to the pyrolysis. The metal ions were oxidized during heat treatment and ensured increased porosity while being easily removed during subsequent acid leaching.[154] A hierarchically open-porous structure has been obtained by the addition of graphitic carbon nitride to ZIF-8 and iron precursor prior to pyrolysis.[139,167,168]

Similarly, ammonium chloride or sodium chloride has been added to the pyrolysis to achieve an edge rich structure with more accessible active sites.[149,169] Wang et al. also achieved an edge rich structure by using iron chloride as a precursor, and both experiments and DFT calculations showed higher catalytic activity of the Fe-N$_x$ sites at edges compared to those at the center of the carbon matrix.[138] Another strategy is to increase the density of active sites as done by Wan et al. by making concave structures.[142]

Wang et al. produced iron oxide NPs in a mesoporous N-doped carbon, which after pyrolysis formed a core–shell structure with iron oxide encapsulated in graphitic carbon, and x-ray photoelectron spectroscopy analysis showed Fe–N active sites.[170]
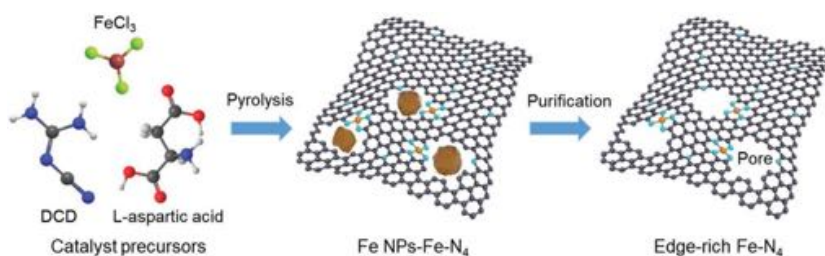
FIG. 12. Formation of Fe–N–C by pyrolysis using L-aspartic acid, dicyandiamide (DCD), and FeCl$_3$ as precursors.[138] Reprinted with permission from Wang et al., Adv. Mater. **32**, 2000966 (2020). Copyright 2020 WILEY-VCH Verlag GmbH & Co. KGaA, Weinheim.

As an alternative to the pyrolysis of MOF and sacrificial support, Wang and Berthon–Fabry synthesized Fe–N–C using the sol–gel method to produce an aerogel.[171]

Highest performance is, however, found for Fe–N–C catalysts using CNTs and/or graphene as the carbon precursor, with the advantage of not needing a sacrificial support.[172] Li *et al.* fabricated carbon nanospheres connected with CNTs to improve the electrical conductivity of the catalyst.[173] Liu *et al.* also anchored Fe single atoms on CNTs[174] but further improved the performance by exchanging CNTs for graphene[175] (Fig. 13). The highest performance and durability of a PGM-free catalyst were achieved by Chen *et al.* through supporting NG doped with
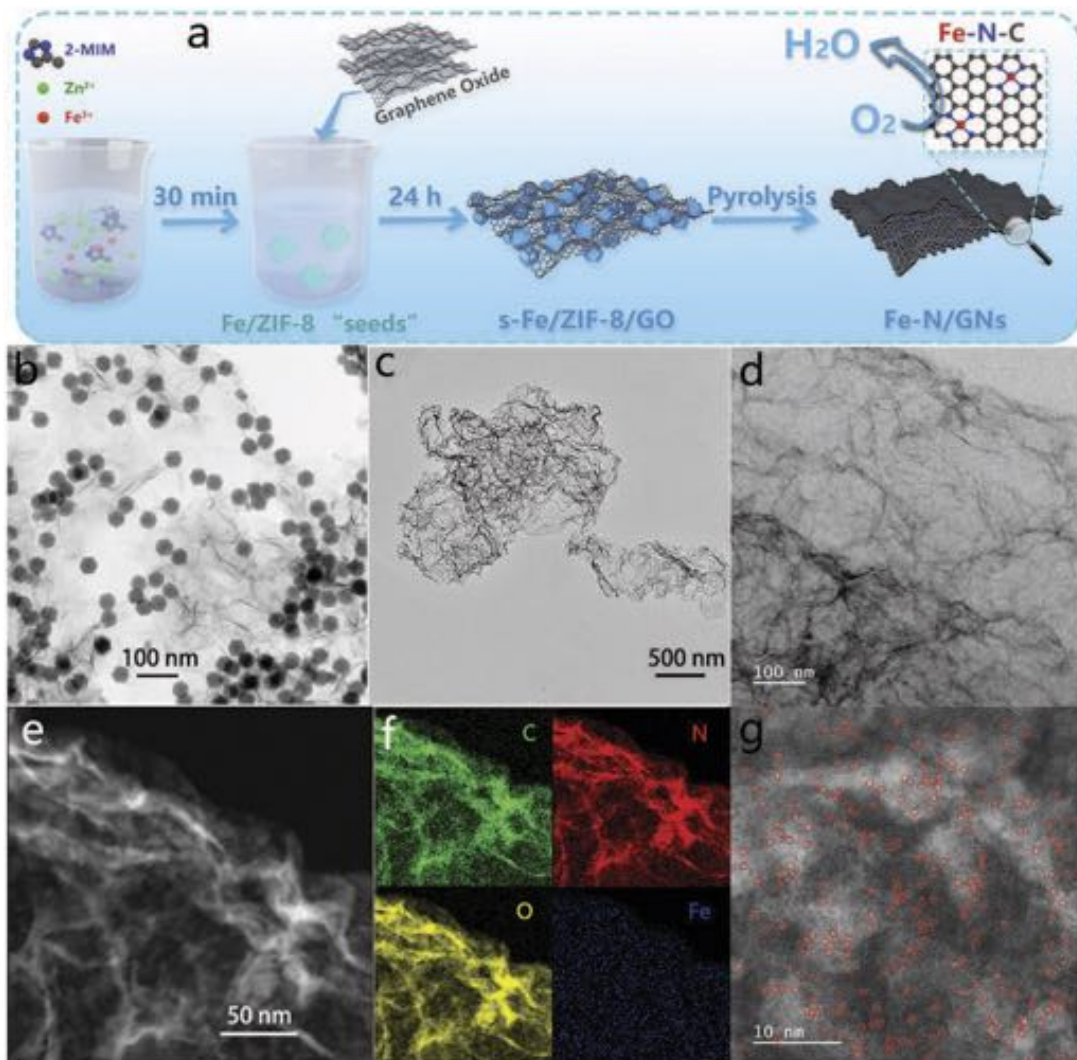
FIG. 13. Scheme of Fe–N–graphene synthesis (a), TEM image of the intermediate Fe/ZIF-8/graphene oxide (b), TEM and STEM images of the Fe–N–graphene [(c)–(e), and (g)], and elemental mapping of the final product (f).[175] Reprinted with permission from Liu *et al.*, Small Methods **4**, 1900827 (2020). Copyright 2020 WILEY-VCH Verlag GmbH & Co. KGaA, Weinheim.

132

TABLE II. Characteristics of the ORR for different PGM-free electrocatalysts. ORR was performed in 0.1 M $HClO_4$ unless stated otherwise. MA and SA are given at 0.8 V. All ECSA were determined by the H_{upd} method. ADT refers to 10 000 cycles between 0.6 and 1.0 V unless stated otherwise. All potentials refer to RHE.

Catalyst	Kinetic current density j_k (mA/cm²)	Half-wave potential $E_{1/2}$ (V)	Tafel slope b (mV/dec)	Mass activity MA (mA/mg)	Specific activity SA (mA/cm²)	Electrochemical surface area ECSA (m²/g)	Retained current density after ADT (%)	Loss in $E_{1/2}$ after ADT (mV)	References
C(N,S)		0.74	60				78[a]		128
C(P,N)[b]	0.96 at 0.5 V								127
N–C		0.76					91[c]		125
N–C		0.61	108				87[d]		126
N–P–S–C		0.64	126				84[a]		129
Co–In–C–N[b]		0.7					79[a]		180
Co–S			62						122
Co–N–C[b]		0.63						15[e]	177
Co–N–C[b]		0.84						40[f]	176
Co–N–C[b]		0.69	48				99[g]		178
Co–S–N–C	5.53 at 0.5 V	0.68					91.7[a]		152
(Co,Ni)–C		0.34	104				87[c]		181
(Co,Zn)–N–CNW		0.80	82					12	182
(Co,Zn)–N–S–C[b]		0.70					85[d]		150
(Co,Zn)–N–C		0.80						n/a	183
Cr–N–C	24 at 0.75 V	0.77	37					15[h]	132
Fe–N–C	5.8 at 0.3 V	0.76							137
Fe–N–C		0.82							142
Fe–N–C[b]		0.75					82[d]		139
Fe–N–C		0.78	65				67[d]		167
Fe–N–C		0.78					90[i]		130
Fe–N–C		0.78		10.5	0.0135		75[j]		140
Fe–Fe₃C/C		0.73	38					27[f]	141
Fe–N–C	37 at 0.75 V	0.8	68				n/a[e]		138
Fe–N–C[b]		0.8	72		6.89[k]			26	143
Fe–N–C		0.81[b]		6.50			45	53	144
Fe–N–C	6.12 at 0.8 V	0.81	63					18	131
Fe–N–C		0.73			503			19[j]	145
Fe–N–C		0.74	59					38	162
Fe–N–C		0.81						16	163
Fe–N–C	6.14 at 0.8 V	0.80						n/a	157
Fe–N–C[b]	3.82 at 0.8 V	0.80	65						169
Fe–N–C[b]		0.84						31[f]	158
Fe–N–C	4.6 at 0.8 V	0.80	66					9	172
Fe–N–C[b]	0.925 at 0.8 V	0.81	75					17	165
Fe–N–C		0.84	73					n/a[a]	175
Fe–N–C		0.79					90.8[h]		168
Fe–N–C		0.76						10[f]	156
Fe–N–C		0.79	72				91[a]		159
Fe–N–C[b]		0.82	92					1	160
Fe–N–CNW	8.0 at 0.8 V	0.82	63					16	154
Fe–N–C/CNT	13.1 at 0.8 V	0.84	67			565		15[e]	173
Fe–N–CNT		0.73						28	174
Fe–Fe₃C/Fe–N–C[b]	0.56 at 0.85 V	0.79							166
Fe₂–N–C[b]	16.4 at 0.75 V	0.78	83					20[h]	184
Fe₂N₆–C[b]		0.84	82	8.48	26.2			24	185
SiO₂–Fe–N–C	5.7 at 0.2 V	0.8							153
Fe–N–NG/RGO		0.84	63					5[m]	146

TABLE II. (*Continued.*)

Catalyst	Kinetic current density j_k (mA/cm^2)	Half-wave potential $E_{1/2}$ (V)	Tafel slope b (mV/dec)	Mass activity MA (mA/mg)	Specific activity SA (mA/cm^2)	Electrochemical surface area ECSA (m^2/g)	Retained current density after ADT (%)	Loss in $E_{1/2}$ after ADT (mV)	References
Fe–N–S–CNN[b]		0.78							151
(Fe,Ni)–N–C								12[e]	179
(Fe,Ni)–N–C		0.84	60				92[a]		164
Fe–O/C–N[b]	3.0 at 0.8 V	0.81						64	170
Mn–N–C[b]		0.78						20	133
NiN		0.49							123
Ti-MOF		0.75	18						134
Zn–N–C		0.75							135

[a]After 30000 s of chronoamperometry.
[b]In 0.5 M H$_2$SO$_4$.
[c]After 10000 s of chronoamperometry.
[d]After 40000 s of chronoamperometry.
[e]After 5000 potential cycles of ADT.
[f]After 30000 potential cycles of ADT.
[g]After 50000 s of chronoamperometry.
[h]After 20000 potential cycles of ADT.
[i]After 20000 s of chronoamperometry.
[j]After 24 h of chronoamperometry.
[k]With respect to BET surface area.
[l]After 3000 potential cycles of ADT.
[m]After 15000 potential cycles of ADT.

Fe and N on RGO with minimal loss after 15 000 potential cycles.[146]

Co–N–C catalysts have also been researched.[152,161,176–178] Although Co–N–C so far has shown lower catalytic activity than Fe–N–C (Table II), Co ions are less critical when released into both the membrane and ionomer since they are not Fenton active, and hence, a better durability is expected.[161] However, the Co–N–C needs advanced engineering to reach potentials comparable to Fe–N–C and Pt. Although half-wave potentials of up to 0.84 V vs RHE have been reached by a surfactant-covered Co–N–C structure,[176] they need to be further stabilized to achieve the superior durability expected.

Promising results have also been obtained by adding more than one metal to the M–N–C such as Fe–Ni,[164,179] Co–In,[180] Co–Ni,[181] and Co–Zn.[150,182,183] Zang *et al.* reported increased activity, both experimentally and from DFT calculations, due to Co–Ni dual active sites,[182] similar to the results produced by Ye and co-workers using Fe–Fe dual sites.[184] Fe–Fe was also studied by Zhang *et al.* by thermal migration of adjacent FeN$_4$ sites to form Fe$_2$N$_6$ dual sites. These dual sites show high selectivity toward the four electron ORR due to the ability to adsorb two O atoms simultaneously.[185] On the other hand, Zhu *et al.* found that Fe and Ni formed single atom sites.[164] This shows the immense number of variations that can be found for SACs, while only a handful has yet been explored, and that further research is needed to find a durable catalyst with a high catalytic efficiency and low production cost.

B. Durability issues

He *et al.* observed an initial high rate of degradation before an apparent stabilization of the Co–N–C. This is similar to what is found in PGM based catalysts and is due to an initial loss of unstable catalytic sites and oxidation of carbon.[176]

Kumar *et al.* found that carbon corrosion is occurring also in Fe–N–C catalysts. The deactivation of the catalyst is increased by the H$_2$O$_2$ byproduct from the ORR on the Fe–N–C, as there is significant increase in corrosion when cycled in O$_2$ compared to Ar.[144] Bae *et al.* studied the effect of H$_2$O$_2$ with varying pH. With the decrease in pH in the presence of H$_2$O$_2$, the amount of oxygen in the sample after the test increased. This is in accordance with the fact that Fenton's reaction is pH dependent and results in reducing the turnover frequency of nearby active sites.[186]

Doping graphene, CNTs, or CNWs with a transition metal and nitrogen has been proven by several groups to increase the durability,[146,154,178] with a further advantage of ensuring good conductivity in the catalyst layer.[182]

A major advantage of the SACs is that they are superior to Pt/C when it comes to methanol tolerance.[148,151] This would lower demands on gas purity for the PEMFC, which further reduces the operating costs.

IV. PEM FUEL CELL TESTING

While the electrochemical activity of a catalyst can be tested in a three electrode setup, PEMFC testing is required to evaluate the

TABLE III. Characteristics of PEMFC tests in H_2/O_2 for different electrocatalysts at 80 °C and 100% relative humidity. ADT refers to cycling between 0.6 V and 1.0 V unless stated otherwise.

Catalyst	Peak power density P_{max} (W/cm²)	Cathode loading (mg/cm²)	Open circuit voltage OCV (V)	Specific activity SA (A/cm²)	Mass activity MA (A/g)	Tafel slope b (mV/dec)	Current retention after ADT (%)	Retention of ECSA after ADT (%)	References
C(N,S)	0.28	2.5	0.78						128
Co–N–C	0.87	4	0.92						176
Co–N–C	0.92	4							161
(Co,Zn)–N–CNW	0.60	4	0.88						182
Fe–N–C	1.18	2.7							142
Fe–N–C	0.48	4							139
Fe–N–C	0.78	1							130
Fe–N–C	0.63	4					49[a]		140
Fe–N–C	0.68	3		0.29					157
Fe–N–C	0.73	3.5	0.98						158
Fe–N–C	0.75	2							172
Fe–N–C	0.7	4	1.01						143
Fe–N–C	0.86	4							169
Fe–N–C	0.65	4							165
Fe–N–C	0.6	4.0							160
Fe–N–S–C	0.53	4							149
Fe_2N_6–C	0.845	4	0.98						185
Fe–Fe_3C/C	0.24	2	0.77						141
Fe–Fe_3C/Fe–N–C	0.76	4							166
Fe–O/C–N	1.05	3.0			2 070				170
(Fe,Ni)–N–C	0.22	4							179
(Fe,Ni)–N–C	0.58	4	0.96						164
SiO_2–Fe–N–C	0.32	3							153
(Zn,Co)–N–C	0.71								183
C(P,N)	0.14	3.5	0.86						127
Ir–N–C	0.93	4 (0.008[b])	0.955						100
Ir–N–C	0.87	3 (0.135[b])							102
Pt/C	1.39	0.11[c]			400	90			94
Pt/C–N	0.33	0.5[c]	0.93						120
Pt/Co–N/C	1.25	0.175[c]							10
Pt/Nb–O/CNT	0.77	0.15					96[d]		87
Pt/Ti–Nb–O		0.2						77[e]	82
Pt/Ti(N,C)O	0.74						94[f]		85
Pt–Co/C	1.16	0.1[c]			720	61			15
Pt–Ni/C	1.21	0.1[c]			660	65			15
Pt–Co/CNT/C	1.02	0.06[c]							22
Pt–Cu/C		0.4	0.39						189
Pt–Cu–Ni/C	0.46	0.2[c]							46
Pt–Fe/C		0.4	0.45						189
Pt–Fe/C	1.08	0.3							92
Pt–Fe/C	0.96	0.01[c]			1 620		50[g]		30
Pt–Ni/C		0.4	0.47						189
Pt–Ni/C	0.82	0.3							92
Pt–Ni/C	0.88	0.31		3.26	70	38	72[h]	40[h]	14
Pt–Ni–Mo/C	0.7[i]	0.1[c]			450[j]				39
Pt–Pd/C	1.14	0.3							92
Pt–Pd/C-CNT	0.31[k]	0.5[c]					96[h]		63

135

TABLE III. (*Continued.*)

Catalyst	Peak power density P_{max} (W/cm^2)	Cathode loading (mg/cm^2)	Open circuit voltage OCV (V)	Specific activity SA (A/cm^2)	Mass activity MA (A/g)	Tafel slope b (mV/dec)	Current retention after ADT (%)	Retention of ECSA after ADT (%)	References
Pt–Zn/C	2.00				520		83[g]		38
Ru–N–C	0.64	4	0.93				76[l]		101

[a] After 8 h at constant voltage.
[b] PGM loading.
[c] Pt loading.
[d] After 96 h at maximum current.
[e] After 500 potential cycles from 1.0 V to 1.5 V.
[f] After 5000 potential cycles from 1.0 V to 1.5 V.
[g] After 30000 potential cycles of ADT.
[h] After 3000 potential cycles of ADT.
[i] Value determined under H$_2$/air supply.
[j] With respect to Pt mass.
[k] At 60 °C.
[l] After 100 h of constant operation.

performance of the catalyst when the electrolyte is changed from liquid to solid. However, comparison of the catalyst performance in a PEMFC is more complex. In Tables III and IV, test conditions and reported performance are shown for PEMFC tests using H$_2$/O$_2$ and H$_2$/air, respectively. Many parameters of PEMFC testing affect the results, although they are reported in varying degrees. The ionomer content in the catalyst layer and coating technique on membrane affect the proton conduction from the catalyst layer. The type of support, choice of gas diffusion layer (GDL), and compression of the cell affect the electrical conductivity. Finally, the porosity in GDL and catalyst layer and the flow field design and size of the cell affect how homogeneously the reactant gases are distributed across the catalyst layer.

Half of the reported tests use air at the cathode, while the rest use O$_2$. Several groups, testing both PGM and PGM-free catalysts, have tested their catalyst in both and found that the peak power density is almost twice as high when using O$_2$ compared to air.[22,130,169,172] Using pure oxygen mitigates some of the mass transport limitations and is more comparable to using air. Contaminants in air are rarely specified, but it is known that CO and SO$_2$ both poison the catalyst.[187,188]

For PGM containing catalysts, the catalyst layer has a thickness of 10 μm and the catalyst loading varies between 0.06 and 0.4 mg/cm^2. The focus of the current research is on improving the corrosion resistance of the carbon support.[92–95] Daş *et al.* tested Pt-M alloys as the anode, cathode, and both and found that the highest performance gain was obtained when the bimetallic catalysts were applied as the anode.[189]

A highly desirable durability in PEMFC application was achieved by Gao *et al.*, where the performance did not decrease even after 50 000 potential cycles of ADT for a Pt-Co/CNW catalyst (Fig. 14).[9]

For PGM-free catalysts, low volumetric activity leads to ten times thicker catalyst layers. Consequently, mass transport and resistance problems that are minimized or already overcome for noble metal catalyst needs to be solved. It should also be noted that although 4 mg/cm^2 is a common loading for SACs, some of the best performances come from catalysts with half the loading.[142] In a recent review by Satjaritanun and Zenyuk, pooling of water at interfaces between the catalyst layer and the microporous layer or the membrane as a result of non-homogeneous fabrication was found as an obstacle for these catalysts.[190] Liu *et al.* concluded that the hydrophobicity of the catalyst layer was the reason for water accumulation in a study where both the catalyst coated membrane and gas diffusion electrode assemblies were analyzed.[191] Yang *et al.* kept the SiO$_2$ support in the Fe–N–C catalyst, which increased the hydrophobicity of the catalyst layer and thus improved the PEMFC performance.[153]

Furthermore, it was concluded that although flooding of micropores is often cited as a major degradation mechanism and it can block O$_2$ transport to the active site, it is not the most important. In the review by Satjaritanun and Zenyuk, Fe–N$_4$ demetalization was instead pointed out as the major degradation mechanism.[190] Electrochemical impedance spectroscopy of aged PEMFCs with Fe–N–C catalysts has confirmed that there is a loss of active sites, which further leads to Fe-ion poisoning of the ionomer and membrane.[192,193]

It should be noted that in alkaline environment, many of the PGM-free catalysts have higher performance than the Pt-based catalyst. Therefore, these catalysts would have an advantage if the PEM was changed to an anion exchange membrane (AEM), ensuring a less corrosive environment in the cell. Seeberger *et al.* demonstrated the feasibility of a bipolar membrane assembly for PGM-free FCs, combining the alkaline ORR with acidic hydrogen oxidation reaction (HOR) by joining a PEM with an AEM as a double membrane.[194]

Fe–N–C has also been pointed out to be an alternative to Pt/C in high temperature PEMFCs. In these cases, where the membrane is polybenzimidazol doped with phosphoric acid, Pt is poisoned by the phosphate ions, while Fe–N–C is immune to the poisoning effect.[156]

TABLE IV. Characteristics of PEMFC tests in H_2/air for different electrocatalysts at 80 °C and 100% relative humidity. ADT refers to cycling between 0.6 V and 1.0 V unless stated otherwise.

Catalyst	Peak power density P_{max} (W/cm^2)	Cathode loading (mg/cm^2)	Open circuit voltage OCV (V)	Specific activity SA (A/cm^2)	Mass activity MA (A/g)	Tafel slope b (mV/dec)	Current retention after ADT (%)	Retention of ECSA after ADT (%)	References
Fe–N–C	0.42	2							142
Fe–N–C	0.46	1					68[a]		130
Fe–N–C	0.35	2							172
Fe–N–C	0.43	4							169
Pt/C		0.22			800				115
Pt/C[b]	0.78	0.10		1.15			91[c]	67	188
Pt/C	0.85	0.1							81
Pt/C	1.20	0.07							96
Pt(N)/C	1.25	0.3							54
Pt/Nb–O/C		0.10			288		68[c]		83
Pt/Ti–C–O/CNT	0.18[b]	0.2							80
Pt–Co/CNW	0.71	0.09[d]					107[e]		9
Pt–Ni/C[f]	0.88	0.4[d]					88[g]		16
Pt–Ni/C	0.92	0.15					>97[h]		12
Pt–Ni–Ir/C	0.40	0.35[d]					80[i]		45
Pt/C + Pd–Au[j]	0.54[b]	0.1[d]			160		79[k]	68[c]	56
Pt/Mn/C		0.12			373			66[l]	93
Pt–Co/C		0.11[d]		0.002	560	63	81[c]		8
Pt$_3$Co/C			0.98				85[m]	79[n]	98
Pt–Co/CNT/C	0.54	0.06[d]							22
Pt–Ir/C		0.4[d]					99[k]		34
Pt–Y–O/C	0.84	0.4							51

[a] Voltage retention after 10 h at constant-current operation.
[b] Tests performed at 60 °C.
[c] After 30000 potential cycles of ADT.
[d] Pt loading
[e] After 50000 potential cycles of ADT.
[f] Tests performed at 80% relative humidity
[g] After 100 h at constant voltage.
[h] After 180 h at constant voltage.
[i] After 1000 potential cycles of ADT.
[j] Pd–Au NPs are coated onto the Nafion membrane, while a conventional Pt/C catalyst is used in addition.
[k] After 15000 potential cycles of ADT.
[l] After 5000 potential cycles from 1.0 to 1.5 V.
[m] After 20000 potential cycles of ADT.
[n] After 10000 potential cycles of ADT.

V. RECYCLING OF PEMFC

Recycling of PEMFC components and particularly of PGM electrocatalysts is of utmost importance considering the current striving toward sustainability. Yet, this is an aspect that deserves larger attention from the scientific community in the field.

Lotrič et al. performed a life cycle assessment of the PEMFC stack and found that Pt is the component in the PEMFC with the largest environmental impact, and hence, recycling of the Pt can reduce the environmental footprint of the PEMFC.[195] In general, the global recycling of PGM has the potential to over 95% recovery.[196] For PGM used in PEMFC specifically, Sharma et al. have

shown that Pt can be dissolved from a gas diffusion electrode by electrochemical dissolution in HCl, with a recovery efficiency of more than 90% when producing a new catalyst from the recycled material.[197,198] However, the gas diffusion electrode was never assembled or cycled before dissolution, and the recovery efficiency may therefore be lower considering Pt dissolution and migration into the membrane and the fact that Pt particles adhered to the membrane upon disassembly. Duclos et al. studied the recovery of PtCo from an MEA by two different hydrometallurgical routes. Both methods include incineration of fluorinated polymers, causing emissions, and the authors point out the need for recycling of the fluorinated polymers as well. The ion exchange resin and solvent separation methods
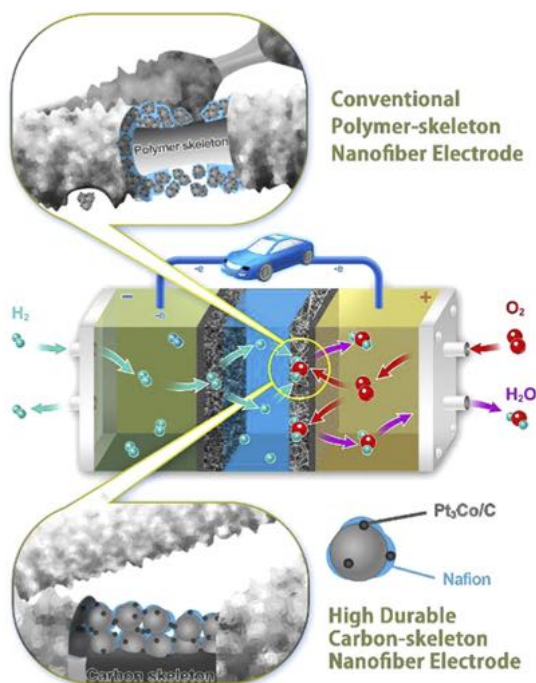
FIG. 14. Illustration of the CNW-supported Pt–Co catalyst in the PEMFC setup, which reached 8.2 W/mg$_{Pt}$.[9] Reprinted with permission from Gao *et al.*, ACS Sustainable Chem. Eng. **8**, 13030 (2020). Copyright 2020 American Chemical Society.

gave Pt yield of 77% and 83%, respectively, while the ion exchange resin is advantageous with respect to synthesizing a new catalyst material from the product.[4]

VI. SUMMARY

Pt remains as the most important component of reliable and efficient PEMFC ORR electrocatalysts—and will continue to do so for the time being. The cost of the fuel cell stacks can be efficiently reduced by lowering the amount of Pt used and by increasing its efficiency through alloying, shape-tuning, and creating NPs with Pt-rich surfaces.

Among the most recent studies, the most promising way for maximizing the efficiency and durability lies in the combination of different approaches: the alloying of Pt with a transition metal, the synthesis of hollow NPs, and the fixation of NPs in an enclosing carbon-based structure, which can prevent the most prominent durability issues, namely, the growth of Pt NPs, and the leaching of Pt alloys. With further reduction of the amount of Pt used and recycling of the MEA after utilization, the impact of the Pt in the PEMFC can be reduced to levels comparable to that from PGMs used in the catalysts of internal combustion engines.

Another important durability issue occurring at high potential cycling, the corrosion of the carbon support, can be tackled by replacing or modifying the carbon support material. Many different approaches and materials have been studied to modify the support of PGM-based catalysts, showing desirable improvements. Considering the high amount of studies on the field in general, optimized support structures can soon be combined with optimized PGM catalysts in order to eliminate all durability issues and to provide reliable performance at low Pt loading. As there is a well-established industry for the production of carbon supported Pt NPs, these improvements can be implemented without needing major changes, and so, the way to commercialization is relatively short.

Regarding PGM-free catalysts, sufficient durability is the key issue. As a result of this being a new technology, current work focuses on performance optimization, while works focusing on their durability are rather scarce. For the SACs, solutions have to be found to effectively prevent metal dissolution in acidic environments and increase durability during potential cycling. Furthermore, optimization of the catalyst layer in the PEMFC, achieving a more homogeneous deposition, and upscaling of the fabrication are key to bringing these catalysts closer to broad commercialization. Otherwise, SACs are readily applicable in AEMFCs.

AUTHORS' CONTRIBUTIONS

L.M. and K.E. contributed equally to this work.

ACKNOWLEDGMENTS

DATA AVAILABILITY

Data sharing is not applicable to this article as no new data were created or analyzed in this study.

REFERENCES

[1] B. G. Pollet, S. S. Kocha, and I. Staffell, "Current status of automotive fuel cells for sustainable transport," Curr. Opin. Electrochem. **16**, 90 (2019).

[2] Fuel Cell Technologies Office, "DOE technical targets for polymer electrolyte membrane fuel cell components," in Multi-Year Research, Development, and Demonstration Plan (2017), Chap. 3.4 Fuel Cells.

[3] M. Shao, Q. Chang, J.-P. Dodelet, and R. Chenitz, "Recent advances in electrocatalysts for oxygen reduction reaction," Chem. Rev. **116**, 3594 (2016).

[4] L. Duclos, R. Chattot, L. Dubau, P.-X. Thivel, G. Mandil, V. Laforest, M. Bolloli, R. Vincent, and L. Svecova, "Closing the loop: Life cycle assessment and optimization of a PEMFC platinum-based catalyst recycling process," Green Chem. **22**, 1919 (2020).

[5] Q. Deng, J. Han, J. Zhao, G. Chen, T. Vegge, and H. A. Hansen, "1D metal-dithiolene wires as a new class of bi-functional oxygen reduction and evolution single-atom electrocatalysts," J. Catal. **393**, 140 (2021).

[6]A. Jain, Z. Wang, and J. K. Nørskov, "Stable two-dimensional materials for oxygen reduction and oxygen evolution reactions," ACS Energy Lett. **4**, 1410 (2019).

[7]T. Yoshida and K. Kojima, "Toyota MIRAI fuel cell vehicle and progress toward a future hydrogen society," Interface **24**, 45 (2015).

[8]J. Li, S. Sharma, X. Liu, Y.-T. Pan, J. S. Spendelow, M. Chi, Y. Jia, P. Zhang, D. A. Cullen, Z. Xi *et al.*, "Hard-magnet L1$_0$-CoPt nanoparticles advance fuel cell catalysis," Joule **3**, 124 (2019).

[9]Y. Gao, M. Hou, L. He, M. Qi, H. Chen, W. luo, and Z. Shao, "Performance- and durability-enhanced carbon-skeleton nanofiber electrode with Pt$_3$Co/C for PEMFCs," ACS Sustainable Chem. Eng. **8**, 13030 (2020).

[10]B. Hu, X. Deng, L. Zhou, J. Dai, G. Yang, W. Tan, W. Zhou, and Z. Shao, "Facile synthesis of synergistic Pt/(Co-N)@C composites as alternative oxygen-reduction electrode of PEMFCs with attractive activity and durability," Compos., Part B **193**, 108012 (2020).

[11]J. Sriwannaboot, A. Kannan, and N. Tantavichet, "Pulse-reverse electrodeposition of Pt-Co bimetallic catalysts for oxygen reduction reaction in acidic medium," Int. J. Hydrogen Energy **45**, 7025 (2020).

[12]X. Tian, X. Zhao, Y.-Q. Su, L. Wang, H. Wang, D. Dang, B. Chi, H. Liu, E. J. M. Hensen, X. W. Lou, and B. Y. Xia, "Engineering bunched Pt-Ni alloy nanocages for efficient oxygen reduction in practical fuel cells," Science **366**, 850 (2019).

[13]Q. Zhao, C. Wang, H. Wang, J. Wang, Y. Tang, Z. Mao, and K. Sasaki, "H$_2$-induced thermal treatment significantly influences the development of a high performance low-platinum core-shell PtNi/C alloyed oxygen reduction catalyst," Int. J. Energy Res. **44**, 4773 (2020).

[14]P. Mardle, G. Thirunavukkarasu, S. Guan, Y.-L. Chiu, and S. Du, "Comparative study of PtNi nanowire array electrodes toward oxygen reduction reaction by half-cell measurement and PEMFC test," ACS Appl. Mater. Interfaces **12**, 42832 (2020).

[15]Z. Zhao, M. D. Hossain, C. Xu, Z. Lu, Y.-S. Liu, S.-H. Hsieh, I. Lee, W. Gao, J. Yang, B. V. Merinov, W. Xue, Z. Liu, J. Zhou, Z. Luo, X. Pan, F. Zaera, J. Guo, X. Duan, W. A. Goddard III, and Y. Huang, "Tailoring a three-phase microenvironment for high-performance oxygen reduction reaction in proton exchange membrane fuel cells," Matter **3**, 1774 (2020).

[16]B. Li, J. Wang, X. Gao, C. Qin, D. Yang, H. Lv, Q. Xiao, and C. Zhang, "High performance octahedral PtNi/C catalysts investigated from rotating disk electrode to membrane electrode assembly," Nano Res. **12**, 281 (2019).

[17]Z. Jiang, Y. Liu, L. Huang, W. H. Gong, and P. K. Shen, "A facile method to synthesize Pt-Ni octahedral nanoparticles with porous and open structure features for enhanced oxygen reduction catalysis," ACS Sustainable Chem. Eng. **7**, 8109 (2019).

[18]F. Kong, Z. Ren, M. N. Banis, L. Du, X. Zhou, G. Chen, L. Zhang, J. Li, S. Wang, M. Li, K. Doyle-Davis, Y. Ma, R. Li, A. Young, L. Yang, M. Markiewicz, Y. Tong, G. Yin, C. Du, J. Luo, and X. Sun, "Active and stable Pt-Ni alloy octahedra catalyst for oxygen reduction via near-surface atomical engineering," ACS Catal. **10**, 4205 (2020).

[19]S. Kühl, M. Gocyla, H. Heyen, S. Selve, M. Heggen, R. E. Dunin-Borkowski, and P. Strasser, "Concave curvature facets benefit oxygen electroreduction catalysis on octahedral shaped PtNi nanocatalysts," J. Mater. Chem. A **7**, 1149 (2019).

[20]J. Wang, X. Zhou, B. Li, D. Yang, H. Lu, Q. Xiao, P. Ming, X. Wei, and C. Zhang, "Highly efficient, cell reversal resistant PEMFC based on PtNi/C octahedral and OER composite catalyst," Int. J. Hydrogen Energy **45**, 8930 (2020).

[21]W. Gong, Z. Jiang, R. Wu, Y. Liu, L. Huang, N. Hu, P. Tsiakaras, and P. K. Shen, "Cross-double dumbbell-like Pt-Ni nanostructures with enhanced catalytic performance toward the reactions of oxygen reduction and methanol oxidation," Appl. Catal. B **246**, 277 (2019).

[22]J. Wang, G. Wu, W. Wang, W. Xuan, J. Jiang, J. Wang, L. Li, W.-F. Lin, W. Ding, and Z. Wei, "A neural-network-like catalyst structure for the oxygen reduction reaction: Carbon nanotube bridged hollow PtCo alloy nanoparticles in a MOF-like matrix for energy technologies," J. Mater. Chem. A **7**, 19786 (2019).

[23]Q. Zhao, C. Wang, H. Wang, J. Wang, Y. Tang, Z. Mao, and K. Sasaki, "Synthesis of a high-performance low-platinum PtAg/C alloyed oxygen reduction catalyst through the gradual reduction method," New J. Chem. **44**, 3728 (2020).

[24]Y. Feng, Q. Shao, F. Lv, L. Bu, J. Guo, S. Guo, and X. Huang, "Intermetallic PtBi nanoplates boost oxygen reduction catalysis with superior tolerance over chemical fuels," Adv. Sci. **7**, 1800178 (2020).

[25]M. Gatalo, F. Ruiz-Zepeda, N. Hodnik, G. Dražić, M. Bele, and M. Gaberšček, "Insights into thermal annealing of highly-active PtCu$_3$/C oxygen reduction reaction electrocatalyst: An in-situ heating transmission electron microscopy study," Nano Energy **63**, 103892 (2019).

[26]L. Zhang, X.-F. Zhang, X.-L. Chen, A.-J. Wang, D.-M. Han, Z.-G. Wang, and J.-J. Feng, "Facile solvothermal synthesis of Pt$_{71}$Co$_{29}$ lamellar nanoflowers as an efficient catalyst for oxygen reduction and methanol oxidation reactions," J. Colloid Interface Sci. **536**, 556 (2019).

[27]Z. Yang, L. Shang, X. Xiong, R. Shi, G. I. N. Waterhouse, and T. Zhang, "Hollow PtFe alloy nanoparticles derived from Pt-Fe$_3$O$_4$ dimers through a silica-protection reduction strategy as efficient oxygen reduction electrocatalysts," Chem. Eur. J. **26**, 4090 (2020).

[28]M. Gong, J. Zhu, M. Liu, P. Liu, Z. Deng, T. Shen, T. Zhao, R. Lin, Y. Lu, S. Yang, Z. Liang, S. M. Bak, E. Stavitski, Q. Wu, R. R. Adzic, H. L. Xin, and D. Wang, "Optimizing PtFe intermetallics for oxygen reduction reaction: From DFT screening to in situ XAFS characterization," Nanoscale **11**, 20301 (2019).

[29]Z. Meng, F. Xiao, Z. Wei, X. Guo, Y. Zhu, Y. Liu, G. Li, Z.-Q. Yu, M. Shao, and W.-Y. Wong, "Direct synthesis of L1$_0$-FePt nanoparticles from single-source bimetallic complex and their electrocatalytic applications in oxygen reduction and hydrogen evolution reactions," Nano Res. **12**, 2954 (2019).

[30]J. Choi, Y. J. Lee, D. Park, H. Jeong, S. Shin, H. Yun, J. Lim, J. Han, E. J. Kim, S. S. Jeon, Y. Jung, H. Lee, and B. J. Kim, "Highly durable fuel cell catalysts using crosslinkable block copolymer-based carbon supports with ultralow Pt loadings," Energy Environ. Sci. **13**, 4921 (2020).

[31]J. Zhu, A. O. Elnabawy, Z. Lyu, M. Xie, E. A. Murray, Z. Chen, W. Jin, M. Mavrikakis, and Y. Xia, "Facet-controlled Pt–Ir nanocrystals with substantially enhanced activity and durability towards oxygen reduction," Mater. Today **35**, 69 (2020).

[32]J.-Y. Park, H.-S. Park, S.-B. Han, D.-H. Kwak, J.-E. Won, T. Lim, and K.-W. Park, "Organic ligand-free PtIr alloy nanostructures for superior oxygen reduction and evolution reactions," J. Ind. Eng. Chem. **77**, 105 (2019).

[33]D. Fang, X. Tang, L. Yang, D. Xu, H. Zhang, S. Sun, Z. Shao, and B. Yi, "Facile synthesis of Pt-decorated Ir black as a bifunctional oxygen catalyst for oxygen reduction and evolution reactions," Nanoscale **11**, 9091 (2019).

[34]J. Bak, H. Kim, S. Lee, M. Kim, E.-J. Kim, J. Roh, J. Shin, C. H. Choi, and E. Cho, "Boosting the role of Ir in mitigating corrosion of carbon support by alloying with Pt," ACS Catal. **10**, 12300 (2020).

[35]A. Brouzgou, A. Seretis, S. Song, P. K. Shen, and P. Tsiakaras, "CO tolerance and durability study of PtMe (Me = Ir or Pd) electrocatalysts for H$_2$-PEMFC application," Int. J. Hydrogen Energy (published online, 2020).

[36]H. Gao, S. Liao, Y. Zhang, X. Jia, L. Zhou, Z. Zheng, and Y. Yang, "Methanol-tolerant SePt/C: Effects of Se content on the structure and electrocatalytic performance for oxygen reduction reaction," Ionics **26**, 1315 (2020).

[37]H. Wang, S. Yin, C. Li, K. Deng, Z. Wang, Y. Xu, X. Li, H. Xue, and L. Wang, "Direct synthesis of superlong Pt–Te mesoporous nanotubes for electrocatalytic oxygen reduction," J. Mater. Chem. A **7**, 1711 (2019).

[38]J. Liang, Z. Zhao, N. Li, X. Wang, S. Li, X. Liu, T. Wang, G. Lu, D. Wang, B. J. Hwang, Y. Huang, D. Su, and Q. Li, "Biaxial strains mediated oxygen reduction electrocatalysis on Fenton reaction resistant L1$_0$-PtZn fuel cell cathode," Adv. Energy Mater. **10**, 2000179 (2020).

[39]F. Dionigi, C. C. Weber, M. Primbs, M. Gocyla, A. Martinez Bonastre, C. Spöri, H. Schmies, E. Hornberger, S. Kühl, J. Drnec, M. Heggen, J. Sharman, R. E. Dunin-Borkowski, and P. Strasser, "Controlling near-surface Ni composition in octahedral PtNi(Mo) nanoparticles by Mo doping for a highly active oxygen reduction reaction catalyst," Nano Lett. **19**, 6876 (2019).

[40]L. Cao, Z. Zhao, Z. Liu, W. Gao, S. Dai, J. Gha, W. Xue, H. Sun, X. Duan, X. Pan, T. Mueller, and Y. Huang, "Differential surface elemental distribution leads to significantly enhanced stability of PtNi-based ORR catalysts," Matter **1**, 1567 (2019).

[41]X. Shen, S. Dai, Y. Pan, L. Yao, J. Yang, X. Pan, J. Zeng, and Z. Peng, "Tuning electronic structure and lattice diffusion barrier of ternary Pt–In–Ni for both

improved activity and stability properties in oxygen reduction electrocatalysis," ACS Catal. **9**, 11431 (2019).

[42]W. Tu, W. Luo, C. Chen, K. Chen, E. Zhu, Z. Zhao, Z. Wang, T. Hu, H. Zai, X. Ke, M. Sui, P. Chen, Q. Zhang, Q. Chen, Y. Li, and Y. Huang, "Tungsten as 'adhesive' in Pt$_2$CuW$_{0.25}$ ternary alloy for highly durable oxygen reduction electrocatalysis," Adv. Funct. Mater. **30**, 1908230 (2020).

[43]Z. Wang, X. Yao, Y. Kang, D. Xia, and L. Gan, "Rational development of structurally ordered platinum ternary intermetallic electrocatalysts for oxygen reduction reaction," Catalysts **9**, 569 (2019).

[44]R. Sriphathoorat, K. Wang, and P. K. Shen, "Trimetallic hollow Pt–Ni–Co nanodendrites as efficient anodic electrocatalysts," ACS Appl. Energy Mater. **2**, 961 (2019).

[45]R. Lin, L. Che, D. Shen, and X. Cai, "High durability of Pt–Ni–Ir/C ternary catalyst of PEMFC by stepwise reduction synthesis," Electrochim. Acta **330**, 135251 (2020).

[46]X. Wang, L. Zhang, F. Wang, J. Yu, and H. Zhu, "Nickel-introduced structurally ordered PtCuNi/C as high performance electrocatalyst for oxygen reduction reaction," Prog. Nat. Sci. **30**, 905 (2020).

[47]C. He, Z. Ma, Q. Wu, Y. Cai, Y. Huang, K. Liu, Y. Fan, H. Wang, Q. Li, J. Qi, Q. Li, and X. Wu, "Promoting the ORR catalysis of Pt-Fe intermetallic catalysts by increasing atomic utilization and electronic regulation," Electrochim. Acta **330**, 135119 (2020).

[48]H. Chen, T. Zheng, Q. He, L. Shang, G. Wang, Q. Wang, X. Wang, X. Shi, M. Gu, and Z. Jiang, "Local coordination and ordering engineering to design efficient core-shell oxygen reduction catalysts," J. Electrochem. Soc. **167**, 144501 (2020).

[49]L. Huang, M. Wei, N. Hu, P. Tsiakaras, and P. K. Shen, "Molybdenum-modified and vertex-reinforced quaternary hexapod nanoskeletons as efficient electrocatalysts for methanol oxidation and oxygen reduction reaction," Appl. Catal. B **258**, 117974 (2019).

[50]W. Tu, K. Chen, L. Zhu, H. Zai, E. Bin, X. Ke, C. Chen, M. Sui, Q. Chen, and Y. Li, "Tungsten-doping-induced surface reconstruction of porous ternary Pt-based alloy electrocatalyst for oxygen reduction," Adv. Funct. Mater. **29**, 1807070 (2019).

[51]T. Chu, M. Xie, D. Yang, P. Ming, B. Li, and C. Zhang, "Highly active and durable carbon support Pt-rare earth catalyst for proton exchange membrane fuel cell," Int. J. Hydrogen Energy **45**, 27291 (2020).

[52]R. Guo, W. Bi, K. Zhang, Y. Liu, C. Wang, Y. Zheng, and M. Jin, "Phosphorization treatment improves the catalytic activity and durability of platinum catalysts toward oxygen reduction reaction," Chem. Mater. **31**, 8205 (2019).

[53]Z. Pu, R. Cheng, J. Zhao, Z. Hu, C. Li, W. Li, P. Wang, I. S. Amiinu, Z. Wang, M. Wang, D. Chen, and S. Mu, "Anion-modulated platinum for high-performance multifunctional electrocatalysis toward HER, HOR, and ORR," iScience **23**, 101793 (2020).

[54]Y. Xiong, Y. Ma, L. Zou, S. Han, H. Chen, S. Wang, M. Gu, Y. Shen, L. Zhang, Z. Xia, J. Li, and H. Yang, "N-doping induced tensile-strained Pt nanoparticles ensuring an excellent durability of the oxygen reduction reaction," J. Catal. **382**, 247 (2019).

[55]M. Luo, Z. Zhao, Y. Zhang, Y. Sun, Y. Xing, F. Lv, Y. Yang, X. Zhang, S. Hwang, Y. Qin, J.-Y. Ma, F. Lin, D. Su, G. Lu, and S. Guo, "PdMo bimetallene for oxygen reduction catalysis," Nature **574**, 81 (2019).

[56]L. Wang, Y. Zhou, J. Timoshenko, S. Liu, Q. Qiao, K. Kisslinger, M. Cuiffo, Y.-C. Chuang, X. Zuo, Y. Xue, Y. Guo, C. Pan, H. Li, C.-Y. Nam, S. Bliznakov, P. Liu, A. I. Frenkel, Y. Zhu, and M. H. Rafailovich, "Designing nanoplatelet alloy/Nafion catalytic interface for optimization of PEMFCs: Performance, durability, and CO resistance," ACS Catal. **9**, 1446 (2019).

[57]J. Uribe-Godínez and A. Altamirano-Gutiérrez, "Systematic study of iridium-based catalysts derived from Ir$_4$(CO)$_{12}$, capable to perform the ORR and HOR," Catal. Today (published online, 2020).

[58]F. Chang, Z. Bai, M. Li, M. Ren, T. Liu, L. Yang, C.-J. Zhong, and J. Lu, "Strain-modulated platinum-palladium nanowires for oxygen reduction reaction," Nano Lett. **20**, 2416 (2020).

[59]X. Deng, S. Yin, X. Wu, M. Sun, Z. Li, Z. Xie, Y. Liang, and Q. Huang, "Scalable preparation of PtPd/carbon nanowires in the form of membrane as highly stable electrocatalysts for oxygen reduction reaction," Int. J. Hydrogen Energy **44**, 2752 (2019).

[60]R. Wu, Y. Li, W. Gong, and P. K. Shen, "One-pot synthesis of Pt–Pd bimetallic nanodendrites with enhanced electrocatalytic activity for oxygen reduction reaction," ACS Sustainable Chem. Eng. **7**, 8419 (2019).

[61]R. Wu, P. Tsiakaras, and P. K. Shen, "Facile synthesis of bimetallic Pt–Pd symmetry-broken concave nanocubes and their enhanced activity toward oxygen reduction reaction," Appl. Catal. B **251**, 49 (2019).

[62]M. Zhou, H. Wang, A. O. Elnabawy, Z. D. Hood, M. Chi, P. Xiao, Y. Zhang, M. Mavrikakis, and Y. Xia, "Facile one-pot synthesis of Pd@Pt$_{1L}$ octahedra with enhanced activity and durability toward oxygen reduction," Chem. Mater. **31**, 1370 (2019).

[63]Y. Y. Rivera-Lugo, K. I. Pérez-Muñoz, B. Trujillo-Navarrete, C. Silva-Carrillo, E. A. Reynoso-Soto, J. C. Calva Yañez, S. W. Lin, J. R. Flores-Hernández, and R. M. Félix-Navarro, "PtPd hybrid composite catalysts as cathodes for proton exchange membrane fuel cells," Energies **13**, 316 (2020).

[64]H. Chen, R. Wu, and P. K. Shen, "One-pot fabrication of site-selective hexapod PtPdCu concave rhombic dodecahedrons as highly efficient catalysts for electrocatalysis," ACS Sustainable Chem. Eng. **8**, 1520 (2020).

[65]Y. Deng, S. Yin, Y. Liu, Y. Lu, X. Cao, L. Wang, H. Wang, Y. Zhao, and H. Gu, "Mesoporous AgPdPt nanotubes as electrocatalysts for the oxygen reduction reaction," ACS Appl. Nano Mater. **2**, 1876 (2019).

[66]F. Kong, S. Liu, J. Li, L. Du, M. N. Banis, L. Zhang, G. Chen, K. Doyle-Davis, J. Liang, S. Wang, F. Zhao, R. Li, C. Du, G. Yin, Z. Zhao, and X. Sun, "Trimetallic Pt–Pd–Ni octahedral nanocages with subnanometer thick-wall towards high oxygen reduction reaction," Nano Energy **64**, 103890 (2019).

[67]C. Li, Y. Xu, K. Deng, S. Yin, Z. Wang, H. Xue, X. Li, L. Wang, and H. Wang, "Metal-nonmetal nanoarchitectures: Quaternary PtPdNiP mesoporous nanospheres for enhanced oxygen reduction electrocatalysis," J. Mater. Chem. A **7**, 3910 (2019).

[68]H. Nan, Y.-Q. Su, C. Tang, R. Cao, D. Li, J. Yu, Q. Liu, Y. Deng, and X. Tian, "Engineering the electronic and strained interface for high activity of PdM$_{core}$@Pt$_{monolayer}$ electrocatalysts for oxygen reduction reaction," Sci. Bull. **65**, 1396 (2020).

[69]H. Wang, Y. Li, K. Deng, C. Li, H. Xue, Z. Wang, X. Li, Y. Xu, and L. Wang, "Trimetallic PtPdNi-truncated octahedral nanocages with a well-defined mesoporous surface for enhanced oxygen reduction electrocatalysis," ACS Appl. Mater. Interfaces **11**, 4252 (2019).

[70]K. Deng, Y. Xu, Z. Dai, H. Yu, S. Yin, Z. Wang, X. Li, L. Wang, and H. Wang, "Enhanced oxygen reduction and methanol oxidation electrocatalysis over bifunctional PtPdIr mesoporous hollow nanospheres," Chem.-Asian J. **14**, 3868 (2019).

[71]C. M. Sánchez-Sánchez, J. Solla-Gullón, F. J. Vidal-Iglesias, A. Aldaz, V. Montiel, and E. Herrero, "Imaging structure sensitive catalysis on different shape-controlled platinum nanoparticles," J. Am. Chem. Soc. **132**, 5622 (2010).

[72]J.-C. Dong, X.-G. Zhang, V. Briega-Martos, X. Jin, J. Yang, S. Chen, Z.-L. Yang, D.-Y. Wu, J. M. Feliu, C. T. Williams, Z.-Q. Tian, and J.-F. Li, "In situ Raman spectroscopic evidence for oxygen reduction reaction intermediates at platinum single-crystal surfaces," Nat. Energy **4**, 60 (2019).

[73]R. Chen, Z. Cao, Z. Lyu, M. Xie, Y. Shi, and Y. Xia, "Continuous and scalable synthesis of Pt multipods with enhanced electrocatalytic activity toward the oxygen reduction reaction," ChemNanoMat **5**, 599 (2019).

[74]H. Cheng, Z. Cao, Z. Chen, M. Zhao, M. Xie, Z. Lyu, M. Chi, and Y. Xia, "Catalytic system based on sub-2 nm Pt particles and its extraordinary activity and durability for oxygen reduction," Nano Lett. **19**, 4997 (2019).

[75]R. Chen, M. Cao, J. Wang, H. Li, and R. Cao, "Decamethylcucurbit[5]uril based supramolecular assemblies as efficient electrocatalysts for oxygen reduction reaction," Chem. Commun. **55**, 11687 (2019).

[76]J. Gan, W. Luo, W. Chen, J. Guo, Z. Xiang, B. Chen, F. Yang, Y. Cao, F. Song, X. Duan, and X. Zhou, "Mechanistic understanding of size-dependent oxygen reduction activity and selectivity over Pt/CNT nanocatalysts," Eur. J. Inorg. Chem. **2019**, 3210.

[77]J. Gan, J. Zhang, B. Zhang, W. Chen, D. Niu, Y. Qin, X. Duan, and X. Zhou, "Active sites engineering of Pt/CNT oxygen reduction catalysts by atomic layer deposition," J. Energy Chem. **45**, 59 (2020).

[78]H. R. Litkohi, A. Bahari, and M. P. Gatabi, "Improved oxygen reduction reaction in PEMFCs by functionalized CNTs supported Pt-M (M = Fe, Ni, Fe-Ni) bi- and

140

tri-metallic nanoparticles as efficient electrocatalyst," Int. J. Hydrogen Energy **45**, 23543 (2020).

[79]R. Wang, Z. Chang, Z. Fang, T. Xiao, Z. Zhu, B. Ye, C. Xu, and J. Cheng, "Pt nanowire/Ti₃C₂Tₓ-CNT hybrids catalysts for the high performance oxygen reduction reaction for high temperature PEMFC," Int. J. Hydrogen Energy **45**, 28190 (2020).

[80]C. Xu, C. Fan, X. Zhang, H. Chen, X. Liu, Z. Fu, R. Wang, T. Hong, and J. Cheng, "MXene (Ti₃C₂Tₓ) and carbon nanotube hybrid-supported platinum catalysts for the high-performance oxygen reduction reaction in PEMFC," ACS Appl. Mater. Interfaces **12**, 19539 (2020).

[81]S. Chung, K. Ham, S. Kang, H. Ju, and J. Lee, "Enhanced corrosion tolerance and highly durable ORR activity by low Pt electrocatalyst on unique pore structured CNF in PEM fuel cell," Electrochim. Acta **348**, 136346 (2020).

[82]C. He, S. Sankarasubramanian, I. Matanovic, P. Atanassov, and V. Ramani, "Understanding the oxygen reduction reaction activity and oxidative stability of Pt supported on Nb-doped TiO₂," ChemSusChem **12**, 3468 (2019).

[83]C. Xu, J. Yang, E. Liu, Q. Jia, G. M. Veith, G. Nair, S. DiPietro, K. Sun, J. Chen, P. Pietrasz, Z. Lu, M. Jagner, K. K. Gath, S. Mukerjee, and J. R. Waldecker, "Physical vapor deposition process for engineering Pt based oxygen reduction reaction catalysts on NbOₓ templated carbon support," J. Power Sources **451**, 227709 (2020).

[84]Z. Ma, S. Li, L. Wu, L. Song, G. Jiang, Z. Liang, D. Su, Y. Zhu, R. R. Adzic, J. X. Wang, and Z. Chen, "NbOₓ nano-nail with a Pt head embedded in carbon as a highly active and durable oxygen reduction catalyst," Nano Energy **69**, 104455 (2020).

[85]E. Lee, C. Park, D. W. Lee, G. Lee, H.-Y. Park, J. H. Jang, H.-J. Kim, Y.-E. Sung, Y. Tak, and S. J. Yoo, "Tunable synthesis of N,C-codoped Ti³⁺-enriched titanium oxide support for highly durable PEMFC cathode," ACS Catal. **10**, 12080 (2020).

[86]S. Hussain, H. Erikson, N. Kongi, A. Tarre, P. Ritslaid, A. Kikas, V. Kisand, J. Kozlova, J. Aarik, A. Tamm, V. Sammelselg, and K. Tammeveski, "Platinum sputtered on Nb-doped TiO₂ films prepared by ALD: Highly active and durable carbon-free ORR electrocatalyst," J. Electrochem. Soc. **167**, 164505 (2020).

[87]R. A. MoghadamEsfahani, S. K. Vankova, E. B. Easton, I. I. Ebralidze, and S. Specchia, "A hybrid Pt/NbO/CNTs catalyst with high activity and durability for oxygen reduction in PEMFC," Renewable Energy **154**, 913 (2020).

[88]R. Yue, M. Xia, M. Wang, P. Chen, W. Gong, S. Liao, Z. Li, F. Gao, L. Zhang, and J. Wang, "TiN and TiC as stable and promising supports for oxygen reduction reaction: Theoretical and experimental study," Appl. Surf. Sci. **495**, 143620 (2019).

[89]J. Kim, S.-I. Kim, S. G. Jo, N. E. Hong, B. Ye, S. Lee, H. S. Dow, D. H. Lee, and J. W. Lee, "Enhanced activity and durability of Pt nanoparticles supported on reduced graphene oxide for oxygen reduction catalysts of proton exchange membrane fuel cells," Catal. Today **352**, 10 (2020).

[90]L. Song, Z. Liang, K. Nagamori, H. Igarashi, M. B. Vukmirovic, R. R. Adzic, and K. Sasaki, "Enhancing oxygen reduction performance of Pt monolayer catalysts by Pd(111) nanosheets on WNi substrates," ACS Catal. **10**, 4290 (2020).

[91]M. A. Abdelkareem, T. Wilberforce, K. Elsaid, E. T. Sayed, E. A. M. Abdelghani, and A. G. Olabi, "Transition metal carbides and nitrides as oxygen reduction reaction catalyst or catalyst support in proton exchange membrane fuel cells (PEMFCs)," Int. J. Hydrogen Energy (published online, 2020).

[92]H. Yang, Y. Ko, W. Lee, A. Züttel, and W. Kim, "Nitrogen-doped carbon black supported Pt-M (M = Pd, Fe, Ni) alloy catalysts for oxygen reduction reaction in proton exchange membrane fuel cell," Mater. Today Energy **13**, 374 (2019).

[93]Z. Qiao, S. Hwang, X. Li, C. Wang, W. Samarakoon, S. Karakalos, D. Li, M. Chen, Y. He, M. Wang, Z. Liu, G. Wang, H. Zhou, Z. Feng, D. Su, J. S. Spendelow, and G. Wu, "3D porous graphitic nanocarbon for enhancing the performance and durability of Pt catalysts: A balance between graphitization and hierarchical porosity," Energy Environ. Sci. **12**, 2830 (2019).

[94]S. Ott, A. Orfanidi, H. Schmies, B. Anke, H. N. Nong, J. Hübner, U. Gernert, M. Gliech, M. Lerch, and P. Strasser, "Ionomer distribution control in porous carbon-supported catalyst layers for high-power and low Pt-loaded proton exchange membrane fuel cells," Nat. Mater **19**, 77 (2020).

[95]E. Padgett, V. Yarlagadda, M. E. Holtz, M. Ko, B. D. A. Levin, R. S. Kukreja, J. M. Ziegelbauer, R. N. Andrews, J. Ilavsky, and A. Kongkanand, "Mitigation of PEM fuel cell catalyst degradation with porous carbon supports," J. Electrochem. Soc. **166**, F198 (2019).

[96]F. Zhou, Y. Yan, S. Guan, W. Guo, M. Sun, and M. Pan, "Solving Nafion poisoning of ORR catalysts with an accessible layer: Designing a nanostructured core-shell Pt/C catalyst via a one-step self-assembly for PEMFC," Int. J. Energy Res. **44**, 10155 (2020).

[97]Y. Nie and Z. Wei, "Surface-confined Pt-based catalysts for strengthening oxygen reduction performance," Prog. Nat. Sci. **30**, 796 (2020).

[98]W. Zhao, Y. Ye, W. Jiang, J. Li, H. Tang, J. Hu, L. Du, Z. Cui, and S. Liao, "Mesoporous carbon confined intermetallic nanoparticles as highly durable electrocatalysts for the oxygen reduction reaction," J. Mater. Chem. A **8**, 15822 (2020).

[99]Y. Li, J. Hart, L. Profitt, S. Intikhab, S. Chatterjee, M. Taheri, and J. Snyder, "Sequential capacitive deposition of ionic liquids for conformal thin film coatings on oxygen reduction reaction electrocatalysts," ACS Catal. **9**, 9311 (2019).

[100]M. Xiao, J. Zhu, G. Li, N. Li, S. Li, Z. P. Cano, L. Ma, P. Cui, P. Xu, G. Jiang, H. Jin, S. Wang, T. Wu, J. Lu, A. Yu, D. Su, and Z. Chen, "A single-atom iridium heterogeneous catalyst in oxygen reduction reaction," Angew. Chem. **131**, 9742 (2019).

[101]M. Xiao, L. Gao, Y. Wang, X. Wang, J. Zhu, Z. Jin, C. Liu, H. Chen, G. Li, J. Ge, Q. He, Z. Wu, Z. Chen, and W. Xing, "Engineering energy level of metal center: Ru single-atom site for efficient and durable oxygen reduction catalysis," J. Am. Chem. Soc. **141**, 19800 (2019).

[102]Q. Liu, Y. Li, L. Zheng, J. Shang, X. Liu, R. Yu, and J. Shui, "Sequential synthesis and active-site coordination principle of precious metal single-atom catalysts for oxygen reduction reaction and PEM fuel cells," Adv. Energy Mater. **10**, 2000689 (2020).

[103]M. Zhao, J. Holder, Z. Chen, M. Xie, Z. Cao, M. Chi, and Y. Xia, "Facile synthesis of Pt icosahedral nanocrystals with controllable sizes for the evaluation of size-dependent activity toward oxygen reduction," ChemCatChem **11**, 2458 (2019).

[104]W. Lei, M. Li, L. He, X. Meng, Z. Mu, Y. Yu, F. M. Ross, and W. Yang, "A general strategy for bimetallic Pt-based nano-branched structures as highly active and stable oxygen reduction and methanol oxidation bifunctional catalysts," Nano Res. **13**, 638 (2020).

[105]Z. Wang, X. Yao, Y. Kang, L. Miao, D. Xia, and L. Gan, "Structurally ordered low-Pt intermetallic electrocatalysts toward durably high oxygen reduction reaction activity," Adv. Funct. Mater. **29**, 1902987 (2019).

[106]S. Yin, Z. Wang, X. Qian, D. Yang, Y. Xu, X. Li, L. Wang, and H. Wang, "PtM (M = Co, Ni) mesoporous nanotubes as bifunctional electrocatalysts for oxygen reduction and methanol oxidation," ACS Sustainable Chem. Eng. **7**, 7960 (2019).

[107]Q. Liu, L. Du, G. Fu, Z. Cui, Y. Li, D. Dang, X. Gao, Q. Zheng, and J. B. Goodenough, "Structurally ordered Fe₃Pt nanoparticles on robust nitride support as a high performance catalyst for the oxygen reduction reaction," Adv. Energy Mater. **9**, 1803040 (2019).

[108]D. Wang, G. Hu, P. Yang, X. Pan, H. Xu, L. Liu, J. Zhang, and M. An, "Using DMH as a complexing agent for pulse electrodeposition of platinum nanoparticles towards oxygen reduction reaction," Ionics **26**, 3473 (2020).

[109]B. Ergul-Yilmaz, Z. Yang, M. L. Perry, K. L. More, N. Macauley, R. L. Borup, and T. Karabacak, "Microstructural evolution and ORR activity of nanocolumnar platinum thin films with different mass loadings grown by high pressure sputtering," J. Electrochem. Soc. **167**, 134514 (2020).

[110]L. Mølmen, A. Alexandersson, and P. Leisner, "Surface technology should improve PEM fuel cell performance," Trans. IMF **97**, 112 (2019).

[111]V. Beermann, M. E. Holtz, E. Padgett, J. F. de Araujo, D. A. Muller, and P. Strasser, "Real-time imaging of activation and degradation of carbon supported octahedral Pt–Ni alloy fuel cell catalysts at the nanoscale using in situ electrochemical liquid cell STEM," Energy Environ. Sci. **12**, 2476 (2019).

[112]R. Mom, L. Frevel, J.-J. Velasco-Vélez, M. Plodinec, A. Knop-Gericke, and R. Schlögl, "The oxidation of platinum under wet conditions observed by electrochemical X-ray photoelectron spectroscopy," J. Am. Chem. Soc. **141**, 6537 (2019).

[113]Z. Wu, Y.-Q. Su, E. J. M. Hensen, X. Tian, C. You, and Q. Xu, "Highly stable Pt₃Ni nanowires tailored with trace Au for the oxygen reduction reaction," J. Mater. Chem. A **7**, 26402 (2019).

141

[114]Y. Feng, B. Huang, C. Yang, Q. Shao, and X. Huang, "Platinum porous nanosheets with high surface distortion and Pt utilization for enhanced oxygen reduction catalysis," Adv. Funct. Mater. **29**, 1904429 (2019).

[115]F. Kong, M. N. Banis, L. Du, L. Zhang, L. Zhang, J. Li, K. Doyle-Davis, J. Liang, Q. Liu, X. Yang, R. Li, C. Du, G. Yin, and X. Sun, "Highly stable one-dimensional Pt nanowires with modulated structural disorder towards the oxygen reduction reaction," J. Mater. Chem. A **7**, 24830 (2019).

[116]F. Calle-Vallejo, J. Tymoczko, V. Colic, Q. H. Vu, M. D. Pohl, K. Morgenstern, D. Loffreda, P. Sautet, W. Schuhmann, and A. S. Bandarenka, "Finding optimal surface sites on heterogeneous catalysts by counting nearest neighbors," Science **350**, 185 (2015).

[117]C. Wei, R. R. Rao, J. Peng, B. Huang, I. E. L. Stephens, M. Risch, Z. J. Xu, and Y. Shao-Horn, "Recommendation practices and benchmark activity for hydrogen and oxygen electrocatalysis in water splitting and fuel cells," Adv. Mater. **31**, 1806296 (2019).

[118]C. Zalitis, A. Kucernak, X. Lin, and J. Sharman, "Electrochemical measurement of intrinsic oxygen reduction reaction activity at high current densities as a function of particle size for $Pt_{4-x}Co_x/C$ ($x = 0, 1, 3$) catalysts," ACS Catal. **10**, 4361 (2020).

[119]B. Garlyyev, K. Kratzl, M. Rück, J. Michalička, J. Fichtner, J. M. Macak, T. Kratky, S. Günther, M. Cokoja, A. S. Bandarenka *et al.*, "Optimizing the size of platinum nanoparticles for enhanced mass activity in the electrochemical oxygen reduction reaction," Angew. Chem., Int. Ed. **58**, 9596 (2019).

[120]P. Varathan, S. Akula, P. Moni, and A. K. Sahu, "Natural aloe vera derived Pt supported N-doped porous carbon: A highly durable cathode catalyst of PEM fuel cell," Int. J. Hydrogen Energy **45**, 19267 (2020).

[121]K. Kocher and V. Hacker, "Polyaniline/platinum composite cathode catalysts towards durable polymer electrolyte membrane fuel cells," ChemistryOpen **9**, 1109 (2020).

[122]W.-W. Zhao, P. Bothra, Z. Lu, Y. Li, L.-P. Mei, K. Liu, Z. Zhao, G. Chen, S. Back, S. Siahrostami, A. Kulkarni, J. K. Nørskov, M. Bajdich, and Y. Cui, "Improved oxygen reduction reaction activity of nanostructured CoS_2 through electrochemical tuning," ACS Appl. Energy Mater. **2**, 8605 (2019).

[123]M. E. Kreider, A. Gallo, S. Back, Y. Liu, S. Siahrostami, D. Nordlund, R. Sinclair, J. K. Nørskov, L. A. King, and T. F. Jaramillo, "Precious metal-free nickel nitride catalyst for the oxygen reduction reaction," ACS Appl. Mater. Interfaces **11**, 26863 (2019).

[124]R. Zhong, Y. Wu, Z. Liang, W. Guo, C. Zhi, C. Qu, S. Gao, B. Zhu, H. Zhang, and R. Zou, "Fabricating hierarchically porous and Fe_3C-embeded nitrogen-rich carbon nanofibers as exceptional electocatalysts for oxygen reduction," Carbon **142**, 115 (2019).

[125]R. Wu, X. Wan, J. Deng, X. Huang, S. Chen, W. Ding, L. Li, Q. Liao, and Z. Wei, "NaCl protected synthesis of 3D hierarchical metal-free porous nitrogen-doped carbon catalysts for the oxygen reduction reaction in acidic electrolyte," Chem. Commun. **55**, 9023 (2019).

[126]K. Tu, L. Zou, C. Yang, Y. Su, C. Lu, J. Zhu, F. Zhang, C. Ke, and X. Zhuang, "Ionic polyimide derived porous carbon nanosheets as high-efficiency oxygen reduction catalysts for Zn-air batteries," Chem. Eur. J. **26**, 6525 (2020).

[127]R. Kobayashi, T. Ishii, Y. Imashiro, and J. Ozaki, "Synthesis of P- and N-doped carbon catalysts for the oxygen reduction reaction via controlled phosphoric acid treatment of folic acid," Beilstein J. Nanotechnol. **10**, 1497 (2019).

[128]R. Li, F. Liu, Y. Zhang, M. Guo, and D. Liu, "Nitrogen, sulfur Co-doped hierarchically porous carbon as a metal-free electrocatalyst for oxygen reduction and carbon dioxide reduction reaction," ACS Appl. Mater. Interfaces **12**, 44578 (2020).

[129]Y. Wang, S. Wang, R. Li, H. Li, Z. Guo, B. Chen, R. Li, Q. Yao, X. Zhang, H. Chen, Y. Li, K. Qu, and Y. Zheng, "A simple strategy for tridoped porous carbon nanosheet as superior electrocatalyst for bifunctional oxygen reduction and hydrogen evolution reactions," Carbon **162**, 586 (2020).

[130]Y. Deng, B. Chi, J. Li, G. Wang, L. Zheng, X. Shi, Z. Cui, L. Du, S. Liao, K. Zang, J. Luo, Y. Hu, and X. Sun, "Atomic Fe-doped MOF-derived carbon polyhedrons with high active-center density and ultra-high performance toward PEM fuel cells," Adv. Energy Mater. **9**, 1802856 (2019).

[131]L. Gao, M. Xiao, Z. Jin, C. Liu, J. Ge, and W. Xing, "Hydrogen etching induced hierarchical meso/micro-pore structure with increased active density to boost ORR performance of Fe–N–C catalyst," J. Energy Chem. **35**, 17 (2019).

[132]E. Luo, H. Zhang, X. Wang, L. Gao, L. Gong, T. Zhao, Z. Jin, J. Ge, Z. Jiang, C. Liu, and W. Xing, "Single-atom Cr–N_4 sites designed for durable oxygen reduction catalysis in acid media," Angew. Chem., Int. Ed. **58**, 12469 (2019).

[133]K. Liu, Z. Qiao, S. Hwang, Z. Liu, H. Zhang, D. Su, H. Xu, G. Wu, and G. Wang, "Mn- and N- doped carbon as promising catalysts for oxygen reduction reaction: Theoretical prediction and experimental validation," Appl. Catal. B **243**, 195 (2019).

[134]X. Qin, Y. Huang, K. Wang, T. Xu, Y. Wang, P. Liu, Y. Kang, and Y. Zhang, "Novel hierarchically porous Ti-MOFs/nitrogen-doped graphene nanocomposite served as high efficient oxygen reduction reaction catalyst for fuel cells application," Electrochim. Acta **297**, 805 (2019).

[135]J. Li, S. Chen, N. Yang, M. Deng, S. Ibraheem, J. Deng, J. Li, L. Li, and Z. Wei, "Ultrahigh-loading zinc single-atom catalyst for highly efficient oxygen reduction in both acidic and alkaline media," Angew. Chem., Int. Ed. **58**, 7035 (2019).

[136]X. X. Wang, D. A. Cullen, Y.-T. Pan, S. Hwang, M. Wang, Z. Feng, J. Wang, M. H. Engelhard, H. Zhang, Y. He *et al.*, "Nitrogen-coordinated single cobalt atom catalysts for oxygen reduction in proton exchange membrane fuel cells," Adv. Mater. **30**, 1706758 (2018).

[137]G. Chen, P. Liu, Z. Liao, F. Sun, Y. He, H. Zhong, T. Zhang, E. Zschech, M. Chen, G. Wu, J. Zhang, and X. Feng, "Zinc-mediated template synthesis of Fe–N–C electrocatalysts with densely accessible Fe-N_x active sites for efficient oxygen reduction," Adv. Mater. **32**, 1907399 (2020).

[138]X. Wang, Y. Jia, X. Mao, D. Liu, W. He, J. Li, J. Liu, X. Yan, J. Chen, L. Song, A. Du, and X. Yao, "Edge-rich Fe–N_4 active sites in defective carbon for oxygen reduction catalysis," Adv. Mater. **32**, 2000966 (2020).

[139]Y. Deng, X. Tian, B. Chi, Q. Wang, W. Ni, Y. Gao, Z. Liu, J. Luo, C. Lin, L. Ling, F. Cheng, Y. Zhang, S. Liao, and S. Zhang, "Hierarchically open-porous carbon networks enriched with exclusive Fe–N_x active sites as efficient oxygen reduction catalysts towards acidic H_2–O_2 PEM fuel cell and alkaline Zn-air battery," Chem. Eng. J. **390**, 124479 (2020).

[140]Y. Deng, B. Chi, X. Tian, Z. Cui, E. Liu, Q. Jia, W. Fan, G. Wang, D. Dang, M. Li, K. Zang, J. Luo, Y. Hu, S. Liao, X. Sun, and S. Mukerjee, "g-C_3N_4 promoted MOF derived hollow carbon nanopolyhedra doped with high density/fraction of single Fe atoms as an ultra-high performance non-precious catalyst towards acidic ORR and PEM fuel cells," J. Mater. Chem. A **7**, 5020 (2019).

[141]M. Karuppannan, J. E. Park, H. E. Bae, Y.-H. Cho, and O. J. Kwon, "A nitrogen and fluorine enriched Fe/Fe_3C@C oxygen reduction reaction electrocatalyst for anion/proton exchange membrane fuel cells," Nanoscale **12**, 2542 (2020).

[142]X. Wan, X. Liu, Y. Li, R. Yu, L. Zheng, W. Yan, H. Wang, M. Xu, and J. Shui, "Fe–N–C electrocatalyst with dense active sites and efficient mass transport for high-performance proton exchange membrane fuel cells," Nat. Catal. **2**, 259 (2019).

[143]N. Zhang, T. Zhou, M. Chen, H. Feng, R. Yuan, C. Zhong, W. Yan, Y. Tian, X. Wu, W. Chu, C. Wu, and Y. Xie, "High-purity pyrrole-type FeN_4 sites as a superior oxygen reduction electrocatalyst," Energy Environ. Sci. **13**, 111 (2020).

[144]K. Kumar, L. Dubau, M. Mermoux, J. Li, A. Zitolo, J. Nelayah, F. Jaouen, and F. Maillard, "On the influence of oxygen on the degradation of Fe–N–C catalysts," Angew. Chem., Int. Ed. **59**, 3235 (2020).

[145]S. Chen, N. Zhang, C. W. Narváez Villarrubia, X. Huang, L. Xie, X. Wang, X. Kong, H. Xu, G. Wu, J. Zeng, and H.-L. Wang, "Single Fe atoms anchored by short-range ordered nanographene boost oxygen reduction reaction in acidic media," Nano Energy **66**, 104164 (2019).

[146]Y. Mun, S. Lee, K. Kim, S. Kim, S. Lee, J. W. Han, and J. Lee, "Versatile strategy for tuning ORR activity of a single Fe–N_4 site by controlling electron-withdrawing/donating properties of a carbon plane," J. Am. Chem. Soc. **141**, 6254 (2019).

[147]K. Artyushkova, S. Rojas-Carbonell, C. Santoro, E. Weiler, A. Serov, R. Awais, R. R. Gokhale, and P. Atanassov, "Correlation between synthesis and performance of Fe-based PGM-free catalysts in acidic and alkaline media: Evolution of surface chemistry and morphology," ACS Appl. Energy Mater. **2**, 5406 (2019).

[148]X. Ao, W. Zhang, Z. Li, J.-G. Li, L. Soule, X. Huang, W.-H. Chiang, H. M. Chen, C. Wang, M. Liu, and X. C. Zeng, "Markedly enhanced oxygen reduction activity of single-atom Fe catalysts via integration with Fe nanoclusters," ACS Nano **13**, 11853 (2019).

[149]G. Wu and Y. Nie, "N, S codoped iron-carbon-based electrocatalyst for oxygen reduction reaction via salt recrystallization strategy," Chem. Lett. **50**, 124 (2021).

[150]D. Liu, B. Wang, H. Li, S. Huang, M. Liu, J. Wang, Q. Wang, J. Zhang, and Y. Zhao, "Distinguished Zn,Co-N_x-C-S_y active sites confined in dentric carbon for highly efficient oxygen reduction reaction and flexible Zn-air batteries," Nano Energy **58**, 277 (2019).

[151]H. Jin, H. Zhou, D. He, Z. Wang, Q. Wu, Q. Liang, S. Liu, and S. Mu, "MOF-derived 3D Fe–N–S Co-doped carbon matrix/nanotube nanocomposites with advanced oxygen reduction activity and stability in both acidic and alkaline media," Appl. Catal. B **250**, 143 (2019).

[152]J. Liu, L. Xu, Y. Deng, X. Zhu, J. Deng, J. Lian, J. Wu, J. Qian, H. Xu, S. Yuan, H. Li, and P. M. Ajayan, "Metallic cobalt nanoparticles embedded in sulfur and nitrogen Co-doped rambutan-like nanocarbons for the oxygen reduction reaction under both acidic and alkaline conditions," J. Mater. Chem. A. **7**, 14291 (2019).

[153]X. Yang, Y. Wang, G. Zhang, L. Du, L. Yang, M. Markiewicz, J. Choi, R. Chenitz, and S. Sun, "SiO_2-Fe/N/C catalyst with enhanced mass transport in PEM fuel cells," Appl. Catal. B **264**, 118523 (2020).

[154]J.-C. Li, F. Xiao, H. Zhong, T. Li, M. Xu, L. Ma, M. Cheng, D. Liu, S. Feng, Q. Shi, H.-M. Cheng, C. Liu, D. Du, S. P. Beckman, X. Pan, Y. Lin, and M. Shao, "Secondary-atom-assisted synthesis of single iron atoms anchored on N-doped carbon nanowires for oxygen reduction reaction," ACS Catal. **9**, 5929 (2019).

[155]Y. Luo, J. Zhang, J. Chen, Y. Chen, Z. Li, J. Shi, G. Wang, and R. Wang, "Dual-template construction of iron–nitrogen-codoped hierarchically ordered porous carbon electrocatalyst for oxygen reduction reaction," Energy Fuels **34**, 16720 (2020).

[156]F. Razmjooei, J.-H. Yu, H.-Y. Lee, B.-J. Lee, K. P. Singh, T.-H. Kang, H.-J. Kim, and J.-S. Yu, "Single-atom iron-based electrocatalysts for high-temperature polymer electrolyte membrane fuel cell: Organometallic precursor and pore texture tailoring," ACS Appl. Energy Mater. **3**, 11164 (2020).

[157]L. Jiao, R. Zhang, G. Wan, W. Yang, X. Wan, H. Zhou, J. Shui, S.-H. Yu, and H.-L. Jiang, "Nanocasting SiO_2 into metal–organic frame works imparts dual protection to high-loading Fe single-atom electrocatalysts," Nat. Commun. **11**, 2831 (2020).

[158]J. Li, H. Zhang, W. Samarakoon, W. Shan, D. A. Cullen, S. Karakalos, M. Chen, D. Gu, K. L. More, G. Wang, Z. Feng, Z. Wang, and G. Wu, "Thermally driven structure and performance evolution of atomically dispersed FeN_4 sites for oxygen reduction," Angew. Chem., Int. Ed. **58**, 18971 (2019).

[159]X. Shi, Z. Pu, B. Chi, M. Liu, S. Yu, L. Zheng, L. Yang, T. Shu, and S. Liao, "Nitrogen and atomic Fe dual-doped porous carbon nanocubes as superior electrocatalysts for acidic H_2–O_2 PEMFC and alkaline Zn-air battery," J. Energy Chem. **59**, 388 (2021).

[160]R. Wang, Y. Yang, Y. Zhao, L. Yang, P. Yin, J. Mao, and T. Ling, "Multiscale structural engineering of atomically dispersed FeN_4 electrocatalyst for proton exchange membrane fuel cells," J. Energy Chem. **58**, 629 (2021).

[161]R. Wang, P. Zhang, Y. Wang, Y. Wang, K. Zaghib, and Z. Zhou, "ZIF-derived Co–N–C ORR catalyst with high performance in proton exchange membrane fuel cells," Prog. Nat. Sci. **30**, 855 (2020).

[162]Y. Qian, Q. Liu, E. Sarnello, C. Tang, M. Chng, J. Shui, T. Li, S. J. Pennycook, M. Han, and D. Zhao, "MOF-derived carbon networks with atomically dispersed Fe–N_x sites for oxygen reduction reaction catalysis in acidic media," ACS Mater. Lett. **1**, 37 (2019).

[163]F. Xiao, G.-L. Xu, C.-J. Sun, M. Xu, W. Wen, Q. Wang, M. Gu, S. Zhu, Y. Li, Z. Wei, X. Pan, J. Wang, K. Amine, and M. Shao, "Nitrogen-coordinated single iron atom catalysts derived from metal organic frameworks for oxygen reduction reaction," Nano Energy **61**, 60 (2019).

[164]Z. Zhu, H. Yin, Y. Wang, C. H. Chuang, L. Xing, M. Dong, Y. R. Lu, G. Casillas-Garcia, Y. Zheng, S. Chen, Y. Dou, P. Liu, Q. Cheng, and H. Zhao, "Coexisting single-atomic Fe and Ni sites on hierarchically ordered porous carbon as a highly efficient ORR electrocatalyst," Adv. Mater. **32**, 2004670 (2020).

[165]X. Zhang, Y. B. Mollamahale, D. Lyu, L. Liang, F. Yu, M. Qing, Y. Du, X. Zhang, Z. Q. Tian, and P. K. Shen, "Molecular-level design of Fe–N–C catalysts derived from Fe-dual pyridine coordination complexes for highly efficient oxygen reduction," J. Catal. **372**, 245 (2019).

[166]H. Wang, F. X. Yin, N. Liu, R. H. Kou, X. B. He, C. J. Sun, B. H. Chen, D. J. Liu, and H. Q. Yin, "Engineering Fe–Fe_3C@Fe–N–C active sites and hybrid structures from dual metal-organic frameworks for oxygen reduction reaction in H_2–O_2 fuel cell and Li–O_2 battery," Adv. Funct. Mater. **29**, 1901531 (2019).

[167]Z. Sun, J. Lin, K. Hou, L. Guan, and H. Zhan, "Pore engineering of an Fe–N–C electrocatalyst to enhance the performance for the oxygen reduction reaction by adding g-C_3N_4 into polyaniline and cyanamide as a precursor," J. Mater. Chem. A **8**, 7273 (2020).

[168]L. Zheng, S. Yu, X. Lu, W. Fan, B. Chi, Y. Ye, X. Shi, J. Zheng, X. Li, and S. Liao, "Two-dimensional bimetallic Zn/Fe-metal-organic framework (MOF)-derived porous carbon nanosheets with a high density of single/paired Fe atoms as high-performance oxygen reduction catalysts," ACS Appl. Mater. Interfaces **12**, 13878 (2020).

[169]X. Fu, N. Li, B. Ren, G. Jiang, Y. Liu, F. M. Hassan, D. su, J. Zhu, L. Yang, Z. Bai, Z. P. Cano, A. Yu, and Z. Chen, "Tailoring FeN_4 sites with edge enrichment for boosted oxygen reduction performance in proton exchange membrane fuel cell," Adv. Energy Mater. **9**, 1803737 (2019).

[170]K. Wang, H. Chen, X. Zhang, Y. Tong, S. Song, P. Tsiakaras, and Y. Wang, "Iron oxide@graphitic carbon core-shell nanoparticles embedded in ordered mesoporous N-doped carbon matrix as an efficient cathode catalyst for PEMFC," Appl. Catal. B **264**, 118468 (2020).

[171]Y. Wang and S. Berthon-Fabry, "One-pot synthesis of Fe–N–containing carbon aerogel for oxygen reduction reaction," Electrocatalysis **12**, 78 (2021).

[172]Z. Yang, Y. Wang, M. Zhu, Z. Li, W. Chen, W. Wei, T. Yuan, Y. Qu, Q. Xu, C. Zhao, X. Wang, P. Li, Y. Li, Y. Wu, and Y. Li, "Boosting oxygen reduction catalysis with Fe–N_4 sites decorated porous carbons toward fuel cells," ACS Catal. **9**, 2158 (2019).

[173]J.-C. Li, M. Cheng, T. Li, L. Ma, X. Ruan, D. Liu, H.-M. Cheng, C. Liu, D. Du, Z. Wei, Y. Lin, and M. Shao, "Carbon nanotube-linked hollow carbon nanospheres doped with iron and nitrogen as single-atom catalysts for the oxygen reduction reaction in acidic solutions," J. Mater. Chem. A **7**, 14478 (2019).

[174]D. Liu, J.-C. Li, Q. Shi, S. Feng, Z. Lyu, S. Ding, L. Hao, Q. Zhang, C. Wang, M. Xu, T. Li, E. Sarnello, D. Du, and Y. Lin, "Atomically isolated iron atom anchored on carbon nanotubes for oxygen reduction reaction," ACS Appl. Mater. Interfaces **11**, 39820 (2019).

[175]D. Liu, J. C. Li, S. Ding, Z. Lyu, S. Feng, H. Tian, C. Huyan, M. Xu, T. Li, D. Du, P. Liu, M. Shao, and Y. Lin, "2D single-atom catalyst with optimized iron sites produced by thermal melting of metal-organic frameworks for oxygen reduction reaction," Small Methods **4**, 1900827 (2020).

[176]Y. He, S. Hwang, D. A. Cullen, M. A. Uddin, L. Langhorst, B. Li, S. Karakalos, A. J. Kropf, E. C. Wegener, J. Sokolowski, M. Chen, D. Myers, D. Su, K. L. More, G. Wang, S. Litster, and G. Wu, "Highly active atomically dispersed CoN_4 fuel cellcathode catalysts derived from surfactant-assisted MOFs: Carbon-shell confinement strategy," Energy Environ. Sci. **12**, 250 (2019).

[177]C.-L. Zhang, B.-R. Lu, F.-H. Cao, Z.-Y. Wu, W. Zhang, H.-P. Cong, and S.-H. Yu, "Electrospun metal-organic framework nanoparticle fibers and their derived electrocatalysts for oxygen reduction reaction," Nano Energy **55**, 226 (2019).

[178]X. Wen, L. Bai, M. Li, and J. Guan, "Atomically dispersed cobalt- and nitrogen-codoped graphene toward bifunctional catalysis of oxygen reduction and hydrogen evolution reactions," ACS Sustainable Chem. Eng. **7**, 9249 (2019).

[179]Y. Zhou, W. Yang, W. Utetiwabo, Y.-m. Lian, X. Yin, L. Zhou, P. Yu, R. Chen, and S. Sun, "Revealing of active sites and catalytic mechanism in N-coordinated Fe, Ni dual-doped carbon with superior acidic oxygen reduction than single-atom catalyst," J. Phys. Chem. Lett. **11**, 1404 (2020).

[180]H. Zhang, W. Xia, H. Shen, W. Guo, Z. Liang, K. Zhang, Y. Wu, B. Zhu, and R. Zou, "Antiperovskite intermetallic nanoparticles for enhanced oxygen reduction," Angew. Chem., Int. Ed. **59**, 1871 (2019).

[181]H. Yoon, S. Lee, S. Oh, H. Park, S. Choi, and M. Oh, "Synthesis of bimetallic conductive 2D metal–organic framework (Co_xNi_y-CAT) and its mass production: Enhanced electrochemical oxygen reduction activity," Small **15**, 1805232 (2019).

[182]J. Zang, F. Wang, Q. Cheng, G. Wang, L. Ma, C. Chen, L. Yang, Z. Zou, D. Xie, and H. Yang, "Cobalt/zinc dual-sites coordinated with nitrogen in nanofibers enabling efficient and durable oxygen reduction reaction in acidic fuel cells," J. Mater. Chem. A **8**, 3686 (2020).

[183]Z. Lu, B. Wang, Y. Hu, W. Liu, Y. Zhao, R. Yang, Z. Li, J. Luo, B. Chi, Z. Jiang, M. Li, S. Mu, S. Liao, J. Zhang, and X. Sun, "An isolated zinc–cobalt atomic pair

for highly active and durable oxygen reduction," Angew. Chem., Int. Ed. **131**, 2648 (2019).

[184] W. Ye, S. Chen, Y. Lin, L. Yang, S. Chen, X. Zheng, Z. Qi, C. Wang, R. Long, M. Chen, J. Zhu, P. Gao, L. Song, J. Jiang, and Y. Xiong, "Precisely tuning the number of Fe atoms in clusters on N-doped carbon toward acidic oxygen reduction reaction," Chem **5**, 2865 (2019).

[185] N. Zhang, T. Zhou, J. Ge, Y. Lin, Z. Du, C. Zhong, W. Wang, Q. Jiao, R. Yuan, Y. Tian, W. Chu, C. Wu, and Y. Xie, "High-density planar-like Fe_2N_6 structure catalyzes efficient oxygen reduction," Matter **3**, 509 (2020).

[186] G. Bae, M. W. Chung, S. G. Ji, F. Jaouen, and C. H. Choi, "pH effect on the H_2O_2-induced deactivation of Fe–N–C catalysts," ACS Catal. **10**, 8485 (2020).

[187] T. Reshetenko, V. Laue, U. Krewer, and K. Artyushkova, "Study of degradation and spatial performance of low Pt-loaded proton exchange membrane fuel cells under exposure to sulfur dioxide in an oxidant stream," J. Power Sources **458**, 228032 (2020).

[188] L. Wang, S. Bliznakov, R. Isseroff, Y. Zhou, X. Zuo, A. Raut, W. Wang, M. Cuiffo, T. Kim, and M. H. Rafailovich, "Enhancing proton exchange membrane fuel cell performance via graphene oxide surface synergy," Appl. Energy **261**, 114277 (2020).

[189] E. Daş, S. A. Gürsel, and A. B. Yurtcan, "Pt-alloy decorated graphene as an efficient electrocatalyst for PEM fuel cell reactions," J. Supercrit. Fluids **165**, 104962 (2020).

[190] P. Satjaritanun and I. V. Zenyuk, "Water management strategies for PGM-free catalyst layers for polymer electrolyte fuel cells," Curr. Opin. Electrochem. **25**, 100622 (2021).

[191] J. Liu, M. R. Talarposhti, T. Asset, D. C. Sabarirajan, D. Y. Parkinson, P. Atanassov, and I. V. Zenyuk, "Understanding the role of interfaces for water management in platinum group metal-free electrodes in polymer electrolyte fuel cells," ACS Appl. Energy Mater. **2**, 3542 (2019).

[192] A. Baricci, A. Bisello, A. Serov, M. Odgaard, P. Atanassov, and A. Casalegno, "Analysis of the effect of catalyst layer thickness on the performance and durability of platinum group metal-free catalysts for polymer electrolyte membrane fuel cells," Sustainable Energy Fuels **3**, 3375 (2019).

[193] T. Reshetenko, G. Randolf, M. Odgaard, B. Zulevi, A. Serov, and A. Kulikovsky, "The effect of proton conductivity of Fe–N–C–based cathode on PEM fuel cell performance," J. Electrochem. Soc. **167**, 084501 (2020).

[194] D. Seeberger, D. McLaughlin, P. Hauenstein, and S. Thiele, "Bipolar-interface fuel cells—An underestimated membrane electrode assembly concept for PGM free ORR catalysts," Sustainable Energy Fuels **4**, 2508 (2020).

[195] A. Lotrič, M. Sekavčnik, I. Kuštrin, and M. Mori, "Life-cycle assessment of hydrogen technologies with the focus on EU critical raw materials and end-of-life strategies," Int. J. Hydrogen Energy **46**, 10143 (2021).

[196] C. Hagelüken, "Recycling the platinum group metals: A european perspective," Platinum Met. Rev. **56**, 29 (2012).

[197] R. Sharma, K. R. Nielsen, P. B. Lund, S. B. Simonsen, L. Grahl-Madsen, and S. M. Andersen, "Sustainable platinum recycling through electrochemical dissolution of platinum nanoparticles from fuel cell electrodes," ChemElectroChem **6**, 4471 (2019).

[198] R. Sharma, S. J. Andreasen, J. Chamier, and S. M. Andersen, "Pt/C electrocatalyst synthesis from recycling of the spent PEMFC membrane electrode assembly: A closed loop circular economy," J. Electrochem. Soc. **166**, F963 (2019).

144

Schedule

The schedule of this work is shown schematically in the following. This doctoral thesis was performed within 3 years and 2.5 months.